Etude et développement de nouveaux matériaux et structures électroactifs pour la récupération d'énergie

Liuqing Wang

$N°$ d'ordre 2014-ISAL-0083 Année 2014

THÈSE

présentée devant

l'Institut National des Sciences Appliquées de Lyon

par

Liuqing WANG

pour obtenir le grade de DOCTEUR

École doctorale : Électronique, Électrotechnique et Automatique de Lyon

Spécialité : Énergie et Systèmes

Soutenue le 05 Novembre 2014 devant la commission d'examen

Étude et développement de nouveaux matériaux et structures électroactifs pour la récupération d'énergie

-

Development of energy harvesting systems based on new electroactive materials and structures

Membres du jury :

Yves	BERNARD	Professeur à l'Université Paris Sud	Rapporteur
Frédéric	GIRAUD	Maître de Conférences HDR à l'Université Lille 1	Rapporteur
Benoît	GUIFFARD	Professeur à l'Université de Nantes	Examinateur
Adrien	BADEL	Maître de Conférences à l'Université de Savoie	Examinateur
Lionel	PETIT	Professeur à l'INSA de Lyon	Directeur
Mickaël	LALLART	Maître de Conférences à l'INSA de Lyon	Co-directeur
Gaël	SEBALD	Maître de Conférences HDR à l'INSA de Lyon	Invité

Laboratoire de Génie Electrique et Ferroélectricité (LGEF)
de l'INSA de Lyon

INSA Direction de la Recherche - Ecoles Doctorales – Quinquennal 2011-2015

SIGLE	ECOLE DOCTORALE	NOM ET COORDONNEES DU RESPONSABLE
CHIMIE	**CHIMIE DE LYON** **http://www.edchimie-lyon.fr** Insa : R. GOURDON	M. Jean Marc LANCELIN Université de Lyon – Collège Doctoral Bât ESCPE 43 bd du 11 novembre 1918 69622 VILLEURBANNE Cedex Tél : 04.72.43 13 95 directeur@edchimie-lyon.fr
E.E.A.	**ELECTRONIQUE, ELECTROTECHNIQUE, AUTOMATIQUE** **http://edeea.ec-lyon.fr** Secrétariat : M.C. HAVGOUDOUKIAN eea@ec-lyon.fr	M. Gérard SCORLETTI Ecole Centrale de Lyon 36 avenue Guy de Collongue 69134 ECULLY Tél : 04.72.18 60 97 Fax : 04 78 43 37 17 Gerard.scorletti@ec-lyon.fr
E2M2	**EVOLUTION, ECOSYSTEME, MICROBIOLOGIE, MODELISATION** **http://e2m2.universite-lyon.fr** Insa : H. CHARLES	Mme Gudrun BORNETTE CNRS UMR 5023 LEHNA Université Claude Bernard Lyon 1 Bât Forel 43 bd du 11 novembre 1918 69622 VILLEURBANNE Cédex Tél : 04.72.43.12.94 e2m2@biomserv.univ-lyon1.fr
EDISS	**INTERDISCIPLINAIRE SCIENCES-SANTE** **http://ww2.ibcp.fr/ediss** Sec : Safia AIT CHALAL Insa : M. LAGARDE	M. Didier REVEL Hôpital Louis Pradel Bâtiment Central 28 Avenue Doyen Lépine 69677 BRON Tél : 04.72.68 49 09 Fax : 04 72 35 49 16 Didier.revel@creatis.uni-lyon1.fr
INFOMATHS	**INFORMATIQUE ET MATHEMATIQUES** **http://infomaths.univ-lyon1.fr**	M. Johannes KELLENDONK Université Claude Bernard Lyon 1 LIRIS - INFOMATHS Bâtiment Nautibus 43 bd du 11 novembre 1918 69622 VILLEURBANNE Cedex Tél : 04.72. 43.19.05 Fax 04 72 43 13 10 infomaths@bat710.univ-lyon1.fr
Matériaux	**MATERIAUX DE LYON**	M. Jean-Yves BUFFIERE Secrétaire : Mériem LABOUNE INSA de Lyon École Doctorale Matériaux Mériem LABOUNE Bâtiment Antoine de Saint-Exupéry 25bis Avenue Jean Capelle 69621 VILLEURBANNE Tel : 04 72 43 71 70 Fax : 04 72 43 72 37 ed.materiaux@insa-lyon.fr
MEGA	**MECANIQUE, ENERGETIQUE, GENIE CIVIL, ACOUSTIQUE (ED n°162)**	M. Philippe BOISSE Secrétaire : Mériem LABOUNE Adresse : INSA de Lyon École Doctorale MEGA Mériem LABOUNE Bâtiment Antoine de Saint-Exupéry 25bis Avenue Jean Capelle 69621 VILLEURBANNE Tel : 04 72 43 71 70 Fax : 04 72 43 72 37 mega@insa-lyon.fr Site web : http://www.ed-mega.com
ScSo	**ScSo*** M. OBADIA Lionel Sec : Viviane POLSINELLI Insa : J.Y. TOUSSAINT	M. OBADIA Lionel Université Lyon 2 86 rue Pasteur 69365 LYON Cedex 07 Tél : 04.78.69.72.76 Fax : 04.37.28.04.48 Lionel.Obadia@univ-lyon2.fr

*ScSo : Histoire, Geographie, Aménagement, Urbanisme, Archéologie, Science politique, Sociologie, Anthropologie

雨中山果落。

王维《秋夜独坐》

Remerciements

Cette thèse a été financée par le China Scholarship Council (CSC) et dirigée par le Prof. Lionel PETIT et le Dr. Mickaël LALLART.

Un jour, j'ai parlé avec BAO Bin du contrôle de vibration. A travers cette discussion autour de ce sujet complexe et face à l'impossibilité d'accomplir totalement l'objectif, j'ai ressenti l'impuissance des être humains. On ne peut pas influencer les particules qui ne nous appartiennent pas (sauf par le son) ; notre existence physique ne peut pas contrôler directement leurs mouvements, leurs façons de bouger. En même temps, je sens l'exception que la conception naturelle nous a laissée - l'esprit. Par cette communication invisible, incorporelle, nous influençons plus que nous ne pouvons imaginer. Et c'est aussi par cette communication perceptible que j'ai senti de l'honnêteté et de la bonté, qui sont comme des sources énergétiques tièdes coulant doucement dans le monde.

Un samedi après-midi, j'étais en train de travailler dans le laboratoire. Le soleil a traversé la fenêtre et a laissé entrer les ombres de feuilles par terre. J'ai senti une tranquillité. Toutes les reconnaissances ont débordé de mon coeur. J'ai pensé aux gens.

Lionel, je te remercie.

Mickaël, je te remercie.

On se rencontrera.

J'exprime toute ma gratitude au Prof. Yves BERNARD et au Dr. Frédérique GIRAUD d'avoir rapporté cette thèse. Je remercie de toute ma sincérité le Prof. Benoît GUIFFARD, le Dr. Adrien BADEL, le Dr. Gaël SEBALD d'avoir fait partie du jury de cette thèse. Je vous remercie d'avoir lu la thèse et de m'avoir posé des questions passionnantes.

Je remercie tous les membres du laboratoire de m'avoir accompagnée pendant les

quatre ans de recherche, de m'aider dans tous les aspects, et pour les bonjours dans un mille jours.

Je pensais qu'il y avait personne. Un jour, je me suis aperçu que vous êtes là, dans le monde. Vos positions sont comme les étoiles dans la carte universelle, étincelantes dans la mémoire.

Et toi, merci d'être là.

感谢上苍，我爱你们。

Je remercie de la tranquilité.

Résumé

La réduction drastique de la consommation des composants électroniques, a engendré une véritable explosion du nombre de dispositifs nomades et autonomes. Néanmoins, cette prolifération est à l'heure actuelle freinée par les batteries primaires, dont les capacités énergétiques limitées conduisent à une autonomie faible, sans compter les problèmes environnementaux soulevés par ces composants. Ainsi la possibilité d'exploiter les sources d'énergies directement disponibles dans l'environnement immédiat du système, conduisant au concept de "récupération d'énergie", s'est avéré une alternative intéressante pour palier les problèmes soulevés par les batteries. Dans cette optique, les travaux menés lors de cette thèse se sont penchés sur l'utilisation de source et/ou couplage novateurs permettant l'auto-alimentation.

La première partie de ces travaux s'est attelée à une nouvelle architecture pour la récupération d'énergie par effet électrostatique, dont le principe de conversion repose sur une variation de capacité. Plus particulièrement, lorsque l'énergie initialement fournie est considérée constante, il est montré que l'énergie récupérée est directement liée au rapport de capacité avant et après le mouvement. Ainsi, augmenter cette variation permet une énergie récupérée importante. Dans cette optique, une architecture basée sur une structure fractale est proposée, permettant d'augmenter les surfaces en regard lorsque les deux électrodes sont proches sans la modifier lorsqu'elles sont éloignées. Ceci permet donc d'augmenter la variation de capacité et donc la quantité d'énergie récupérée. En particulier, il est montré que l'ordre fractal optimal dépend de l'amplitude du déplacement relatif des électrodes ; un ordre important permettant d'augmenter l'énergie récupérée par cycle de plusieurs ordres de grandeur uniquement dans le cas de vibrations importantes.

Dans un deuxième temps, cette thèse s'est intéressée à l'élaboration d'un modèle simple pour la récupération d'énergie vibratoire à l'aide d'éléments électrostrictifs;

ces derniers étant particulièrement adaptés à la récupération d'énergie basse fréquence et/ou sous de grandes déformations. Le but de ce travail est de fournir un outil simple mais cependant efficace pour la conception d'interfaces électriques de récupération. Le modèle élaboré se base sur une analyse énergétique de la conversion du domaine électrique vers mécanique et vice-versa, conduisant à un jeu de deux équations couplées : une dans le domaine mécanique représentée par un système masse-ressort sur lequel la tension électrique exerce une force supplémentaire, et une dans le domaine électrique consistant en une source de courant contrôlée à la fois par la tension électrique et la vitesse, le tout en parallèle avec un élément capacitif.

Enfin, la dernière partie de ces travaux s'est intéressée à la récupération d'énergie thermique exploitant des matériaux ferromagnétiques qui ont la particularité d'avoir une perméabilité fortement dépendante de la température autour de la température de Curie. Ainsi, en appliquant un champ magnétique de polarisation ou par l'utilisation de cycles dérivées de la thermodynamique (Ericsson ou Stirling), il est possible de naturellement obtenir une variation de tension en sortie de l'élément ferromagnétique. Connecté à une charge, de l'énergie électrique peut donc être récupérée à partir de l'énergie thermique. L'étude montre par ailleurs des pistes d'amélioration, comme l'utilisation de matériaux à faibles pertes ou, moins immédiat, l'utilisation de matériaux dont la perméabilité reste relativement faible.

Mots-clés : *récupération d'énergie, électromécanique, électrocalorique, électrostatique, électrostrictif, ferromagnétique*

Abstract

This thesis has been devoted to electrostatic mechanical energy harvesting based on capacitors inspired by fractal geometry, to mechanical energy harvesting based on beams with electrostrictive polymers, and to thermal energy harvesting based on ferromagnetic materials.

For electrostatic energy harvesting without electrets, interdigitated capacitors are usually applied as in-plane overlap varying and in-plane gap closing electrostatic generators. In consideration of the limit of aspect ratio for fingers in the capacitor, we would like to improve the capacitor configuration by taking advantage of self-similarity patterns. The concept is to gradually add fingers of smaller widths between original ones to form a mountain-shape capacitor. According to the different width ranges of capacitors, they are classified as of different orders whose performances vary with the vibration amplitude. Harvested energy over one cycle for capacitors of order 1, 2 and 3 has been demonstrated by theoretical and FEM results. In application, the order of capacitor needs to be properly chosen to maximize the harvested energy.

Electrostrictive polymer (polyurethane) has been utilized along with a beam to perform mechanical energy harvesting. Two models have been analyzed: clamped-free beam with a polymer film attached at the clamped end, clamped-free bimorph beam. The simple model for electrostrictive devices under flexural solicitation is set up on the base of analysis of energy conversion and it shows that the electrostrictive system can be reduced to a simple spring-mass-damper system with a quadratic dependence with the applied voltage on the mechanical side and to a current source controlled by the applied voltage with a capacitive internal impedance on the electrical side. Experiments based on the clamped-free beam with a polymer film attached to the clamped end have been carried out to evaluate the mechanical to electrical conversion.

The thermal energy generator is based on a ferromagnetic material, a magnet

and a coil. As the magnetic permeability of ferromagnetic materials encounters drastic variation around the Curie temperature, the concept of the generator is to take advantage of the permeability variation caused by temperature decrease to generate sharp variation in magnetic flux which induces a current in the coil. According to theoretical results, the generated current is closely related to the temperature variation and the variation velocity. Experiments have been carried out on $Ni_{30}Fe$ of which the Curie temperature is 55 °C. When the temperature decreases from 20.5 °C to −42.4 °C, the maximum power is about 4×10^{-7} W with the load to be 2 Ω.

Keywords: *energy harvesting, electromechanical, electrocaloric, electrostatic, electrostrictive, ferromagnetic*

Contents

List of Figures

List of Tables

Résumé français

Chapitre FR-I

Introduction / Etat de l'art

FR-I.1 Motivations, enjeux et principes de la récupération d'énergie

Le développement des dispositifs nomades et des réseaux de capteurs autonomes a connu une augmentation exponentielle au cours de la dernière décennie. Une étude menée parla société Ericsson a estimé que d'ici 2020, des dizaines de milliards de systèmes connectés seront déployés dans le monde entier ([Eri12]). Une croissance sans précédent s'explique par la réduction drastique de la consommation des dispositifs électroniques pour assurer une fonction particulière (Figure FR-I-1). Néanmoins, la limitation des batteries en termes de capacité et de durée de vie (Figure FR-I-2) limite tout de même la prolifération des ces systèmes. Afin de répondre à cette limitation, la possibilité d'utiliser l'énergie environnant le dispositif a récemment émergé comme alternative viable aux batteries, permettant d'étendre leur durée de vie par une recharge régulière voire même de les remplacer à termes.

Ce concept de "récupération d'énergie" couvre un large domaine, allant des disciplines de la mécanique ou thermique par exemple jusqu'au domaine de l'électricité, en passant par l'aspect matériaux. Typiquement, un système de récupération d'énergie inclut plusieurs étapes pour aller de la source originale jusqu'à l'étage de stockage de l'énergie électrique, qui sera à disposition de la charge connectée. Le diagramme du flux d'énergie typique est représenté en Figure FR-I-3, qui montre que des étapes intermédiaires, telles que la structure permettant l'énergie de la source de rentrer dans le système (par exemple une poutre dans le cas vibratoire) ou encore l'étage d'extraction de l'énergie électrique disponible sur le transducteur. Un aspect très important représenté dans cette Figure consiste en l'importance des couplages inverses (par exemple l'effet piézoélectrique inverse), qui modifie le système en

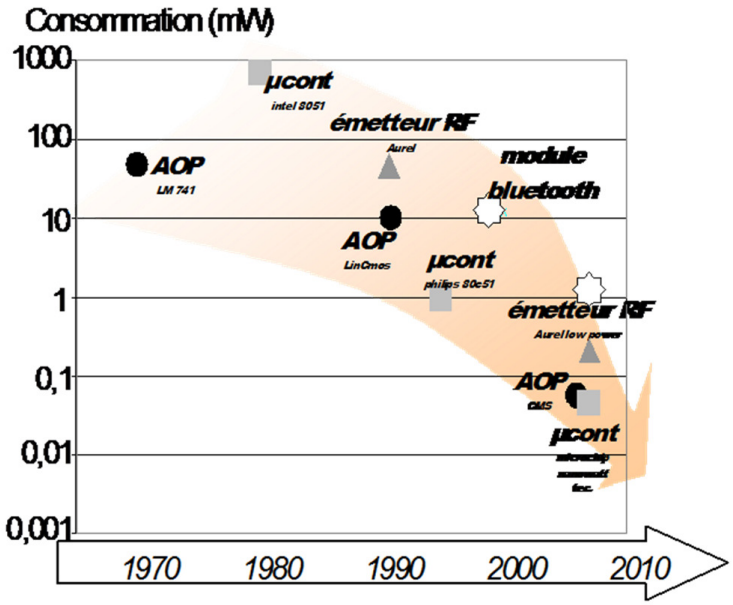

Figure FR-I-1: Consommation typique de quelques circuits électroniques en fonction du temps ([PGLM07]).

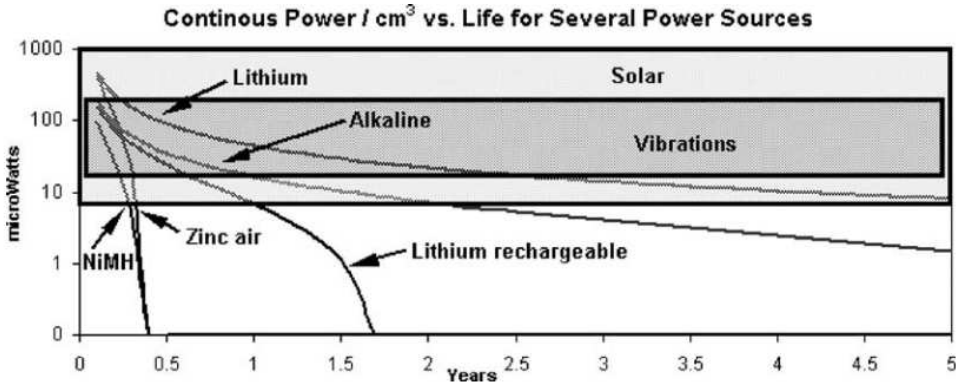

Figure FR-I-2: Densité de puissance des batteries en fonction du temps et comparaison avec les niveaux d'énergie typiques de sources environnantes ([RWR03]).

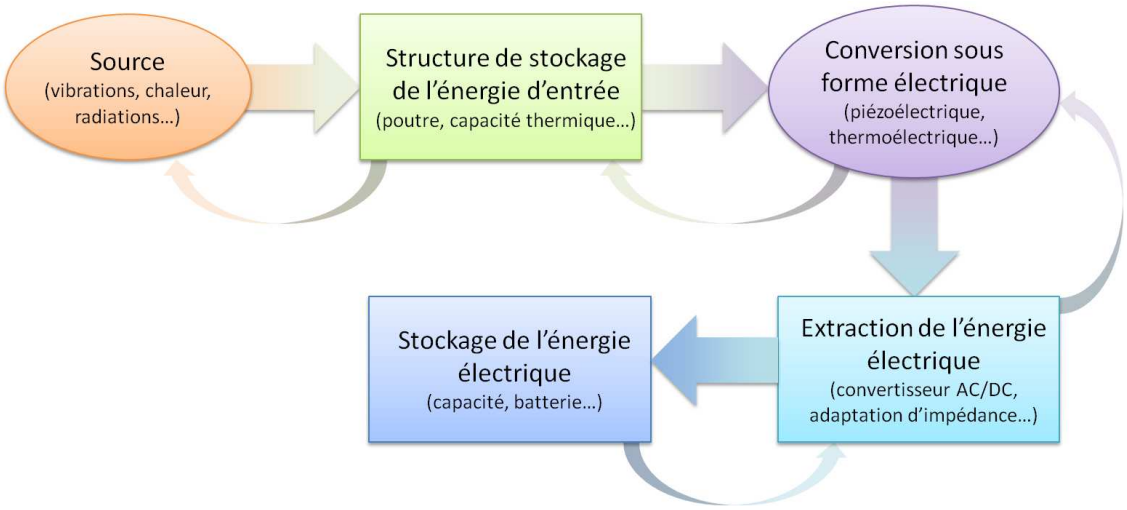

Figure FR-I-3: Chaîne de transfert d'énergie typique des microgénérateurs.

amont. Ceci montre l'importance d'une conception et d'une optimisation globale du système pour disposer d'un microgénérateur efficace.

FR-I.2 Sources potentielles

L'environnement ambiant peut présenter de nombreuses sources d'énergie. Néanmoins, selon l'application et les conditions d'utilisation, certaines sont plus adaptées que d'autres. Cette partie propose d'exposer succinctement ces différentes sources, avec une attention plus particulière sur les aspects mécaniques et thermiques, qui seront au cœur des chapitres suivants.

FR-I.2.1 Energie mécanique

L'énergie mécanique est l'une des plus aisément disponible dans l'environnement des capteurs, que ce soit par les mouvements humains, les machines tournantes ou le trafic routier par exemple. Les vibrations sont généralement disponibles sur une large gamme de fréquence, allant typiquement de quelques Hertz à quelques kiloHertz, avec des amplitudes d'accélérations également variées, ainsi que reporté dans le Tableau FR-I.1. La capture de l'énergie vibratoire potentiellement disponible peut se faire de plusieurs manières. La façon la plus directe consiste à placer le transducteur sur la structure hôte (Figure FR-I-4(a)), ce qui a pour avantage de donner une très bonne image des l'état vibratoire de la structure, mais rend l'installation et la maintenance difficile. Afin de palier à ce problème, il est possible d'utiliser

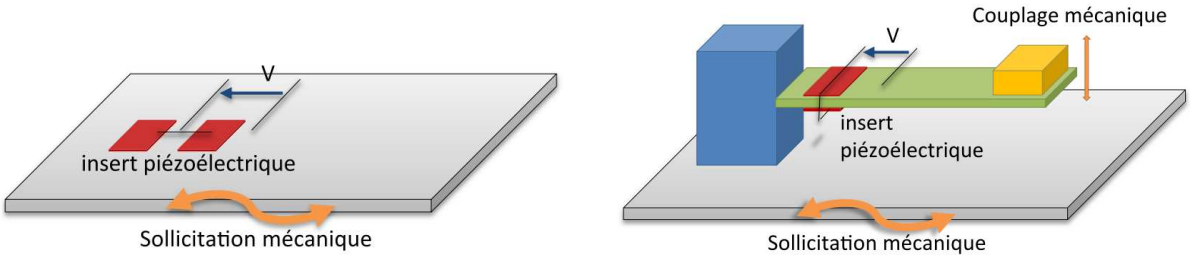

(a) (b)

Figure FR-I-4: Types généraux de conversion vibratoire ([Bad05]): (a) couplage direct ; (b) couplage indirect.

une structure mécanique supplémentaire afin de faciliter l'intégration (Figure FR-I-4(b)), au prix d'une réponse accordée sur un mode particulier et d'une sensibilité de l'accordage aux changements des paramètres environnementaux.

FR-I.2.2 Energie thermique

L'énergie thermique est l'énergie de base, présente dans tout système, ne serait-ce que par le biais de l'agitation thermique dans la matière. Bien qu'assez communément disponible dans la plupart des environnements, ce type de source est limitée, en termes de puissance de sortie, par le rendement de Carnot η_{Carnot}, donné par le rapport entre température de la

Tableau FR-I.1: Amplitude et fréquence d'accélération de sources vibratoires potentielles parmi des dispositifs commerciaux typiques ([CCTS08, Wu13])

Source de vibration	*Accélération* ($m.s^{-2}$)	*Fréquence* (*pic* - Hz)
Compartiment de moteur de voiture	12	200
Base d'une machine-outil 3 axes	10	70
Boitier d'un mixeur de cuisine	6.4	121
Sèche-linge	3.5	121
Personne tapant ses talons	3	1
Tableau de bord de voiture	3	13
Enceinte de porte juste après la fermeture de cette dernière	3	125
Petit four à micro-ondes	2.5	121
Events de climatiseur dans un immeuble commercial	0.2-1.5	60
Fenêtre proche d'une route fréquentée	0.7	100
CD dans un ordinateur portable	0.6	75
Plancher d'un étage d'un immeuble commercial fréquenté	0.2	100

source froide T_f et de la source chaude T_c:

$$\eta_{Carnot} = 1 - \frac{T_f}{T_c} \tag{FR-I.1}$$

avec les températures exprimées en Kelvin. Ainsi, à l'ambiante, ce rendement théorique maximum est relativement faible. Par exemple, pour une différence de température de 10 K à la température ambiante (25 ° C), sa valeur est de seulement $3,25$ %. Néanmoins, ceci est à balancer par le fait que les énergies mises en jeu lors de déplacement de chaleur sont très importantes.

En termes de récupération d'énergie, l'énergie thermique se présente généralement sous deux formes. La première consiste en un gradient de température entre deux points spatialement espacés (l'un correspondant à la source chaude, et l'autre à la source froide). Dans l'environnement quotidien (en addition à la chaleur générée par la corps humain), Matiko *et al.* a mené une étude intensive sur les sources d'énergies dans les bâtiments, incluant une certaine attention à la chaleur. Ainsi, il a été montré que des gradients de plusieurs dizaines de degrés peuvent facilement être atteints, notamment proche des radiateurs.

La seconde catégorie de source thermique consiste en une fluctuation temporelle de la chaleur, qui ne considère donc qu'une portion limitée de l'espace. Pour la récupération d'énergie par variation temporelle de la température, l'application visée est bien évidemment différente. Citons à titre d'exemple l'étude menée par Sébald *et al.* ([SGA09]), qui a montré que des fluctuations de température de plusieurs dizaines de degrés peuvent être observées dans l'activité quotidienne d'une personne (par exemple lors de l'entrée ou de la sortie d'un bâtiment), comme indiqué en Figure FR-I-5.

FR-I.2.3 Autres sources

La dernière source communément utilisée pour les dispositifs de récupération d'énergie à échelle centimétrique consiste en l'énergie radiative. Celle-ci peut se trouver sous différente forme, l'une des plus connues étant l'énergie solaire. Dans ce cas, les densités surfaciques de puissance incidente sont de l'ordre quelques centaines de milliWatts par centimètre carré au zénith. Néanmoins, les capacités de conversion actuelles ont des rendements qui ne dépassent pas une dizaine de pour-cent, et se situer dans les conditions optimales d'éclairement est rarement aisé.

L'autre source assez répandue d'énergie radiative réside dans les ondes magnétiques. La prolifération des moyens de télécommunication engendre ainsi un monde où les ondes sont

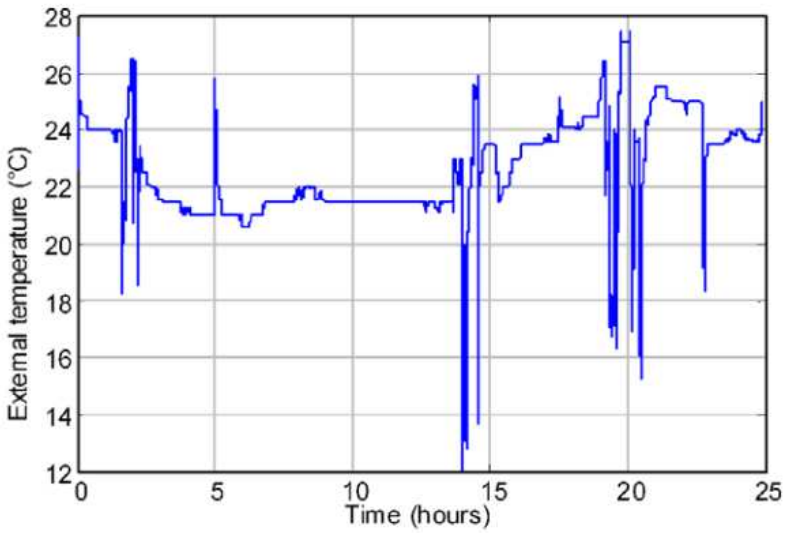

Figure FR-I-5: Température sur les vêtement d'une personne sur une période d'une journée ([SGA09]).

très présentent dans l'environnement quotidien. Néanmoins cette énergie est très limitée, notamment en champ lointain qui correspond à la très grande majorité des cas, avec des densités surfaciques de puissance inférieure au microWatt par mètre carré.

Enfin, il peut également être cités les générateurs biologiques. Dans ce cas, les biopiles tirant partie des réactions chimiques avec des sédiments, sont un exemple relativement répandu ([TGG+08]).

FR-I.3 Techniques de récupération

Les différentes sources d'énergie ayant été exposées dans la partie précédente, ce paragraphe s'intéressera plus au moyen de convertir l'énergie de ces sources sous forme électrique, et plus particulièrement pour dans le cas des sources vibratoires et thermiques, qui seront l'objet des chapitres suivants.

FR-I.3.1 Récupération sur source vibratoire

La conversion d'énergie vibratoire sous forme électrique peut se faire selon plusieurs mécanismes ; les trois manières les plus utilisées consiste en l'effet piézoélectrique, le magnétisme et l'électrostatique. L'effet piézoélectrique permet une relation directe et bidirectionnelle entre les grandeurs mécaniques que sont la contrainte et la déformation avec les grandeurs électriques de champ électrique et d'induction électrique. Cette relation peut avoir plusieurs

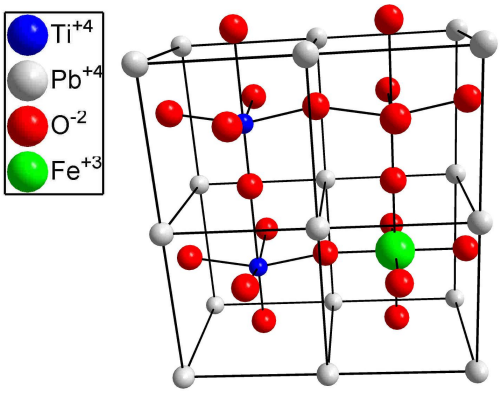

Figure FR-I-6: Exemple d'une maille cristalline de PZT [FR.I-1].

origines, la plus connue étant une non-coïncidence des barycentres des charges positives et négatives due à la non-centrosymmétrie de la maille cristalline (ainsi, la maille se déformant, la distance entre les barycentres change créant une apparition de charges en surface pour conserver l'électroneutralité en circuit ouvert), ce qui restreint par ailleurs l'effet piézoélectrique qu'à certaines classes de matériaux. Les éléments piézoélectriques, intégrables et présentant des densités de puissance assez élevés, sont ainsi très bien adaptés à la récupération d'énergie vibratoire à basse échelle. Afin de profiter pleinement des performances des éléments piézoélectriques, ceux-ci se doivent d'être placés dans les zones de plus forte déformation de la structure.

Un autre mécanisme couramment utilisé consiste en une variation de flux magnétique dans une bobine. Ainsi, par induction et selon la loi de Lenz-Faraday, une tension apparaît en circuit ouvert. La façon la plus directe d'obtenir ce changement de flux consiste à utiliser un aimant qui présente un mouvement relatif à la bobine (Figure FR-I-7). Du fait de cette nécessité de mouvement, et comme la tension générée dépend de la variation de flux, les éléments magnétiques pour la récupération d'énergie doivent être placés dans les zones de plus grande vitesse. Bien que très performants et avec des couplages électromécaniques très importants dans des dimensions relativement grandes, les densités de puissance des systèmes de récupération d'énergie magnétique sont grandement diminuées à petite échelle.

La dernière approche typique de récupération d'énergie basse échelle consiste en l'utilisation de systèmes électrostatiques basés sur la variation de capacité, qui peut être obtenue par des déplacements relatif des électrodes dans le plan ou hors du plan (Figure FR-I-8(a)). Néanmoins, une telle technique nécessite une pré-charge électrique du système, et ne peut travailler de manière autonome contrairement aux systèmes piézoélectriques ou magnétiques. Une fois chargés, ces systèmes peuvent travailler soit à tension constante (cycle d'Ericsson),

[FR.I-1] http://www.tu-darmstadt.de/fb/ch/PCIII/

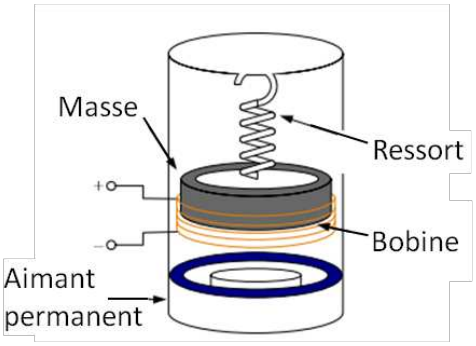

Figure FR-I-7: Principe général de la récupération d'énergie magnétique ([AC98]).

soit à charge constante (cycle de Stirling), comme indiqué en Figure FR-I-8(b).

Enfin, d'autres effets sont encore relativement peut exploités pour la récupération d'énergie vibratoire, mais suscitent un intérêt scientifique croissant. En particulier, les systèmes électrostrictifs, et en particulier les polymères électrostrictifs diélectriques, qui présentent une déformation variant de manière quadratique avec le champ appliqué et un déplacement électrique dépendant du produit de la contrainte par le champ électrique, sont des matériaux

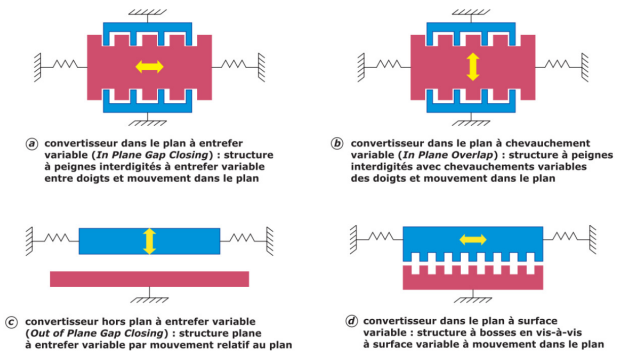

(a)

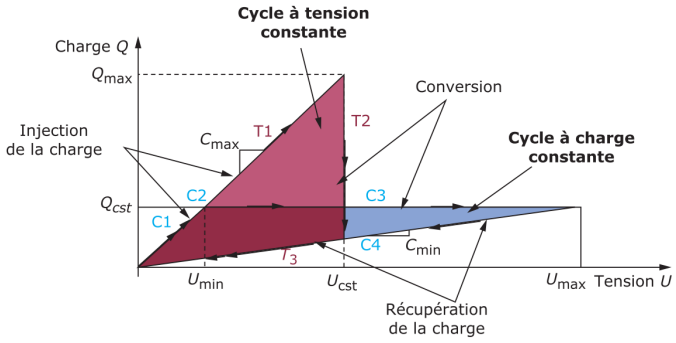

(b)

Figure FR-I-8: Topologies et exemple de cycles électrostatiques ([BDC10]).

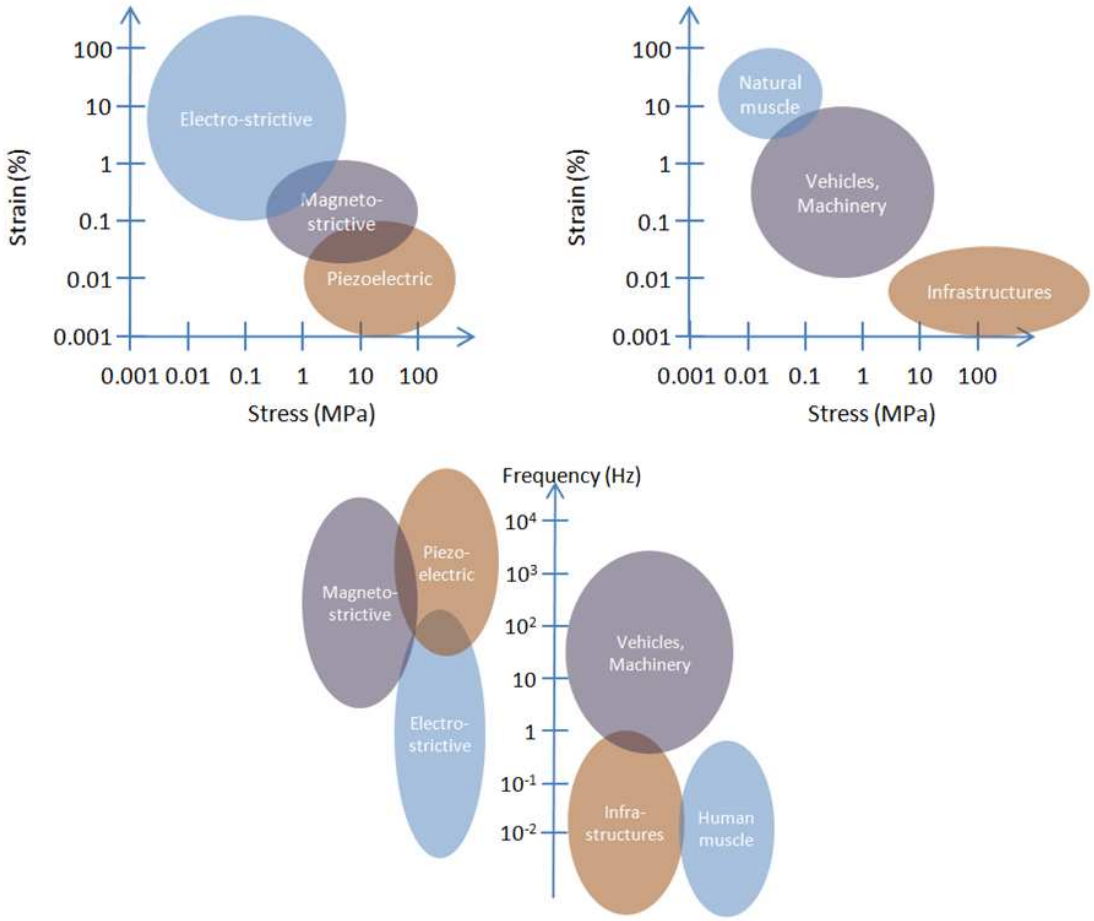

Figure FR-I-9: Place des effets de conversion et comparaison par rapport à des applications-cibles typiques ([LCGL12]).

souples, conformables avec des possibilités de grandes déformations à faible fréquence. Ceci fait ainsi d'eux des éléments de choix pour des applications nécessitant de grandes déformations à de grandes périodes temporelles ([LCGL12]). Ces matériaux nécessitent cependant l'application d'un champ électrique de polarisation pour activer leur couplage électromécanique ([Wan11, LCS+90]). De manière duale, il est également possible d'utiliser des matériaux magnétostrictifs, dont la conversion se fait par l'intermédiaire du magnétisme, et plus particulièrement de l'effet Villari.

En guise de comparaison, la Figure FR-I-9 représente la place des différents effets exposés en fonction des conditions extérieures ainsi que celle d'applications-cibles typiques.

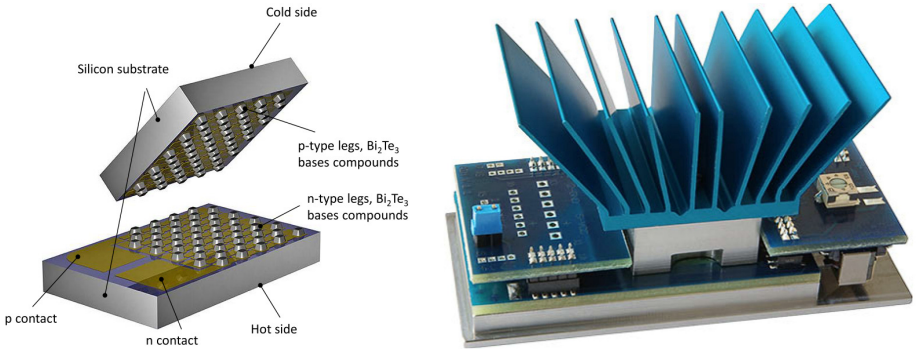

(a) (b)

Figure FR-I-10: Exemple de générateurs thermoélectriques: (a) principes et (b) réalisation (www.micropelt.com).

FR-I.3.2 Récupération sur source thermique

Ainsi que précédemment exposé, la récupération d'énergie thermique peut se faire à partir d'un gradient de température (correspondant à un flux de chaleur constant) ou via une variation temporelle de cette dernière. Dans le cas d'un gradient, l'utilisation de l'effet Seebeck sur des jonctions semi-conductrices PN permet de disposer de dispositifs thermoélectriques permettant de convertir un gradient de température en grandeurs électriques continues (Figure FR-I-10). Les performances des générateurs thermoélectriques sont généralement définies par leur figure de mérite ZT, dont la valeur dépend de l'inverse de la conductivité thermique du matériau, de sa conductivité électrique, de son coefficient Seebeck et enfin de sa température (les autres paramètres étant également dépendants de cette dernière). A l'heure actuelle, le rendement par rapport au rendement de Carnot des générateurs thermoélectriques commerciaux ne dépasse cependant pas les 10%. De plus, les générateurs thermoélectriques présentent une conductivité thermique relativement importante, ce qui rend difficile l'application du gradient (le flux de chaleur est alors très important), et nécessite l'utilisation de radiateurs (voir Figure FR-I-8(b)) pour avoir des puissances de sortie importantes.

La seconde manière de récupérer de l'énergie à partir de la chaleur se fait à partir de variation temporelle de la température. Pour ce faire, l'utilisation de matériaux pyroélectriques, qui agissent de manière similaire aux éléments piézoélectriques mais à partir de la thermique plutôt que de la mécanique (induction électrique directement dépendante de la température). Ainsi, il est possible de directement utiliser les interfaces disponibles pour les éléments piézoélectriques ([GSP+09]). L'utilisation de cycles thermodynamiques, exploitant par exemple les non-linéarités intrinsèques du matériau (transition de phase ferroélectrique-ferroélectrique

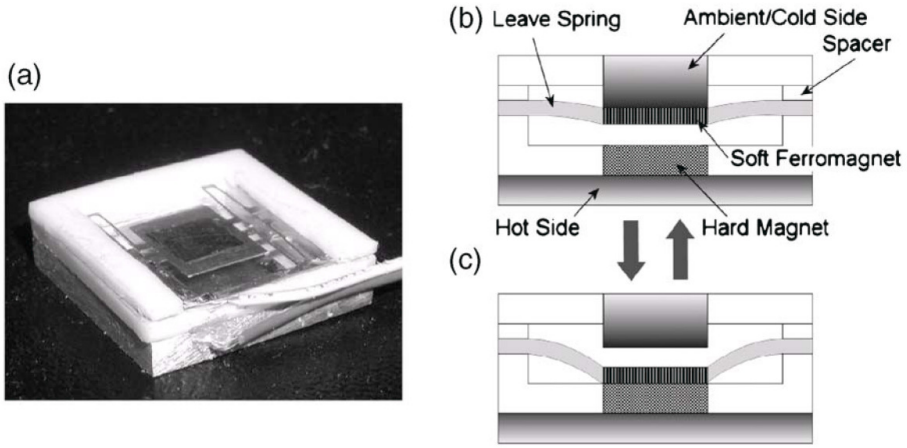

Figure FR-I-11: Machine thermique permettant la récupération d'énergie à partir de gradient de température ([UCL07]).

ou ferroélectrique-paraélectrique par exemple) permet de significativement augmenter les densités de puissance, pouvant atteindre plusieurs centaines de milliJoules par centimètre cube ([SPG08]). Bien que le mécanisme de conversion soit totalement différent, les éléments pyroélectriques peuvent dépasser les thermoélectriques en termes de densité de puissance même à des fréquences de variation de température très faibles (de l'ordre du centième de Hertz - [SPG08]). On pourra enfin noter que le principe de changement de phase pour la récupération d'énergie thermique à partir de variations temporelles de la température peut également être appliqué à d'autre effet que la pyroélectricité, comme par exemple en utilisant des polymères électrostrictifs ([ZPCG11]).

Enfin, un moyen de passer d'un gradient à une variation de température est possible par l'utilisation de machines thermiques. Citons à titre d'exemple le concept présenté par Ujihara dans ([UCL07]) qui, par l'utilisation de matériaux ferromagnétiques qui deviennent paramagnétiques au contact de la source chaude, permettent de créer des oscillations mécaniques associées à des variations de température (Figure FR-I-11).

Chapitre FR-II

Récupération d'énergie électrostatique par structure fractale

FR-II.1 Introduction / Motivations

Les récupérateurs d'énergie électrostatique sont une classe de microgénérateurs très populaires, notamment pour les microsystèmes, car ils sont facilement intégrables. Le principe de ces récupérateurs repose sur la variation de capacité induite par le déplacement relatif de deux électrodes séparées par un milieu isolant. Plusieurs configurations sont possibles, selon que la vibration est dans le plan des électrodes ou hors du plan ([BDC10]). Néanmoins, les générateurs électrostatiques souffrent d'un mécanisme de conversion nécessitant un apport initial d'énergie (via l'application d'une tension de polarisation), et il est donc nécessaire d'utiliser des cycles "actifs" dérivés des cycles thermodynamiques (typiquement Stirling ou Ericsson)[FR.II-1]. Par exemple, dans le cas d'un cycle de Stirling, le système est laissé à charge constante (circuit ouvert) lors de la vibration. Dans ce cas, il peut être montré que l'énergie globale récupérée W est donnée par:

$$W = \frac{1}{2}\left(\frac{C_{max}}{C_{min}} - 1\right) C_{max} {V_0}^2 \qquad \text{(FR-II.1)}$$

avec C_{min} et C_{max} les valeurs de capacités maximales et minimales du système et V_0 la tension initialement appliquée lors de la charge du dispositif. Cette expression montre donc clairement que l'augmentation des capacités de conversion (et donc de l'énergie récupérée) est directement liée au rapport des capacités maximales et minimales, qu'il faut donc maximiser.

[FR.II-1] L'utilisation d'électrets permet de passiver le système. Néanmoins, les niveaux d'énergie récupérée sont bien plus faibles que dans le cas de l'utilisation de cycles actifs.

Ainsi l'objectif de cette partie est de présenter une structure de capacité tirant avantage des effets d'augmentation de surface offerts par les constructions fractales afin d'augmenter la variation de capacité et donc l'énergie récupérable.

FR-II.2 Principes et modélisation de l'architecture de capacité fractale

Nous nous intéresserons ici à une structure simple de générateur électrostatique consistant en des peignes interdigités avec une vibration dans le plan, dont on ne considérera qu'une partie formée de trois doigts (Figure FR-II-1) pour des raisons de simplicité. Dans cette configuration, la capacité est donnée par, en fonction de la distance entre électrodes d et en négligeant la distance inter-électrodes d_h devant l'épaisseur des peignes, ainsi que les effets de bords et les capacités parasites:

$$C = \begin{cases} \frac{\varepsilon_0 L w}{d} + 2\frac{\varepsilon_0 (h-d) w}{d_h} & \text{pour } d \leq h \\ \frac{\varepsilon_0 L w}{d} & \text{pour } d > h \end{cases} \tag{FR-II.2}$$

Ainsi, on voit que pour maximiser la variation de capacité, il est avantageux de travailler sur le second terme (capacité latérale), en augmentant la hauteur et en diminuant la largeur des doigts (pour la largeur, ceci permet d'augmenter la densité de doigts). Malheureusement, les contraintes technologiques imposent un facteur d'échelle γ entre la largeur et la hauteur des doigts qui, de fait, limitent les capacités de conversion:

$$h_{max} = \gamma l \tag{FR-II.3}$$

Afin de dépasser les limites induites par ce facteur d'échelle, il est proposé ici de construire une capacité fractale en ajoutant progressivement des doigts à la structure. Ceci permet ainsi

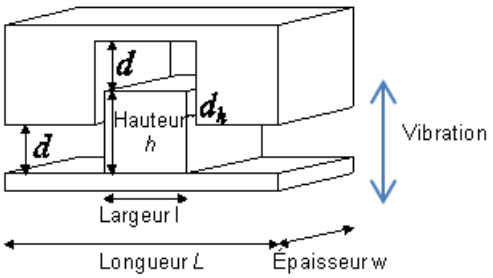

Figure FR-II-1: Configuration d'une architecture interdigitée simple.

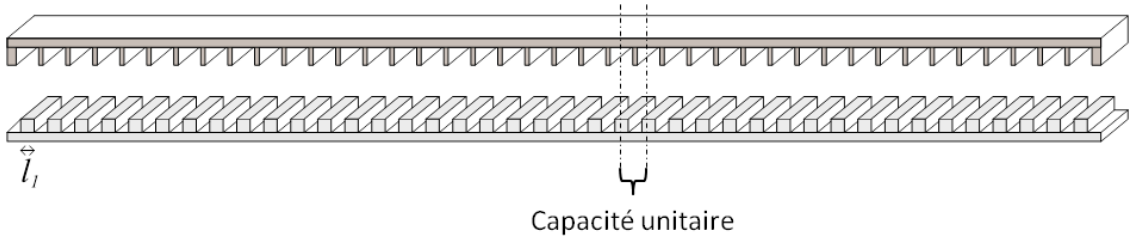

(a) Ordre 1

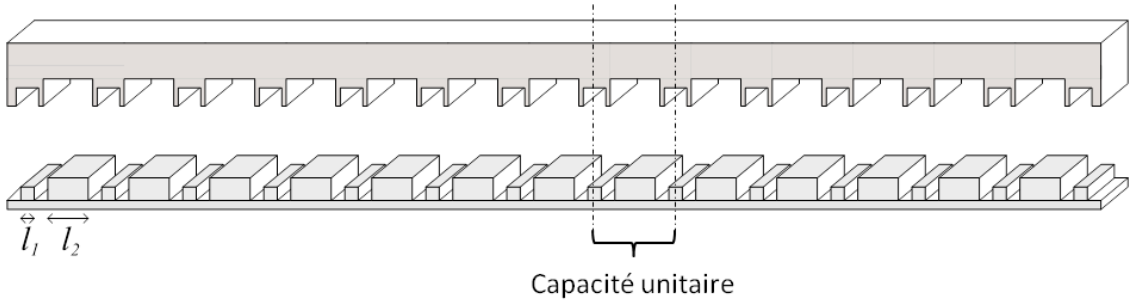

(b) Ordre 2

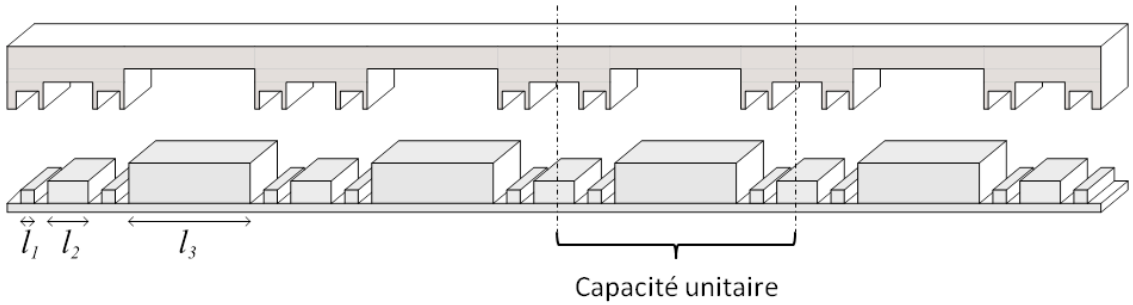

(c) Ordre 3

Figure FR-II-2: Construction "progressive" de la capacité fractale.

d'augmenter la surface latérale utilisée et donc d'augmenter la variation de capacité. Cet ajout peut se faire en considérant que la structure de base (ordre 1) correspond aux plus petites dimensions technologiquement réalisables (construction "progressive" - Figure FR-II-2) ou constitue la forme de plus grandes dimensions (construction "dégressive" - Figure FR-II-3). Dans les deux cas, la capacité surfacique (normalisée par rapport à la longueur et l'épaisseur) peut être modélisée sous les mêmes conditions que dans le cas précédent par:

$$C_{norm} = \frac{\varepsilon_0}{d} + 2\frac{\varepsilon_0 {S_v}^{1D}}{d_h} \qquad \text{(FR-II.4)}$$

où le premier terme correspond à la surface horizontale en regard et ${S_v}^{1D}$ à la surface normalisée (par rapport à la longueur totale L et l'épaisseur w) en regard entre les doigts, dont

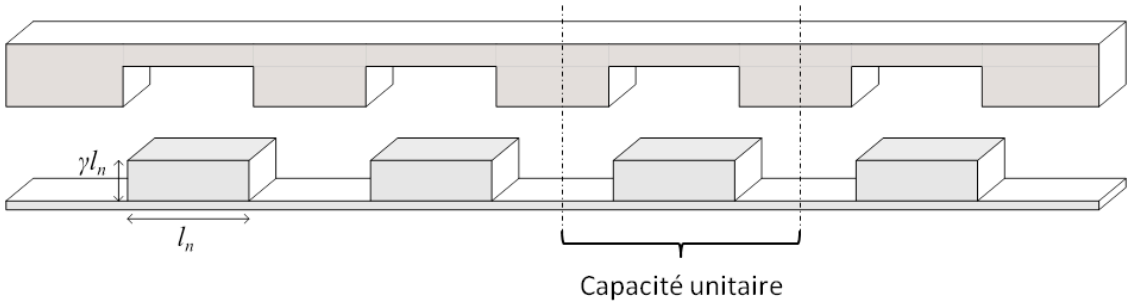

(a) Ordre 1

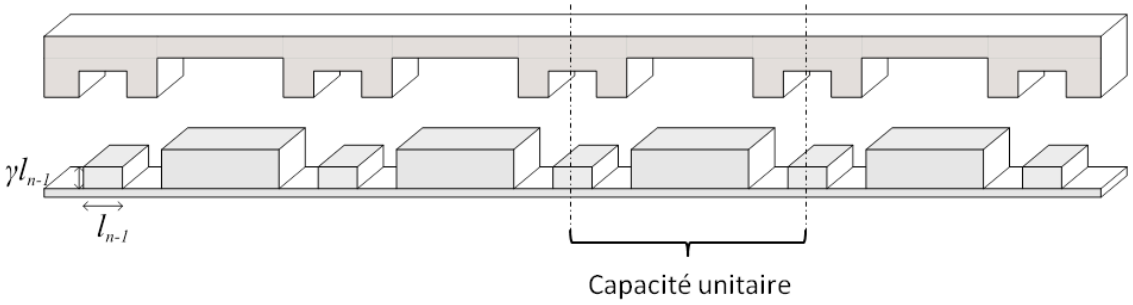

(b) Ordre 2

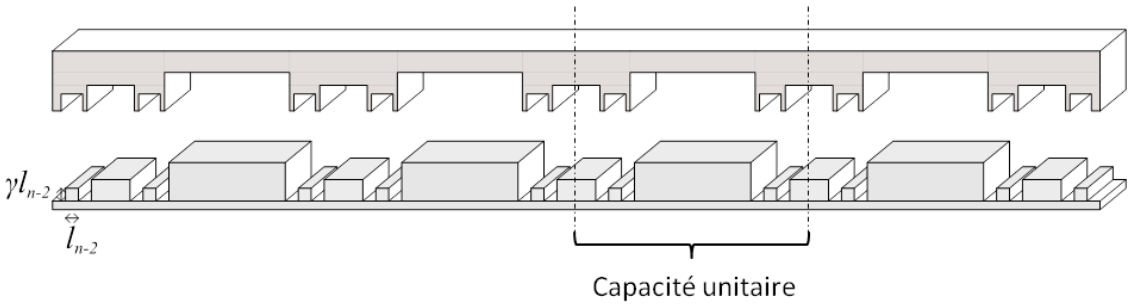

(c) Ordre 3

Figure FR-II-3: Construction "dégressive" de la capacité fractale.

l'expression pour l'ordre fractal n en fonction de la distance inter-électrode d est donnée par:

$$S_v{}^{1D} = \begin{cases} \gamma\left[2 - \left(\frac{2}{3}\right)^{n-i}\right] - 2^{n-i}\frac{d}{l_n} & \text{pour } h_{i-1} < d \leq h_i,\ 1 \leq i \leq n\ (h_0 = 0) \\ 0 & \text{pour } h_n < d \end{cases} \quad \text{(FR-II.5)}$$

Pour les deux types de constructions, l'expression de $S_v{}^{1D}$ est la même, néanmoins les hauteurs de séparation des doigts diffèrent, et sont données par:

$$h_i = 3^{i-1}\gamma l_1 \quad \text{(FR-II.6)}$$

pour la construction progressive (avec l_1 la plus petite largeur de doigt) et par:

$$h_i = 3^{i-1}\gamma\frac{L}{2} \quad \text{(FR-II.7)}$$

pour la construction dégressive (avec L la longueur totale).

FR-II.3 Résultats de simulation et expérimentaux

On se propose ici de valider par simulation par éléments finis (logiciel ANSYS) dans le cas d'une construction progressive. Les trois structures considérées sont (Figure FR-II-2):

- 40 capacités unitaires d'ordre 1
- 13 capacités unitaires d'ordre 2
- 4 capacités unitaires d'ordre 3

En prenant un facteur d'échelle $\gamma = 20$ et une distance entre les doigts d_h d'un dixième de la largeur minimale d'un doigt (prise unitaire, $l_1 = 1$), les résultats en termes de valeur capacité (normalisée par rapport à la largeur) en fonction de la distance sont représentés en Figure FR-II-4.

Cette Figure démontre clairement l'augmentation de la capacité pour des faibles déplacements entre les électrodes. On remarquera également une assez bonne corrélation entre résultats théoriques et de simulation, excepté lors de la séparation des électrodes du fait de la négligence des effets de bords en théorie. Cette Figure montre également, pour le cas de construction progressif considéré, que la rupture correspondant à la séparation des électrodes intervient plus tôt pour les ordres fractals faibles du fait de la hauteur moins importante des électrodes.

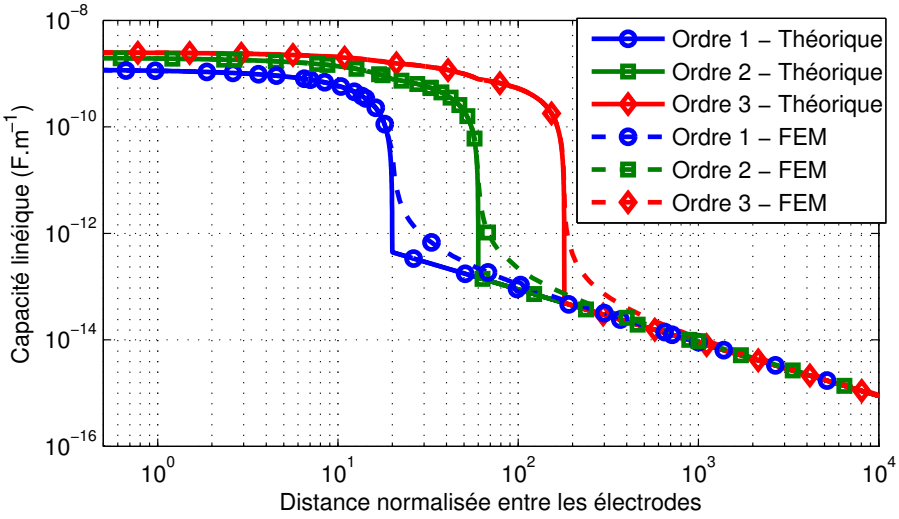

Figure FR-II-4: Résultats théoriques et de simulation de la valeur de capacité normalisée par rapport à la largeur en fonction de la distance normalisée par rapport à la largeur minimale des doigts.

Ainsi la variation de capacité intervient plus tôt, mais est moins importante que dans le cas des ordres fractals élevés.

Concernant la construction dégressive, des structures expérimentales ont été réalisées (Figure FR-II-5). Des mesures effectuées à l'impédancemètre sont représentées en Figure FR-II-6, ainsi que les prédictions théoriques. On remarque une bonne corrélation entre théorie et résultats expérimentaux, avec encore une fois une différence lors de la séparation des électrodes due aux effets de bords. Contrairement à la structure progressive, l'augmentation de l'ordre fractal est toujours bénéfique pour la variation de capacité. Néanmoins, pour un ordre donné et particulièrement pour les ordres faibles, la plus grande densité de doigts (malgré des hauteurs plus faibles) rend la structure progressive plus intéressante pour la variation de capacité (et donc pour la récupération d'énergie).

FR-II.4 Application à la récupération d'énergie

A partir des valeurs de capacités obtenues en théorie, simulation et pratique, il est ainsi possible d'estimer l'énergie récupérable en utilisant les structures fractales. Ainsi, en utilisant l'expression (FR-II.1), l'énergie normalisée récupérable par cycle pour une tension unitaire dans le cas d'une construction progressive (en théorie et par simulation) est représentée en Figure FR-II-7, et en Figure FR-II-8 pour la structure dégressive (théorie et pratique). Outre les différences déjà notées au moment de la séparation des doigts (du fait de la négligence des

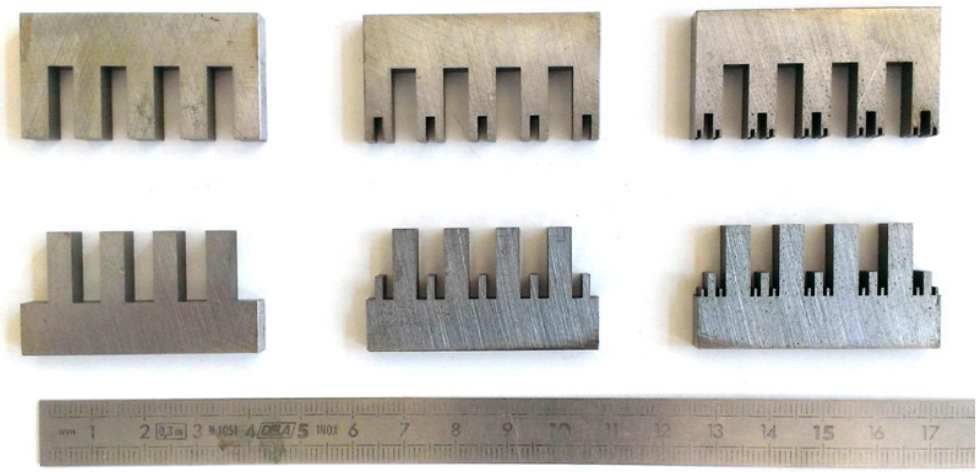

Figure FR-II-5: Structures expérimentales.

effets de bords en théorie), on notera, ainsi que précédemment supposé, une différence notable entre structure progressive et structure dégressive. Ainsi, dans le premier cas, la différence de hauteur maximale des doigts conduit à un choix d'ordre fractal étroitement lié à l'amplitude de la vibration: plus cette dernière est importante, et plus un ordre fractal élevé est à considérer. Par contre, dans le cas de la construction dégressive, un ordre fractal plus élevé conduira toujours à une énergie récupérée plus importante. Dans les deux configurations, il est ainsi possible de gagner jusqu'à un ordre de grandeur sur l'énergie récupérée en utilisant la structure fractale (avec plus de contraintes sur les amplitudes de vibration pour la structure progressive).

FR-II.5 Conclusion

Ce Chapitre s'est intéressé à la récupération d'énergie par effet électrostatique et plus précisément à une méthode pour augmenter la variation de capacité ; cette dernière étant directement liée à l'énergie qui peut être convertie et récupérée. Pour ce faire, il a été utilisé les propriétés remarquables des structures fractales pour augmenter les surfaces en regard entre les électrodes. Selon la structure envisagée (progressive ou dégressive), il a été montré théoriquement et par simulation ou expériences que l'augmentation des capacités de récupération pouvait être sujette à des conditions. En particulier, pour la structure progressive, le choix de l'ordre fractal est étroitement dépendant de l'amplitude de vibration (plus cette dernière est importante, plus l'ordre fractal optimal est élevé). Les travaux reportés ici sont bien évidemment extensibles à d'autres motifs. En particulier, en gardant un motif

similaire, il est possible d'augmenter les variations de capacité en "creusant" également les doigts (Figure FR-II-9). L'implémentation de motifs tridimensionnels, inspirés par exemple des tapis de Sierpinski, est également une piste envisageable (Figure FR-II-10).

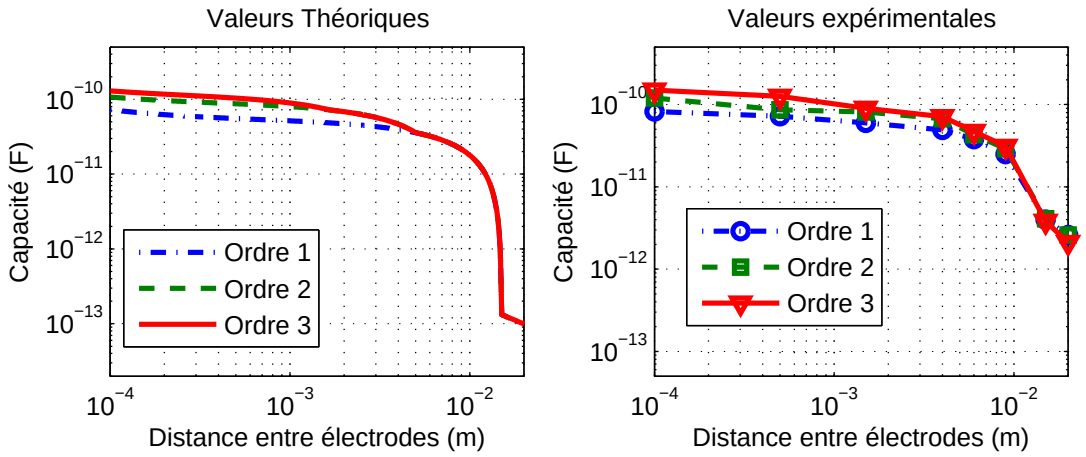

Figure FR-II-6: Résultats théoriques et expérimentaux de la valeur de capacité.

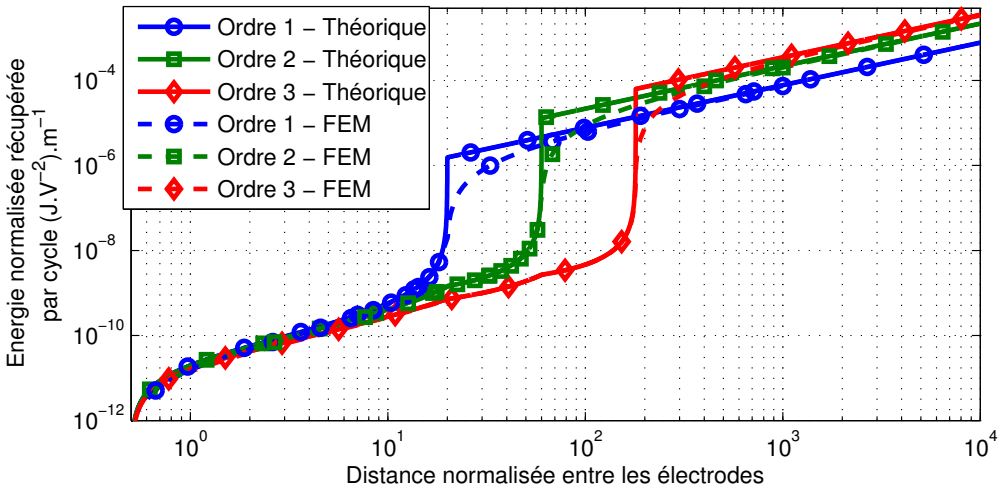

Figure FR-II-7: Estimation théorique et par simulation de l'énergie récupérée en fonction de la distance pour la structure progressive.

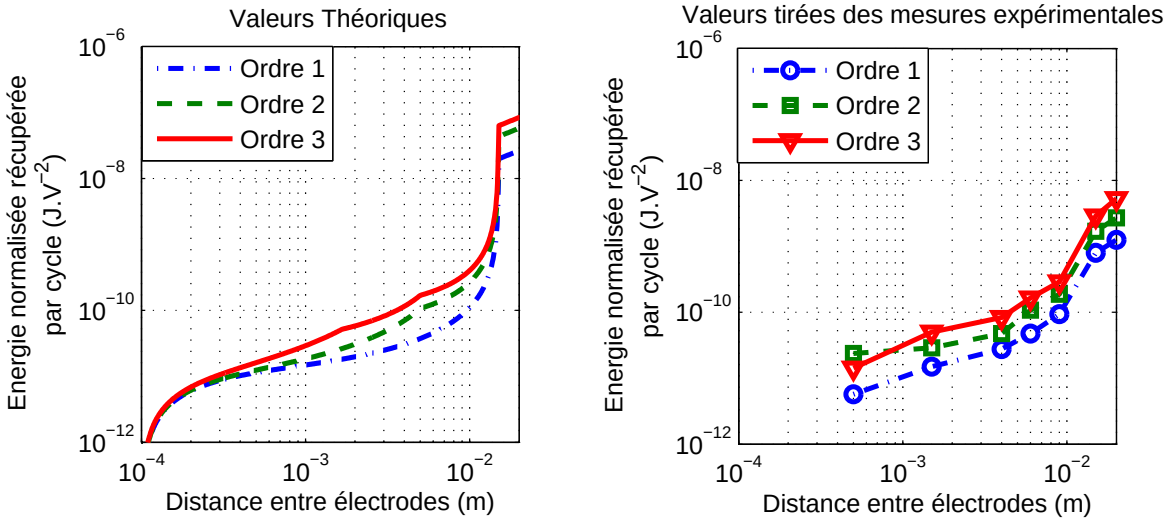

Figure FR-II-8: Estimation théorique et expérimentale de l'énergie récupérée en fonction de la distance pour la structure dégressive.

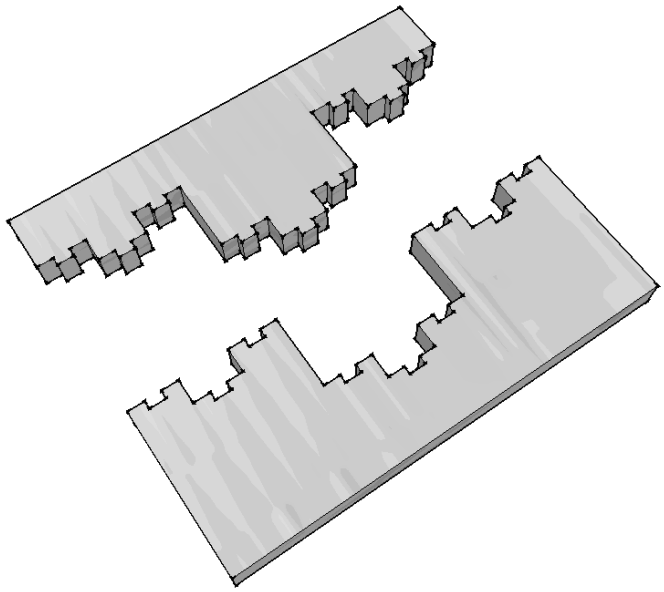

Figure FR-II-9: Capacité fractale symétrique.

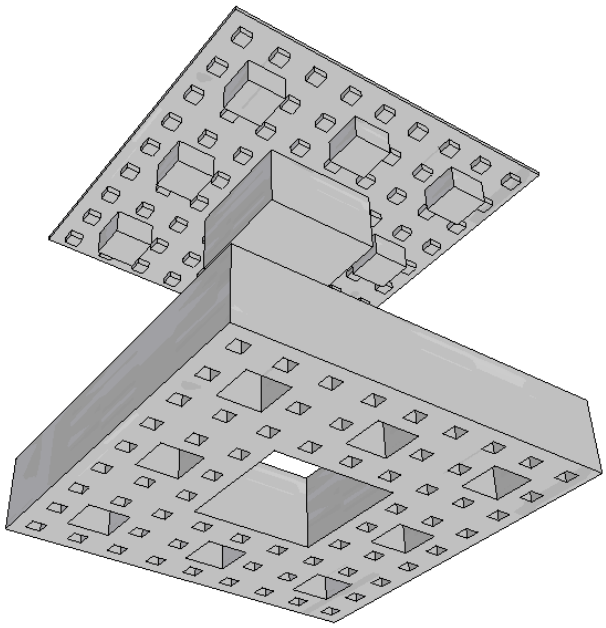

Figure FR-II-10: Capacité fractale 3D en tapis de Sierpinski.

Chapitre FR-III

Modélisation des polymères électrostrictifs pour la récupération d'énergie

FR-III.1 Introduction / Motivations

Ainsi que vu dans les parties précédentes, la récupération d'énergie vibratoire peut se faire sous des formes très différentes. Néanmoins, lorsque l'excitation se fait de manière basse fréquence et pour de larges déformations, les polymères électrostrictifs sont tout indiqués pour assurer la conversion électromécanique (Figure FR-III-1), du fait de leur flexibilité et conformabilité.

L'effet électrostrictif s'explique par l'orientation des dipôles induite par l'application d'un champ électrique, ce qui conduit à l'apparition de charges sur les électrodes et par conséquent à une force de Maxwell qui engendre une déformation ([CLC+12]). De manière inverse, lorsque l'élément est soumis à une déformation, l'alignement des segments de la chaine polymérique permet une meilleure orientation des dipôles et donc à une polarisation plus importante ([LCS+90]). Partant de ces principes, les équations constitutives de l'électrostriction s'écrivent:

$$\begin{aligned} S_{ij} &= M_{ijkl}E_kE_l + s^E_{ijkl}T_{kl} \\ D_i &= \varepsilon^T_{ik}E_k + 2M_{ijkl}E_lT_{kl} \end{aligned} \qquad \text{(FR-III.1)}$$

avec S, T, E et D dénotant respectivement la déformation, la contrainte, le champ électrique et le déplacement électrique. Les paramètres M, s^E et ε^T représentent le coefficient d'électrostriction,

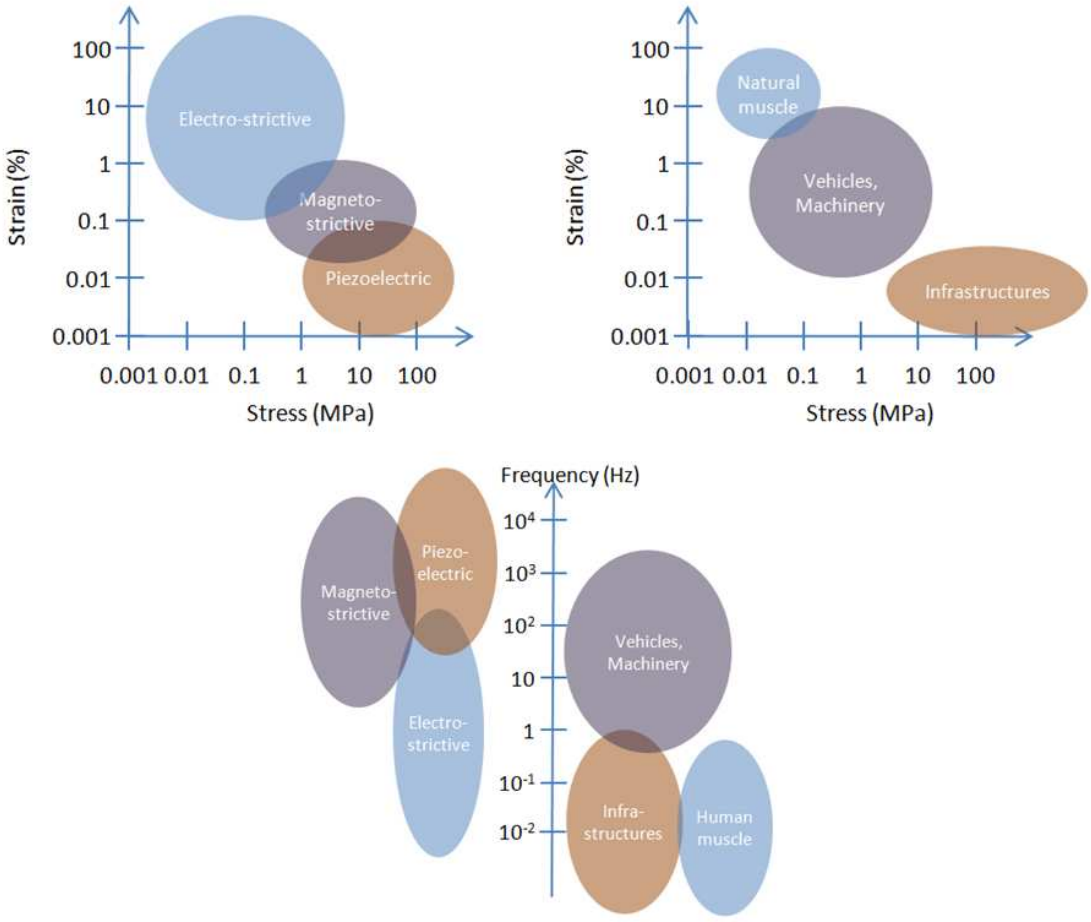

Figure FR-III-1: Place des polymères électrostrictifs dans les mécanismes de conversion d'énergie vibratoire et comparaison avec des applications typiques ([LCGL12]).

la souplesse à champ constant et la permittivité à contrainte constante. Les indices représentent les axes considérés. On remarque ainsi une dépendance quadratique de la déformation avec le champ électrique, alors que la conversion du domaine mécanique vers électrique requiert une activation par une polarisation avec un champ électrique (afin d'avoir une polarisation moyenne non nulle).

Alors que l'analyse du lien entre ces aspects locaux et les aspects macroscopiques dans le cadre de l'actionnement ont fait l'objet d'études antérieures ([LRS+12]), les travaux exposés dans cette partie proposent de développer un modèle pour l'application de ces polymères en tant que capteurs ou microgénérateurs. On pourra noter que, basé sur un modèle développé dans le cadre de la récupération d'énergie par effet piézoélectrique proposé par Badel et al. dans ([BLG+07]), un modèle macroscopique de récupérateurs électrostrictifs a déjà été utilisé ([Cot10]), mais sans justification. Ainsi on se propose ici d'analyser ce lien entre aspects locaux et microscopiques afin de scientifiquement valider ce modèle.

FR-III.2 Développement du modèle

FR-III.2.1 Principes

Le développement du modèle macroscopique se base sur l'analyse énergétique des énergies mécaniques et électriques mises en jeu, lors de l'application d'une grandeur électrique (pour la conversion électromécanique - permettant d'avoir l'équation mécanique) ou d'une grandeur mécanique (dans le cas de la conversion mécanoélectrique - conduisant à l'équation électrique du modèle). Dans tous les cas et afin de faciliter le développement théorique sans compromettre la généralité du modèle, on considèrera un système de type poutre et que le matériau est transverse isotropique, permettant de réécrire les équations constitutives sous la forme suivante, en utilisant la notation de Voigt et en admettant que le champ n'est appliqué que selon l'axe 3 et que l'axe 1 correspond à la plus grande dimension de la poutre:

$$\begin{aligned} S_1 &= s_{11}^E T_1 + s_{12}^E T_2 + s_{13}^E T_3 + M_{31} {E_3}^2 \\ S_2 &= s_{11}^E T_1 + s_{11}^E T_2 + s_{13}^E T_3 + M_{31} {E_3}^2 \\ D_3 &= \varepsilon_{33}^T E_3 + 2M_{31} T_2 E_3 + 2M_{33} T_3 E_3 \end{aligned} \tag{FR-III.2}$$

En considérant de plus un mouvement de flexion avec des déformations relativement faibles, il est possible d'appliquer les hypothèses d'Euler-Bernouilli ($S_2 = 0$ et $T_3 = 0$) qui

conduisent à la simplification du problème:

$$T_1 = c_p^E S_1 - \left(1 - \nu_p^E\right) c_p^E M_{31} {E_3}^2 \text{ avec } c_p^E = \frac{Y^E}{1 - \nu_p^{E2}} \tag{FR-III.3}$$

avec ν_p^E le coefficient de Poisson et Y^E le module d'Young du matériau électrostrictif.

De plus, afin de pouvoir disposer d'une réponse mécanique ou électrique non nulle, le polymère doit être déposé sur un substrat mécanique afin de décaler la ligne neutre. Selon la loi de Hooke et en faisant toujours les hypothèses précédentes, la déformation de ce substrat est reliée à la contrainte par:

$$T_1 = c_b S_1 \text{ avec } c_b = \frac{Y_b}{1 - {\nu_b}^2} \tag{FR-III.4}$$

avec ν_b le coefficient de Poisson et Y_b le module d'Young du substrat. A partir des équations de la contrainte dans le polymère et le substrat, il est alors possible de remonter à la déformation:

$$S_1 = -\left(x_3 - h_n\right) \frac{\partial^2 u_3\left(x_1\right)}{\partial {x_1}^2} \tag{FR-III.5}$$

où x_i est la position sur l'axe i, u_3 le déplacement de flexion et h_n représente la fibre neutre:

$$h_n = \begin{cases} \frac{{h_b}^2 c_b + 2 h_b h_p c_p^E + {h_p}^2 c_p^E}{2\left(h_b c_b + h_p c_p^E\right)} & \text{dans la zone active (polymère + substrat)} \\ \frac{h_p}{2} & \text{dans la zone passive (substrat uniquement)} \end{cases} \tag{FR-III.6}$$

avec h_p et h_b les épaisseurs respectives du polymère et du substrat.

FR-III.2.2 Aspect électrique

A partir des expressions précédentes reliant contrainte et déformation, l'expression du déplacement électrique peut s'écrire:

$$D_3 \approx \varepsilon_{33}^T E_3 + 2 M_{31} \left(1 - \nu_p^E\right) c_p^E S_1 E_3 \tag{FR-III.7}$$

Ainsi, en appliquant un champ électrique pour la génération des charges et en considérant que le polymère est assez fin pour considérer que le champ électrique est uniforme, la variation d'énergie électrique est donnée par (w dénote la largeur de la poutre - identique pour le

polymère et le substrat - et L_p la longueur de polymère):

$$\begin{aligned} dW_{prov,elec} &= \int_0^w \int_0^{L_p} \int_{h_b-h_n}^{h_b+h_p-h_n} E_3 dD_3 dx_3 dx_1 dx_2 \\ &\approx \frac{wL_p\varepsilon_{33}^T}{h_p} V dV - \frac{M_{31}\left(1-\nu_p^E\right)h_b c_b c_p^E w}{h_p}\left(\frac{h_p+h_b}{h_p c_p^E + h_b c_b}\right) V^2 d\left(\left.\frac{\partial u_3}{\partial x_1}\right|_{x_1=L_p}\right) \\ &\quad - \frac{M_{31}\left(1-\nu_p^E\right)h_b c_b c_p^E w}{h_p}\left(\frac{h_p+h_b}{h_p c_p^E + h_b c_b}\right)\left(\left.\frac{\partial u_3}{\partial x_1}\right|_{x_1=L_p}\right) V dV \end{aligned} \quad \text{(FR-III.8)}$$

avec V la tension appliquée aux bornes du polymère. Cette expression peut ainsi être décomposée en deux types d'énergies, une purement électrique et une électromécanique, que l'on peut identifier à une génération de charge Q de la forme:

$$Q = C_0 V - \alpha(x) V u_3(x) \quad \text{(FR-III.9)}$$

où C_0 représente la capacité bloquée et α le coefficient électromécanique (dépendant de la position considérée):

$$\begin{aligned} C_0 &= \frac{wL_p\varepsilon_3 3^T}{h_p} \\ \alpha(x)u_3(x) &= \frac{M_{31}\left(1-\nu_p^E\right)h_b c_b c_p^E w}{h_p}\left(\frac{h_p+h_b}{h_p c_p^E + h_b c_b}\right)\left(\left.\frac{\partial u_3}{\partial x_1}\right|_{x_1=L_p}\right) \end{aligned} \quad \text{(FR-III.10)}$$

FR-III.2.3 Aspect mécanique

Dans cette partie, on considère que le système est soumis à une excitation mécanique dont l'énergie s'exprime par (L_b est la longueur totale de la poutre):

$$\begin{aligned} dW_{prov,meca} &= \int_0^w \int_0^{L_b} \int_{-h_n}^{h_b+h_p-h_n} T_1 dS_1 dx_3 dx_1 dx_2 \\ &= c_b I_b \int_0^{L_b} \frac{\partial^2 u_3(x_1)}{\partial {x_1}^2} d\left(\frac{\partial^2 u_3(x_1)}{\partial {x_1}^2}\right) dx_1 + A\int_0^{L_p} \frac{\partial^2 u_3(x_1)}{\partial {x_1}^2} d\left(\frac{\partial^2 u_3(x_1)}{\partial {x_1}^2}\right) dx_1 \\ &\quad + \frac{1}{2}\frac{M_{31}\left(1-\nu_p^E\right)h_b c_b c_p^E w}{h_p}\left(\frac{h_p+h_b}{h_p c_p^E + h_b c_b}\right) V^2 d\left(\left.\frac{\partial u_3}{\partial x_1}\right|_{x_1=L_p}\right) \end{aligned} \quad \text{(FR-III.11)}$$

avec I_b (le second moment d'inertie du substrat) et A donnés par:

$$\begin{aligned} I_b &= \frac{{h_b}^3 w}{12} \\ A &= \frac{w}{12}\left(\frac{{c_b}^2{h_b}^4 + 4c_b c_p^E {h_b}^3 h_p + 6c_b c_p^E {h_b}^2 {h_p}^2 + 4c_b c_p^E h_b {h_p}^3 + {c_p^E}^2 {h_p}^4}{c_b h_b + c_p^E h_p}\right) \end{aligned} \quad \text{(FR-III.12)}$$

De manière analogue au cas précédent, il est possible de séparer ces énergies sous la forme

d'une énergie mécanique et d'une énergie de couplage et de l'identifier à:

$$dW_{prov,meca} = K(x)u_3(x)du_3(x) + \frac{1}{2}\alpha(x)V^2 du_3(x) \tag{FR-III.13}$$

où K est la raideur équivalente du système et α le coefficient électromécanique (dont on pourra remarquer l'équivalence avec l'expression obtenue en (FR-III.10)):

$$\begin{array}{rcl} K(x){u_3}^2(x) & = & c_b I_b \int_0^{L_b} \left[\frac{\partial^2 u_3(x_1)}{\partial {x_1}^2}\right]^2 dx_1 + A\int_0^{L_p}\left[\frac{\partial^2 u_3(x_1)}{\partial {x_1}^2}\right]^2 dx_1 \\ \alpha(x)u_3(x) & = & \frac{M_{31}\left(1-\nu_p^E\right)h_b c_b c_p^E w}{h_p}\left(\frac{h_p+h_b}{h_p c_p^E + h_b c_b}\right)\left(\left.\frac{\partial u_3}{\partial x_1}\right|_{x_1=L_p}\right) \end{array} \tag{FR-III.14}$$

Une fois ce modèle statique obtenu, il est tout à fait possible d'y inclure une partie dynamique par la définition d'une masse dynamique M donnée par (toujours par un raisonnement énergétique):

$$M(x) = \frac{1}{{u_3}^2(x)}\int_0^{L_b} m\left(x_1\right){u_3}^2\left(x_1\right)dx_1 \tag{FR-III.15}$$

avec $m\left(x_1\right)$ la masse linéique de la structure (ρ_b et ρ_p dénotant respectivement les masses volumiques du substrat et du polymère):

$$m\left(x_1\right) = \begin{cases} w\left(h_b\rho_b + h_p\rho_p\right) & \text{dans la zone active } (x_1 \in [0; L_p]\,) \\ w h_b \rho_b & \text{dans la zone passive } (x_1 \in]L_p; L_b]\,) \end{cases} \tag{FR-III.16}$$

FR-III.2.4 Modèle global

En résumé, le jeu d'équation obtenu s'exprime par un système masse-ressort dont une force supplémentaire due au couplage électromécanique, et proportionnelle au carré de la tension, s'applique en plus de celle externe F, couplé à un générateur de courant (en convention générateur - c'est-à-dire sortant du polymère) dont le courant de court-circuit dépend de la vitesse et la tension:

$$\begin{array}{c} M(x)\ddot{u}_3(x) + K(x)u_3(x) = F - \frac{1}{2}\alpha(x)V^2 \\ I = \alpha(x)V\ddot{u}_3(x) + \alpha(x)\dot{V}u_3(x) - C_0\dot{V} \end{array} \tag{FR-III.17}$$

Enfin, afin d'être plus réaliste, il est possible d'incorporer des pertes visqueuses représentées par un amortisseur $C(x)$, aussi dépendant de la position considérée, conduisant au modèle

global:

$$\begin{aligned} M(x)\ddot{u}_3(x) + C(x)\dot{u}_3(x) + K(x)u_3(x) &= F - \tfrac{1}{2}\alpha(x)V^2 \\ I = \alpha(x)V\dot{u}_3(x) + \alpha(x)\dot{V}u_3(x) - C_0\dot{V} & \end{aligned} \tag{FR-III.18}$$

FR-III.3 Application à une structure de type poutre encastrée-libre

La partie précédente a montré que les paramètres du modèle macroscopique sont dépendants de la déformée de la structure, et donc, de manière similaire, des conditions aux limites. Dans le cas d'une poutre encastrée-libre avec une force F s'exerçant au bout (Figure FR-III-2), l'expression du déplacement peut être obtenu à partir du moment exercé par cette force qui conduit à la relation:

$$(L_b - x_1)\, F = w \int_{-h_n}^{h_b+h_p-h_n} T_1 x_3 dx_3 \tag{FR-III.19}$$

La résolution de cette expression en remplaçant la contrainte par les relations précédemment établies dans les zones passives et actives (en considérant la continuité du déplacement et de sa dérivée), ainsi que l'hypothèse que la contribution du champ électrique au déplacement est négligeable, permet ainsi de déterminer le coefficient électromécanique en fonction de la

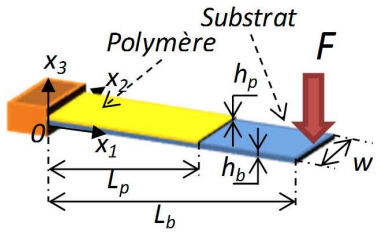

Figure FR-III-2: Structure considérée.

position x sur l'axe x_1:

$$\alpha(x) = \begin{cases} \frac{M_{31}\left(1-\nu_p^E\right)h_b c_b c_p^E w}{h_p} \left(\frac{h_p+h_b}{h_p c_p^E + h_b c_b}\right) \times \left(\frac{-2L_pL_b+{L_p}^2}{\frac{1}{3}x^3 - L_b x^2}\right) & \text{dans la zone active} \\ & (0 \le x \le L_p) \\ \frac{M_{31}\left(1-\nu_p^E\right)h_b c_b c_p^E w}{h_p} \left(\frac{h_p+h_b}{h_p c_p^E + h_b c_b}\right) \times \left[\frac{\left(-2L_bL_p+{L_p}^2\right)c_b {h_b}^3 w}{2A(-6L_bx^2-2x^3)+(a_1x+a_2)c_b{h_b}^3 w}\right] & \text{dans la zone passive} \\ & (L_p < x \le L_b) \end{cases} \quad \text{(FR-III.20)}$$

avec:

$$\begin{aligned} a_1 &= \frac{12L_bL_p}{c_b{h_b}^3 w} - \frac{6{L_p}^2}{c_b{h_b}^3 w} - \frac{L_bL_p}{A} + \frac{{L_p}^2}{2A} \\ a_2 &= -\frac{6L_b{L_p}^2}{c_b{h_b}^3 w} + \frac{4{L_p}^3}{c_b{h_b}^3 w} + \frac{L_b{L_p}^2}{2A} - \frac{{L_p}^3}{3A} \end{aligned} \quad \text{(FR-III.21)}$$

On remarque ainsi que le coefficient électromécanique calculé, sous les hypothèses précédentes, est indépendant de la force appliquée.

FR-III.4 Validation expérimentale

Afin de valider le modèle théorique précédemment exposé, il est ici proposé d'évaluer les capacités de conversion d'une structure de type poutre encastrée-libre formée d'un substrat en métal sur lequel est collé un film de polyuréthane. Le banc de test utilisé est schématisé en Figure FR-III-3.

FR-III.4.1 Evaluation de la conversion et comparaison théorique

La première partie de la validation du modèle consiste à mesurer le courant généré par la vibration lorsque le polymère est soumis à une tension de polarisation. Dans ce cas, une résistance faible (1 MΩ) devant l'impédance présentée par le polymère est utilisée tel que le système soit considéré en court-circuit. A partir de la mesure du courant de court-circuit et de l'amplitude de la vibration (prise en différents points de la structure), il est possible de remonter à la valeur du coefficient électromécanique. La valeur du coefficient électromécanique en fonction de la position considérée est représentée en Figure FR-III-4. Cette Figure montre clairement la validité du modèle, avec une très bonne concordance entre théorie et pratique. Ainsi, la valeur du coefficient électromécanique diminue avec la position

comme le déplacement augmente et que le courant généré est constant. On remarquera enfin qu'aucune différence visible n'apparaît pour deux tensions de polarisation différentes, ce qui confirme l'hypothèse selon laquelle le champ électrique n'a pas d'influence sur la déformée de la structure à ces niveaux.

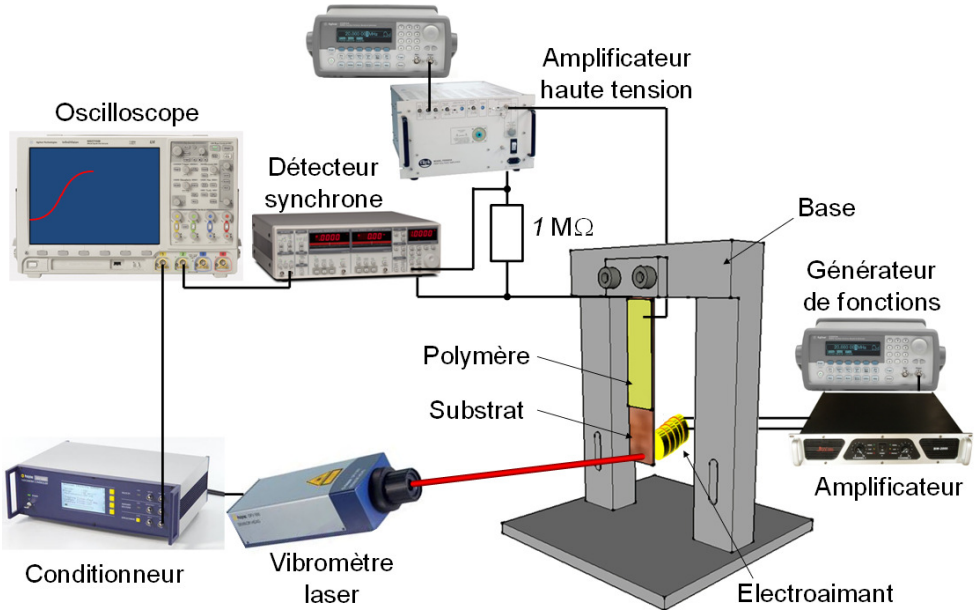

Figure FR-III-3: Dispositif expérimental.

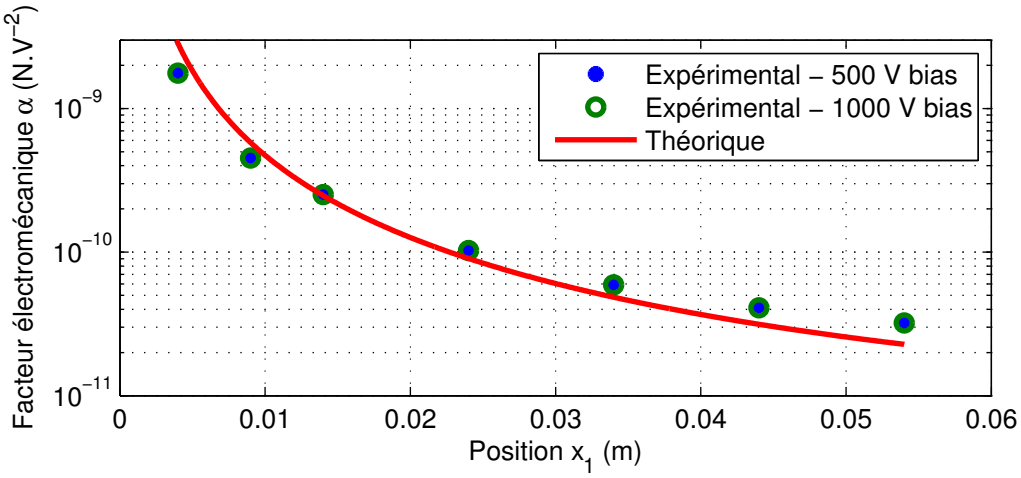

Figure FR-III-4: Résultats expérimentaux et comparaison théorique du facteur électromécanique.

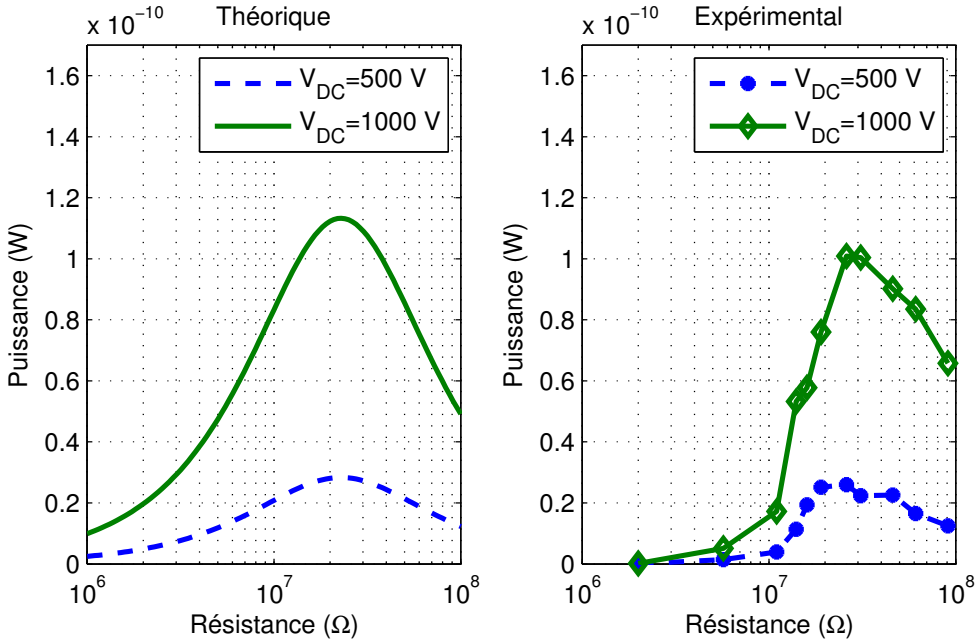

Figure FR-III-5: Résultats expérimentaux et comparaison théorique de l'énergie récupérée.

FR-III.4.2 Application à la récupération d'énergie

Afin de valider plus en avant le modèle, la charge (précédemment utilisée comme shunt pour la mesure du courant) est cette fois-ci variée pour utiliser le système comme récupérateur d'énergie. Les mesures, ainsi que les prédictions théoriques, sont illustrés en Figure FR-III-5. Ces résultats montrent encore une excellente corrélation entre prédiction et théorie, que ce soit en termes d'amplitude ou de position du maximum de puissance.

FR-III.5 Conclusion

Cette partie s'est attelée à l'élaboration d'un modèle macroscopique des générateurs électrostrictifs utilisés en flexion. Basé sur une analyse de la conversion de l'énergie électrique sous forme mécanique et inversement, le modèle globale consiste:

- D'un point de vue mécanique: système masse-ressort-amortisseur avec une force électromécanique dépendant du carré de la tension.
- D'un point de vue électrique: source de courant commandée par la tension de polarisation du polymère et la vitesse, et ayant une impédance interne capacitive.

Un exemple concret basé sur une poutre encastrée-libre a été présenté afin d'illustrer l'utilisation de ce modèle, et la validation expérimentale a montré une très bonne corrélation entre prédictions théoriques et mesures. Ainsi, un tel modèle, simple mais précis, facilitera la conception d'interfaces électriques pour les microgénérateurs électrostrictifs avec un jeu de paramètres réduit.

Chapitre FR-IV

Récupération d'énergie thermique à l'aide de matériaux ferromagnétiques

FR-IV.1 Introduction / Motivations

Alors que les Chapitres précédents se sont penchés sur la récupération d'énergie vibratoire, cette partie s'attachera à la source thermique. L'énergie thermique est la forme la plus basse d'énergie, et est largement disponible dans de nombreux environnements. La récupération d'énergie thermique peut se faire à partir de gradients spatiaux de température, à l'aide d'éléments thermoélectriques exploitant l'effet Seebeck ([DiS99]), ou à partir de variation temporelle de la température, par l'utilisation de l'effet pyroélectrique ([GSP+09]). Bien que ces deux effets (thermoélectrique et pyroélectrique) soient les plus couramment utilisés pour la récupération d'énergie thermique, d'autres mécanismes peuvent être employés. Dans ce Chapitre en particulier seront exploités des matériaux ferromagnétiques qui ont la propriété remarquable de présenter une perméabilité magnétique fortement liée à la température, notamment proche de la température de Curie T_C à laquelle une transition de phase conduisant à un changement drastique de la perméabilité apparaît. On pourra noter que les matériaux ferromagnétiques ont déjà été utilisés pour générer une oscillation à partir d'un gradient de température ([UCL07]), permettant ainsi une récupération d'énergie magnétique, mais peu d'études ont réellement mis en avant l'aspect de conversion directe ([SSBJ11]). Ainsi, ce Chapitre propose de formaliser les capacités de récupération d'énergie thermique des matériaux ferromagnétiques, à partir d'une structure simple et autonome.

FR-IV.2 Principes de la récupération d'énergie

Le concept exposé dans ce Chapitre consiste à exploiter la capacité des matériaux ferromagnétiques à présenter une variation de leur perméabilité face à une variation de température. Ainsi, lorsque ces matériaux sont polarisés par un champ magnétique, ceci permet une variation du flux et donc l'apparition d'une tension induite (loi de Lenz-Faraday), dénotant une possibilité de récupération d'énergie sous forme magnétique. Par la suite, il est considéré que le matériau ferromagnétique est soumis à un champ magnétique B[FR.IV-1]. A partir de la relation entre l'entropie σ du système, la température T et le champ magnétique H:

$$d\sigma = c\frac{dT}{T} + \gamma dH \tag{FR-IV.1}$$

avec c la capacité calorifique et γ le coefficient de couplage magnétocalorique, l'expression de la chaleur fournie par l'environnement extérieur s'exprime par:

$$Q = \int T d\sigma = c\delta T + \gamma \int T dH \tag{FR-IV.2}$$

On voit ainsi que cette chaleur se décompose en un terme d'énergie thermique pur et un terme correspondant à l'énergie thermomagnétique couplée du système.

Ainsi, lorsque le matériau a une température inférieure à la température de Curie et qu'on lui fournit une quantité de chaleur Q (réchauffement), celle-ci est transférée en partie sous forme potentielle thermique pure au matériau (via sa capacité calorifique), l'autre partie étant utilisée pour faire bouger les dipôles magnétiques, conduisant à un changement de l'énergie couplée au sein du matériau. Si un système de récupération est connecté au système, c'est à partir de ce réservoir et du réservoir couplé que l'énergie est puisée (Figure FR-IV-1(a)). Lors d'un cycle de refroidissement, l'énergie potentielle thermique pure emmagasinée est intégralement restituée à l'environnement extérieur, alors que l'énergie potentielle couplée n'est restituée qu'en partie, l'autre partie étant possiblement transférée au système de récupération (Figure FR-IV-1(b)). Il est ainsi possible de récupérer cette énergie thermomagnétique lors de chaque transfert, et donc à la fois sur la phase d'échauffement et sur celle de refroidissement, à condition qu'un champ magnétique soit présent. Cette récupération se fait simplement à l'aide d'un bobinage captant la variation de flux magnétique.

Concernant l'application du champ, celui-ci peut se faire uniquement sur les phases de refroidissement (de manière analogue aux cycles de récupération électrostatique - Figure FR-IV-2(a)), ou en appliquant un champ constant à l'aide d'un aimant (de manière analogue

[FR.IV-1] La façon d'appliquer ce champ sera détaillée plus tard.

aux cycles pseudo-piézoélectriques dans les cas des matériaux électrostrictifs diélectriques - Figure FR-IV-2(b)).

Dans le premier cas (cycle actif), le courant de magnétisation I_1 est appliqué par la source, conduisant en l'application d'un champ magnétique H_0. Pour avoir une énergie récupérée positive, l'application de ce courant doit se faire à perméabilité maximale (donc température minimale) et le retour à l'état initial à perméabilité minimale (température maximale, conduisant au cycle représenté en Figure FR-IV-3. Comme l'énergie récupérée W_{act} est donnée par l'intégrale du produit BdH, elle correspond d'un point de vue graphique à l'aire sous la courbe, dont l'expression est:

$$W_{act} = \frac{1}{2}\left[\mu\left(T_c\right) - \mu\left(T_h\right)\right] {H_0}^2 \tag{FR-IV.3}$$

avec μ la perméabilité totale du circuit magnétique (dépendant de la température). Néanmoins,

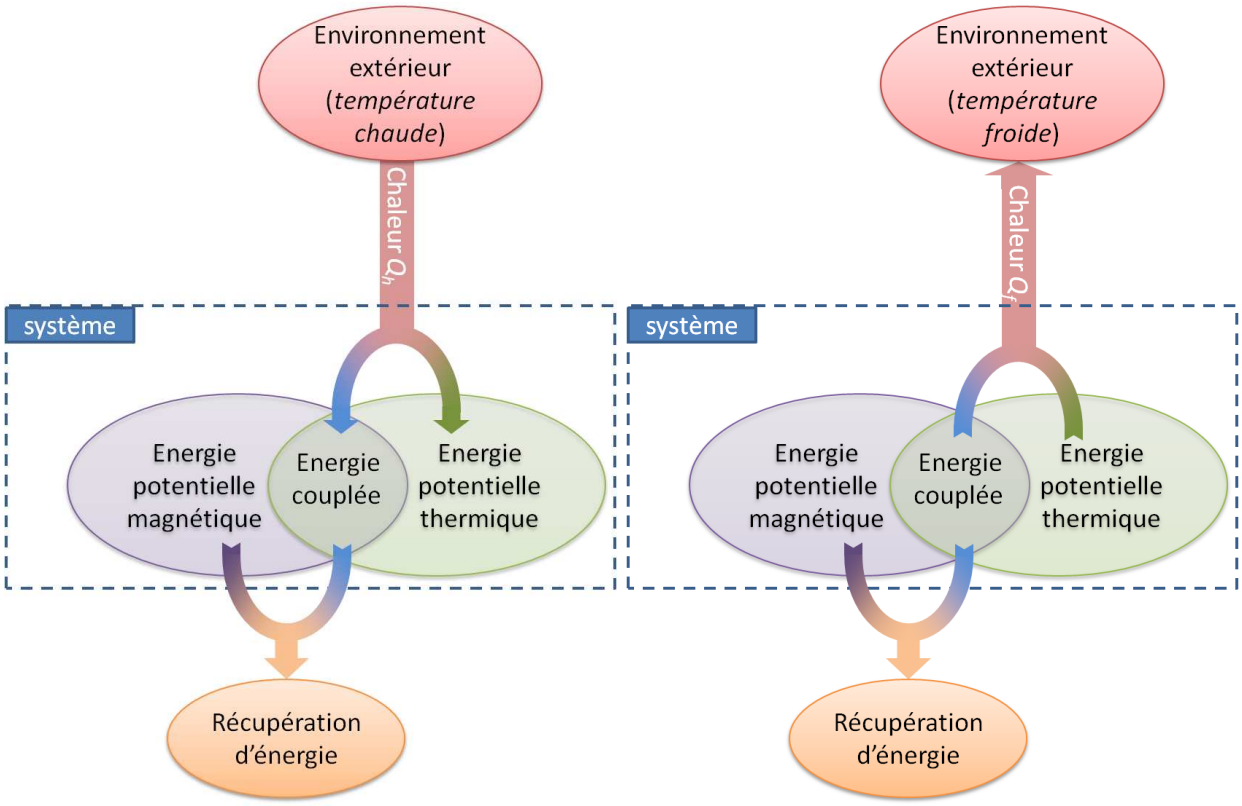

(a) Echauffement (b) Refroidissement

Figure FR-IV-1: Chaîne de transfert de l'énergie dans le système considéré (T dénote la température, Q_h la chaleur apportée lors de l'échauffement et Q_c celle restituée lors du refroidissement).

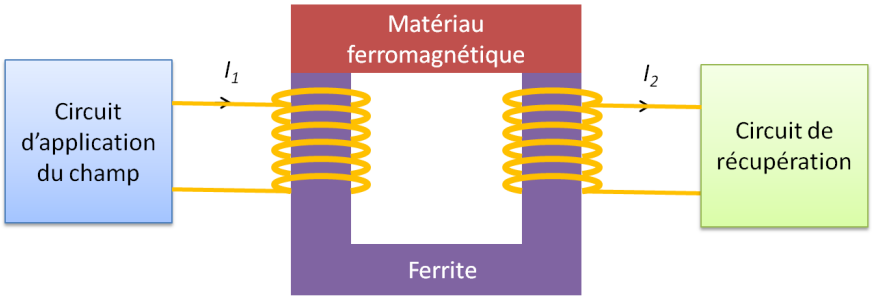

(a) Cycle actif

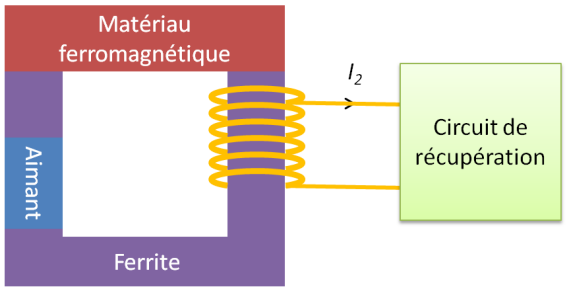

(b) Technique passive

Figure FR-IV-2: Magnétisation du circuit pour la récupération d'énergie.

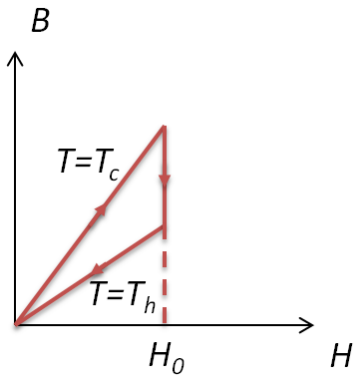

Figure FR-IV-3: Allure du cycle de récupération pour la technique active (T_h dénote la température chaude et T_c la température froide).

d'un point de vue réaliste, la nécessité d'application d'un courant primaire conduit à des pertes très importantes, de telle manière à ce qu'une telle technique n'est pas viable. Par conséquent, par la suite, on ne s'intéressera qu'à la technique passive.

FR-IV.3 Développement théorique

La technique de récupération d'énergie thermique par matériau ferromagnétique nécessite l'utilisation d'un aimant permanent pour l'application d'un champ B_r (champ rémanent de l'aimant). Sous ces conditions, en considérant les dimensions et propriétés du système, ainsi qu'une canalisation parfaite des lignes de champ et la conservation du flux ϕ, on obtient l'équation suivante à partir de la loi d'Ampère:

$$\phi = \left[\frac{l_a}{S_a\mu_a} + \frac{l_f}{S_f\mu_f} + \frac{l_p}{S_p\mu_p(T)}\right]^{-1}\left(N_2I_2 + \frac{B_r}{\mu_a}\right) \tag{FR-IV.4}$$

avec l et S la longueur et la surface de matériau et μ leur perméabilité. Les indices a, f et p correspondent respectivement à l'aimant, la ferrite et le matériau ferromagnétique. T est la température et N_2 le nombre d'enroulements au secondaire. Ainsi, il est possible d'obtenir la tension V induite au secondaire à l'aide de la loi de Lenz-Faraday:

$$\begin{aligned} V &= -{N_2}^2\left[\tfrac{l_a}{S_a\mu_a} + \tfrac{l_f}{S_f\mu_f} + \tfrac{l_p}{S_p\mu_p(T)}\right]^{-1}\tfrac{dI_2}{dt} \\ &= -N_2\left(N_2I_2 + \tfrac{B_r}{\mu_a}\right)\left(\tfrac{l_p}{S_p{\mu_p}^2(T)}\right)\left[\tfrac{l_a}{S_a\mu_a} + \tfrac{l_f}{S_f\mu_f} + \tfrac{l_p}{S_p\mu_p(T)}\right]^{-2}\tfrac{d\mu_p(T)}{dT}\tfrac{dT}{dt} \\ &= -L\tfrac{dI_2}{dt} - \beta\tfrac{dT}{dt} \end{aligned} \tag{FR-IV.5}$$

On reconnaît ainsi le premier terme qui est un terme d'inductance pure L, alors que le second terme traduit le couplage électrothermique β (les deux dépendant de la température mais linéarisables pour des variations faibles de la température). Par la suite, le circuit étant par exemple connecté à une charge résistive R simulant un circuit, il est possible d'avoir le courant I_2 tel que:

$$L\frac{dI_2}{dt} + RI_2 = -\beta\frac{dT}{dt} \tag{FR-IV.6}$$

ce qui conduit à l'expression de l'énergie récupérée W_{pas}:

$$W_{pas} = \frac{1}{R}\int V^2 dt \tag{FR-IV.7}$$

FR-IV.4 Discussion théorique

A partir des résultats théoriques et en prenant comme paramètres initiaux du système les données du Tableau FR-IV.2, la dépendance de la tension de sortie et de l'énergie maximale récupérée est représentée en figure pour une variation sinusoïdale de la température entre 295 K et 310 K à une fréquence de 1 Hz. Ces courbes ont été obtenues par résolution numériques utilisant la méthode de Runge-Kutta 4. Cette Figure montre une forte dépendance de la tension à vide en fonction du champ rémanent de l'aimant (Figure FR-IV-4), comme le prédit l'Equation (FR-IV.5) avec une relation linéaire du coefficient électrothermique en fonction de champ, et donc une relation quadratique avec l'énergie. Néanmoins, en pratique,

Tableau FR-IV.1: Paramètres théoriques initiaux du système.

Ferrite		
l_f (m)	S_f(m^2)	μ_f (H.m^{-1})
$0,125$	$3,75.10^{-4}$	10^{-3}
Aimant		
l_a (m)	S_a(m^2)	μ_a (H.m^{-1})
$0,004$	$7,854.10^{-5}$	$1,05\pi.10^{-7}$
Ferromagnétique		
l_p (m)	S_p(m^2)	μ_p (H.m^{-1})[FR-IV.2]
$0,035$	$5,5.10^{-5}$	$7,85.10^{-7} \times (T - 345)$

[FR-IV.2] T est la température en K; le terme "345" correspond à la température de transition en Kelvin.

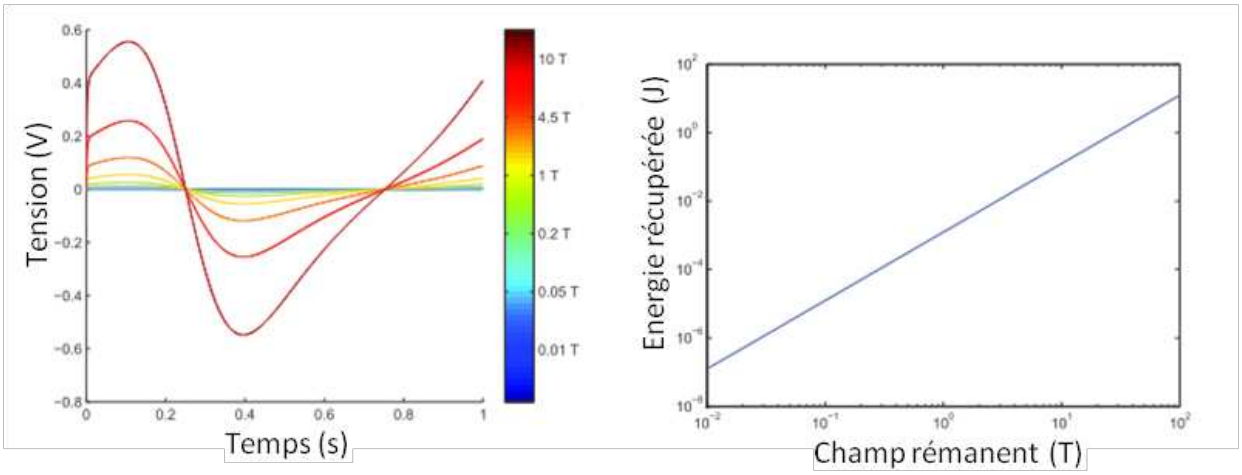

Figure FR-IV-4: Dépendance de la tension de sortie à vide et de l'énergie maximale récupérée en fonction du champ rémanent de l'aimant.

ce champ est limité à moins de 2 T pour les aimants en terre rare. On remarque également Figure FR-IV-5 une dépendance quasi-nulle de la tension et de l'énergie récupérée avec la perméabilité de la ferrite, qui s'explique par la forte valeur de cette dernière par rapport à celle de l'aimant et du matériau ferromagnétique (malgré les dimensions plus importantes de la ferrite). La perméabilité de l'aimant étant par contre bien plus faible que les deux autres, la tension et l'énergie sont fortement dépendantes à ce paramètre, et une valeur optimale apparaît en termes d'énergie (Figure FR-IV-6). Enfin, la tension de sortie à vide croît avec la résistance de charge connectée (Figure FR-IV-7), mais une valeur optimale apparaît pour l'énergie récupérée. Cette valeur est néanmoins très faible (quelques milliOhms) du fait de la fréquence faible et de la valeur également peu élevée de l'inductance, de telle manière que la résistance du bobinage soit prépondérante, comme il sera vu dans la partie expérimentale. Néanmoins, on peut remarquer que, cette faible valeur de résistance optimale mise à part, l'énergie récupérée par cycle peut atteindre plus centaines de milliJoules par cycle.

FR-IV.5 Validation expérimentale

Afin de valider le concept précédemment exposé ainsi que le modèle établi, cette partie propose d'étudier expérimentalement le système et de comparer les résultats à la partie théorique. Le système est formé d'une ferrite en U, de deux aimants néodymes pour la polarisation magnétique du circuit, et du matériau ferromagnétique $Ni_{30}Fe$ (communément appelé Phytherm© 55). Le bobinage, effectué autour de la ferrite, est composé de 500 tours, et est connecté à une charge résistive dont la tension est mesurée à l'aide d'un détecteur syn-

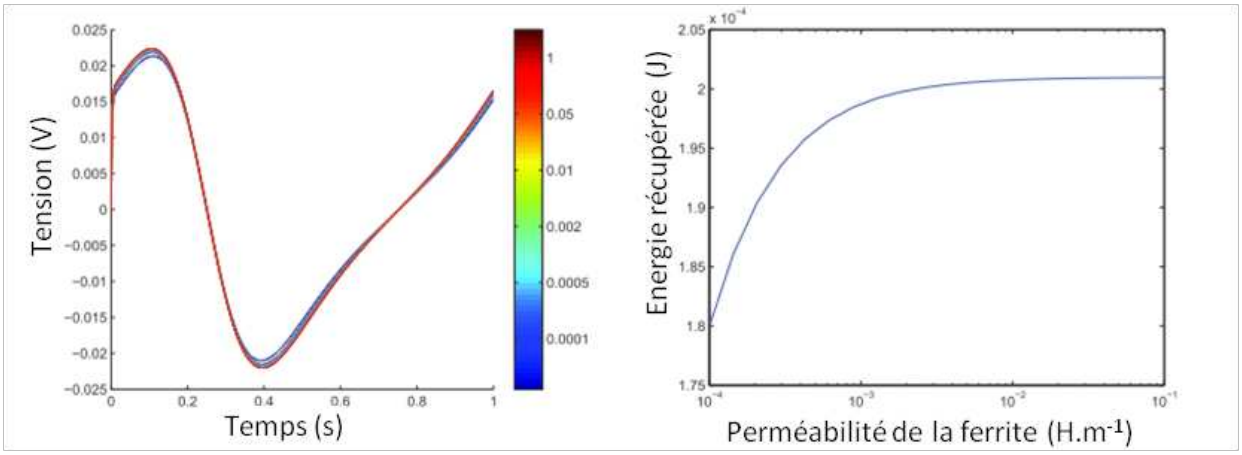

Figure FR-IV-5: Dépendance de la tension de sortie à vide et de l'énergie maximale récupérée en fonction de la perméabilité de la ferrite.

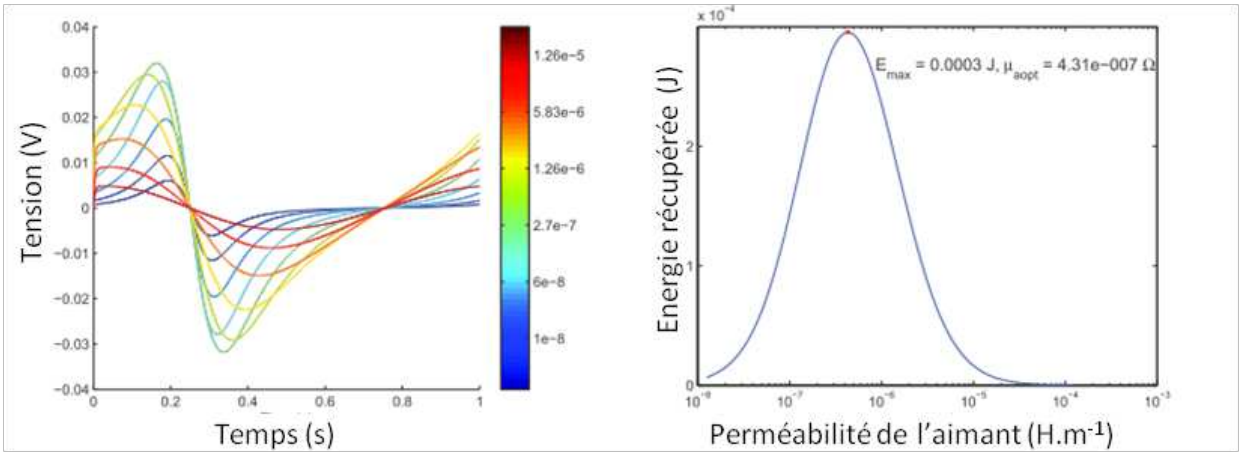

Figure FR-IV-6: Dépendance de la tension de sortie à vide et de l'énergie maximale récupérée en fonction de la perméabilité de l'aimant.

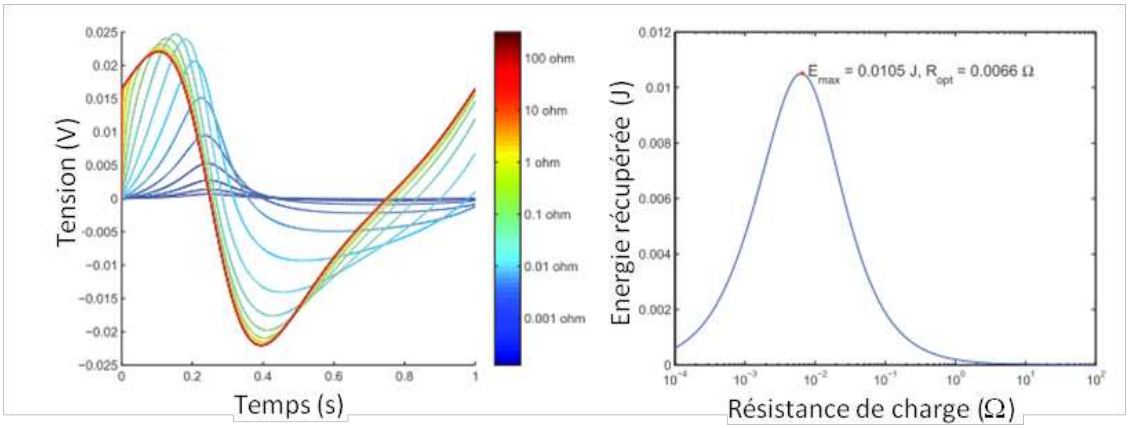

Figure FR-IV-7: Dépendance de la tension de sortie à vide et de l'énergie maximale récupérée en fonction de la résistance de charge.

chrone. Un thermocouple est utilisé pour mesurer la température du système. Les paramètres du système sont donnés dans le Tableau FR-IV.2. Le chauffage est effectué à l'aide d'un décapeur thermique et le refroidissement avec une bombe d'air sec en spray. Afin de prendre en compte la résistance interne r du bobinage ($r = 2,2\ \Omega$), un terme supplémentaire est ajouté à l'équation électrique du système:

$$L\frac{dI_2}{dt} + (R + r)I_2 = -\beta\frac{dT}{dt} \tag{FR-IV.8}$$

Les résultats en termes de profil de température et de tension de sortie pour une charge de 100 Ω (soit quasiment à vide comparé à l'impédance de sortie du système) sont donnés en Figure FR-IV-8, qui montre une très bonne corrélation entre résultats simulés et mesurés. La puissance récupérée associée (normalisée par rapport au carrée de la variation de température) en fonction de la charge est donnée en Figure FR-IV-9. Du fait de la présence de la résistance du bobinage dont la valeur est très supérieure à la valeur de l'impédance présentée par l'inductance aux pseudo-fréquences considérées, la valeur de puissance maximale est largement diminuée. Néanmoins, en prenant en compte cette résistance supplémentaire, on remarque une bonne corrélation entre mesure et simulation basée sur le modèle théorique.

FR-IV.6 Conclusion

Ce Chapitre s'est intéressé à un couplage relativement peu étudié consistant en une conversion de l'énergie thermique sous forme électrique basée sur la variation de perméabilité des matériaux ferromagnétiques. Ce couplage, nécessitant une polarisation du système, peut être activé soit par l'utilisation de cycles dérivés de cycle thermodynamiques, soit

Tableau FR-IV.2: Paramètres expérimentaux du système.

Ferrite		
l_f (m)	S_f(m^2)	μ_f (H.m^{-1})
$0,125$	$3,75.10^{-4}$	10^{-3}
Aimant		
l_a (m)	S_a(m^2)	μ_a (H.m^{-1})
$0,004$	$7,854.10^{-5}$	$1,05\pi.10^{-7}$
Ferromagnétique		
l_p (m)	S_p(m^2)	μ_p (H.m^{-1})[FR-IV.3]
$0,055$	$5,5.10^{-5}$	$7,85.10^{-7} \times (T - 345)$

[FR-IV.3] T est la température en K; le terme "345" correspond à la température de transition en Kelvin.

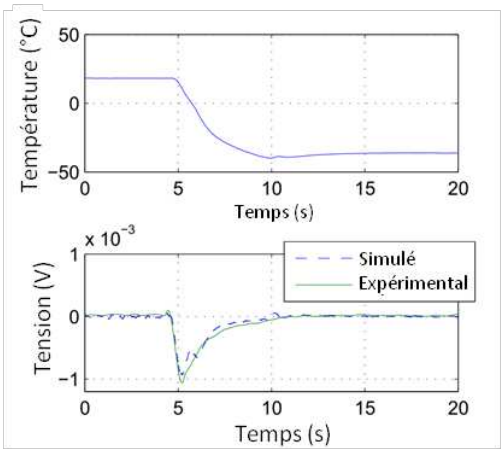

Figure FR-IV-8: Résultats expérimentaux et simulés de la tension de sortie.

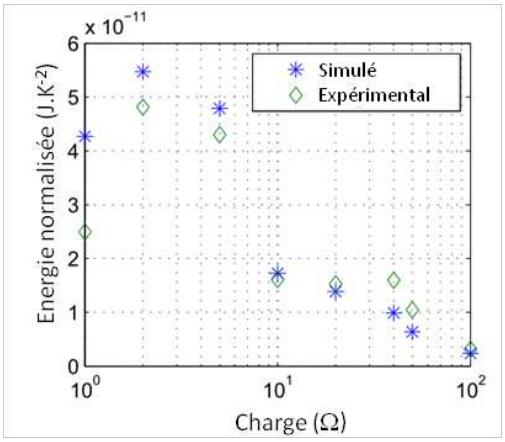

Figure FR-IV-9: Résultats expérimentaux et simulés de l'énergie récupérée.

en utilisant un mode de fonctionnement dynamique autour d'un champ de polarisation. Cette dernière méthode semble plus réaliste car exempte des pertes inhérentes aux cycles de charge/décharge (élevée dans le cas magnétique car nécessitant une circulation d'un courant). Une analyse théorique a permis de mettre en avant les facteurs importants permettant d'optimiser la récupération d'énergie. D'un point de vue pratique néanmoins, il a été montré que la résistance supplémentaire introduite par les bobinages limitait grandement l'énergie récupérée.

Chapitre FR-V

Conclusion générale et perspectives

Cette thèse s'est intéressée à la récupération d'énergie sous plusieurs formes. A l'heure où les dispositifs intégrés embarqués et où l'électronique nomade connaît un essor sans précédent, une telle thématique trouve sa place à la fois dans le milieu scientifique, dans le domaine industriel ainsi que dans l'environnement socio-économique.

Dans un premier temps, deux Chapitres se sont penchés sur la récupération d'énergie à partir de sources mécaniques vibratoires. Le premier s'est attelé à une nouvelle structure d'électrodes pour la récupération d'énergie vibratoire basée sur la variation de capacité due au mouvement d'une des électrodes. Comme la valeur de la capacité est étroitement liée aux variations de surfaces en regard et que celle-ci est limitée par des contraintes technologiques, il a été proposé de prendre avantage des structures fractales qui, lorsque les électrodes sont proches, augmentent significativement les surfaces en regards. Deux architectures, selon que la dimension de référence soit la plus grande (architecture "dégressive") ou la plus petite (architecture "progressive"), ont été discutées. Il a ainsi été montré que pour l'architecture dégressive la structure fractale permet une augmentation des capacités de récupération d'énergie quel que soit le déplacement d'une électrode, mais que l'architecture progressive permet de récupérer plus d'énergie et est plus proche des structures généralement conçues. Dans ce cas, l'augmentation des capacités de récupération est étroitement liée à l'amplitude de vibration: plus cette dernière est importante, plus l'ordre fractal optimal est important.

Le second Chapitre s'est quant à lui penché sur l'élaboration d'un modèle haut niveau pour les microgénérateurs d'énergie basés sur les polymères électrostrictifs diélectriques fonctionnement en flexion. Le but de ce modèle est de fournir un jeu d'équations couplées (dans le domaine électrique et mécanique) afin de fournir un modèle simple mais efficace, par ex-

emple pour la conception de l'interface électrique ou l'évaluation rapide des capacités de récupération d'énergie. Ce modèle est basé sur l'analyse des différentes énergies (mécanique et électrique) dans le cas d'une excitation électrique ou mécanique. Il a ainsi été montré que le système peut être simplement représenté mécaniquement par un système masse-ressort-amortisseur avec un terme de force dépendant du carré de la tension appliquée et électrique par une source de courant contrôlée par la vitesse et la dérivée temporelle de la tension avec une capacité en parallèle. Le lien entre la partie mécanique et électrique (et inversement) se fait via l'intermédiaire d'un coefficient électromécanique dont la valeur dépend des paramètres mécaniques, électriques et électromécaniques de la structure et dépendant du point considéré.

Enfin, le dernier Chapitre s'est intéressé à la source d'énergie thermique, et plus particulièrement sur un couplage basé sur la propriété des matériaux ferromagnétiques de présenter une perméabilité fortement dépendante à la température. Ainsi, il a été montré qu'en polarisant un circuit magnétique comprenant un tel matériau à l'aide d'un champ magnétique, il était possible d'obtenir un flux variable avec la température (la variation de la perméabilité du matériau ferromagnétique changeant la reluctance totale du circuit). Ainsi, en enroulant un bobinage autour du circuit magnétique, cette variation de flux génère une tension qui peut être utilisée pour récupérer de l'énergie magnétique. Deux approches sont possibles, selon qu'un enroulement primaire génère la magnétisation du circuit (permettant l'utilisation de cycles dérivés de la thermodynamique) ou qu'un champ rémanent d'un aimant permanent polarise le système ; ce dernier cas étant plus réaliste du fait des pertes importantes de l'approche par cycle. La modélisation du système a montré qu'outre le comportement inductif du système, il était possible d'extraire un facteur de conversion électrothermique dépendant des paramètres de la structure mais aussi de la température de travail. Cependant, la validation expérimentale a montré que la résistance interne du bobinage, bien supérieure à l'impédance de l'inductance, conduit à une diminution drastique de l'énergie récupérable.

En conclusion, ces travaux de thèse ont dégagé trois pistes aux objectifs scientifiques et techniques bien distincts:

- L'amélioration des capacités de récupération d'énergie des systèmes électrostatiques.
- La modélisation haut niveau du comportement de récupérateurs d'énergie électrostrictifs exploitant des mouvements de flexion.
- L'utilisation d'un nouvel effet de couplage électrothermique pour la récupération d'énergie.

Les résultats présentés ici, en particulier pour le premier et le dernier point, sont réellement exploratoires et sujets à de nombreuses améliorations. Citons par exemple l'utilisation d'architectures d'électrodes en trois dimensions pour les structures fractales et l'optimisation paramétrique des systèmes de conversion de l'énergie thermique exploitant les éléments ferromagnétiques. Ainsi, grâce à ces structures optimisées, de nouvelles alternatives réalistes pour l'alimentation de microsystèmes électroniques seront possibles.

Références

[AC98] Rajeevan Amirtharajah and Anantha P. Chandrakasan. Self-powered signal processing using vibration-based power generation. *IEEE Journal of Solid-State Circuits*, 33:687–695, 1998.

[Bad05] A. Badel. *Récupération d'énergie et contrôle vibratoire par éléments piézoélectriques suivant une approche non linéaire.* PhD thesis, Université de Savoie / INSA de Lyon, 2005.

[BDC10] S. Boisseau, G. Despesse, and A. Chaillout, J.-Jand Sylvestre. Microstructures électrostatiques de récupération d'énergie vibratoire pour les microsystèmes. Technical Report RE160, Techniques de l'ingénieur, 2010.

[BLG+07] A. Badel, M. Lagache, D. Guyomar, E. Lefeuvre, and C. Richard. Finite element and simple lumped modeling for flexural nonlinear semi-passive damping. *Journal of Intelligent Material Systems and Structures*, 18:727–742, 2007.

[CCTS08] K. A. Cook-Chennault, N. Thambi, and A. M. Sastry. Powering mems portable devices - review of non-regenerative and regenerative power supply systems with special emphasis on piezoelectric energy harvesting systems. *Smart Materials and Structures*, 17(4):043001, 2008.

[CLC+12] J.-F. Capsal, M. Lallart, P.-J. Cottinet, J. Galineau, G. Sébald, and D. Guyomar. Evaluation of macroscopic polarization and actuation abilities of electrostrictive dipolar polymers using microscopic debye/langevin formalism. *J. Phys. D.: Appl. Phys.*, 45(20):205401, 2012.

[Cot10] P.-J. Cottinet. *Actionnement et récupération d'énergie à l'aide de polymères électro-actifs.* PhD thesis, INSA Lyon, 2010.

[DiS99] F. J. DiSalvo. Thermoelectric cooling and power generation. *Science*, 285:703–706, 1999.

[Eri12] Ericsson. Traffic and market report. Technical report, Ericsson AB, 2012.

[GSP+09] Daniel Guyomar, Gaël Sebald, Sébastien Pruvost, Mickaël Lallart, Akram Khodayari, and Claude Richard. Energy harvesting from ambient vibrations and heat. *Journal of Intelligent Material Systems and Structures*, 20(5):609–624, 2009.

[LCGL12] Mickaël Lallart, Pierre-Jean Cottinet, Daniel Guyomar, and Laurent Lebrun. Electrostrictive polymers for mechanical energy harvesting. *Journal of Polymer Science Part B: Polymer Physics*, 50:523–535, 2012.

[LCS+90] M. Lallart, J.-F. Capsal, G. Sebald, P.-J. Cottinet, and D. Guyomar. Converse electrostrictive effect in dielectric polymers. *Sens. Act. B.: Chem.*, 259-264:2014, 190.

[LRS+12] M. Lallart, C. Richard, P. Sukwisut, L. Petit, D. Guyomar, and N. Muensit. Electrostrictive bending actuators: Modeling and experimental investigation. *Sens. Act. A.: Phys.*, 179:169–177, 2012.

[PGLM07] L. Petit, D. Guyomar, M. Lallart, and T. Monnier. *Les controverses technologiques de l'INSA de Lyon*, chapter Les micro-dispositifs électroniques énergétiquement autonomes : du concept à la réalité. INSA Lyon, 2007.

[RWR03] S. Roundy, P. K. Wright, and J. Rabaey. A study of low level vibrations as a power source for wireless sensor nodes. *Computer Communications*, 26:1131–1144, 2003.

[SGA09] Gael Sebald, Daniel Guyomar, and Amen Agbossou. On thermoelectric and pyroelectric energy harvesting. *Smart Materials and Structures*, 18(12):125006, 2009.

[SPG08] Gael Sebald, Sebastien Pruvost, and Daniel Guyomar. Energy harvesting based on ericsson pyroelectric cycles in a relaxor ferroelectric ceramic. *Smart Mater. Struct.*, 17:015012, 2008.

[SSBJ11] V. Srivastava, Y. Song, K. Bhatti, and R. D. James. The direct conversion of heat to electricity using multiferroic alloys. *Advanced Energy Materials*, 1:97–104, 2011.

[TGG+08] Leonard M. Tendera, Sam A. Graya, Ethan Grovemanb, Daniel A. Lowyc, Peter Kauffmand, Julio Melhadoe, Robert C. Tycef, Darren Flynnf, Rose Petreccag,

and Joe Dobarrog. The first demonstration of a microbial fuel cell as a viable power supply: Powering a meteorological buoy. *J. Power Sources*, 179:571–575, 2008.

[UCL07] M. Ujihara, G. P. Carman, and D. G. Lee. Thermal energy harvesting device using ferromagnetic materials. *Applied Physics Letters*, 91:093508, 2007.

[Wan11] Liuqing Wang. Minimisation de l'énergie pour polariser un polymère électrostrictif dans la récupération de l'énergie. Master's thesis, INSA Lyon, 2011.

[Wu13] Y.-C. Wu. *Analysis and practical considerations of linear and nonlinear piezoelectric energy conversion and harvesting techniques.* PhD thesis, INSA Lyon, 2013.

[ZPCG11] H. Zhu, S. Pruvost, P. J. Cottinet, and D. Guyomar. Energy harvesting by nonlinear capacitance variation for a relaxor ferroelectric poly(vinylidene fluoride-trifluoroethylene-chlorofluoroethylene) terpolymer. *Appl. Phys. Lett.*, 98:222901, 2011.

English part

Chapter I

Introduction

Nature contains millions of lives - animals, plants, bacterium, virus, etc, which compose a complex, giant autonomous system. In this way, nature may serve as an excellent example of how an efficient, intelligent system works. As a part of nature, in the path of technology development human beings tend to approach the same principle: numerous work is subconsciously or consciously imitating the patterns of living beings. In the energy harvesting field, the concept originates from the wish that how wonderful it is if a device may provide energy to itself. The wish has bred mechanical watches in former days and wireless charging nowadays. Systems can use energy harvesting techniques as methods to capture ambient energy for self-sustaining, similar to the food hunting for animals and light capture for plants. They could be further equipped with the abilities of detecting energy density and of moving, allowing them to pursue more suitable living environments. Driven by the seeking of longer existence and along with the developments in other fields, people tend to construct systems which are able to seek profits and avoid potential harms while performing their own tasks. Little by little, people may one day attain the goal of constructing lives and build an analogical nature system. However, like the perpetual motion machine, the autonomous system will demonstrate some kind of internal radiation which causes a leakage of energy and would eventually lead to a breakdown of the system due to internal exhaustion. Then look back to nature - the much more complex system, according to the rule, it will also come to the end of its life one day. It's a long story. Now let's come back to the topic of this thesis.

I.1 Energy harvesting and the potential energy sources

Energy harvesting, also known as power harvesting or energy scavenging, generally relates to the process of using ambient energy (e.g. kinetic energy, thermal energy, wind energy, solar energy), which is captured and stored in order to power small and autonomous electronic devices.

The concept of energy harvesting can date back to the windmill and the waterwheel. People have searched for ways to store the energy from heat and vibrations for many decades. Numerous ambient energy exists which could be converted into electrical energy, including waste heat, vibration, electromagnetic waves, wind, flowing water, and solar energy [AS07] and the available energy sources in the surrounding are given in Table (I.1) [Pri07]. This section focuses on potential ambient energy sources and the corresponding energy harvesting techniques.

I.1.1 Mechanical energy harvesting

First the omnipresent kinetic energy is presented which is usually in form of vibrations, random displacements or forces. Suitable vibrations can be found in numerous applications including common household goods (fridges, washing machines, microwave ovens, etc.), industrial plant equipment, moving structures such as automobiles and aeroplanes and structures such as buildings and bridges [RWR03]. Mechanical energy is converted into electrical energy usually by piezoelectric effect, variable capacitors, electromechanical coupling or other

Table I.1: Sources of energy available in the surrounding which are/can be tapped for generating electricity [Pri07]

Human body	**Vehicles**	**Structures**	**Industrial**	**Environment**
Breathing, blood pressure, exhalation, body heat	Aircraft, UAV, helicopter, automobiles, trains	Bridges, roads, tunnels, farm house structures	Motors, compressors, chillers, pumps, fans	Wind, solar, temperature gradient, daily temperature
Walking, arm motion, finger motion, jogging, swimming, eating, talking	Tires, tracks, peddies, brakes shock absorber, turbines	Control-switch, HVAC systems, ducts, cleaners	Conveyers, cutting and dicing, vibrating machine	Ocean currents, acoustic waves, EM waves, RF signal

methods.

Piezoelectric energy harvesting

To better understand piezoelectric materials, the classification of crystals are first introduced. Crystals are usually classified into seven systems according to their geometry: triclinic, monoclinic,orthorhombic, tetragonal, trigonal, hexagonal, and cubic. The systems can again be subdivided into 32 crytal classes, according to the number of rotational axes and reflection planes they exhibit that leave the crystal structure unchanged. 11 of them are centrosymmetric and possess no polar properties. 20 of the remaining 21 non-centric crystals exhibit piezoelectric effect. Of the 20 piezoelectric crystal classes 10 are pyroelectric. One class of pyroelectric crystals is ferroelectric which has two or more orientational axes in absence of an electric field and can be shifted from one to another of these states by an electric field.

The piezoelectric effect was discovered by in 1880 by French physicists Jacques and Pierre Curie. It may be understood as a linear electromechanical interaction between the mechanical and the electrical state in crystalline materials with no inversion symmetry (non-centrosymmetric). Piezoelectric materials demonstrate reversible processes: the direct piezoelectric effect (generation of electrical charges with the application of a mechanical strain) and the reverse piezoelectric effect (generation of a mechanical strain with the application of an electric field). Flexible piezoelectric materials are promising as a power harvesting candidate for their ability to withstand large amounts of strain which provide more mechanical energy available for energy conversion. The application of piezoelectric materials usually employs two coupling modes: the 31 mode and the 33 mode (Fig.(I-1)). With the 31 mode, strain is applied perpendicular to the poling direction, and the generated voltage is perpendicular to the applied force; with the 33 mode, the strain is applied perpendicular to the electrodes, and the generated voltage is along the same axis as the applied force. Materials typically have a d_{33} coefficient that is higher than the d_{31} coefficient, but the 31 mode is easier to implement in devices for vibration energy harvesting [BTW06]. Anton and Sodano [AS07] concluded that under a small force, low vibration level environment, the 31 cantilever configuration is more efficient, but in a high force environment, such as a heavy manufacturing facility or in large operating machinery, a stack configuration would be more durable and generates useful energy.

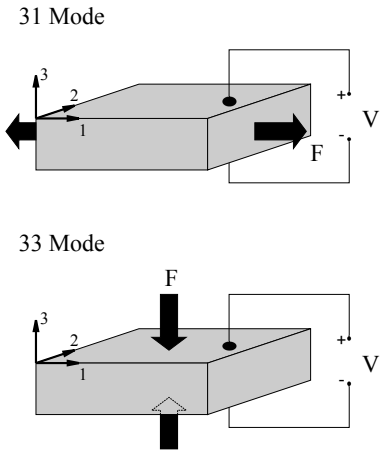

Figure I-1: Illustration of 31 mode and 33 mode for piezoelectric materials

Human powered piezoelectric generators The use of piezoelectric generators to power human-wearable systems has been extensively studied. Human motion is characterized by large amplitude movements at low frequencies, which brings difficulties in designing a miniature resonant generator [BTW06]. Kymissis *et al.* have proposed in 1998 an energy generator for human walking referred as parasitic power harvesting in shoes [KKPG98]. They developed a sneaker insole made of a laminate foil shaped into an elongated hexagon, as shown in Fig.(I-2). This stave is a bimorph built around a central 2 mm flexible plastic substrate with eight-layer stacks of 28 μm PVDF (polyvinylidineflouride) sheets. The bending movement of the sole strains the PVDF stacks and produces a charge from the d_{31} mode. The device produced an average power of 1.3 mW with a 250 kΩ load at a frequency of footfall of 0.9 Hz. Based on the work of Kymissis *et al.*, Shenck and Paradiso [SP01] developed another approach involving the use of a non bending, compressive bimorph as depicted in Fig.(I-3). Two Thunder TH-6R transducers are incorporated using a semiflexible piezoceramic manufacturing process with each transducer composed of 5×5 cm^2, 0.015 inch PZT strip bonded to a prestressed, neutrally curved, 5×8.5 cm^2 sheet of spring steel. As the heel of the shoe hits the ground, the transducers are forced to deform and, as the heel is lifted, the transducers spring back into their original shape. At a 0.9 Hz walking pace, the PZT bimorph produced an average power of 8.4 mW in a 500 kΩ load.

Generators using impact force of a moving mass hitting a piezoelectric structure have also been developed [RWN09]. Renaud *et al.* have described in 2005 a linear impact-based generator, aiming at harvesting energy from human-limb motion [RSF+05]. The device comprised an inertial mass (750 mg) confined within a frame (12×10 mm^2) but free to slide along one axis and piezoelectric cantilever beams at the ends of the frame for a maximum of

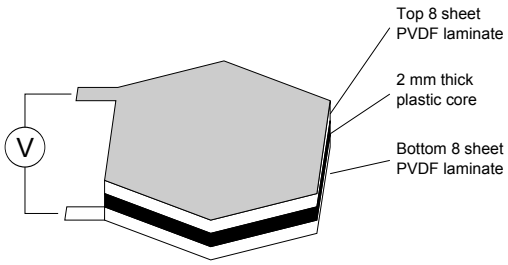

Figure I-2: PVDF shoe insole [KKPG98]

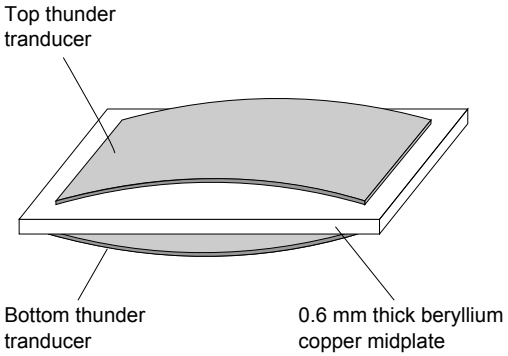

Figure I-3: Piezoelectric bimorph [SP01][BTW06]

10 mm displacement. Every time the mass hits the cantilevers, they vibrate and mechanical energy can be harvested. It is predicted that the device may generate an electrical power up to 40 μW from a volume of 1 cm^3 under an excitation amplitude of 10 cm at 1 Hz (0.1 m s^{-2}). Further work by Renaud *et al.* (2009) devised a prototype capable of producing 47 μW when rotated every second (25 cm^3 and 60 g), and 600 μW was obtained for a 10 Hz frequency with a 10 cm linear displacement amplitude [RFvSvH12].

Cantilever-based piezoelectric generators Piezoelectric materials with high electromechanical coupling coefficients are generally ceramics, with lead zirconate titinate being the most common material. Such materials do not tolerate high strain levels, so some form of lever is required to combine them with devices of significant relative displacement. The most common geometry is to apply the piezoelectric material as a thin layer to a cantilever beam [MYR$^+$08]. The structure is designed to operate in a bending mode thereby straining the piezoelectric films and generating a charge from the d_{31} mode. Roundy and Wright have developed a composite piezoelectric cantilever beam generator [RWR03][RW04] and built up a mathematical model in [RW04]. One prototype was fabricated with a PZT-5A shim attached to each side of a steel center beam. A cubic mass made from an alloy of tin (Sn) and bismuth (Bi) was attached to the end with the resonance frequency of generator to be

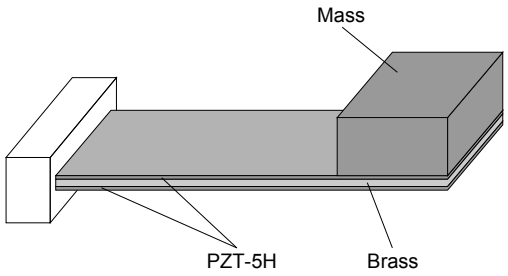

Figure I-4: Schematic of cantilever piezoelectric generator [RW04]

120 Hz. The generator produced a maximum power output up to 80 μW with a 250 kΩ load under 2.5 m s^{-2} acceleration. Another prototype utilized PZT-5H attached to a 0.1 mm thick central brass shim (Fig.(I-4)). Designs of 1 cm^3 in size generated a power output of 375 μW from a vibration of 2.5 m s^{-2} at 120 Hz. A 1 cm^3 generator was used to power a custom designed 1.9 GHz radio transmitter from the same vibration source. Sodano *et al.* have also investigated piezoelectric cantilever generators and developed an alternative mathematical analysis of a cantilever based on energy methods. The model is a cantilever PZT bimorph similar to Fig.(I-4) but without proof mass and the PZT does not extend to the end of the beam.

Modeling and analysis of the influence of load on the output power of cantilevered piezoelectric bimorph generators was presented by Lu *et al.* [LLL04] [BTW06]. The optimal load depends on different piezoelectric generators (Eq.(I.1)).

$$R_{opt} = \frac{t}{bL\varepsilon_{33}\omega} = \frac{1}{\omega C_p} \tag{I.1}$$

where t denotes the thickness of piezoelectric layer, b the beam width, L the length of piezoelectric film on the beam, ε_{33} the dielectric constant, ω the frequency and C_p the capacitance of piezoelectric element. Richards *et al.* discussed the efficiency of a piezoelectric device excited at its resonance by a harmonic force with constant amplitude [RABR04]. They confirmed the existence of an optimal load and the energy harvesting efficiency is strongly dependent on the product of the mechanical quality factor Q_M and electromechanical coupling factor k^2.

Electrical circuitry optimization The piezoelectric generator can be improved by optimizing the power circuitry. The complete system of piezoelectric harvester is shown in Fig.(I-5) [Wu13]: the left part of the figure is the equivalent model of vibrating piezoelectric element, the right part is the harvesting circuit which usually consists of an AC-DC con-

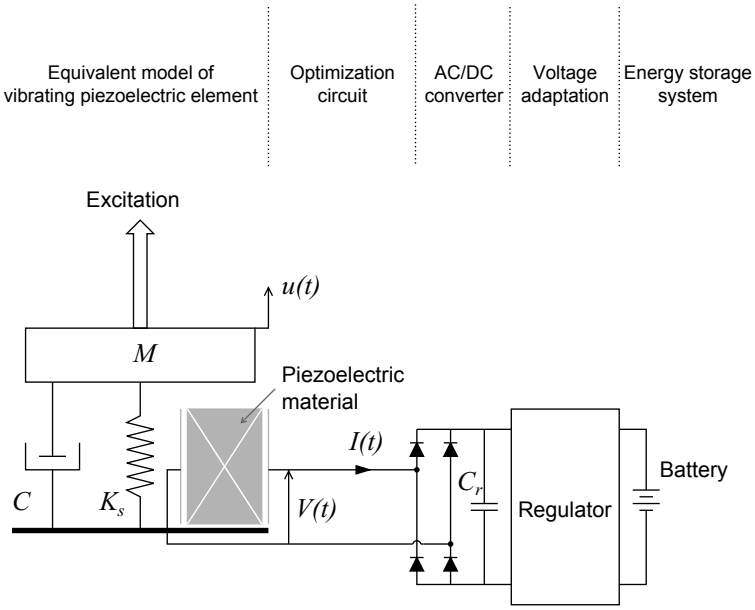

Figure I-5: An equivalent model for a piezoelectric vibration energy harvesting system [Wu13]

verter with an output capacitor, an electromechanical battery and a switch mode DC-DC converter that controls the energy flow into the battery [OHBL02]. The interface circuit design is of considerable importance in the piezoelectric energy harvesting system as it can actively change the mechanical-electrical properties of vibrating piezoelectric element.

Guyomar *et al.* have proposed a self-adaptive power harvesting circuit "Synchronized Switch Harvesting on Inductor" (SSHI) to optimize the extracted energy from the piezoelectric element [GBLR05]. The principle of this nonlinear interface is the synchronization of piezoelectric open-circuit voltage with the system vibration to improve the efficiency of the energy conversion process. A switch device is added up in parallel with the piezoelectric element as shown in Fig.(I-6). The device is composed of a switch and an inductance connected in series. The switch is almost always open, except when a displacement extremum occurs. At this instant, the switch is closed and the capacitance of piezoelectric element and the inductance constitute an oscillator. The switch will be kept closed until the voltage on the piezoelectric element is reversed. Such a technique leads to a significant increase of electrical harvested power by 900% comparatively with the standard technique.

Other piezoelectric generators Bio-piezoelectric devices have been described by Lee *et al.*. They have developed a bio-piezoelectric device based on genetically modified bacterial viruses (M13 phages) with an aligned protein coat structure to form the necessary electrical dipole [LZZ+12][BKWD13]. The liquid-crystalline property of these phages enables self-

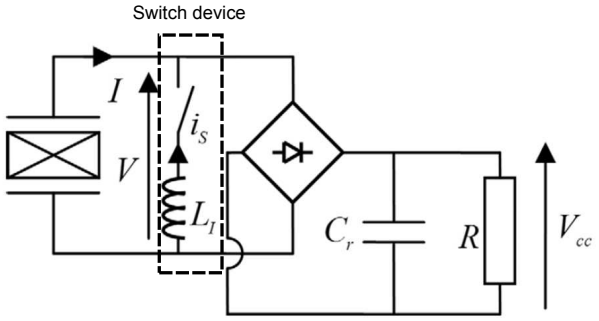

Figure I-6: SSHI energy harvesting device in steady state operation [GBLR05]

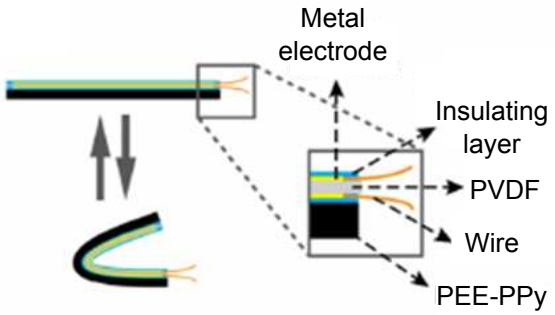

Figure I-7: The assembly of a piezoelectric PVDF element with a PEE-PPy actuator to form the generator [MGAL13]

assembly into phage films which exhibit piezoelectric strengths of up to 7.8 pm V^{-1}. The phage piezoelectric generator produces up to 6 nA of current and 400 mV of potential which is a sufficient energy output to turn on a liquid-crystal display.

Based on water-responsive polymer [ILSS13][KK13], a generator driven by water gradients [MGAL13] has been developed to harvest mechanical vibration power. The flexible actuator (PEE-PPy) was developed based on a combination of a rigid matrix (polypyrrole) and a dynamic network (polyol-borate) and can exchange water with the environment to induce film expansion and contraction, resulting in rapid and continuous locomotion (Fig.(I-7)). A 9-μm-thick PVDF film was metalized, wired and insulated on both faces. A 27-μm-thick PEE-PPy actuator was attached to one face of the PVDF element. When placed on a moist substrate with the actuator facing down, the actuator bends and stretches the piezoelectric element repeatedly. The generator outputs alternating electricity at about 0.3 Hz with a peak voltage of $\sim$ 1.0 V. Besides mechanical vibration energy, the generator can utilize ubiquitous low-temperature water gradients as its energy source.

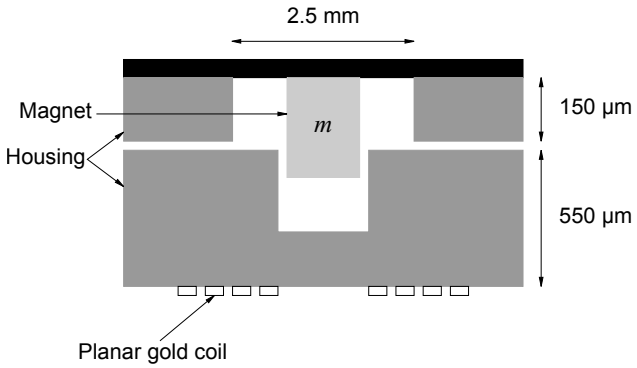

Figure I-8: Cross-section of the electromagnetic generator proposed by Williams *et al.*[WSH+01]

Electromagnetic energy harvesting

The electromagnetic induction was first discovered by Faraday. An electric current is generated in a coil placed in a magnetic field either by the relative movement of the magnet and coil, or by the changes in the magnetic field. Usually electromagnetic microgenerators[I-1] can harvest micro- to milli-watt levels of power using rotational or linear devices. An electromagnetic energy harvesting device has been proposed by Williams ane Yates [WSH+01]. The generator consists of a seismic silicon mass m of 15 mg and a spring k as shown in Fig.(I-8). The device occupies a volume of $5 \times 5 \times 1$ mm^3. When a generator is vibrated, the mass moves out of phase with the generator housing, so that there is a relative movement between the mass and the housing. This relative displacement is assumed to be sinusoidal in amplitude and may drive a suitable transducer to generate electricity. For an excitation at 70 Hz and 9.7 m s^{-2}, the predicted power output was 1 μW, assuming that the generator could be fabricated to resonate at 70 Hz. Shearwood and Yates [SY97] have fabricated a generator consisting of a planar pick-up coil and flexible polyimide membrane of 2 mm diameter with attached magnet. A planar gold coil with 13 turns was patterned on a separate wafer. At an excitation frequency of 4.4 kHz, the generated power is 0.3 μW which is lower than the predicted value which was attributed to nonlinear membrane displacement caused by the spring stiffening effect, which occurred as the excitation amplitude was increased.

Glynne-Jones *et al.* [GJTBW04] have developed electromagnetic generators based on a moving coil and two fixed magnets (the initial device) or on a moving coil and four fixed magnets (Fig.(I-9)). The prototypes are fabricated using batch machining and hand assembly

[I-1] Microgenerators are usually referred as generators which possess relatively small volume and light weight compared to the host structure on which they are implemented, thus not influencing the performances of the system in which they are integrated.

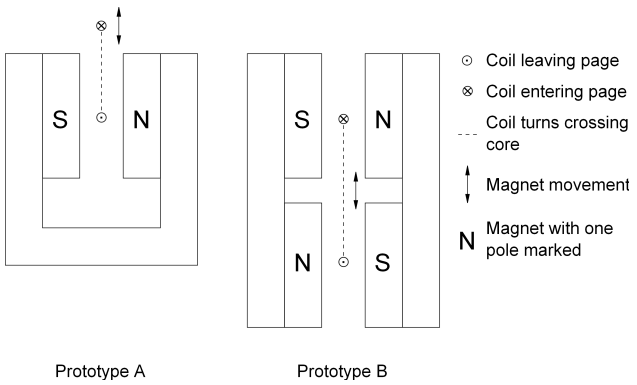

Figure I-9: Electromagnetic generator geometry by Glynne-Jones *et al.*[GJTBW04]

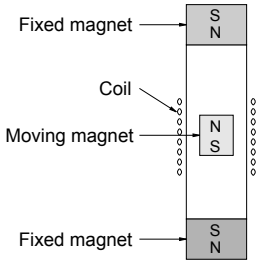

Figure I-10: Magnetic spring generator structure [SOWM08]

with different magnet configurations. The initial device (prototype A) occupying an overall volume of 0.84 cm^3 generated electrical power leveling up to 180 μW for a free-end beam displacement of 0.85 mm, however the output voltage is too low for practical application. With the same input vibration, prototype B produced more than twice the output voltage and hence more than four times the instantaneous power. When mounted on the engine block of a car, the device based on geometry of prototype B is described to produce an average power of 157 μW.

A magnetic spring generator is described in [SOWM08] aiming at supplying power to body worn sensors or electronic devices. It is designed to be beneficial over the cantilever structure for random vibration signal. Two magnets are fixed at both ends of the tube in such a way that the facing surfaces of the fixed and moving magnets have the same polarization. A middle permanent magnet is free to move but is suspended between both fixed end magnets in the generator housing due to the repulsive force. A coil is wrapped around the outside of the tube. When the tube is vibrated, the middle magnet vibrates up and down and a voltage will be induced in the coil. The prototype generators generated 0.3 - 2.46 mW when placed inside a rucksack which was worn during walking and slow running. With a simple diode capacitor rectifier, the prototype was able to transfer 3.54 J to a rechargeable battery in 1

h [Har11]. This energy level is enough to power low-power sensor modules without battery [BOST04].

Liao *et al.* [LCC+09] have fabricated a self-powered miniaturized rotary generator with a size of $10 \times 10 \times 2$ mm^3 including its energy harvesting circuit chip. The designed generator is composed of patterned planar copper coil and a multipolar hard magnetic ring made of NdFeB. The optimized device was described to offer 4.5 V and 7.23 mW in root mean square (rms) at 10000 r min^{-1}. Its compact circuit chip employed Dickson charge pump with diode-connected MOS transistors and was capable of collecting AC power into the form of a DC voltage across an output capacitor.

Sari *et al.* have worked on electromagnetic harvesters aiming at enlarging or lowering the working frequency. In 2008, they developed an electromagnetic micropower generator for wideband environmental vibrations [SBK08]. The reported generator covers a wide band of external vibration frequency by implementing a number of serially connected cantilevers in different lengths resulting in an array of cantilevers with varying natural frequencies. The tests show that by utilizing 35 cantilevers, the fabricated device generates 10 mV voltage and 0.4 μW power continuously in an external vibration frequency range of 4.2 - 5 kHz, covering a band of 800 Hz (however the power density is largely reduced). In 2010 they proposed a generator that accepts low-frequency vibrations as input and creates high-frequency vibrations to act as a linear motion transformer by employing the frequency upconversion (FupC) technique [SBK10]. The generator (Fig.(I-11)) is composed of two mechanical structures: a magnet attached to a diaphragm that resonates with ambient frequency (in the range of 1 - 100 Hz), and an array of cantilevers (resonance frequency in the range of $2 - 3$ kHz) located right below the diaphragm. At the tip of each cantilever, nickel is electroplated for interaction with the magnet. As the diaphragm resonates in response to external vibrations, the magnet catches the cantilevers at a certain instance of its movement, pulls them up, and releases them at another point. The released cantilevers start resonating at their high damped natural frequency with the given initial condition, realizing the FupC. The motion of the released cantilevers exponentially decays out, and before it completely dies, the cycle starts again. The experimental result shows that from a natural diaphragm frequency of 113 Hz, the system is able to produce a peak power and peak voltage of 0.25 nW and 0.57 mV respectively from a single cantilever at microscale design.

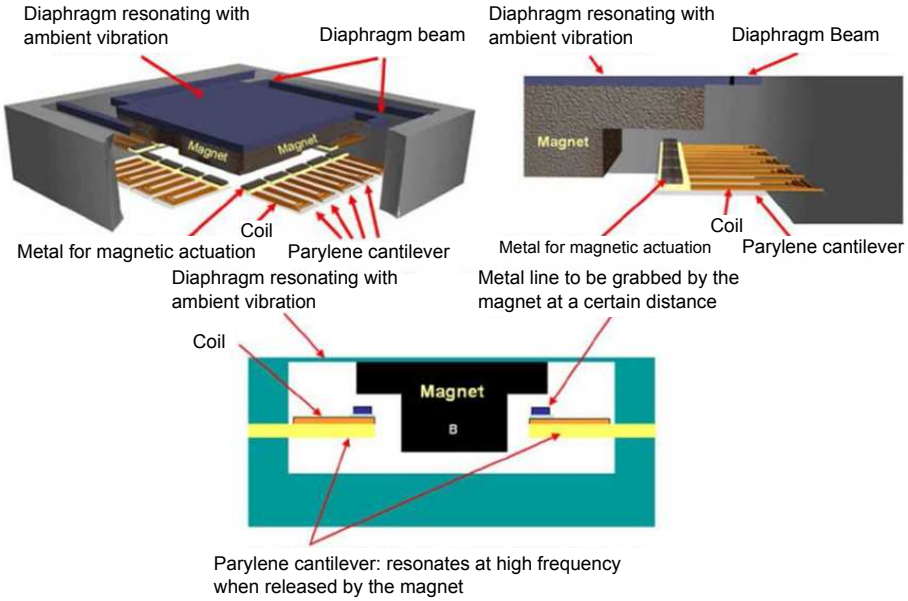

Figure I-11: Electromagnetic generator for frequency upconversion[SBK10]

Electrostatic energy harvesting

A capacitor typically consists of two plates which are electrically isolated from each other usually by air, vacuum or an insulator. Electrostatic energy harvesting is based on the charging of capacitor plates. The plates of an already charged capacitor are separated by vibration or other motions, leading to a change in capacitance. The fundamental definition of the capacitance is given by:

$$C = \frac{Q}{V} \tag{I.2}$$

where C is the capacitance, Q is the charge on the plate and V is the voltage on the plates. When a charge Q is on the capacitor and the capacitance is changed by the variation of distance between the plates caused by an external force, the voltage on the plate V varies, leading to an electromechanical coupling due to Coulomb force interaction. Meninger *et al.* has proposed two energy harvesting cycles based on the capacitance variation - charge-constrained cycle and voltage-constrained cycle [MMMA+01], which will be introduced in detail in Chapter II. Electrostatic energy harvesters may be classified into three main categories according to their configurations: in-plane overlap varying, in-plane gap closing and out-of-plane gap closing (Fig.(I-12)). Roundy *et al.* concludes that in-plane gap closing configuration offers the highest power output with an optimized design producing 100μW cm^{-3}; out-of-plane gap closing is the next highest followed by in-plane overlap varying.

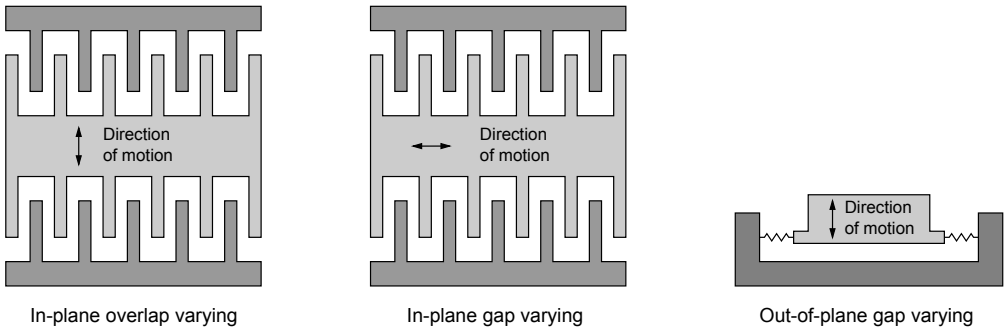

Figure I-12: Three configurations for electrostatic generators

Meninger *et al.* [MMMA+01] simulated an in-plane overlap varying electrostatic generator. The interdigitated structure generated 8 μW from 2.5 kHz input motion. An architecture for closing a loop around the system by means of energy feedback was proposed to offer more robust operation. With this control scheme the generator produced approximately 5.6 μW of usable power. Despesse *et al.* have developed an electrostatic transduction structure able to recover power over a large spectrum below 100 Hz [DJJJ+05]. They chose an in-plane gap closing structure with a charge-constrained cycle. The electrical damping is due to the electrostatic force which has to counterbalance in a high damping configuration almost entirely the mechanical spring force. A high damping was achieved by choosing an electrical stiffness close to the mechanical stiffness. The device of volume 18 cm^2 $\times$ 1 cm with a 0.104 kg inertial mass produced a global scavenged power of 1052 μW for a vibration amplitude of 90 μm at 50 Hz, which corresponds to a scavenged efficiency of 60%. Tashiro *et al.* [TKK+02] have developed an electrostatic generator of out-of-plane gap closing type with a honeycomb structure. The aim is to create a power supply for use with a device such as a cardiac pacemaker. The capacitor was made by repeatedly folding a pair of long electrodes made of aluminum-evaporated polyester film. Two sheets of 5 μm thick, 30 mm wide, and 5 m long, were mated together by using double-sided adhesive tape at regular 5 mm interval. Then the mated sheets were repeatedly folded and joined by using double-sided adhesive tape. The variable capacitor has 20 cells per layer and 50 layers; thus, it has 1000 cells. The honeycomb variable capacitor was suspended between the acrylic boards by 12 tension coil springs. Driven in real time by simulating the vibration of the left ventricular wall with a vibration mode simulator, the device generated a mean power of 36 μW with the peak value up to 500 μW.

Hoffmann *et al.* [HFM11] have brought modifications to the configuration of in-plane overlap varying and in-plan gap closing types. Trapezoidal electrode structures were pro-

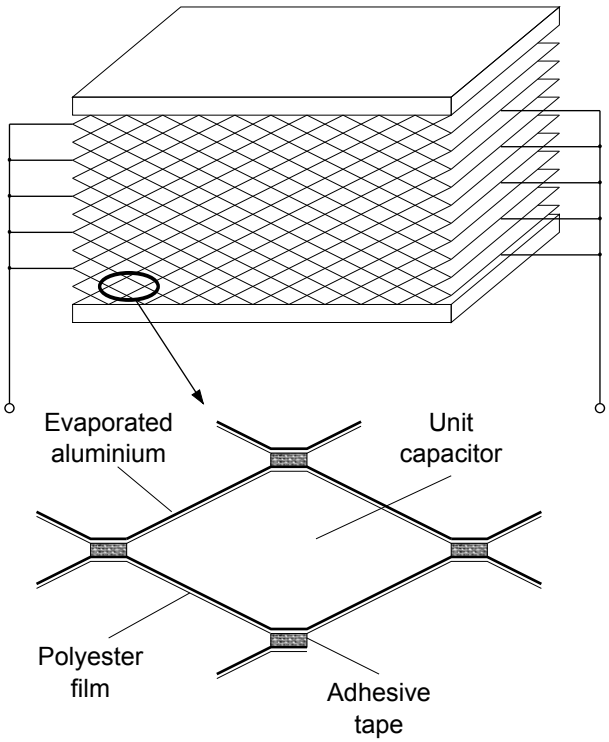

Figure I-13: Fundamental structure of a honeycomb variable capacitor [TKK+02]

posed to increase the capacitance change per unit displacement (Fig.(I-14)). According to the analysis of structure, the value of trapezoidal angle α depends on the maximum capacitance which increases for decreasing values of α. A capacitor of 20 μF generated 123 μJ in about 5 min under an excitation level of 20 m s^{-2}. This structure caused a nonlinear frequency response which may be used to tune the resonance frequency of the device and to increase the effective bandwidth.

Non-resonant electrostatic generators Mitcheson *et al.* [MMS+04] reported an electrostatic non-resonant prototype designed to operate in applications in which the amplitude of the external motion is larger than the maximum internal displacement of the proof mass of the generator. The device design follows the coulomb-force parametric-generator architecture which is well suited for large amplitudes and low frequencies (Fig.(I-15)). This coulomb-force generator uses the contact force to damp the movement of the parallel plate capacitor. Energy conversion only starts when the acceleration of the frame is greater than the damping force per unit of proof-mass, thus causing the mass to move relatively to the frame. An active capacitor plate area of 200 mm^2 with a proof mass composed of three stacked silicon plates (10 mm $\times$ 11 mm $\times$ 0.4 mm) with a maximum displacement of $\sim$ 450 μm was fabricated.

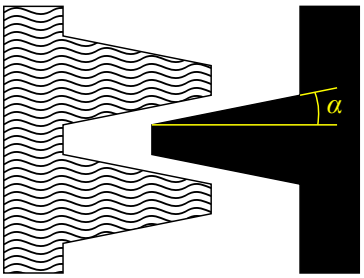

Figure I-14: Schematic view showing a triangular electrode structure [HFM11]

A capacitance variation from 15 pF to 127 pF produced a final discharge voltage of 250 V with 11 pF of parasitic capacitance [RWN09]. Miao *et al.* made further development of the non-resonant energy harvester [MMH+06]. Harvested energy was leveled up to 120 nJ per cycle with output voltage up to 220 V. When using silicon as the proof mass material, an optimized generator can generate about 2.6 μJ per cycle at 30 Hz. A replacement of silicon by gold as the proof mass material may increase the power output tenfold.

Kiziroglou *et al.* have developed in 2008 a non-resonant electrostatic energy harvester composed of a substrate including the dielectric covered plates, the input and output contacts, and of an external, free rolling rod as the proof mass [KHY08] [KHY09] as depicted in Fig.(I-16). Glass instead of silicon was used as a substrate to reduce parasitic capacitance effects. A series of strip electrodes form the fixed plates of the variable capacitor, and are covered by a thin dielectric layer. A metal cylinder forms the moving counter-electrode. When the cylinder is aligned with one of the strip electrodes, it makes direct contact with an additional charging contact, by which the necessary pre-charge is applied. This creates an electrostatic force between the cylinder and the strip electrode. Motion of the substrate then induces rolling of the cylinder, causing it to break contact with the pre-charge supply; the separation is then increased at constant charge, so that as the capacitance reduces, the

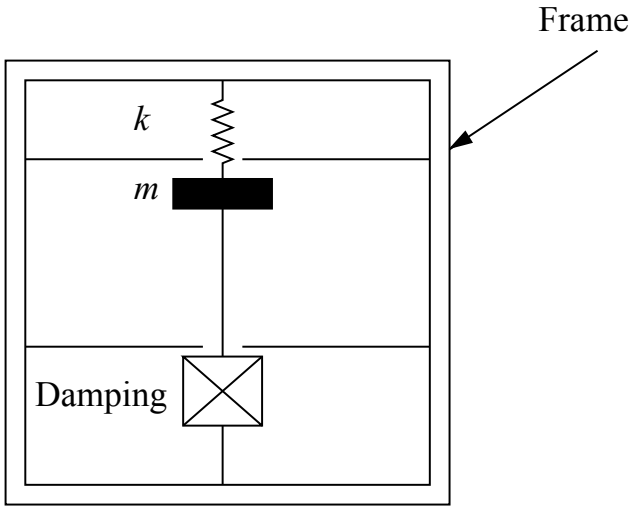

Figure I-15: Generic model of motion-driven electrical generator [MMS+04]

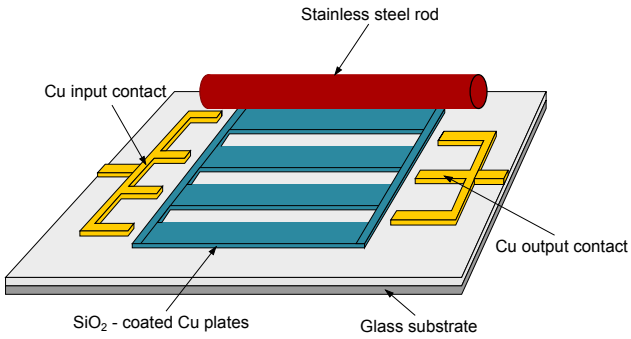

Figure I-16: Schematic illustrating physical construction of the non-resonant device [KHY08]

stored energy increases due to the work done against the electrostatic force. The device of about 9.25 mm ×10 mm ×650 nm generated a peak voltage of 48 V corresponding to a voltage gain of 2.4. In 2010 based on the previous model they presented a new rolling rod device employing a flexible semi-cylindrical substrate to allow the formation of a concave structure [KHY10]. The metal rod can roll inside the fixed concave substrate which includes the dielectric covered plates and the input and output contacts. Higher substrate curvature results in larger maximum and minimum rod to plate capacitance and hence in higher power transduction. The largest achievable capacitance corresponds to the extreme case of the rod being wrapped by the substrate. The device structure also benefits from the natural confinement of the rod inside the concave substrate. With a rod oscillation frequency of 10 Hz and an input resistance 10 MΩ the device generated an output power of 0.5 μW.

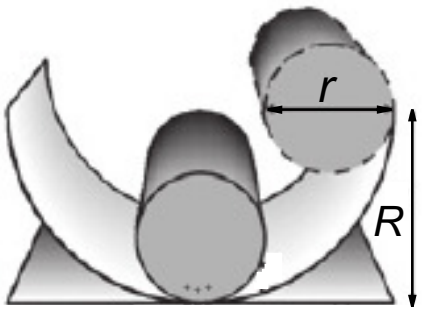

Figure I-17: Flexible substrate device [KHY10]

Generators using charged electrets An electret is a dielectric material with quasi-permanent charges. The lifetime of charges can be stabilized for tens of years [OB92][Ses99]. Takamatsu has examined the longterm stability of carnauba wax electrets and the surface charge density was found to be unchanged after 35 years [Tak91]. Sterken *et al.* described the technique of running an electrostatic generator with an electret [SFB+03][SFB+04]. The SiO_2/Si_3Ni_4 electret is placed in parallel with two variable comb drive capacitors operating in antiphase as illustrated in Fig.(I-18), resulting in charge transfer between the variable capacitors as the proof mass moves. The power harvested with such a technique could be maximized by applying an active cycle which is composed of three steps: 1 maximizing the capacitance change per unit displacement of inertial mass; 2 tuning the damping until the inertial mass displacement is at its maximum permitted by the structure; 3 maximizing the polarization voltage 300 V realized in real device [SFB+04]. Mitcheson *et al.* have noticed that with the use of two variable capacitors, the generated current does not have to flow through the electret capacitor to avoid the low-pass filtering effect of the electret [MYR+08]. In later work they modified the design where only one variable capacitor was used for optimization. The modified device was capable of generating 5 nW from a 500 Hz, 3 mm s^{-1} vibration. Mizuno and Chetwynd [MC03] described an electret-based out-of-plane, gap closing, voltage constrained variable capacitor. The device uses an electret with a variable air gap and under testing produced a 16 mV output when excited at the resonant frequency of 743 Hz, with an input amplitude of 0.64 μm.

Arakawa *et al.* [ASK04] presented an in-plane, overlap varying, voltage constrained, variable capacitor using amorphous perfluoropolymer (CYTOP) as the dielectric. For a 1 mm displacement amplitude at 10 Hz, the two-wafer glass device of 20 mm $\times$ 20 mm $\times$ 2 mm volume generated an output power of 6 μW at 200 V with an optimized load of 10^8 Ω. Tsutsumino *et al.* further developed this design [TSKS06]. The electret material was

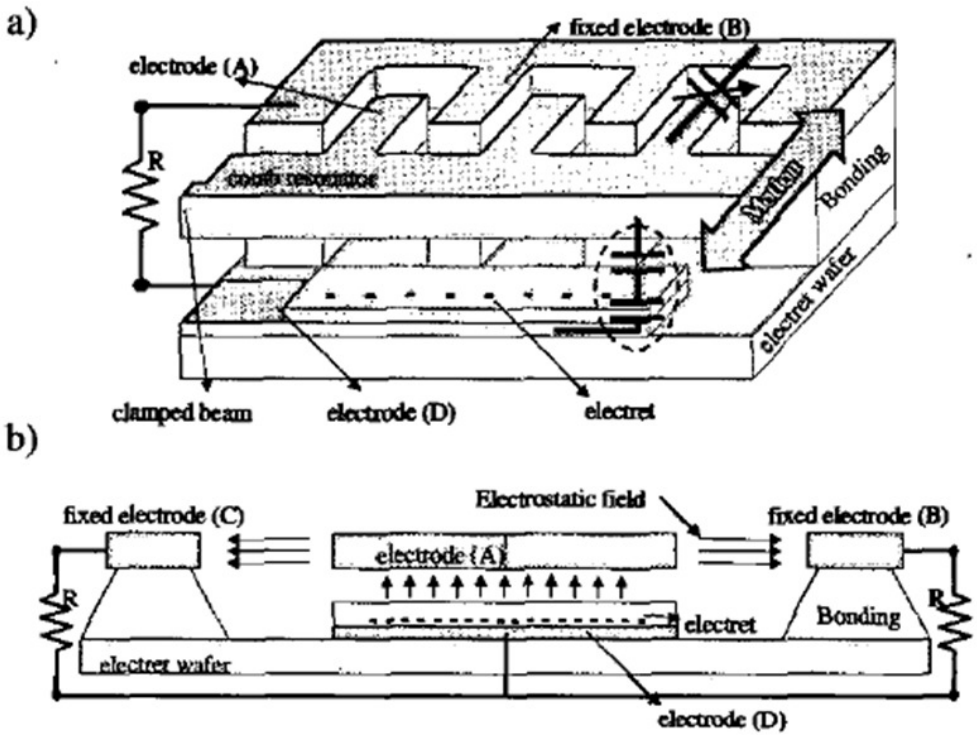

Figure I-18: Cross-section (a) and side view (b) of the proposed implementation [SFB+03]

charged through corona discharging for a charge density as large as 1.37 mC m^{-2} (employing a 15 μm film) with an average surface voltage close to 1000 V. The maximum power output was 38 μW tested at 20 Hz with a 2 mm peak-to-peak amplitude vibration, and about 150 V sinusoidal peak-to-peak waveform was measured.

Other electrostatic generators In recent years, fluids have also participated in the operation of electrostatic energy harvesters. Yang *et al.* [YHD12] have utilized a conductive droplet as an electrode (Fig.(I-19)). With two solid electrodes and an electret, the droplet electrode forms two variable capacitors on the glass. The energy could be extracted with droplet motion which changes the relative position between the droplet electrode and solid electrodes and leads to a capacitance variation. The output voltage depends on the diameter of the droplet. For a single droplet of 1.2 mm diameter which slides on a 2 μm thick electret film, the prototype could generate a peak output power of 0.18 μW.

Galchev *et al.* have proposed an electrostatic generator for converting multi-axial and low-frequency motion from humans and the environment. The harvester uses attraction between a springless spherical magnetic proof mass and a magnetic fluid to induce a physical parameter change in a variable capacitor. The generator is composed of a spherical magnet

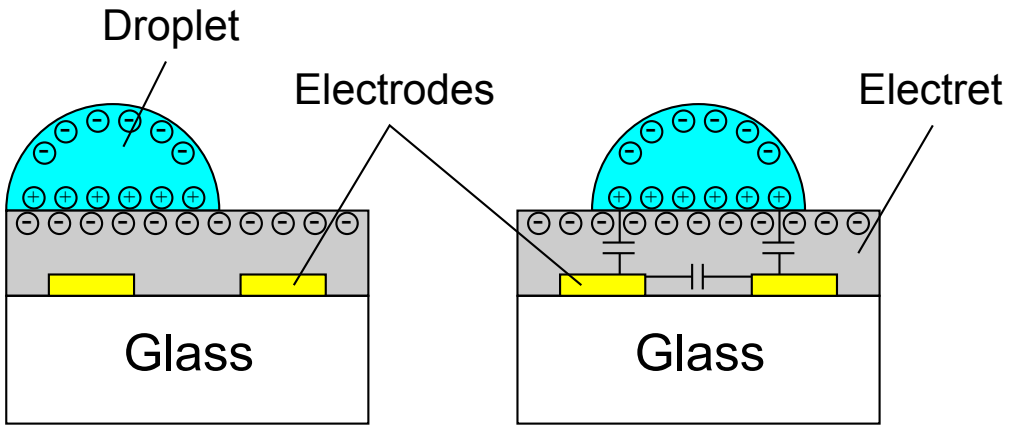

Figure I-19: The fluidic energy harvester based on conductive droplet [YHD12]

rolling above a cell array of capacitors. The movement of a ferrofluid in the gap of capacitor altered its dielectric permittivity and the capacitance change was realized by substituting one dielectric material for another with different permittivity. It is reported that for a 25 mm^2 prototype capacitor cell, the device generated 472 nJ per transition with a 100 V pre-bias for magnet velocity of 6 mm s^{-1}.

Other conversion effects for mechanical energy harvesting

Electrostrictive effect For applications in low frequency and large stroke mechanical excitations, electrostrictive polymers are better candidates compared to piezoelectric ceramics or piezoelectric polymers as they are more flexible, able to generate large strain (about 5%) under moderate electric field intensity (400−800 V on a 20 μm film), and of mechanical energy density comparable to that of piezoelectric single crystal [LRHZ05][BC04]. Lallart *et al.* have evaluated the energy harvesting ability of electrostrictive terpolymer composites filled with 1 vol% carbon black poly(vinylidene-fluoride-trifluoroethylene-chlorofluoroethylene) [LCL+10]. The carbon-filled terpolymer exhibits a figure of merit 2000 times higher than pure polyurethane. In energy harvesting applications, Cottinet *et al.* have shown that under an electric field of 5 V μm^{-1} and a strain of 0.2% at 100 Hz, the highest power harvested for pure P(VDF-TrFE-CFE) is 7.2 μW cm^{-3}, while that for carbon-filled polymer is 15.3 μW cm^{-3} [CGL+11]. More details about energy harvesting using electrostrictive effect will be discussed in Chapter III.

Magnetostrictive effect Mechanical energy harvesting could also benefit from magnetostrictive effect - Villari effect which is vibration-induced strain of an magnetostrictive material (MsM) produces a change in its magnetization. Two commercial MsMs are practical in

energy harvesting applications: crystalline alloy Terfenol-D ($Tb_{0.3}Dy_{0.7}Fe_{1.9-2}$) [Lac93] and Metglas 2605SC ($Fe_{81}B_{13.5}Si_{3.5}C_2$) [Met14]. Wang and Yuan have developed a new class of energy harvesting scheme based on amorphous Metglas 2605SC which demonstrates higher energy conversion efficiency, longer life cycles, lack of depolarization and higher flexibility compared to piezoelectric materials [WLS+07][WY08]. The MsM energy harvesting device was described to be equivalent to an electromechanical gyrator in series with an inductor. An energy harvesting circuit was designed on a printed circuit board (PCB) with plane dimension 25 mm × 35 mm, consisting of a voltage quatrupler, a 3 pF ultracapacitor and a smart regulator. For a working prototype under a vibration with resonance frequency of 1.1 kHz and peak acceleration of 8.06 m s^{-2} (0.82 g), the average power and power density during charging the ultracapacitor can achieve 576 μW and 606 μW cm^{-3}.

I.1.2 Thermal energy harvesting

Thermal resources are ubiquitous in the nature and human society. The electrical power converted from thermal energy one day may serve as a replacement of the batteries in small scale applications. Thermal energy harvesting are usually achieved by thermoelectric or pyroelectric effects. The difference relies in that thermoelectric effect is based on spatial temperature gradient while pyroelectric effect is caused by temporal temperature variation.

Thermoelectric energy harvesting

In 1822 Thomas Johann Seebeck found that a circuit made of two similar metals, with junctions at different temperatures could deflect a compass needle. It is later discovered that a current is induced by the temperature difference and deflects the needle by Ampère's law. In 1834, Jean Charles Athanase Peltier discovered that on passing a current across a junction of two different conductors there is a liberation or absorption of heat at the point of union - the temperature rising or falling according as the current flowed down or up the potential gradient [Spa51]. In the 1850s, Lord Kelvin predicted and subsequently observed that when a current is driven through a conductor with a temperature gradient a continuous version of the Peltier effect will occur, which is named the Thomson effect. He also attributed that the reversible heat flow discovered by Peltier was associated with an entropy and the Seebeck coefficient was a measure of the entropy associated with the electric current [Pau14]. The first two effects may be termed together as the Seebeck-Peltier effect. The Seebeck-Peltier and Thomson effects are thermodynamically reversible and are not independent of, but rather a combination of each other.

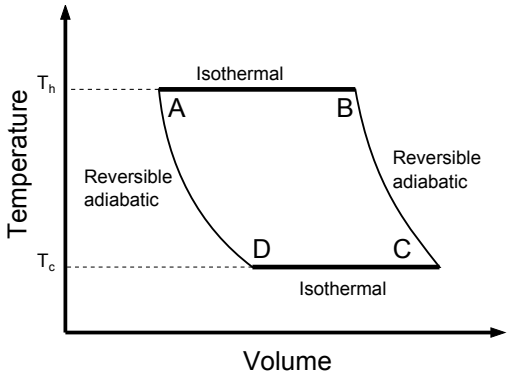

Figure I-20: The temperature-volume phase diagram for the Carnot thermodynamic cycle

The thermoelectric effects arise from the fact that the charge carriers in metals or semiconductors may carry charges as well as heat. When a temperature gradient is applied to the material, the charge carriers at the hot side are in higher energy status and preferentially diffuse to the cold side and build up a net charge at the cold end, producing an electrostatic potential. The buildup of charge helps to reach an equilibrium between the chemical potential for diffusion and the electrostatic repulsion [ST08]. This property, known as the Seebeck effect, is the basis of thermoelectric power generation.

Global conception of thermoelectric energy harvesting Carnot cycle will first be introduced as it admits the maximum efficiency for converting a given amount of thermal energy into work done and therefore serves as a standard for any thermal system. As depicted in Fig.(I-20), the gas experiences a reversible isothermal expansion at the hot temperature from A to B; then it goes through an isentropic (reversible adiabatic) expansion from B to C with temperature reduced; it is compressed in a reversible isothermal way from C to D; then continuously being compressed isentropically from D to A and back to the original status. The efficiency of such a cycle depends on the maximum (T_h) and minimum (T_c) temperatures:

$$\eta_C = 1 - \frac{T_c}{T_h} \tag{I.3}$$

The thermodynamic efficiency of thermoelectrics was first demonstrated by Altenkirch in 1911. The efficiency is defined as:

$$\eta = \frac{\text{Power supplied to a load}}{\text{Heat absorbed at the hot junction}} \tag{I.4}$$

By a series of derivation (chapter 4 in [Pau14]), the maximum efficiency for a thermo-

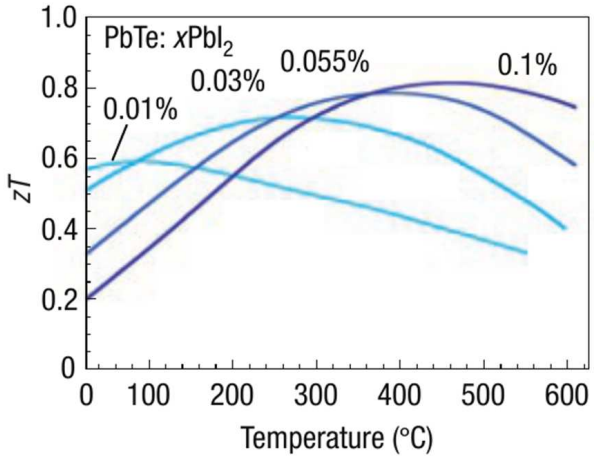

Figure I-21: The peak zT and the temperature where the peak appears in PbTe are tuned by changing the dopant concentration [BKGS06]

electric generator is given as:

$$\eta = \left(1 - \frac{T_c}{T_h}\right) \frac{\sqrt{1+ZT}-1}{\sqrt{1+ZT}+\frac{T_c}{T_h}} \tag{I.5}$$

with ZT the device figure of merit defined as

$$ZT = \frac{\alpha\sigma}{\kappa}T \tag{I.6}$$

where $T = \frac{1}{2}(T_h + T_c)$, α denotes the Seebeck coefficient, σ denotes the electrical conductivity and κ is the thermal conductivity.

This efficiency may be improved by increasing the Seebeck coefficient and figure of merit of device ZT. For the latter one, one possible solution is to tune the material to provide a large average figure of merit of the material zT (lower class used to distinguish from the device figure of merit ZT) in the temperature range of interest. The peak zT in PbTe may be tuned from 300 °C to 600 °C as depicted in Fig.(I-21) [BKGS06]. For large temperature differences, segmenting with different materials with peak zT at different temperatures can improve device ZT [Sny04]. Besides, functionally graded materials can also be used to continuously tune zT [MDSK03].

Thermoelectric generators Thermoelectric technology has been applied for capturing ambient energy in wide areas recently. First applications for portable devices using thermoelectric energy harvesting have been found in the watch industry. Bulova has presented a thermogenerated wristwatch *Thermatron* in 1980 and commercialized the product in 1982.

Figure I-22: The thermoelectric wristwatch Thermomatron developed by Bulova [Bul82]

The thermogenerator consists of two metal plates (red and blue) as depicted in Fig.(I-22) that hold 4 groups of thermal couples in each corner. Couples made of antimon, bismut and tellurium produce a voltage of 0.25 mV when a temperature difference of 1.5 °C occurs. The 700 couples (175 in each group) produce a combined voltage of 175 mV which by means of the electronic circuit and coil transform the insufficient voltage to the output 1.4 V to run the movement [Bul80][Bul82]. Seiko Instruments presented a similar thermoelectric module in 1999 [KNH+99]. The thermal generator has an overall size of $2 \times 2 \times 1.3$ mm^3 composed of ten modules. One module consists of 104 thermoelements and each element is of volume $600 \times 80 \times 80$ μm^3 and made of sintered BiTe. The device generated a steady open-circuit voltage of 300 mV and after a DC-DC converter, the output voltage was boosted to 1.5 V to power electronics.

The ability to fabricate exceedingly small semiconducting thermoelements has enabled the possibility of harvesting very small amounts of heat for low power applications such as wireless sensor networks, mobile devices, and even medical applications [PS05][Sny08].

Strasser *et al.* have developed in 2002 a miniaturized thermoelectric generator based on poly-Si and poly-SiGe surface micromachining [SAFW02]. The generators were fabricated in a BiCMOS production facility which is amenable to low cost applications, each one consisting of 59400 thermocouples. They were integrated on an area of about 6 mm^2 (Fig.(I-23)) and able to generate an open circuit voltage in the range between 100 and 200 mV K^{-1}. Snyder *et al.* have exposed a thermoelectric microdevice fabricated by a MEMS-like electrochemical technique. Several different metals and thermoelectric materials were fabricated on three-dimensional bridging structures. The device contains 126 n-type and p-type $(Bi, Sb)_2Te_3$ thermoelectric elements that are, 20 μm tall and 60 μm in diameter with bridging metal interconnexions. When the top inter-connexions were coated with black antimony telluride

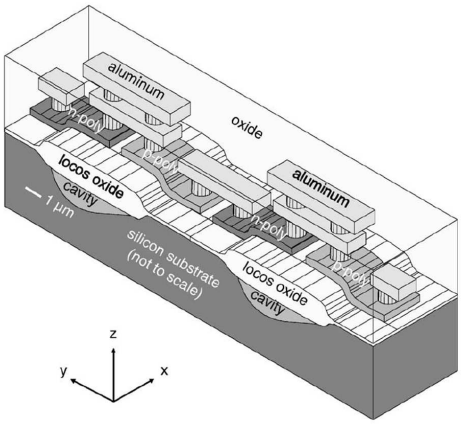

Figure I-23: Schematic view of two thermoelectric couples of the BiCMOS realization [SAFW02]

by electrochemical deposition and the device was heated by illumination with a lamp, the power output may rise to 40 μW cm^{-2} and the short circuit current is up to 40 mA cm^{-2}.

Stark *et al.* have developed an in-plane thermoelectric module with thermopiles on flexible foils [SS99]. One film of Bi_2Te_3 was deposited on Kapton®. The advantage of such a planar design is that the height can be enlarged to a few millimeters and the width can be reduced to a few tens of micrometers, thus increasing the aspect ratio. Although the high thermal conductivity of the substrate will reduce the efficiency and decrease the temperature difference across the device, the generator gains from the density and length of the thermoelectric elements such that 5 V can be produced with a 10 K temperature drop. The device has been commercialized later as Thermo Life® [Sta06] which is of an outer diameter 9.3 mm and of thickness 1.4 mm. The further developed device is capable of generating an open circuit voltage of 5.2 V and a short circuit current of 22 μA for a 5 K temperature gradient. Karabetoglu *et al.* have experimented a commercially available and relatively inexpensive Bi_2Te_3 based thermoelectric power generator in low temperature range of $100 - 375$ K [KSFOS12]. The variation of maximum power output with the mean temperature showed the critical mean operating temperature to be 250 K.

Several flexible thermoelectric generators have been reported which are competitive candidates for applications in wearable self-powered systems. Francioso *et al.* presented a micro thermoelectric generator for ambient assisted living wearable biometric sensors [FDPF+11]. Sb_2Te_3 and Bi_2Te_3 thin films alloys were deposited on Kapton® HN polyimide foil by RF magnetron co-sputtering technique. The prototype, integrating an array of 100 thin films thermocouples of Sb_2Te_3 and Bi_2Te_3, generates, at a temperature gradient of 40 °C, an open

circuit output voltage of 430 mV and an electrical output power up to 32 nW with matched load. Another flexible Bi_2Te_3-Sb_2Te_3 based thermoelectric generator has been reported by Cao *et al.* [CKT+13]. The thermocouple was fabricated using screen printing technology. The dimension of each planar thermoleg is 39.3 mm × 3 mm with a thickness of 67 μm for Bi_2Te_3 leg and 62 μm for Sb_2Te_3 leg. A single thermocouple with this dimension generates a voltage of 6 mV and a peak output power of 48 nW at a temperature difference of 20 °C. Kim *et al.* have presented a flexible glass fabric-based flexible TE generator using screen printing technique with thickness about 500 μm and weight about 0.13 g cm^{-2} [KWC14]. The device is able to generate an electric power about 3.5 mW cm^{-2} and 28 mW g^{-1} for a temperature gradient of 50 °C.

Pyroelectric energy harvesting

The phenomenon of pyroelectricity has been known for long time , it may be understood as the possession by some materials of a temperature-dependent spontaneous electric dipole moment. Such materials demonstrate the ability to attract objects when heated. As introduced above, there are 10 classes of pyroelectric crystals of all 32 crystal classes, characterized by having a unique polar axis.

Origin of pyroelectric effect Crystals of pyroelectric classes are defined as polar as they possess a spontaneous polarization P_s in the absence of an applied electric field, where P_s is the average electric dipole moment per unit volume [Lan05]. The polarization leads to a layer of bound charge on each flat surface of the material and free charges (ions or electrons) are attracted to the charged surfaces to form a layer of unbound charge. Usually this spontaneous polarization cannot be detected by charges on the surface of crystal because the depolarizing field resulting from the bound charge distribution can be compensated by the flow of free charge (unbound charge) within the crystal and in the surrounding medium. However, as the polarization level is dependent on temperature, the existence of the spontaneous polarization can be detected by observing the flow of charge to and from the surfaces on change of temperature [LG01]. The dependence of polarization on temperature is the origin of pyroelectric effect. When the material is heated ($dT/dt > 0$) its polarization level decreases as dipoles lose their orientation and the level of unbound charges on the material surface decreases [Lan05][BKWD13]; this results in an electric current and power generation. Similarly, as the pyroelectric is cooled ($dT/dt < 0$) the dipoles regain their orientation leading to an increase in the level of polarization, thus reversing the electric current flow.

This is termed the primary pyroelectric effect and is relevant to perfectly clamped materials under constant strain. As pyroelectric crystals also demonstrate piezoelectric effect, a secondary pyroelectric effect is present: thermal expansion induces a strain that alters the electric displacement via the piezoelectric effect [BN80].

The secondary pyroelectric effects have been reported to significantly contributed to the overall pyroelectric effect [LLC+12]. It has been observed by Mane *et al.* that when the PZT composites are pre-stressed, the pyroelectric generator may harvest energy 40% larger than that with simple PZT ceramics [MXLM11]. Chang and Huang have developed laminated structures with differing thermal expansion and stiffness characteristics to enhance the contribution of the secondary pyroelectric coefficient for energy harvesting [CH10]. Lead zirconate titanate and stainless steel laminate composite with 88% pyroelectric coefficient enhancement is shown to increase its maximum power density, efficiency, and electrothermal coupling factor by 254%.

The direct pyroelectric energy harvesting can be realized by connecting a resistive load to the material which is subject to a temperature change to harvest energy. A pyroelectric micro-generator comprised of polyvinylidene difluoride (PVDF) films was developed [GSLK08]. The synchronized switch harvesting on inductor (SSHI) was applied to improve the effectiveness of the energy conversion. For several amplitude variations of temperature from 0.5 to 8.0 K, the conversion efficiency of Carnot thermodynamic cycle with a standard interface was increased by the SSHI technique from 0.02% to 0.05%. The produced electrical power for temperature amplitude 7 K at 0.2 Hz is 0.32 mW for an energy harvesting device composed of 8 g of active material. Increased power could be produced by increasing the temperature amplitude, frequency and using a material with higher pyroelectric coefficients. Pyroelectric cells based on fabricated screen-printed PZT and commercial PVDF films are proposed as thermal energy harvesting sources for low-power autonomous sensors [CGF10]. The cells are electrically modeled as a current source in parallel with output capacitor. Heating and cooling temperature fluctuations generated by air currents were applied to the pyroelectric converters. The generated currents of 10^{-7} A and charges of 10^{-5} C were achieved for temperature fluctuations from 300 K to 360 K in a time period over 100 s, which agreed with a first order electrical model based on a current and an output capacitor. The current from cyclic temperature fluctuations was rectified and stored in a 1 μF load capacitor. Energies up to 0.5 mJ have been achieved, enough to power typical autonomous sensor nodes during a measurement and transmission cycle.

A pyroelectric generator was proposed by Leng *et al.* based on a polyvinylidene fluoride

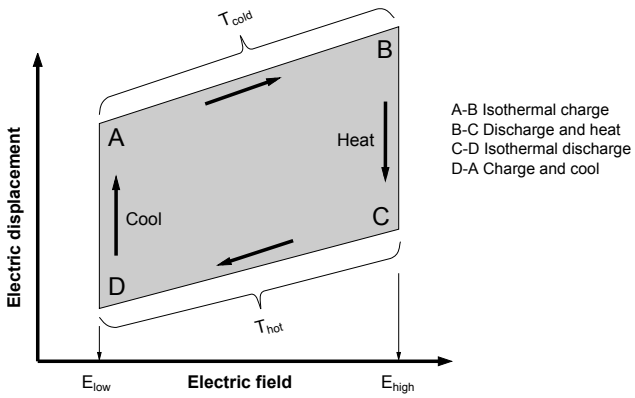

Figure I-24: Olsen cycle [LGM+12]

film for harvesting the heat energy from hot/cold water [LCG+14]. By contacting a hot flow and cold flow alternately, the device produces an output open-circuit voltage and short-circuit current of 192 V and 12 μA (maximum values), respectively, under a temperature change of 80 °C. The output power density can reach 14 μW cm^{-2}, which can drive 42 green light-emitting diodes or charge a commercial capacitor (100 μF) to 3.3 V in 90 s. Xie *et al.* examined pyroelectric energy harvesting using thin devices based on PMN-PT, PVDF PZT-5A, with experimental peak power densities of 0.33, 0.20 and 0.12 μW cm^{-2} respectively. The study has indicated that the large surface area and high pyroelectric coefficient of the material are advantageous to obtain high power density.

Thermodynamic cycles for pyroelectric energy harvesting In order to increase the generated power in pyroelectric energy harvesting, thermodynamic cycles are examined. The Carnot cycle is necessary consideration when considering energy conversion from heat as it allows the maximum energy that can be converted from a given temperature variation.

However, pyroelectric conversion involves state quantities, such as electric field, electric induction, temperature and entropy, then it is not realistic to perform Carnot cycles as it is difficult to control successive adiabatic and isothermal conditions, and one needs excessive electric fields for even limited temperature variations [SPG08]. As a consequence, other cycles are examined, such as the Stirling cycle (two constant electric induction paths and two isothermal paths) or Ericsson cycles (also termed the Olsen cycles - two constant electric field paths and two isothermal paths) [OB82][OBB85][OE83][Iku02] [SLG08]. It has been shown experimentally that Olsen cycles produce more power than Stirling cycles under fixed maximum voltage [NVBP10]. The Olsen cycles will be introduced in the following.

A typical Olsen cycle is presented in Fig.(I-24) as an electric displacement *versus* electric

field (D-E) diagram. Process A-B consists of charging the pyroelectric element at a low temperature T_{cold} by increasing the applied electric field from a low electric field E_{low} to a high field E_{high} . Process B-C corresponds to discharging the element by heating it from T_{cold} to T_{hot} under constant electric field E_{high}. Process C-D consists of reducing the electric field from E_{high} to E_{low} under isothermal conditions at T_{hot}. Finally, process D-A closes the cycle by cooling the piezoelectric element from T_{hot} to T_{cold} under constant electric field E_{low}. The steps described above are intended to effectively reverse the direction of conventional polarization-field hysteresis loops which convert electrical energy into heat [Ols82]. The area enclosed in Fig.(I-24) is the electrical energy produced per unit volume of material per cycle.

Sebald *et al.* have compared the direct pyroelectric energy harvesting (e.g., connecting an adapted resistance) with Olsen-cycle-based energy harvesting. The latter technique produces energy 100 times higher [SPG08]. With the prototype as 0.90Pb($Mg_{1/3}Nb_{2/3}$)O_3-0.10PbTiO_3 ceramic, the scavenged energy reached 186 mJ cm^{-3} for 50 °C temperature variation and electric field change of 3.5 kV mm^{-1}. Based on operation at a frequency of 2 Hz with a 10 °C temperature change a power level of hundreds of mJ cm^{-3} was considered feasible. However, such a cycle requires a constant control of the electric field, which may induce additional losses in the system.

Pyroelectric energy harvesting from spatial temperature gradients Usually pyroelectric energy harvesting benefits from temporal temperature oscillation, not spatial temperature gradients which are mainly for thermoelectric energy harvesting. Pyroelectric generators (PEGs) have been integrated into a self-oscillating micro heat engine to generate electric power from a spatial temperature gradient in 2012 [RKW12]. The micro heat engine moves the PEGs between a hot and cold reservoirs, thus bringing them in an alternating contact with a higher and lower temperature. By their pyroelectric nature, the PEGs convert this periodic temperature variation into electrical energy. The micro heat engine is fabricated from a 280 μm thick bimetallic strip and the PEGs from a 250 μm thick PZT sheet. The device generates an electric power of 4.4 μW from a 96 K temperature difference at a mechanical oscillation frequency of 0.19 Hz.

Cha and Ju have proposed a device concept in 2013 which may convert spatial temperature gradients into temporal temperature oscillations necessary for pyroelectric energy harvesting by utilizing liquid-based thermal interfaces [CJ13]. Similar to the previous device, an assembly containing a pyroelectric material is oscillating up and down between two substrates which serve respectively as a high temperature source and a cold heat sink and, the pyroelectric plate repeatedly makes the thermal contact to undergo temperature oscilla-

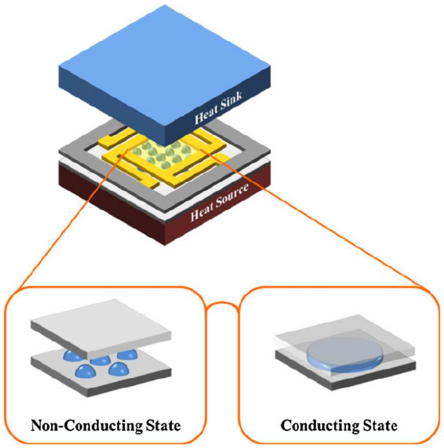

Figure I-25: Pyroelectric energy harvesting module [CJ13]

tions. On the surface of each substrate (Fig.(I-25)) is an array of circular hydrophilic islands, which are separated from each other by a contiguous hydrophobic coating. In the thermally non-conducting state, the assembly is physically separated from the hot (cold) surface and the liquid exists as discrete droplets on the hot (cold) surface. In the thermally conducting state, the assembly is pressed against the hot (cold) surface to deform the liquid droplets and force them to merge and form a continuous thin liquid layer. These surface-tension driven morphological transformation of the microscale liquid elements is reversible. Despite the low thermal conductivity of a dielectric liquid, the thermal interface mediated by such a thin (< 10 μm) liquid layer can achieve a thermal resistance comparable to that of direct solid-solid contacts at loading pressures orders of magnitude smaller [CJ09][JCJ12]. The pyroelectric cycles operate at 1 Hz with film-level power densities to be 110 mW cm^{-3}. The work did not put into consideration the energy input necessary for mechanical oscillation nor application of bias fields. The authors considered that a hybrid device configuration might be a solution to the need of external actuation power [BJCL11].

I.1.3 Other potential sources

RF energy harvesting

Background RF radiation is omnipresent in the urban environment due to numerous telecommunication antennas and other radiation-emitting devices. Electromagnetic radiations of frequencies below 10^{11} Hz, including radio waves and microwaves, can be converted into electrical power [HA08]. The average of the density in broadband ($1\ \text{GHz} - 3.5\ \text{GHz}$) is in the order of -12 dBm m^{-2} (63 μW m^{-2}) [BDLV10]. RF energy harvesting system with

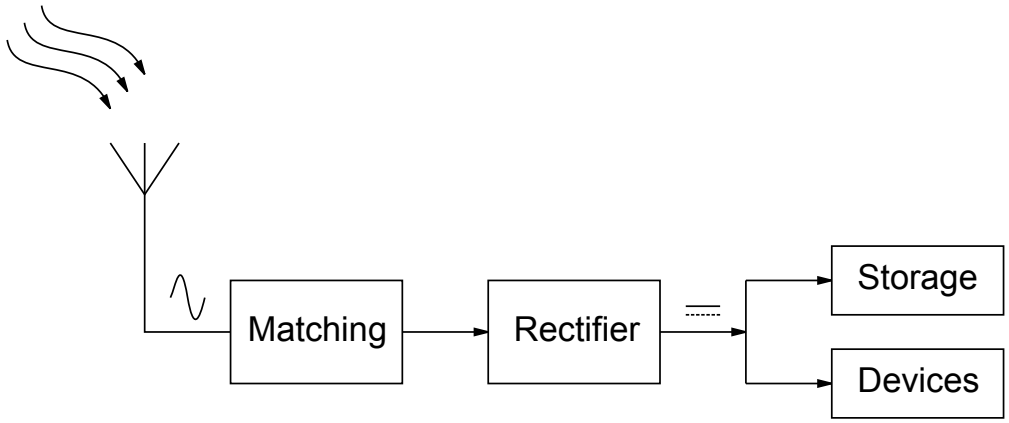

Figure I-26: Principle of RF energy harvesting system with a matching circuit [BDLV10]

a matching circuit is depicted in Fig.(I-26).

Hagerty *et al.* have studied the reception and rectification of broadband time-varying microwave radiation by applying broadband rectenna arrays [HHM+04]. The rectenna array is 64-element dual-circularly-polarized spiral, designed and characterized over a frequency range of $2 - 18$ GHz with single-tone and multitone incident waves. The antenna and rectifier are integrated by using a combination of full-wave electromagnetic field analysis and harmonic balance nonlinear circuit analysis, eliminating matching and filtering circuits. Mi *et al.* have located multiple antenna in one space [MMCS05]. The prototype had an increase of 83% in area and gave a 300% increase in available power to power given device.

It is also possible to transfer wireless power via RF waves. Brown described wireless power transmission as a three-step process: conversion of a DC power source to RF power, transmission of the power through space to some distant point, and collection and AC-DC conversion of the power with a rectenna [Bro84][Bro96]. He introduced a rectenna for low power density levels of 50 mW m^{-2} [Bro91]. With the different design that multiple collecting elements were integrated in a single rectifier, the rectenna produced 10 mW of power at 7 V DC from a source of 20 mW. Karthaus and Fischer developed a passive transponder integrated circuit that operated at $868 - 915$ MHz and used a Schottky diode voltage multiplier for RF-DC conversion [KF03]. This multiplier produced a DC voltage of 1.5 V. Power consumption was 2.2 μW from a RF input of 12.5 μW (18% efficiency).

Solar energy

Solar energy is the most universal renewable energy and photovoltaic (PV) cells have been widely studied. Green described the future trends in PV by reference to three generation

of solar cells [Gre01]. The first generation are the (poly) crystalline silicon cells usually applied for powering motorway signs and on residential rooftops. The second generation are composed of thin films that contain less silicon, or from alternative materials such as copper-indium-diselenide. The PV cells of the second generation have comparable efficiency to 1st generation cells, but are with lower costs. The 3rd generation cells use combinations of different semiconductor layers, each harvesting a specific fraction of the sunlight and thus relatively high efficiencies (above 30%). In parallel with the work on 3rd generation cells, research has been carried out on cells based on novel materials such as semiconducting polymers and nanostructure systems.

Usually commercial crystalline silicon wafers are with thickness between $180 - 300$ μm. Li *et al.* has proposed polymer solar cells based on a bulk heterojunction of polymer poly(3-hexylthiophene) and methanofullerene with the thickness of active layer to be $\sim 210-230$ nm [LSH+05]. The control of active layer growth rate by varying the film solidification time resulted in an increased hole mobility and balanced charge transport. This improvement together with the enhanced absorption of active layer leads to a power conversion efficiency of 4.4%.

To improve polymer PV cells, instead of increasing the thickness of active layer to absorb more light, Kim *et al.* has changed the device architecture to spatially redistribute the light intensity inside the device by introducing an optical spacer (Titanium dioxide) between the active layer and the Al electrode [KKL+06]. The authors anticipated that utilizing both a semiconducting polymer with an energy gap well matched to the solar spectrum and the optical spacer concept can result in polymer solar cells with greater than 10% efficiency for conversion of sunlight to electricity.

Plasmonics has been applied for improving PV devices as it provides methods to guide and localize light at nanoscale. The ability to construct optically thick but physically very thin photovoltaic absorbers could revolutionize high-efficiency photovoltaic device designs. Design approaches based on plasmonics can improve absorption in PV devices and permit a considerable reduction in the physical thickness of PV absorber layers [AP10].

The application of virus in PV devices has been reported in 2011 for increasing electron collection ability [DYH+11]. A genetically engineered M13 virus served as a template for single-walled carbon nanotube - TiO_2 nanocrystal core - shell nanocomposites which was used as photoanodes in dye-sensitized solar cells. The electron collection efficiency could be increased by even small fractions in nanotubes, corresponding to an increase of power conversion efficiency which was reported to be raised to 10.6%.

Energy harvesting with microorganisms

Besides producing fuels, such as ethanol, methane and hydrogen from organic matter, microorganisms are also able to convert the chemical energy stored in organic matter into electrical energy by devices known as microbial fuel cells (MFCs). In contrast with the fuels for abiotic fuel cells which demand high purification, the microorganisms for MFCs can oxidize a diverse range of 'dirty' fuels that are often of little perceived value, including organic waste and the organic matter in soils and sediments; besides, the oxidation of the organic matter and of renewable biomass only releases recently fixed carbon back into the atmosphere and they could be considered as 'carbon-neutral' [Lov06].

The electron recovery (Coulombic efficiency) is extremely high (97%) [RSS06], however, the very low electron attraction rate leads to a low power generation of MFC [TRS+02][DC02]. Rechargeable devices have been proposed to solve this problem [IGM03]. In the biologically inspired robot EcoBot I, charges generated by the MFCs were accumulated in capacitors which work in a pulsed manner, and then distributed to end-users. MFCs are also applied in Gastrobots as an energy supply by self-feeding the biomass collected by themselves [Wil00]. MFCs have also been reported to be able to harvest energy from aquatic plants - the root deposits supply sufficient organic substrate for energy conversion [DCZ12]. Rare applications have been reported as microbial fuel technology is not yet sufficiently developed to provide substantial quantities of power in a cost-effective way. Tender *et al.* have presented a MFC application with short term potential for powering devices in remote locations [TRS+02]. Based on the voltage gradient across the water-sediment interface in marine environments, a fuel cell consisting of an anode embedded in marine sediment and a cathode in overlying seawater is able to produce an average power density of ~ 28 mW m^{-2} at 0.27 V in Newport, Oregon, and to generate a maximum power of 26.6 mW m^{-2} in Tuckerton, New Jersey. The longterm sustained power generation was considered to be limited yet by reactant flux to the anode.

Biological applications

Mercier *et al.* have reported an *in vivo* energy harvesting chip based on endocochlear potential (EP) which is a battery-like electrochemical gradient found in and actively maintained by the inner ear [MLB+12]. The chip was integrated with a wireless sensor capable of monitoring the EP itself and extracted a minimum of 1.12 nW from the EP of a guinea pig for up to 5 h, enabling a 2.4 GHz radio to transmit measurement of the EP every $40-360$ s. The technique is envisioned to be applied in the inner ear to power chemical and molecu-

lar sensors, or drug-delivery actuators for diagnosis and therapy of hearing loss and other disorders.

Recently, researchers have turned to blood as a power source, because it carries energy in the form of electron-rich molecules like glucose and delivers it to all parts of the body. Implantable biofuel cells based on glucose have been suggested as sustainable micropower sources operating in living organisms. The first biofuel cell implanted in small living creatures has been reported in 2012 [HHB+12], immersed in the snails' blue, blood-like hemolymph and continuously producing electrical power over a long period of time using physiologically produced glucose as a fuel. Scientists have also worked on energy harvesters powered by human blood instead of hemolymph as human blood is better than snail hemolymph at distributing glucose, but most of its oxygen is trapped in hemoglobin and humans also have strong immune systems that attack foreign bodies [Lau12]. Single glucose biofuel cells have also been implanted in rats and produced an average open-circuit voltage of 0.57 V and a power output of 38.7 μW [ZCA+13].

Chapter II

Fractal-based electrostatic energy harvesting devices

This chapter is interested on electrostatic energy harvesting based on variable capacitors. The objective is to propose an improved capacitor configuration in order to increase the capacitance variation during the oscillation which determines the harvested power.

The concept is based on interdigitated capacitors and inspired by fractal geometry. First two cycles for electrostatic energy harvesting are introduced, which reveal the importance of capacitance variation to harvested power; then a brief introduction of fractal geometry is given.

The modeling of simple plate capacitors and interdigitated capacitors is presented and the influence of vibration amplitudes on capacitance variation is discussed. Based on analysis on interdigitated capacitors, the improved capacitor can be constructed either in a progressive or a degressive way, and is defined to be of a specific order according to its characteristics.

In the end, the order choice in applications for the progressive series of capacitors and for the degressive series is discussed as well as mass influences of capacitors of high orders.

II.1 Principles of electrostatic energy harvesting

Electrostatic energy conversion is usually based on variable capacitors. As the capacitor oscillates between the maximum and minimum capacitance, its capacitance varies either by

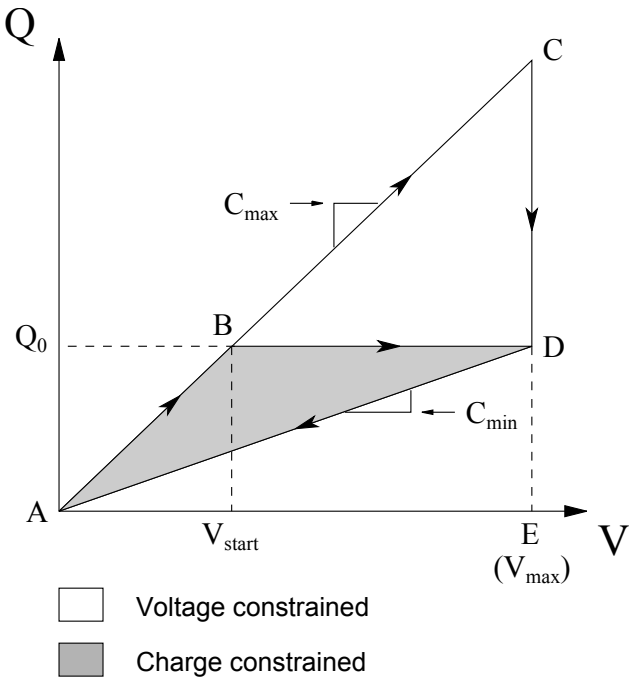

Figure II-1: Two energy conversion cycles for electrostatic energy harvesting [MMMA+01]

the dimension changes or by permittivity change. With the capacitance variation, mechanical energy is converted into electrical energy which could be stored and then used by a load. The conversion cycles could be either charge-constrained or voltage-constrained. Meninger et al. have come up with two possible energy conversion cycles for the charge-voltage plane for a MEMS transducer as depicted in Fig.(II-1) [MMMA+01]. Path A-C-D-A is the voltage constrained cycle and path A-B-D-A is the charge constrained cycle. The name of cycle is to describe which property is held constant during the conversion process while the other changes during the capacitance variation. For a voltage constrained cycle, the cycle starts at a maximum capacitance $C_{\max}$; the capacitor is charged to $V_{\max}$ at its maximum capacitance from a reservoir, corresponding to the segment AC; then during the conversion process the voltage is held constant at the value $V_{\max}$ and the capacitance is decreased to its minimum value $C_{\min}$ with the movement of plates, corresponding to path CD; the charge remaining on the plates is then recovered at the minimum capacitance following path DA. This voltage constrained cycle requires an additional source to hold the voltage on the device constant during the conversion process. The net energy gained in voltage constrained cycle is the area of triangle ACD in Fig.(II-1):

$$E_{\text{voltcons}} = \frac{1}{2}(C_{\max} - C_{\min})V_{\max}^2 \tag{II.1}$$

In charge constrained case, the capacitor is first charged at its maximum capacitance to a certain voltage as an initial voltage, following the path AB; then the capacitance is reduced to its maximum value $C_{\min}$ through movement of plates and during this process the charge on the plates is held constant (path BD), corresponding to an increase of voltage to its maximum value $V_{\max}$ according to the definition of capacitance:

$$C = \frac{Q}{V} \tag{II.2}$$

where Q, C and V denote respectively the charge on the capacitor, the capacitance and the voltage. During the transition from B to D, the device is in open-circuit status with respect to the rest of the system so that no current path exists. Then the charge is returned to the reservoir along path DA. The net energy harvested in such a cycle is the area of triangle ABD in Fig.(II-1):

$$E_{\text{chrgcons}} = \frac{1}{2}(C_{\max} - C_{\min})V_{\text{start}}V_{\max} \tag{II.3}$$

A comparison between Eq.(II.1) and Eq.(II.3) reveals that when the maximum voltage is fixed, the energy available in charge constrained case is less than that in voltage constrained case, but can be much greater under fixed electric field. The former cycle benefits from the fact that only constant charge source is necessary to initiate this cycle and its value can be much less than $V_{\max}$. The comparison also shows that in the energy cycles - either voltage constrained or charge constrained - when the boundary conditions are given (V_{start}, $V_{\max}$), the harvested energy is proportional to capacitance variation ($\Delta C = C_{\max} - C_{\min}$), which could be noted as:

$$E_{\text{cycle}} = const. \times \Delta C \tag{II.4}$$

Roundy *et al.* have come up with three configurations of capacitor: in-plane overlap varying, in-plane gap varying and out-of-plane gap varying which are depicted in Chapter I in Fig.(I-12) [RWP02][Rou03]. The additional fingers in the first two configurations (Fig.(II-2)) are aimed to increase the possible capacitance variation, thus, as mentioned above, improving the harvested energy in electrostatic energy harvesting. Based on the configuration of in-plane overlap varying and in-plane gap closing and in inspiration of the self-similarity of fractal geometry, a new configuration of capacitor is proposed in this chapter, aiming at improving its energy harvesting ability. First a brief introduction of fractal geometry will be given; then the configuration of a fractal-based capacitor is described and modeled; simulation and

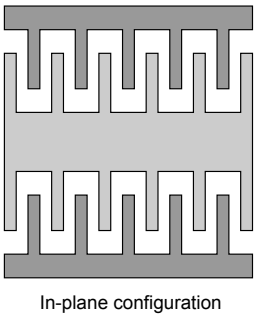

Figure II-2: The in-plane configuration of variable capacitors

experimental results will be given followed with the analysis of energy harvesting ability of the capacitors; other possible configurations will be presented in the end of this chapter.

II.2 Fractal geometry

A fractal is a natural phenomenon or a mathematical set that exhibits a repeating pattern that displays at every scale. If the replication is exactly the same at every scale, it is called a self-similar pattern. Such a pattern may possess exact self-similarity or statistical self-similarity. This characteristic is not limited to geometric patterns, but can also describe processes in time. Fractal geometry has been widely applied as it provides a general framework for the study of irregular sets which provide a much better representation of many natural phenomena than do the figures of classical geometry. Fractal patterns with various degrees of self-similarity have been rendered or studied in images [Jac93][Fis95][WDJ99], architecture [BL94][Bov96] and sounds [Bro07], and found in medicine [BJ00][LMNW01][TCET09][DGG+11], economics [Pet89][Pet94][MH14][Eve95] [TTO+00], psychology [Tay06], and law [Stu13].

According to Pickover, the mathematics behind fractals began to take shape in the 17th century when the mathematician and philosopher Gottfried Leibniz pondered recursive self-similarity [Pic09]. The emergence of such unfamiliar concepts has met with resistance and been regarded as mathematical "monsters" [LGRE06]. The fractal geometry ploughed through two centuries and it was not until the end of the nineteenth century that in 1872 Karl Weierstrass presented the first definition of a function with a graph that would today be considered fractal [Edg93]; later in 1883, Georg Cantor published examples of subsets of the real line known as Cantor sets, now recognized as fractals [Edg93]. In 1904, Helge Von Koch extended the work of Poincaré in the late nineteenth century and gave a geometric definition along with hand drawn images of a similar function which is now referred as Koch

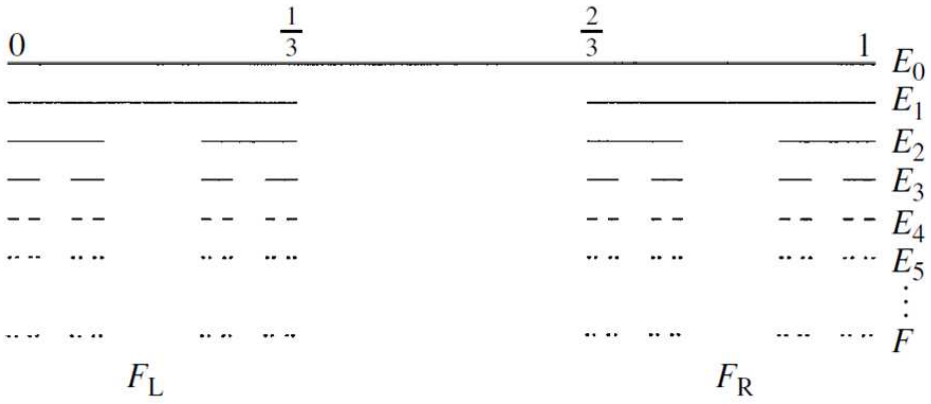

Figure II-3: Construction of the middle third Cantor set F, by repeated removal of the middle third of intervals. Note that F_L and F_R, the left and right parts of F, are copies of F scaled by a factor 1/3 [Fal13]

curve [Man83]. Later in 1915 Waclaw Sierpinski constructed the famous triangle and his carpet one year later. In the following years, mathematiciens have worked on the description of fractal behavior, their dimension and self-similarity [Man67][Man83][LGRE06]. In 1975, Benoît Mandelbrot solidified hundreds of years of thoughts and mathematical developments in coining the word "fractal" and illustrated his mathematical definition with striking computer-constructed visualizations.

The middle third Cantor set is one of the most easily constructed fractals. It is constructed from a unit interval by a sequence of deletion operations. Let E_0 be the interval $[0, 1]$. Let E_1 be the set obtained by deleting the middle third of E_0, so that E_1 consists of the two intervals $[0, \frac{1}{3}]$ and $[\frac{2}{3}, 1]$. Deleting the middle thirds of these intervals gives E_2; thus E_2 comprises the four intervals $[0, \frac{1}{9}]$, $[\frac{2}{9}, \frac{1}{3}]$, $[\frac{2}{3}, \frac{7}{9}]$, $[\frac{8}{9}, 1]$. We continue in this way, with E_k obtained by deleting the middle third of each interval in E_{k-1}. Thus E_k consists of 2^k intervals each of length 3^{-k}. The middle third Cantor set F consists of the numbers that are in E_k for all k (Fig.(II-3)).

The Koch curve is usually utilized for imitating the snow and the coastline. E_0 is set to be a line segment of unit length. The set E_1 consists of the four segments obtained by removing the middle third of E_0 and replacing it by the other two sides of the equilateral triangle based on the removed segment. E_2 is constructed by applying the same procedure to each of the segments in E_1, and so on. The iteration number k tends to infinity, the sequence of polygonal curves E_k approaches a limiting curve F, called the Koch curve (Fig.(II-4(a))). Three Koch curves fitted together can form a snow flake as depicted in Fig.(II-4(b)).

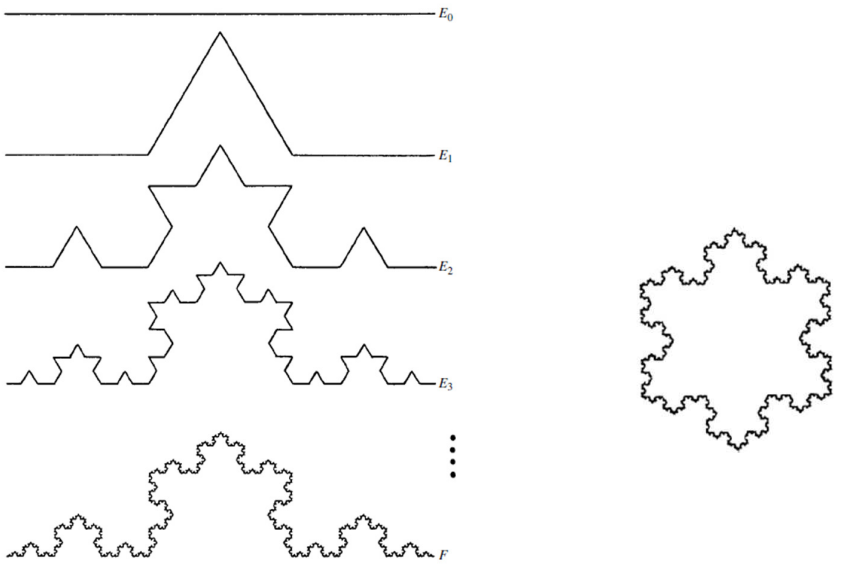

(a) Construction of the von Koch curve F (b) Koch snowflake

Figure II-4: Koch curve [Fal13]

Figure II-5: Construction of the Sierpinski triangle

Another example of basic self-similar sets is the Sierpinski triangle which is constructed by repeatedly replacing an equilateral triangle by three triangles of half the height.

All three examples above are constructed using such recursive methods and possess certain complexity which serves as a basis for capacitor improvement. The fractal inspired electrostatic device based on the in-plane configuration (Fig.(II-2)) and its construction will be introduced in the next section.

II.3 Principles and modeling of fractal-based capacitors

As the device is based on the in-plane configuration, first the modeling of the basic in-plane device - referred as single finger configuration - is given.

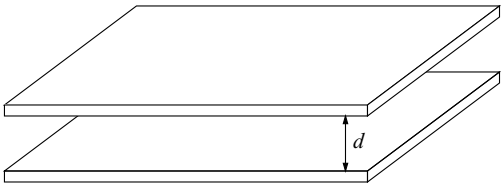

Figure II-6: Simple capacitor with two plate electrodes

II.3.1 Single finger configuration

For a simple capacitor depicted in Fig.(II-6), its capacitance is:

$$C = \varepsilon_r \varepsilon_0 \frac{S}{d} \tag{II.5}$$

where C is the capacitance, S is the overlapping area of two plates, ε_r is the relative static permittivity for the material between the plates, ε_0 denotes the electric constant ($\varepsilon_0 \approx 8.854\times 10^{-12}$ F m^{-1}) and d is the separation distance between the plates. Suppose the electrode in Fig.(II-6) is of length L and width w and the distance between electrodes oscillates between $d_{\max}$ and $d_{\min}$, then the capacitance difference is:

$$\Delta C = \frac{Lw(d_{\max} - d_{\min})}{d_{\max} d_{\min}} \tag{II.6}$$

For the in-plane capacitor introduced in this section, the modeling becomes a little more complicated as the device has additional fingers. The capacitor in Fig.(II-2) is simplified as Fig.(II-7). The device is of length L and consists of N ($N \gg 1$) even sized interdigitated electrodes. l_1 and h denote respectively the length and height of finger, γ is the aspect ratio of device. However, the design is constrained by the maximum aspect ratio which is caused both by fabrication technology and material characteristics. The silicon DRIE (Deep Reactive-Ion Etching) process with which this converter may be fabricated has a maximum aspect ratio of about 107 [WKP10][YWSS05][MRS+05][MNBC08][CAZS02].

The maximum finger height h is then determined by the length of each finger and the maximum aspect ratio of device, given as:

$$h = \gamma \frac{L}{2N} \tag{II.7}$$

where $L/(2N)$ is the length of each even sized finger by considering that the length of finger and the distance between them are equal.

The overlapping area of two plates S mentioned in Eq.(II.5) is then composed of horizontally overlapping area (as for simple capacitors) and vertically overlapping area (for

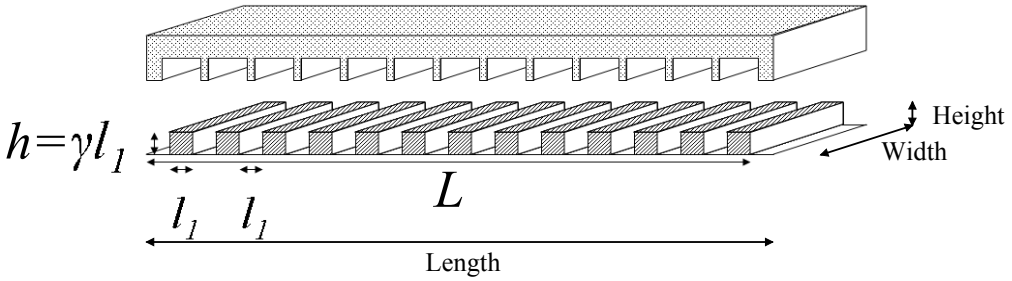

Figure II-7: Single finger configuration capacitor of length L

additional fingers). In addition, because of the additional fingers the capacitor has two different status according to the vertical separation between electrodes: separated when the distance is larger than finger height h and overlapped when the distance is inferior to finger height (Fig.(II-8)). When the distance is large enough, the two electrodes are separated and the overlapping area is only the horizontal part as depicted in Fig.(II-8(a)):

$$S = S_h \approx Lw \tag{II.8}$$

where S_h is the horizontal overlapping area, w denotes the width of capacitor. d_v the distance between every two fingers when they overlap as shown in Fig.(II-8(b)). Fig.(II-9) is a front view of the capacitor in separated status. Actually all the horizontal surface is always in an overlapping status (the dotted lines in Fig.(II-9)), for most part of electrodes, the distance between them is d; however, the distance between electrodes of the area $2Nd_vw$ (the short thick lines in Fig.(II-9)) is $(h+d)$ not d, which makes the capacitance of this part

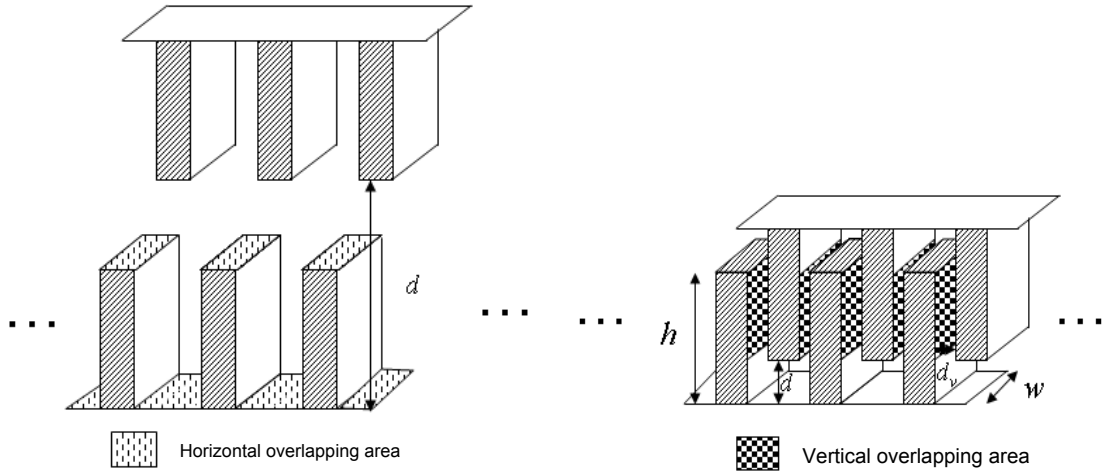

(a) Horizontal active surfaces (b) Vertical active surfaces

Figure II-8: Overlapping surfaces of the capacitor

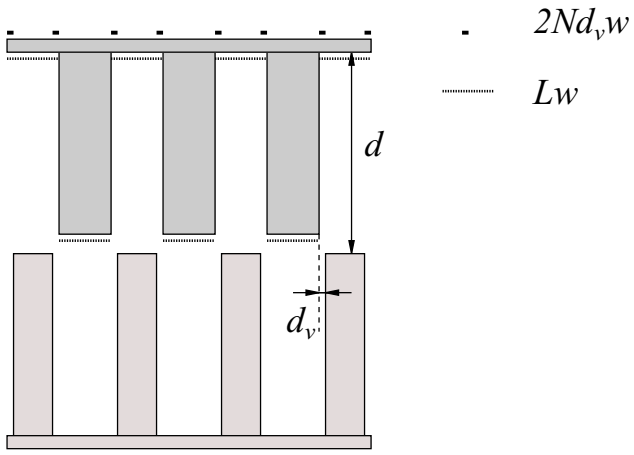

Figure II-9: The overlapping area when the capacitor is in a separated status

of electrodes comparably small. More precisely, the area S_h needs to be divided into two parts in the calculation of capacitance; here as the distance between overlapping fingers d_v is rather small ($d_v \ll L/2N$), the overlapping area in Eq.(II.8) took an approximation. The capacitance in this situation is:

$$C = \frac{\varepsilon L w}{d} \qquad \text{for } d \geq h \tag{II.9}$$

where ε denotes the permittivity for the material between the plates.

When the distance d is inferior to the height of finger h, the fingers overlap, adding up to more overlapping area:

$$\begin{aligned} S &= S_h + S_v \\ &= Lw + 2Nw(h-d) \\ &= Lw + w\gamma L - 2Nwd \end{aligned} \tag{II.10}$$

It must be noted here that the overlapping area S cannot be applied directly in Eq.(II.5) as there are two different distances d and d_v for the overlapping status. With contribution of additional fingers the capacitance is raised to:

$$\begin{aligned} C &= \frac{\varepsilon S_v}{d_v} + \frac{\varepsilon S_h}{d} \\ &= \frac{\varepsilon(w\gamma L - 2Nwd)}{d_v} + \frac{\varepsilon L w}{d} \end{aligned} \qquad \text{for } d < h \tag{II.11}$$

Suppose the single finger device oscillates from its highest capacitance (minimum distance

$d_{\min}$) corresponding to an overlapping of electrodes:

$$C_{\max} = \frac{\varepsilon\left(w\gamma L - 2Nwd_{\min}\right)}{d_v} + \frac{\varepsilon S_h}{d_{\min}} \tag{II.12}$$

According to the relationship between the amplitude of vibration and the finger height, the minimum capacitance (maximum distance $d_{\max}$) may occur when the capacitor is overlapping of separated:

$$C_{\min} = \begin{cases} \dfrac{\varepsilon\left(w\gamma L - 2Nwd_{\max}\right)}{d_v} + \dfrac{\varepsilon wL}{d_{\max}} & \text{for } d_{\max} < h \text{ (overlapping electrodes)} \\ \dfrac{\varepsilon wL}{d_{\max}} & \text{for } d_{\max} \geq h \text{ (no overlap)} \end{cases} \tag{II.13}$$

Thus the capacitance difference becomes:

$$\Delta C = \begin{cases} \dfrac{2\varepsilon Nw(d_{\max} - d_{\min})}{d_v} + \dfrac{Lw(d_{\max} - d_{\min})}{d_{\max}d_{\min}} & \text{for } d_{\max} < h \\ \dfrac{\varepsilon\left(w\gamma L - 2Nwd_{\min}\right)}{d_v} + \dfrac{Lw(d_{\max} - d_{\min})}{d_{\max}d_{\min}} & \text{for } d_{\max} \geq h \end{cases} \tag{II.14}$$

Compare Eq.(II.6) and Eq.(II.14), it can be seen that the first terms in Eq.(II.14) describe the contribution of single fingers to capacitance variation.

The capacitance variation can also be evaluated by the ratio of the maximum capacitance to the minimum capacitance ($C_{\max}/C_{\min}$) given as:

$$\eta = \begin{cases} \dfrac{\dfrac{\varepsilon\left(w\gamma L - 2Nwd_{\min}\right)}{d_v} + \dfrac{\varepsilon S_h}{d_{\min}}}{\dfrac{\varepsilon\left(w\gamma L - 2Nwd_{\max}\right)}{d_v} + \dfrac{\varepsilon S_h}{d_{\max}}} & \text{for } d_{\max} < h \left(N < \dfrac{\gamma L}{2d_{\max}}\right) \\ \dfrac{\dfrac{\varepsilon\left(w\gamma L - 2Nwd_{\min}\right)}{d_v} + \dfrac{\varepsilon S_h}{d_{\min}}}{\dfrac{\varepsilon wL}{d_{\max}}} & \text{for } d_{\max} \geq h \left(N \geq \dfrac{\gamma L}{2d_{\max}}\right) \end{cases} \tag{II.15}$$

As the maximum distance $d_{\max}$ is determined by the vibration amplitude which are given conditions in applications, observation of Eq.(II.15) reveals that the relationship between the finger height h and the maximum distance decides the capacitance variation. The former parameter is determined by the number of fingers N for a capacitor of given length L (Eq.(II.7)). Considering aspect ratio constraints, a trade-off appears between the finger

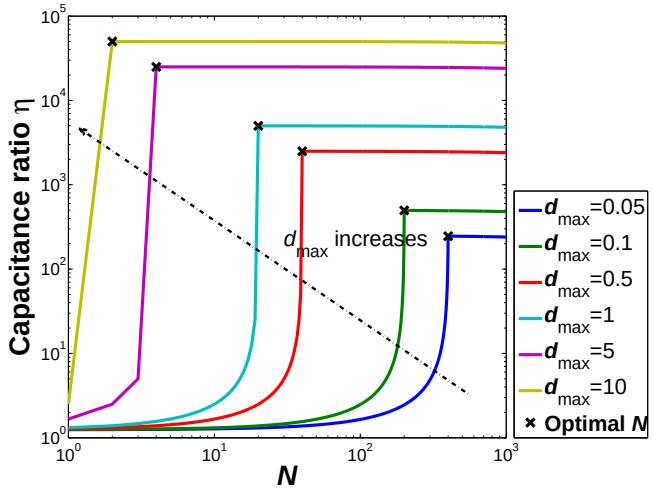

Figure II-10: Influence of finger number N on capacitance ratio $\eta = \frac{C_{\max}}{C_{\min}}$ for a capacitor of given length L

density and the finger height. For different maximum distances $d_{\max}$, i.e. different environmental vibrations, the finger number N will lead to different capacitance variation as depicted in Fig.(II-10). In the calculation of Fig.(II-10), L is set to be 1, γ is set to be 40, d_v and $d_{\min}$ are equal to 0.0001. When $N < \dfrac{\gamma L}{2d_{\max}}$, η is an increasing function of N; when $N \geq \dfrac{\gamma L}{2d_{\max}}$, η is decreasing with N. For a capacitor with given length, given maximum and minimum electrode distance (environmental conditions), a critical number of fingers exists which optimizes the finger length and maximizes the capacitance variation. The optimal design of one finger configuration occurs when the height of fingers is slightly inferior to $d_{\max}$.

II.3.2 Fractal finger configuration

The concept of fractal-based capacitor construction is to add gradually fingers to the structure, which allows increasing the vertical surface and thus increasing the possible capacitance variation. This construction could be either degressive or progressive. In Fig.(II-12) a degressive construction is shown. It is based on a single finger configuration with large fingers. The basic device is of length L with N fingers of length l_n. Suppose the minimum technologically allowed length is l_1 with $l_n \gg l_1$, then the space between every two fingers which is equal to l_n could be exploited by adding fingers of finer lengths: fingers of length l_{n-1} could be placed in the middle of the space (Fig.II-11(b)), fingers of length l_{n-2} could be placed between l_n and l_{n-1} (Fig.II-11(c)), and so on until the length of added fingers

decreases to l_1.

The description above is mainly about the lower electrode. The upper one is designed according to its shape, which means for a finger in the lower electrode of length l_i, another finger of the same height should be placed in the upper one to make its vertical surface active when they overlap. Thus the length l_i should satisfy the following inequality:

$$l_i \leq \frac{l_{i+1}}{3} \tag{II.16}$$

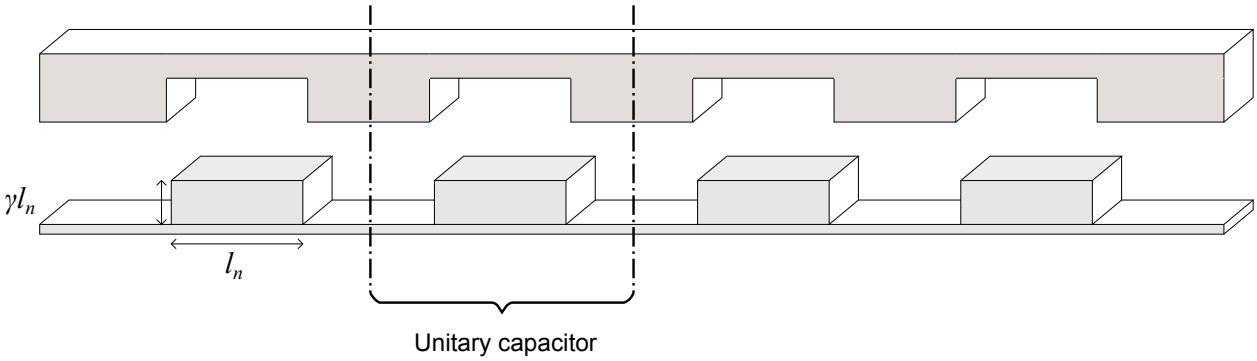

(a) Step 1

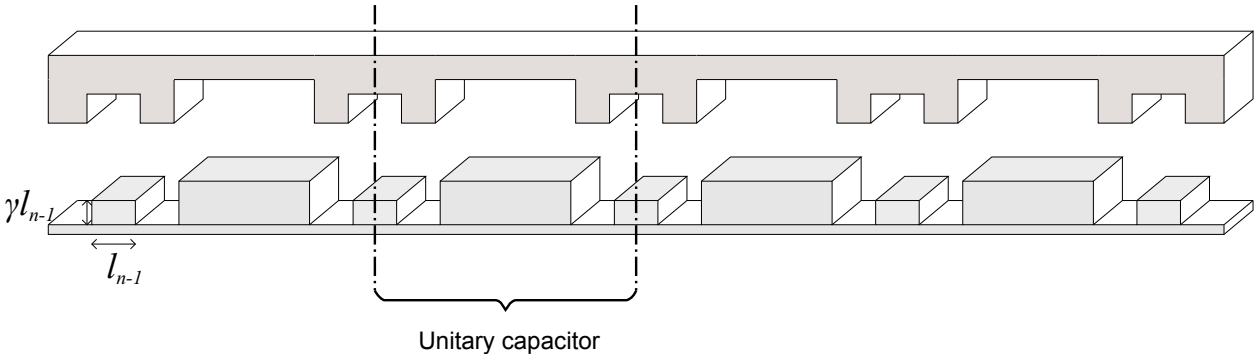

(b) Step 2

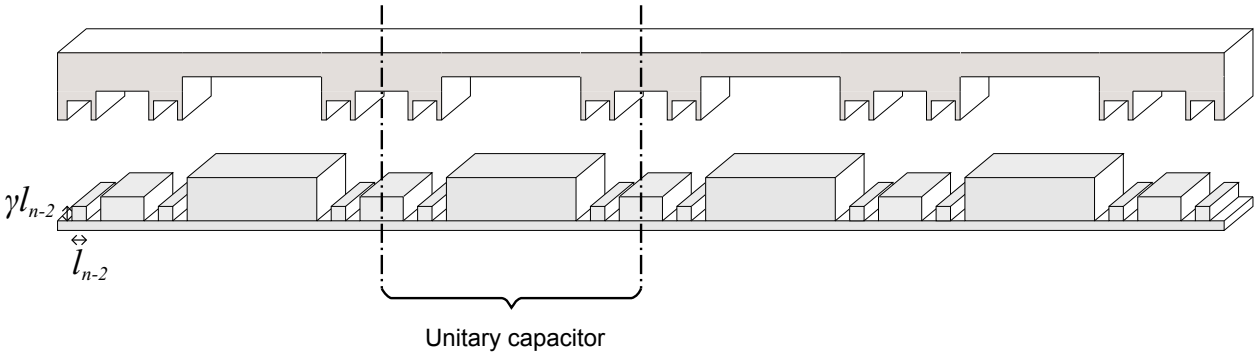

(c) Step 3

Figure II-11: Degressive construction of a fractal capacitor based on a single-finger capacitor

to ensure the fingers of upper electrode to be feasible by respecting the same aspect ratio.

In this paper, the maximum value of l_i is taken and the relation between lengths is given as:

$$l_{n-i} = 3^{-i} l_n \tag{II.17}$$

The construction could also be progressive as depicted in Fig.(II-11). The basic configuration consists of fingers of the smallest technologically allowed width l_1. The unitary capacitor is composed of one finger of length l_1. Then the unitary capacitor is replaced by another composed of one finger of length $l_2 = 3l_1$ and two halves of finger of length l_1, and so on, until the largest length of finger reaches l_n.

Such a fractal structure not only increases the capacitance variation, but also contributes when $d_{\max}$ decreases. As mentioned in the previous section, the optimal design of one finger configuration occurs when the height of fingers is slightly inferior to $d_{\max}$, however, in application, the amplitude varies with the environment. When the amplitude of vibration decreases, fingers of less important heights play the role of optimal fingers, thus giving the capacitor adaptability to some extent.

Suppose the fractal capacitor in Fig.(II-12(c)) is of a total length L and of width w, consisting of N largest fingers. By considering $d_v \ll l_1$, the horizontally overlapping surface S_h is still Eq.(II.8). The total vertical surface $S_v|_{total}$ (all the vertical surface - including the no-overlapping part) is:

$$\begin{aligned} S_v &= w \left[2N\gamma l_n + \sum_{i=1}^{\infty} 2^i \left(N+1\right) \gamma l_{n-i} \right] \\ &= 2 \left[2N + 1 - \left(N+1\right) \left(\frac{2}{3}\right)^{n-1} \right] w\gamma l_n \end{aligned} \tag{II.18}$$

To simplify the following calculation and simulation of the model, the overlapping surface will be divided by the thickness of device w as:

$$S_v^{1D} = 2 \left[2N + 1 - \left(N+1\right) \left(\frac{2}{3}\right)^{n-1} \right] \gamma l_n \tag{II.19}$$

The unitary capacitor composed of fingers of length from l_n to l_1 in Fig.(II-12(c)) is considered to be of order n. When trying to evaluate a capacitor containing various lengths of fingers, it is relatively easy to compare unitary capacitors. Unitary capacitors in Fig.(II-12(a)) and Fig.(II-12(b)) and Fig.(II-12(c)) are of different orders and of different total lengths. So

their respective capacitance will be divided by their respective total length with the unit of capacitance to be F m^{-2}; or it may be considered that it is the overlapping area that is is divided by the total length (Eq.(II.5)). Thus, for a unitary capacitor of order N, its horizontally overlapping surface in 1D is:

$$S_h{}^{1D} = \frac{S_h}{wL} = 1 \tag{II.20}$$

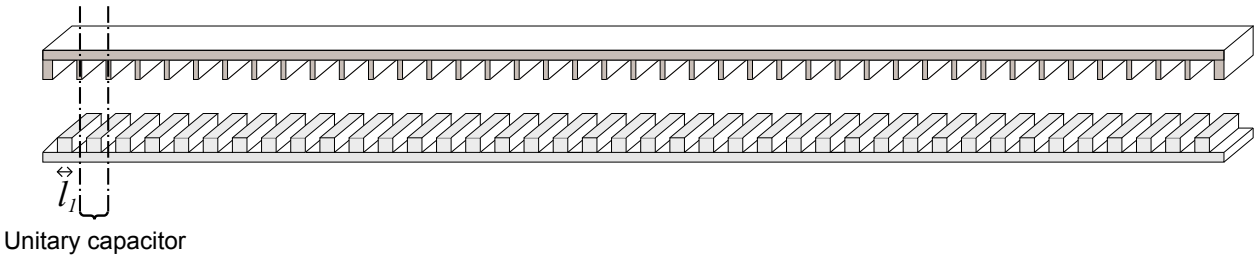

(a) Step 1

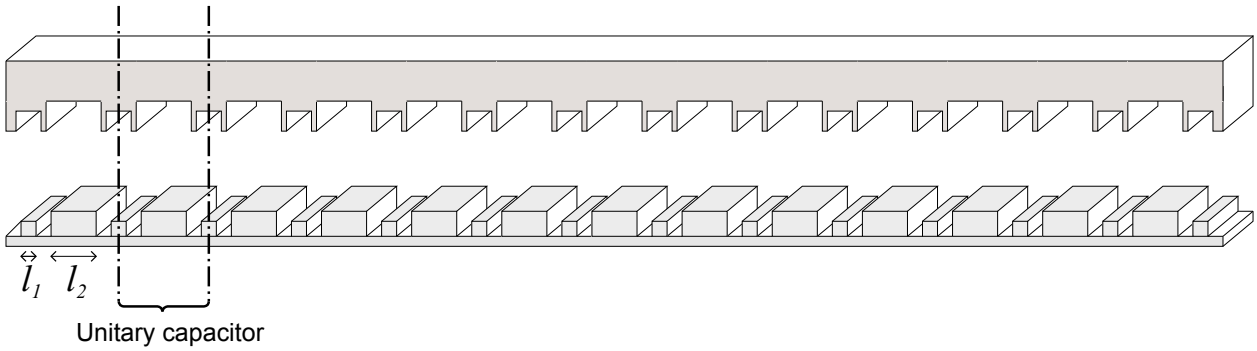

(b) Step 2

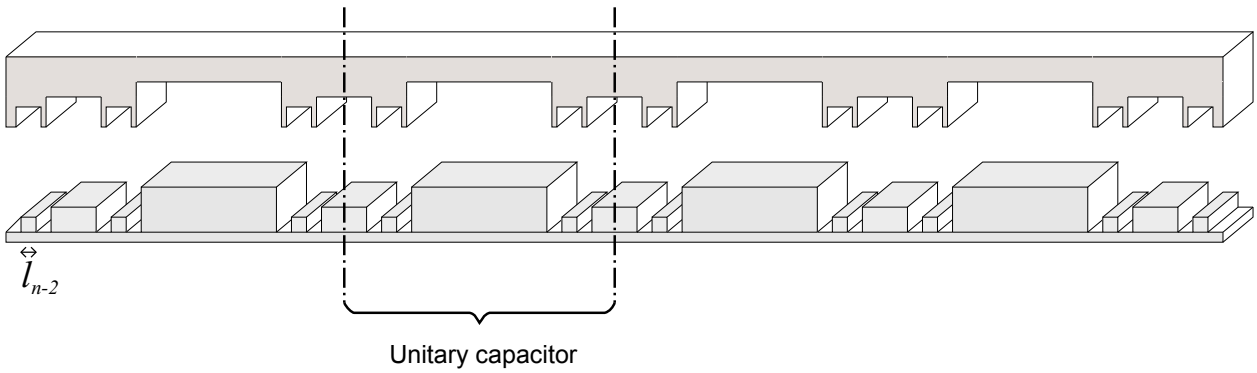

(c) Step 3

Figure II-12: Progressive construction of a fractal capacitor based on a single-finger capacitor

and its vertically overlapping surface in 1D is:

$$S_v{}^{1D} = \frac{S_v}{wL} = \frac{S_v}{w \cdot (3l_n)} = 2\left[1 - \left(\frac{2}{3}\right)^n\right]\gamma \tag{II.21}$$

The horizontal area keeps overlapping under oscillation, while the vertically overlapping area varies with the distance d. Take a unitary capacitor of order 3 for example (Fig.(II-13)): the vertical area overlaps when the distance is reduced to h_3 (Fig.(II-13(a))); the overlapping part increases gradually as the distance d decreases and then sharply as the distance is reduced to h_2 as at this moment the vertical area of fingers of height h_2 becomes overlapping (Fig.(II-13(b))); for the same reason, the overlapping area is raised sharply again when the distance is reduced to h_1 (Fig.(II-13(c))). The overlapping area experiences a series of variation with the decrease of distance. More generally for a unitary capacitor of order n (the total length of such a unitary capacitor is $(2l_n = 2 \times 3^{n-1}l_1)$, the relation of its one dimension vertically overlapping surface divided by the total length of unitary capacitor and the distance is shown in Table (II.1), where h_0 is defined to be 0. With overlapping area for both horizontal and vertical part, the capacitance of a fractal-based capacitor may be calculated with:

$$C = \frac{\varepsilon S_v}{d_v} + \frac{\varepsilon S_h}{d} \tag{II.22}$$

It can be noted that the expression of their surface is the same whatever the configuration (degressive or progressive); the difference between the two begin the expression of h_i:

$$h_i = 3^{i-1}\gamma l_1 \tag{II.23}$$

for the progressive construction (l_1 is the smallest finger width) and:

$$h_i = 3^{i-1}\gamma \frac{L}{2} \tag{II.24}$$

for the degressive construction (L is the total width).

II.4 Simulation results

II.4.1 Theoretical calculation

The configuration introduced in the previous section will be theoretically analysed in this section. The configuration considered in this section is the progressive construction (Fig.(II-

Table II.1: One dimension vertically overlapping area of a unitary capacitor divided by its total length varies with the capacitor distance

	$d > h_n$	$h_{i-1} < d \leq h_i (1 \leq i \leq n)$
Vertical active surface	0	$\left[2 - \left(\frac{2}{3}\right)^i\right] \gamma - \frac{2^{i-1}}{3^{n-1}} \frac{d}{l_1}$

Table II.2: Parameter set for theoretical calculations and simulations

Aspect ratio	Finger length of order 1	Number of single finger	Vertical distance	Minimum horizontal distance
γ	l_1	N	d_v	$d_{\min}$
20	1	1	0.1	0.1

11)). The parameters are given in Table(II.2). The technologically allowing length l_1 is set to be 1 as a unitary length without notifying its unit. The distance between fingers d_v is set to be one tenth of the minimum length. The capacitor will be oscillated at its maximum capacitance corresponding to the minimum distance between electrodes $d_{\min}$ which is also one tenth of the minimum length l_1. The aspect ratio has a medium value - 20.

As mentioned above, the capacitance variation determines the harvested energy in one cycle, here it is analysed by the ratio of the maximum capacitance to the minimum capacitance. Fig.(II-14) depicts this ratio for unitary capacitors of order 1, 2, 3 and 4 with a fixed minimum distance $d_{\min}$ demonstrated in Table(II.2) (which indicates a fixed maximum

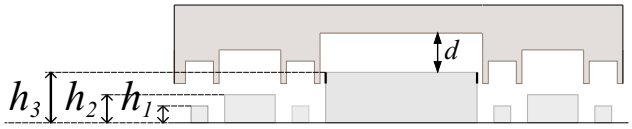

(a) $h_2 \leq d < h_3$

(b) $h_1 \leq d < h_2$

(c) $0 \leq d < h_1$

Figure II-13: One dimension vertically overlapping area of a unitary capacitor varies with the capacitor distance

capacitance), the maximum distance between electrodes varying from 10 to 1000 (which indicates that the actual distance d varies from $l_1/10$ to $1000l_1$). As the maximum distance has a wide range of variation, the capacitors can experience all the status - various overlapping conditions of fingers. When the oscillation permits a maximum distance 10 as depicted in Fig.(II-14(a)), for all four unitary capacitors, no matter how they are vibrated, all fingers keep overlapping. As the unitary capacitor of order 1 possesses the most fingers, it has the largest capacitance variation. When the oscillation has larger amplitude and permits greater maximum distance as $d_{\max} = 40$ ($h_1 < d_{\max} < h_2$), the fingers of the smallest length l_1 will be separated when the distance is raised up to 20. The unitary capacitor of order 1 will be completely separated while the other three are partially separated. This separation is demonstrated in the capacitance variation for order 1 as a sharp decrease and the unitary capacitor of order 1 still has the largest capacitance variation. With the gradual increase of the maximum distance ($d_{\max} = 100$ in Fig.(II-14(c)) and $d_{\max} = 200$ in Fig.(II-14(d))), unitary capacitors of order 2 and 3 can also be completely separated during the oscillation and have larger capacitance variation compared with that of order 1 as they have higher fingers which would add to the capacitance variation when vibrated. Finally, when the oscillation permits a rather large maximum distance ($d_{\max} = 100$ in Fig.(II-14(e)), all the unitary capacitors could be totally separated under vibration. The capacitor of highest order (order 4) has the largest capacitance variation as it has the highest fingers which help to increase the variation. So in summary, for progressive series of fractal configuration: when the oscillation is rather slight, the single finger configuration (order 1, small fingers) could help to increase the capacitance variation thus increasing the harvested energy; when the oscillation is of medium amplitudes, capacitors of medium orders are preferable as on one hand they have sufficient fingers to increase the capacitance and on the other hand they have high fingers to continue to increase the capacitance variation when small fingers are separated; when the oscillation is very important, capacitances of high orders are reasonable choice to guarantee a large capacitance variation.

When it comes to the application, to get better energy harvesting performance, the vibration amplitude of the environment should be estimated and the capacitor order need to be chosen according to this estimation. When the maximum distance is great enough, a unitary capacitor of higher order has a larger capacitance variation ratio; however, when $d_{\max}$ reduces, it is far less efficient compared to that of lower orders. As in reality the vibration amplitude has certain uncertainty, it is preferable to choose an intermediate order among several alternatives to guarantee a relatively high efficiency in case of a varying (increasing

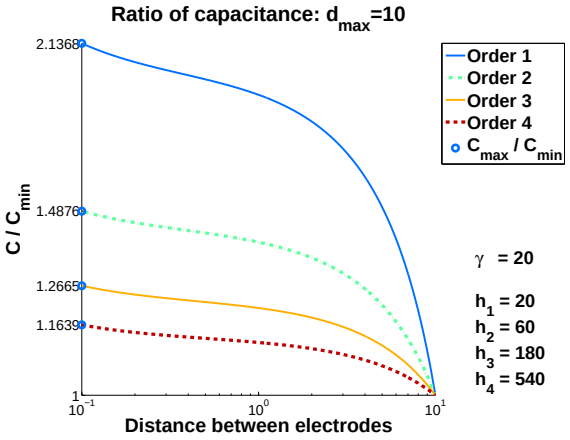

(a) $d_{\max} = 10$

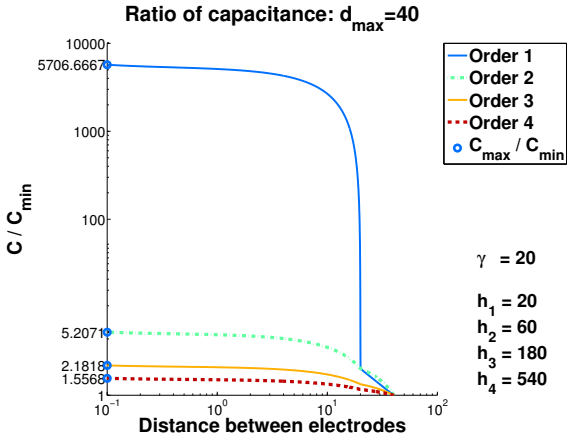

(b) $d_{\max} = 40$

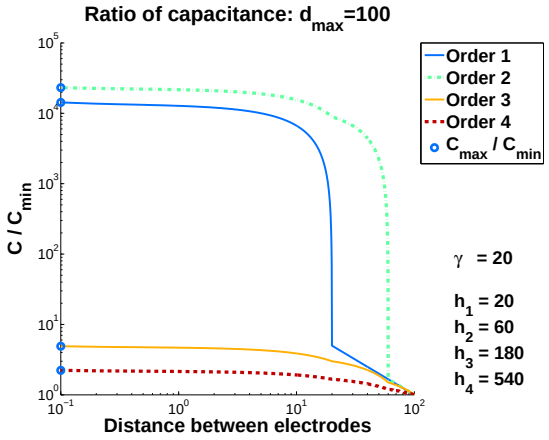

(c) $d_{\max} = 100$

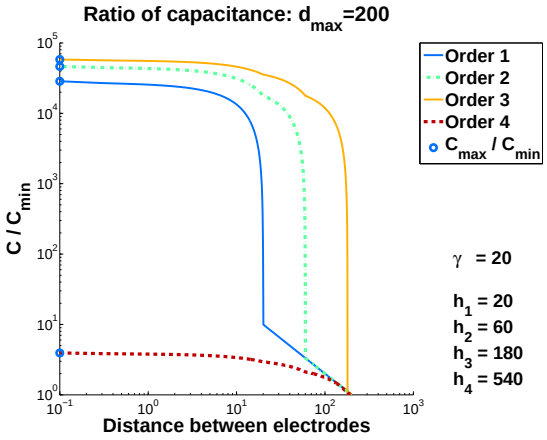

(d) $d_{\max} = 200$

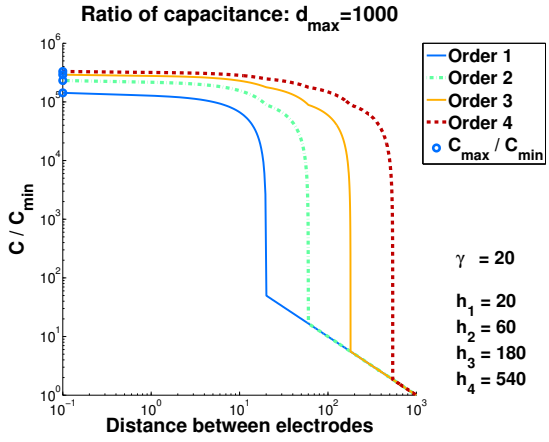

(e) $d_{\max} = 1000$

Figure II-14: Capacitance ratio for different maximum distances

or decreasing) vibration amplitude.

II.4.2 FEM validation and discussion

The progressive series of fractal-based configuration is also analyzed with Finite Element Methods. The simulation of capacitors of order 1, 2 and 3 is realized in ANSYS and their structures are shown in lower order Fig.(II-11): all three capacitors are of the same length; there are 40 unitary capacitors for order 1, 13 for order 2 and 4 for order 3. Restrained by the number limit of software, like the theoretical ones, the FEM results are obtained by ignoring the width of capacitor (in $2D$).

The configuration parameters in FEM remain unchanged (Table(II.2)) except that the minimum distance $d_{\min}$ is increased to 1.5. This analysis is mainly to show the capacitance variation with the distance, so the maximum distances for capacitors of order 1, 2 and 3 are large enough to observe a total separation and they are respectively 10^3, 4×10^3, 10^4, which are all much superior to the highest finger height. When the distance is very large and the electrodes are totally separated, in theoretical calculation the capacitor is approximated to a simple capacitor, however, the actual electric field generated by fingers is rather complicated because of edge effects. This error between theoretical results and simulation ones has been shown in Fig.(II-15(a)): for the capacitor of order 1, when the distance is inferior to the finger height, FEM and theoretical results have a good agreement; when the distance is around the finger height, the edge effects are taken into consideration in FEM and the sharp change in theoretical calculations becomes much smoother with FEM ones; as the distance increases, electrodes could be approximated to plates, the capacitance decreases slowly. Generally speaking, when the fingers overlap or are totally separated and far from each other, there is no much difference between the theoretical and simulation results; during the period from the moment the fingers begin to separate to the moment the fingers are far away from each other, the edge effect is rather important and FEM results can describe more precisely the capacitance variation during this period. Thus, for the capacitors of order 2 and 3, each time when the distance is large enough to totally separate the electrodes, FEM results give precise description of the edge effect shown as a smoother capacitance variation. When the distance is small (overlapping of electrodes) and very large (large distance between separated fingers), FEM and theoretical results are in good agreement for both capacitors.

In order to evaluate the energy harvesting ability of the three devices, energy harvesting is supposed to be realized in a voltage-constrained cycle and the capacitors are oscillated from the same smallest distance (corresponding to their respective maximum capacitance)

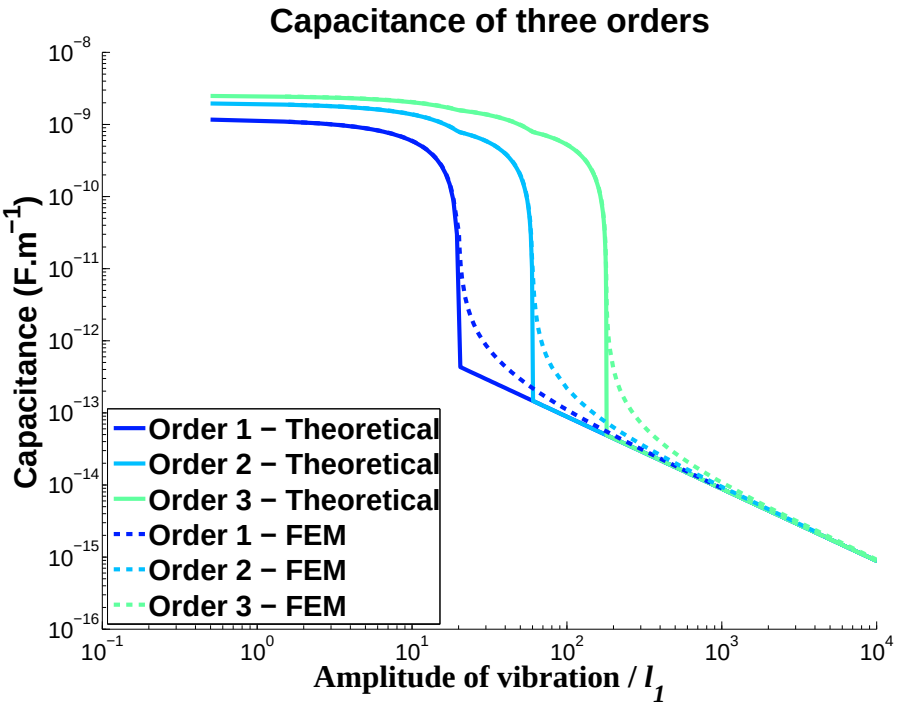

(a) Capacitance

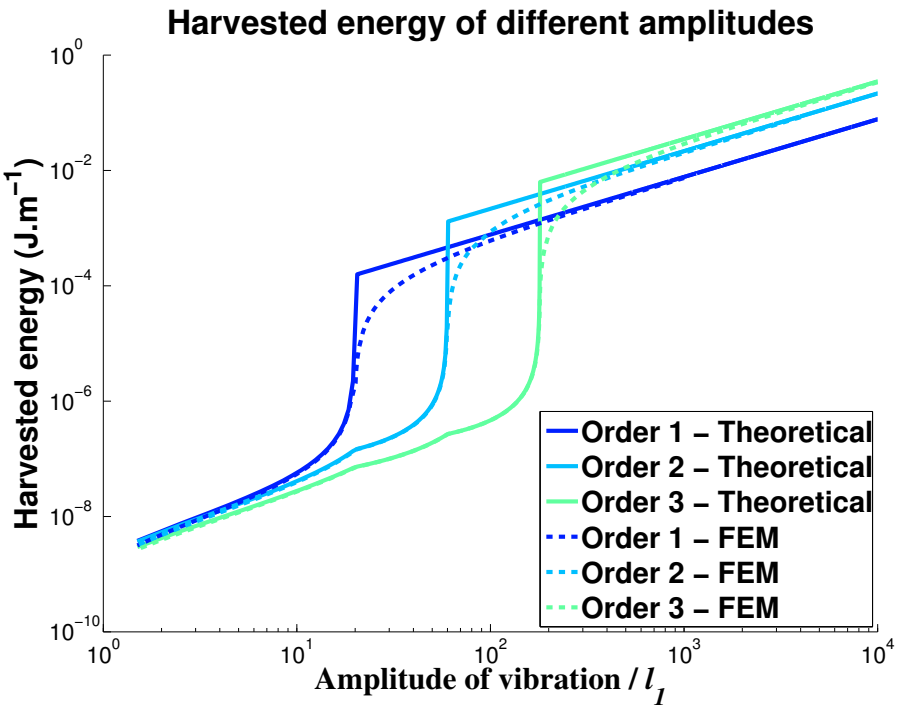

(b) Energy

Figure II-15: Ratio of $C_{\max}$ to $C_{\min}$ and harvested energy (normalized by being divided by the width of capacitor) for different maximum distances

and the amplitude of vibration is raised from below the smallest finger height h_1 to above the highest finger height h_3 (Fig.(II-15(b))). When the devices are under slight oscillation (amplitude is inferior to h_1), capacitors of order 1, 2 and 3 have similar energy harvesting abilities. When the amplitude of vibration is raised to be higher than h_1, the fingers in the capacitor of order 1 are totally separated, which induces a large capacitance variation (Fig.(II-15(a))), leading to significantly higher harvested energy (about 10^3 times more of energy compared to capacitors of order 2 and 3). When the amplitude is further raised to be larger than h_2, the capacitor of order 2 harvests the most energy, benefiting from a total separation of fingers and from its higher fingers compared to that of order 1. When the amplitude is superior to h_3, the capacitor of order 3 is able to harvest the most energy as for the large maximum distance and its high fingers. The energy harvesting ability of the three devices is up to the vibration: for a small vibration environment, capacitors of small order are reasonable choices; for a highly oscillated environment, it is preferable to choose capacitors of large order.

The influence of capacitor order on the harvested energy is studied. In Fig.(II-16) the given results are based on progressive series of capacitors of order from 1 to 20. The horizontal ordinate is the capacitor order, the longitudinal ordinate is the ratio of energy harvested by a high order capacitor in one cycle to energy harvested by a order 1 capacitor in one cycle. Fig.(II-16(a)) are results got from a large amplitude vibration which satisfies a total separation of all capacitors (the amplitude is $10^{11}l_1$); Fig.(II-16(b)) are results got from a vibration of not so large amplitude with which the capacitors of order 18, 19 and 20 keep overlapping (the amplitude is $10^9 l_1$). For a large vibration in Fig.(II-16(a)), the scavenged

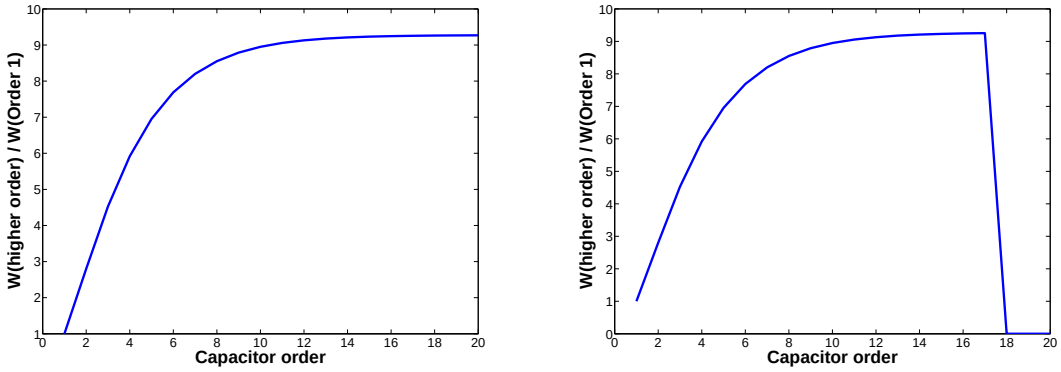

(a) Large maximum distance (b) Small maximum distance

Figure II-16: Ratio of harvested energy of higher order to that of order 1 for different maximum distances

energy raises with the order, however, this increase begins to slow down when the order reaches 6 and almost stops when it is superior to 10. When the vibration amplitude is reduced to the normalized value of 10^9, capacitors of high order (18, 19, 20) still overlap at the maximum distance, therefore, energies harvested by capacitors of order 18, 19, 20 are significantly reduced and are much less than that of order 1 (about 10^{-11} times of that of order 1), which indicates that the order of capacitor should be properly chosen according to the vibration amplitude to avoid low energy harvesting efficiency. By considering the increase of harvested energy with order introduced above, it can be inferred that order less than 6 should be chosen to avoid low efficiency caused by amplitude variation.

Furthermore, the increase of capacitor order also increases significantly the capacitor mass. Compare Fig.(II-12(a)), Fig.(II-12(b)) and Fig.(II-12(c)), evidently with the increase of order the capacitor gains much weight. For a unitary capacitor of order n, its mass could be approximated to:

$$m = \frac{1}{7}\left(8 \cdot 3^{2n-2} - 2^{n-1}\right)\gamma w \rho {l_1}^2 \tag{II.25}$$

where m denotes the mass of capacitor, w denotes the width of capacitor, ρ is the mass density of electrodes. As finger length l_1 is not in consideration for the reason of normalization, the model is calculated in two dimensions and because γ and ρ depend on the materials, the relative weight increase is only dependent on the factor $\frac{1}{7}\left(8 \cdot 3^{2n-2} - 2^{n-1}\right)$ depicted in Figure II-17. When the order is superior to 6, capacitor mass increases so quickly that capacitors are no longer quite suitable for application as they are usually integrated in microsystems. However, the weight increase may have positive influence on the application as vibration sources are usually in the frequency range from 0 Hz to 500 Hz [RWR03], which are relatively low frequencies. The resonance frequency of structure is determined by the stiffness k and the mass m by $\omega = \sqrt{\frac{k}{m}}$ where ω represents the angular resonance frequency. The weight increase could therefore decrease the resonance frequency of the configuration and thus benefit in the harvesting energy process.

II.5 Experimental results and discussions

The degressive series of fractal-based capacitors of order from 1 to 3 have been experimented (Fig.(II-18)). Actually, unlike the progressive series of capacitors, a unitary capacitor contains the largest finger and is considered to be of order 1; that containing the largest and the second largest fingers is considered to be of order 2, and so on. The smallest finger length

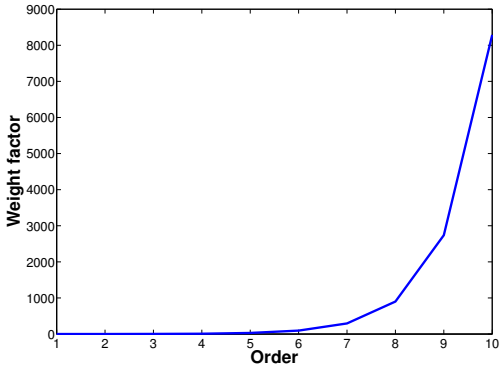

Figure II-17: Weight factor for fractal unitary capacitors of order from 1 to 10

l_1 of prototype is 0.5 mm, detailed configuration design is reported in Appendix A.

The capacitances are measured with an impendancemeter as depicted in Fig.(II-19). The experimental and theoretical results generally show a good agreement. Unlike the progressive series of fractal-based capacitors, the degressive series are aimed to explore the space between the largest fingers, the total separation of capacitors happens when the distance between electrodes exceeds the highest finger height $h_3 = 13.5$ mm. As depicted in Fig.(II-19), theoretical capacitances of all three devices drop dramatically to a value about 10^{-3} times smaller than the overlapping capacitances; experimental capacitances also experience a sharp drop to a small value which is about 10 times higher than the corresponding theoretical one. This error is caused by the edge effect as although the fingers are separated they are still close to each other and the interaction between them adds to the actual capacitance. When the capacitors overlap ($h_2 = 4.5$ mm $< d < h_3 = 13.5$ mm), the three capacitors have the same capacitance as they are under the same overlapping status; when the distance is reduced to be between h_1 and h_2 (1.5 mm $< d <$ 4.5 mm), capacitors of order 2 and 3 have the same more fingers overlapping, increasing the overlapping area and demonstrate higher capacitances over the capacitor of order 1; finally, when the distance is decreased to be less than 1.5 mm, capacitor of order 3 has the highest capacitance as it owns the most fingers which increases the vertical overlapping area. In summary, in the degressive series of fractal-based capacitors, it is always the capacitor of the highest order that contributes the most to capacitance variation as it explores in the best way the space and contains the most fingers. However, it needs to pay attention that the degressive highest order is limited by fabrication technology.

Accordingly, when the devices are applied in a voltage-constrained cycle for energy harvesting, it is the capacitor of order 3 that harvests the most energy as depicted in Fig.(II-20)

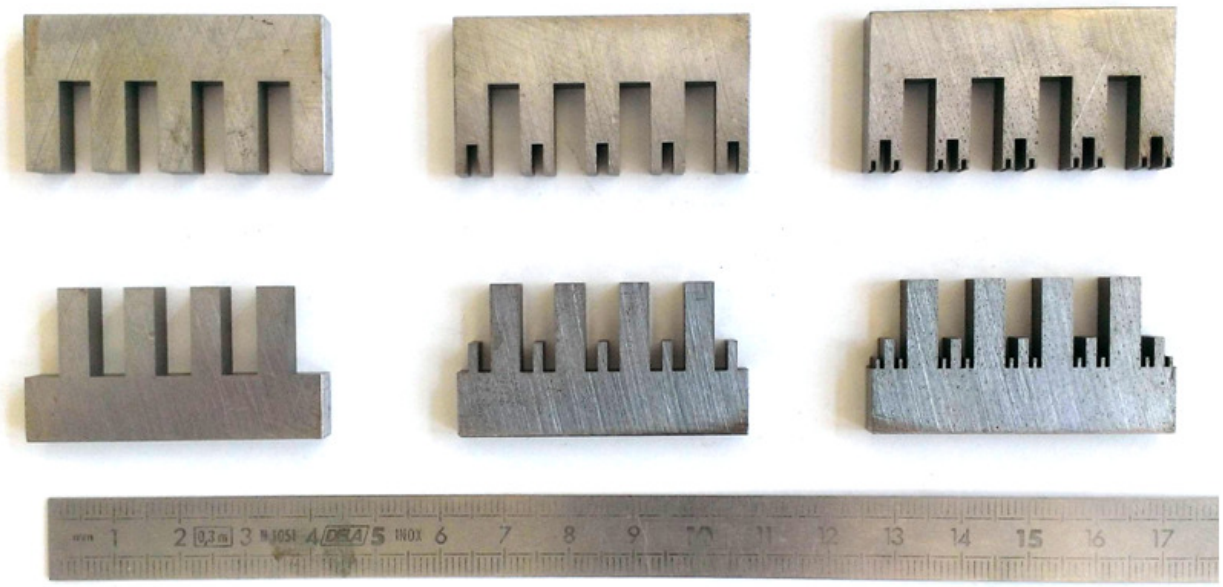

Figure II-18: The degressive series of fractal-based capacitors of order from 1 to 3

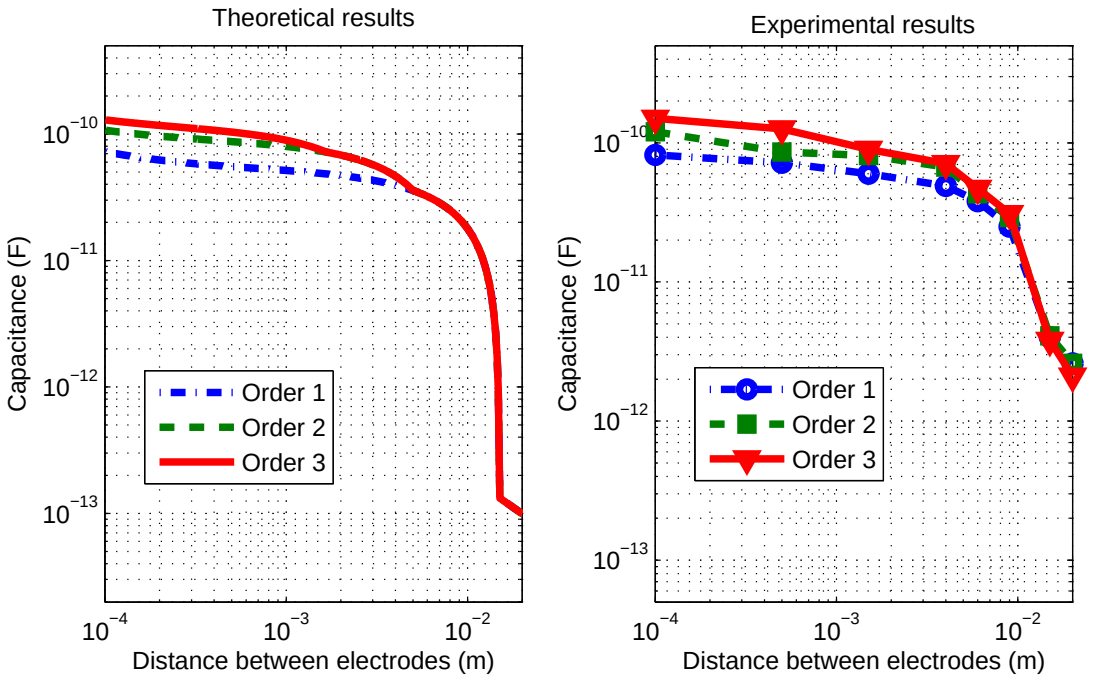

Figure II-19: Theoretical and experimental results of capacitance for three capacitors

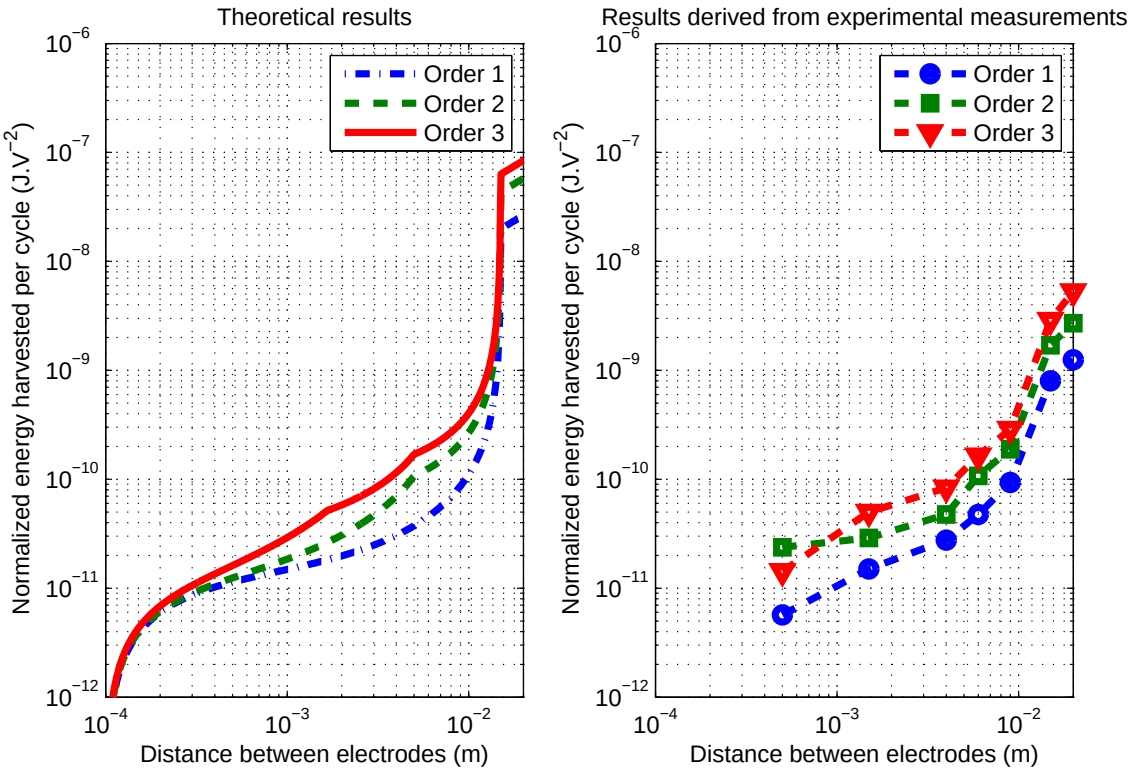

Figure II-20: Theoretical results and results derived from experimental capacitance measurement for energy harvesting for the three capacitors

where the energy is demonstrated with the maximum distance between electrodes varying (The energy harvesting results are derived from the capacitance measurements, not real energy harvesting measurements). Especially when the maximum distance $d_{\max}$ is between h_1 and h_3, the capacitor of order 3 could well benefit from the separation of fingers of length l_1 and l_2 and gain large capacitance variation.

II.6 Conclusion

This chapter has been dedicated to electrostatic energy harvesting, or more precisely to a method to increase capacitance variation which is directly related to the ability of harvesting mechanical energy. To realize this objective, the fractal geometry has served as an inspiration and a fractal-based configuration has been proposed to improve the capacitance variation through increasing the overlapping area between electrodes. Such a configuration can be constructed either in a progressive or a degressive way, and it has been demonstrated theoretically and by simulation or experimentally that capacitance variation increase is pos-

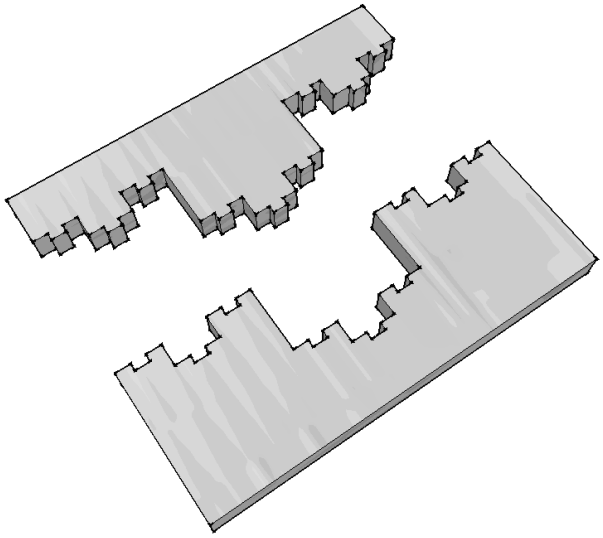

Figure II-21: Fractal-based symmetric capacitor

sible according to different conditions. Especially for the progressive series of fractal-based capacitors, their performance depends on the amplitude of vibration (for vibration of large amplitude, it is preferable to choose progressive capacitors of high order).

The work introduced here could also be extended to other configurations by taking advantage of other fractal shapes. By keeping the same configuration, it is possible to add more fingers to the device proposed in this chapter (Fig.(II-21)), however, this configuration may encounter certain fabrication problems when in use of DRIE process. Another capacitor configuration inspired by Sierpinski carpet is depicted in Fig.(II-22).

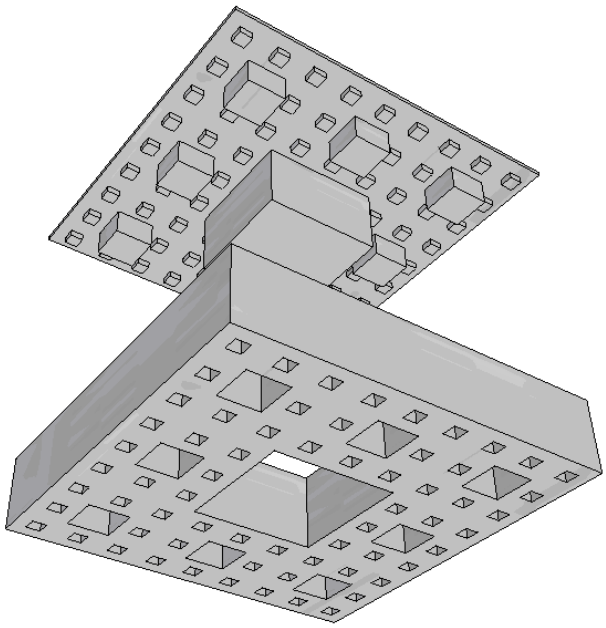

Figure II-22: Fractal-based capacitor inspired by Sierpinski carpet

Chapter III

Lumped model for bending electrostrictive transducers for energy harvesting

This chapter also focuses on mechanical energy harvesting with attention shifting towards electrostrictive polymers which are flexible, low cost and demonstrate outstanding electromechanical performances. Piezoelectric bending systems have been widely studied, in this chapter the modeling of electrostrictive bending system will be established by energetic analysis.

The energetic analysis is carried out from the electric aspect and mechanical aspect and an electromechanical coefficient is proposed; then a global lumped model based on the previous analysis is given.

Two configurations have been theoretically analyzed - a clamped-free beam with an electrostrictive film attached at the clamped end and with a force applied at the free end, a clamped-free bimorph beam with two electrostrictive films attached to the two faces of the clamped end and with a force applied at the free end. The first configuration has been experimented, and measured electromechanical coefficients and harvested electrical power are discussed.

III.1 Introduction

Numerous recent researches have focused on electrostrictive polymers as such materials can exhibit large pseudo-piezoelectric effect by applying DC bias field. It is discovered

that electrostrictive polymers are able to generate large strain (above 5%) under moderate electric field intensity ($400 - 800$ V on a 20 μm film) [PI08]. Besides, electrostrictive polymers have an operating frequency suiting in a much better way the mechanical frequency spectra of typical systems compared with piezoelectric materials [LCGL12]. Nevertheless, while local constitutive equations of electrostriction have been derived from formal analysis (using phenomenological approach [EYS+99][MRC05][HZZS08][ZS08] or physical interpretation [CLG+12][LCS+14]), no macroscopic expression of the induced electrical quantities for the design of efficient sensors or energy harvesters have been proposed in the literature. In this chapter, a lumped model is established for cantilever-based energy harvesters with electrostrictive polymers. The objective is to make a mathematical analysis to model systems composed of a beam and electrostritive polymers, using energy analysis approach. The model will help to clarify the energy conversion on a beam and provide a tool to evaluate the electromechanical behavior of the system in a high-level design.

III.2 Electrostriction

Electroactive polymers, or EAPs, are polymers that exhibit a change in size or shape when stimulated by an electric field. EAPs are divided into two major categories according to their activation mechanisms: dielectric (driven by dipolar orientation) and ionic (involving mobility or diffusion of ions). The dielectric polymers (electrostrictive, electrostatic, piezoelectric and ferroelectric) are materials in which actuation is caused by electrostatic forces between two electrodes which squeeze the polymer. They require high activation field (> 150 V μm^{-1}) close to the breakdown level [BC04]. However, dielectric polymers are capable of very high strains and hold the induced displacement under activation of a DC voltage, and they have a faster response which allows them to be operated in air with no major constrains. Ionic EAP materials in which actuation is caused by the displacement of ions inside the polymer, require a drive voltage as low as $1 - 5$ V, nevertheless their wetness needs to be maintained and it is difficult to sustain the DC-induced displacements except for conductive polymers. The work in this chapter focuses on dielectric electrostrictive polymers which are a variety of electroactive polymers that deform due to the electrostatic interaction between two electrodes with opposite electric charges.

When an electric field is applied to a piezoelectric material, it produces strains proportional to the field; for all materials, piezoelectric or not, the application could produce a strain which is quadratic yet not linear with the field. The latter property is termed elec-

trostriction [Dev54]. Despite numerous studies, electrostrictive strain of polymers is still a subject of controversy. Electrostriction in dielectric polymers is defined as the strain induced by attractive forces exerted by an electrostatic force [Str07]; at the same time, the behavior of the material could be well described by a thermodynamic analysis [RO10]. In a microscopic way, the origin of electrostrictive strain may be explained by the model in terms of dipole moment and saturation of dipole orientation and by Maxwell forces which is generated by dipolar orientation and induced surface charges [CLG+12].

Devonshire (p95 in [Dev54]) has described electrostriction of electrostrictive polymers for small signals with the following linearized equations:

$$\begin{cases} S_h = -s^E_{hi} T_i + d_{mn} E_m \\ P_m = -d_{mh} T_h + \chi^T_{km} E_k \end{cases} \tag{III.1}$$

$$\begin{cases} T_h = -c^E_{hi} S_i + a_{mn} P_m \\ E_m = -a_{mh} S_h + \eta^T_{km} P_k \end{cases} \tag{III.2}$$

where S_h and T_h are the components of stress and strain respectively; E_m and P_m are the components of electric field and polarization; s^E is the compliance measured under constant electric field, c^E is the elastic constant measured under constant electric field; d and a are electrostrictive coefficients; χ^T is the dielectric susceptibility measured at constant stress and η^E denotes the permeability measured at constant stress. The Voigt notation is used, so that the subscripts h and i take six values; T_1, T_2, T_3 for longitudinal and T_4, T_5, T_6 for shear stresses; S_1, S_2, S_3 for longitudinal and S_4, S_5, S_6 for shears. The subscript k and m take only three values. The summation convention is that any subscript occurring twice in a product is to be summed. Finally, the superscripts define the constant quantity.

In this expression, the electromechanical coupling effects arise from piezostriction, quadratic electrostriction and higher order electrostriction respectively. The Devonshire phenomenology approach provides a clear basis for this, as outlined belows. In a ferroelectric material that exhibits both spontaneous and induced polarizations, P^s_i and P^i_j, the strains arising from spontaneous polarization, piezoelectricity, and electrostriction may be formulated as ([SN92]):

$$S_{ij} = Q_{ijkl} P^s_k P^s_l + 2 Q_{ijkl} P^s_k P^i_l + Q_{ijkl} P^i_k P^i_l \tag{III.3}$$

where Q_{ijkl} is the polarization-related electrostriction tensor coefficient.

For application of electrostriction in mechanical-to-electrical energy harvesting, the strain

S_{ij} and the electric flux density D_{ij} are expressed as independent variables of electric field density E_m, E_n and the stress T_{ij} by the constitutive relation as [LRHZ05]:

$$\begin{cases} S_{ij} = s^E_{ijkl} T_{kl} + M_{mnij} E_n E_m \\ D_m = \varepsilon_{mn} E_n + 2 M_{mnij} E_n T_{ij} \end{cases} \tag{III.4}$$

where s^E_{ijkl} is the elastic compliance, M_{nmij} is known as the electric-field-related electrostriction coefficient, and ε_{mn} is the linear dielectric permittivity.

An isotropic electrostrictive polymer film contracts along the thickness direction and expands along the film direction when an electric field is applied across the thickness, assuming that the only nonzero stress is applied along the length of the film. The constitutive relation is then simplified as [LCL+10]:

$$\begin{cases} S = sT + ME^2 \\ D = \varepsilon E + 2METT \end{cases} \tag{III.5}$$

III.3 Electrostrictive polymers in energy harvesting

Under a high DC electrical bias field, the electrostrictive polymer induces a large electromechanical effect with a higher mechanical-to-electrical coupling parameter d_{31} compared to conventional piezoelectric polymers. It has been shown that at room temperature the dielectric constant can reach almost 60 and the electrostrictive polymer has demonstrated a high strain of about 5% under 150 MV m^{-1} electric field ([ZBZ98a])[ZBZ+98b][CXB+99][LST+01]). Poly(vinylidene fluoride-trifluoroethylene) or P[VDF-TrFe] copolymers have been shown to exhibit d_{31} of 8.0×10^{-11} pC N^{-1}, and polyurethane has d_{31} of 1.7×10^{-10} pC N^{-1}. A theoretical investigation conducted by Liu *et al.* [LRHZ05] has shown that energy densities of the order of 0.221 J cm^{-3} is possible in constant field condition using polyurethane material [PI08].

Possible techniques for harvesting the energy converted by electrostrictive polymers have been discussed in [LRS+12][CGG+10]. Basically, three approaches can be considered in mechanical energy harvesting based on electrostrictive polymers: electrostatic cycle inspired from purely capacitive techniques, electrostrictive cycles based on charge and discharge operation and pseudo-piezoelectric process by applying a bias voltage on the material.

For electrostatic-derived cycles, there are two typical ones: Ericsson cycle (voltage constrained) and Stirling cycle (charge constrained). The latter cycle permits converting more energy compared with the former one, while the Ericsson cycle has a better control of the

electric field, ensuring that the maximal admissible value is never reached [LRS+12]. Based on the electrostrictive nature of materials, it is possible to break the symmetry between the stretching and contracting process of the electrostrictive polymer by adjusting the mechanical and electrical boundary conditions in quasistatic mechanical-to-electrical energy harvesting, leading to the formation of electrostrictive cycles. Liu *et el.* [LRHZ05] have proposed four electrical boundary conditions to form a loop of energy harvesting: constant field and open-circuit electrical boundary conditions, constant-field boundary conditions during stressing and unstressing of material, open-circuit boundary conditions during stressing and unstressing of material, passive diode circuit for energy harvesting. By investigation, the best energy harvesting density occurs when the electric field in the material increases from zero to its maximum at maximum stress and decreases from its maximum back to zero at minimum stress. The pseudo-piezoelectric process consists of applying a bias electric field to the sample, allowing simpler operations than charge and discharge cycles. A nonlinear approach similar to the "synchronized switch harvesting on inductor" for piezoelectric elements can be applied to increase the conversion efficiency [GBLR05][SLW07]. A comparison among the three techniques reveals that electrostatic-based approach permits the highest harvested energy, however, losses during the charge and discharge process may significantly reduce the performance of the techniques [WLP+14]. The pseudo-piezoelectric methods, especially those applying the nonlinear switching approaches, harvest an energy density about $5-10$ times less than the electrostatic-based approaches, but may avoid losses during charge and discharge from zero initial conditions as for this approach the system operates around a bias voltage. The three cycles above all require driving the electrical conditions of the materials for a significant period of time. A passive energy harvesting circuit using diodes is proposed in [LRHZ05] and [MVA+04] which permits a pure passive energy harvesting and facilitates its implementation. The principles of this device consist of providing energy to the polymer when its voltage reaches V_L (it is considered that the diode threshold voltages are negligible) and harvesting when it attains V_H (Fig.(III-1)). Despite the simplicity of this method, it requires that the voltage V_H is reached by the electrostrictive material, thus necessitating a minimal operating stress value [LRS+12].

III.4 Behavior of a beam

A structure can be analyzed with beam models when one of its dimensions is much larger than the other two. The axis of the beam is defined along the longest dimension, and the

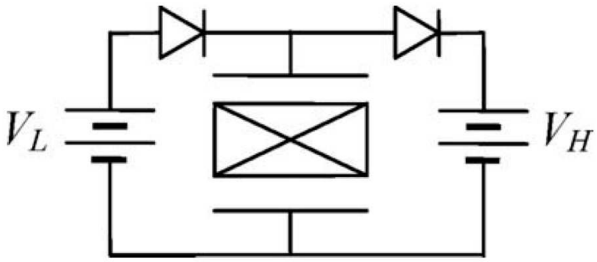

Figure III-1: Passive energy harvesting circuit

cross-section normal to this axis is considered to vary in a smooth way along the length of the beam [BC09]. Several beam theories have been developed based on different assumptions, and correspond to different level of accuracy. The basic assumptions are as follows [HBW99].

➢ One dimension of the structure is considerably larger than the other two.

➢ The material consisting the beam is linearly elastic and will not deform plastically (i.e., it obeys Hooke's law).

➢ The cross-section area is symmetric so that the neutral and centoidal axes coincide.

➢ The cross-section normal to the neutral axis remains normal after deformation.

➢ The angle of rotation is small so that the small angle assumption can be used.

While specifically for The Euler-Bernoulli beam theory, apart from the above assumptions three more are required:

1 The beam is subjected to pure bending, which indicates that the shear force is zero.

2 The material is isotropic and homogeneous.

3 The cross-section of a beam remains plane after deformation.

The assumptions are confirmed by experimental results to be valid for long, slender beams made of isotropic materials with solid cross-section. The Euler-Bernoulli beam theory may be inaccurate when one or more assumptions are not satisfied.

When the beam is subjected to transverse loads, it will have transverse displacement and curvature of the beam axis. Detailed derivations for the Euler-Bernoulli model can be found in books by S. S. Rao [Rao86], D. Inman [Inm13] and O.A. Bauchau and J. I. Craig [BC09]. The governing equation under the transverse deflection of the beam is given below:

$$\frac{d^2}{dx_1^2}\left(H_{33}^c \frac{d^2 u_3}{dx_1^2}\right) = p_3(x_1) \tag{III.6}$$

where H_{33}^c is the centroidal bending stiffness defined as $H_{33}^c = \int_{\mathcal{A}} E x_3^2 \, \mathrm{d}\mathcal{A}$ with E the Young's

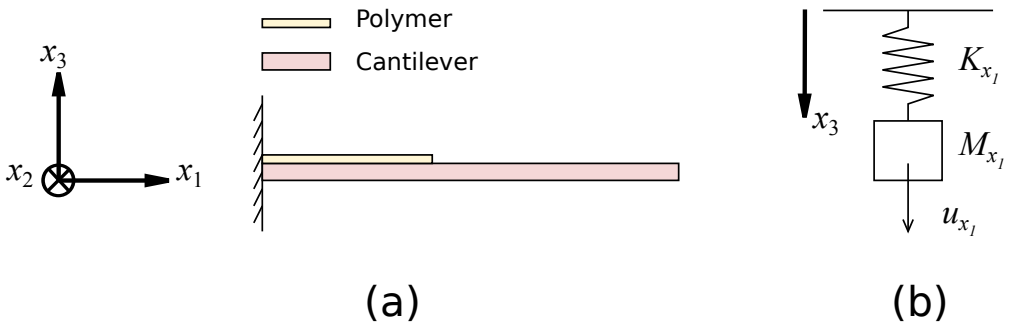

Figure III-2: Lumped model for a cantilever-based system coupled with polymer films

modulus, u_3 is the displacement along the axis x_3 and $p_3(x_1)$ is a distributed load along the axis x_3. To solve Eq.(III.6) for the transverse displacement field, $u_3(x_1)$, with a given distributed load, four boundary conditions are required, two at each end of the beam. In this chapter, four models will be discussed: clamped-free beam with an electrostrictive polymer film attached to the clamped end, clamped-clamped beam with two electrostrictive polymer films attached respectively to two ends, clamped-clamped beam with an electrostrictive polymer film attached in the middle, clamped-free bimorph beam. They correspond to different boundary conditions and configurations, and corresponding transverse displacement solutions will be given in Section(III.6).

III.5 Beam with electrostrictive polymer films

When the beam is combined with one or several electrostrictive polymer films, the polymers may generate a transverse distributed force on the beam through an electromechanical coupling, conversely the polymer films attached on the beam are vibrated by its displacement and generate a current also through an electromechanical coupling. For both cases, the energy flow is an interesting key point to work on.

Before a further study on these two aspects, we may notice that for a cantilever-based system coupled with polymer films (Fig.(III-2(a))), a lumped model could be established according to the observation position along axis x_1 (Fig.(III-2(b))) with the stiffness K, the system mass M and the displacement u dependent of x_1. The objective of this chapter is to evaluate the electromechanical coupling ability of such a lumped model for whichever position of observation via energetic analysis.

III.5.1 Principles

The development of the macroscopic model is based on the energetic analysis of mechanical and electrical energies. To facilitate the general theoretical analysis, the beam in the system is considered to be transverse and isotropic which allows the constitutive equations to be expressed as below:

$$\begin{cases} S_1 &= s_{11}^E T_1 + s_{12}^E T_2 + s_{31}^E T_3 + M_{31} E_3^2 \\ S_2 &= s_{12}^E T_1 + s_{11}^E T_2 + s_{31}^E T_3 + M_{31} E_3^2 \\ D_3 &= \varepsilon_{33}^T + 2M_{31} T_2 E_3 + 2M_{33} T_3 E_3 \end{cases} \tag{III.7}$$

In consideration that the beam is vibrated with small deformation, the assumptions of Euler-Bernoulli ($S_2 = 0$, $T_3 = 0$) may be applied to Eq.(III.7), leading to:

$$T_1 = c_p^E S_1 - (1 - \upsilon_p^E) c_p^E M_{31} E_3^2 \tag{III.8}$$

where $c_p^E = \dfrac{Y_E}{1 - (\upsilon_p^E)^2}$ with Y_E the Young's module and $\upsilon_p^E = \dfrac{s_{12}^E}{s_{11}^E}$ the Poisson's ratio.

However, in order to have a non-null response in the case of bending, the neutral axis should not be in the middle of the polymer. A substrate is added to the structure. According to Hooke's law, the relationship between the stress T_1 and strain S_1 on the substrate along axis 1 is given by

$$T_1 = c_b S_1 \tag{III.9}$$

where $c_b = \dfrac{Y_b}{1 - \nu_b^2}$ with Y_b and ν_b respectively referring to the Young modulus and Poisson's ratio of the substrate.

R.G. Ballas [Bal07] has given a theoretical analysis of neutral axis for piezoelectric multilayered beam bending configuration. For a piezoelectric bending actuator consisting of N layers (Fig.(III-3)), the different geometrical dimensions of the individual layers and their material properties would usually generate a change of the neutral axis position h_n which is defined as the distance to the lower edge of the multilayered beam bender. With three conditions for the derivation of the neutral axis position, it is given as Eq.(III.10).

$$h_n = -\frac{\sum_{i=1}^{N} \frac{w_i}{s_{11,i}} h_i^2 - 2 \sum_{i=1}^{N} \frac{w_i}{s_{11,i}} h_i \sum_{j=1}^{i} h_j}{2 \sum_{i=1}^{N} \frac{w_i}{s_{11,i}} h_i} \tag{III.10}$$

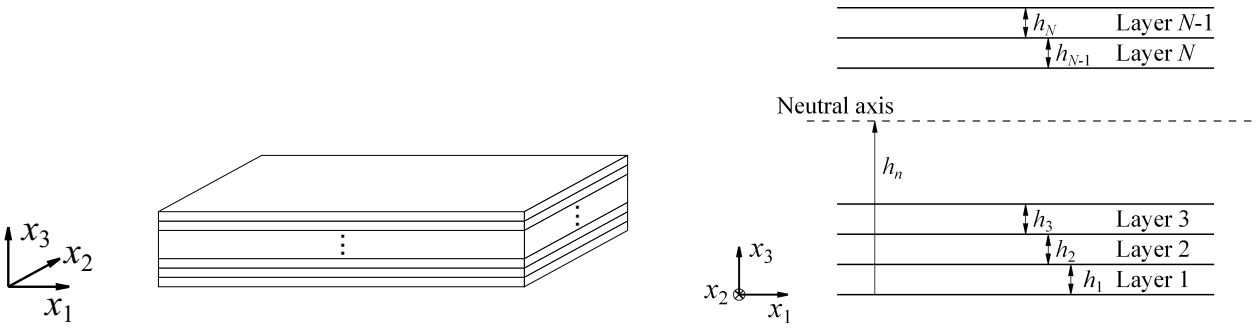

(a) 3D (b) 2D

Figure III-3: A multilayer beam

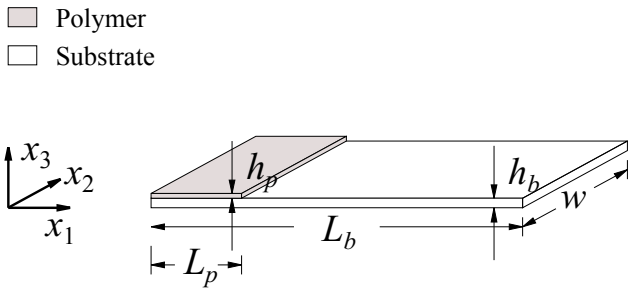

Figure III-4: Simple configuration of a beam attached with electrostritive polymer

w_i is the width of ith layer, $s_{11,i}$ is the compliance of material in the ith layer. This model is also valid for electrostrictive multilayered beam bending configuration (the difference between those two is mainly the compliance of material $s_{11,i}$). For a relatively simple configuration as demonstrated in Fig.(III-4), the neutral axis is:

$$h_n = \begin{cases} \dfrac{h_b^2 c_b + 2h_b h_p c_p^E + h_p^2 c_p^E}{2(h_b c_b + h_p c_p^E)} & \text{for active part (polymer + substrate)} \\ \dfrac{h_b}{2} & \text{for passive part (only substrate)} \end{cases} \tag{III.11}$$

where h_b is the thickness of beam and h_p the thickness of polymer.

III.5.2 Electrical aspect

Now the mechanical expression of the strain (which depends on the stress and electric field) obtained, and using the electrical constitutive equation in eq(III.7), it is possible to derive the electric displacement as a function of electric field E_3 and the strain S_1 in the active layer as:

$$\begin{aligned} D_3 &= \left\{\varepsilon_{33}^S + 2M_{31}(1-\upsilon_p^E)c_p^E S_1 - 2M_{31}^2\left[(1-\upsilon_p^E)^2 c_p^E + \tfrac{1}{s_{11}^E}\right]E_3^2\right\}E_3 \\ &\approx \varepsilon_{33}^S E_3 + 2M_{31}(1-\upsilon_p^E)c_p^E S_1 E_3 \end{aligned} \tag{III.12}$$

The provided electrical energy could be estimated by the variation of electric displacement and the electric field:

$$\begin{aligned} dW_{provided} &= E_3 dD_3 \\ &\approx \varepsilon_{33}E_3 dE_3 + 2M_{31}(1-\upsilon_p^E)c_p^E S_1 E_3 dE_3 + 2M_{31}(1-\upsilon_p^E)c_p^E E_3^2 dS_1 \end{aligned} \tag{III.13}$$

From this equation and from the strain-flexural displacement expression in the polymer (only the latter layer receives the electrical energy, so that the thickness ranges from $h_b - h_n$ to $h_b + h_p - h_n$ in the following expression) and, assuming that the thickness h_p is small enough to approximate the relationship between the electric field E_3 and voltage V as $E_3 = -V/h_p$, the expression of the provided electrical energy is:

$$\begin{aligned} dW_{provided} &= \int_0^w \int_0^{L_p} \int_{h_b-h_n}^{h_b+h_p-h_n} E_3 dD_3 dx_3 dx_1 dx_2 \\ &\approx \frac{wL_p\varepsilon_{33}^S}{h_p} V dV - M_{31}(1-\nu_p^E)h_b c_b c_p^E w \left(\frac{h_p+h_b}{h_b c_b + h_p c_p^E}\right)\left(\frac{V}{h_p}\right) V d\left(\frac{\partial u_3}{\partial x_1}(L_p)\right) \\ &\quad - M_{31}(1-\nu_p^E)h_b c_b c_p^E w \left(\frac{h_p+h_b}{h_b c_b + h_p c_p^E}\right)\left(\frac{V}{h_p}\right)\left(\frac{\partial u_3}{\partial x_1}(L_p)\right) dV \end{aligned} \tag{III.14}$$

where the first term stands for the electrical energy stored in the polymer and the two last terms are the converted energy. From the previous expression, it is possible to decompose the energy variation into a purely dielectric energy and a coupling energy (part of the provided

electrical energy is converted into mechanical energy):

$$dW_{prov,elec} = dW_{elec} + dW_{coupling,elec} \tag{III.15}$$

which may be identified as:

$$\begin{cases} dW_{elec} &= C_0 V dV \\ dW_{coupling,elec} &= \alpha(x_1) V d\left(u_3(x_1) V\right) = \alpha(x_1) V^2 du_3(x_1) + \alpha(x_1) V u_3(x_1) dV \end{cases} \tag{III.16}$$

with C_0 the equivalent clamped capacitance and $\alpha(x_1)$ the coupling coefficient of unit $\mathrm{A}^2\ \mathrm{s}^4\ \mathrm{kg}^{-1}\ \mathrm{m}^{-3}$ which actually depends on the position of observation along the x_1 axis of the flexural displacement $u_3(x_1)$:

$$C_0 = \frac{w L_p \varepsilon_{33}^S}{h_p} \tag{III.17}$$

$$\alpha(x_1) u_3(x_1) = N \left(\frac{\partial u_3}{\partial x_1}(L_p) \right) \tag{III.18}$$

with

$$N = \left(\frac{M_{31}(1-\nu_p^E) h_b c_b c_p^E w}{h_p} \right) \left(\frac{h_p + h_b}{h_b c_b + h_p c_p^E} \right)$$

The provided electrical energy being given by the voltage and charge Q provided by the source, the lumped expression of the electrical relationship is then given as:

$$Q = C_0 V - \alpha(x_1) V u_3(x_1) \tag{III.19}$$

In an electrical-to-mechanical energy conversion, the product of the electromechanical coefficient and the displacement is proportional to the deformation at $x_1 = L_p$, which is constant at a certain moment for any point on the beam. It is physically reasonable as in Eq.(III.19) this product along with the polarization electric field is a description of the whole charge on the electrostrictive polymer, not a specific point on the beam. At a certain moment, for at any observation point on the beam the coupling coefficient is reciprocal to the displacement, which indicates that the greater the displacement is, the smaller the coefficient will be. The charge in Eq.(III.19) is composed of two terms - the first term originates from stored electrical energy and the second term is composed of the coupling coefficient, the

applied voltage and the displacement. The composition of the second term clearly indicates that the charge can be influenced by the movement of polymer u_3 which is the result of electromechanical coupling. Physically, a part of the provided electrical energy is converted into mechanical energy - demonstrating as the movement of the electrostrictive polymer and of the beam. This mechanical movement of polymer then in return generates a electric charge also by coupling. So the coefficient here is to describe a electromechanical coupling - the ability of coupling mechanical movement to generate electric charges.

III.5.3 Mechanical aspect

This subsection proposes to investigate the mechanical aspect of bending electrostrictive systems. It is now considered that the energy is provided by a mechanical source. A force F is applied on the beam (the position of application is not fixed here to provide a general condition). Converse electrostriction requires an activation mechanism in order to allow mechanical to electrical energy conversion, as dipoles in electrostrictive polymer need to be pre-oriented [LCS+14]. So the electrostrictive polymer is polarized by a high electric field and at the same time subjected to a transverse force field, the provided mechanical energy could be estimated by the strain and stress in the system.

$$\begin{aligned} dW_{provided} &= T_1 dS_1 \\ &= c_p^E S_1 dS_1 - (1-\nu_p^E) c_p^E M_{31} E_3^2 dS_1 \end{aligned} \tag{III.20}$$

As the mechanical energy is provided to the whole system, the integration is not only on the polymer, but also on the beam:

$$\begin{aligned} dW_{provided} &= \int_0^w \int_0^{L_b} \int_{-h_n}^{h_b+h_p-h_n} T_1 dS_1 dx_3 dx_1 dx_2 \\ &= A c_p^E w \int_0^{L_b} \frac{\partial^2 u_3}{\partial x_1^2} d\left(\frac{\partial^2 u_3}{\partial x_1^2}\right) dx_1 + c_b I_b \int_0^{L_b} \frac{\partial^2 u_3}{\partial x_1^2} d\left(\frac{\partial^2 u_3}{\partial x_1^2}\right) dx_1 \\ &\quad + \frac{1}{2} M_{31}(1-\nu_p^E) h_b c_b c_p^E w \left(\frac{h_p+h_b}{h_b c_b + h_p c_p^E}\right) \frac{V^2}{h_p} d\left(\frac{\partial u_3}{\partial x_1}(L_p)\right) \end{aligned} \tag{III.21}$$

where

$$A = \frac{w}{12}\left(\frac{c_b^2 h_b^4 + 4c_b c_p^E h_b^3 h_p + 6c_b c_p^E h_b^2 h_p^2 + 4c_b c_p^E h_b h_p^3 + (c_p^E)^2 h_p^4}{c_b h_b + c_p^E h_p}\right)$$

and I_b denotes the second moment of area of the substrate:

$$I_b = \frac{h_b^3 w}{12} \tag{III.22}$$

Part of the mechanical energy is presented as the displacement of the system - this corresponding mechanical energy is the first term in Eq.(III.21), the rest part is converted into electrical energy - this converted mechanical energy is the second term in Eq.(III.21).

From the following analysis, it is possible to identify the terms with the following equation giving the balance between the applied external force F, the restoring force of the beam (given by the stiffness K and the displacement u), and the force generated by the electromechanical coupling $F_{coupling}$:

$$F = Ku + F_{coupling} \tag{III.23}$$

An external force is exercised on the beam as a source of mechanical energy which is interpreted as the first term in Eq.(III.23); interestingly, the coupling causing voltage along with the voltage for polarization has been the source of the coupling force in Eq.(III.23). Similar to the phenomenon in the previous subsection, the mechanical energy is converted into electrical one which is presented as a coupling voltage; then the coupling voltage induces a mechanical strain which is the origin of the second term in Eq.(III.23).

The provided mechanical energy could also been interpreted as work of the applied force.

$$dW_{provided} = Kudu + F_{coupling}du \tag{III.24}$$

By comparing Eq.(III.21) and Eq.(III.24) and by considering influence of voltage on the force $F_{coupling}$, the force on the beam is further identified as:

$$F = Ku + \frac{1}{2}\alpha_F(x_1)V^2 \tag{III.25}$$

where $F_{coupling} = \frac{1}{2}\alpha_F V^2$.

The provided mechanical energy in Eq.(III.24) becomes:

$$dW_{provided} = Kudu + \frac{1}{2}\alpha_F V^2 du \tag{III.26}$$

$$\alpha_F(x_1)u_3(x_1) = N\frac{\partial u_3}{\partial x_1}(L_p) \tag{III.27}$$

$$K(x_1)u_3^2(x_1) = Ac_p^E w\int_0^{L_b}\left[\frac{\partial^2 u_3}{\partial x_1^2}\right]^2 dx_1 + c_b I_b\int_0^{L_b}\left[\frac{\partial^2 u_3}{\partial x_1^2}\right]^2 dx_1 \tag{III.28}$$

Like Eq.(III.21), the electromechanical coefficient in Eq.(III.26) also shows a relationship with the position of observation. Through a comparison between Eq.(III.21) and Eq.(III.26), both the stiffness and the coupling coefficient α_F are obtained. It can be also noted that the stiffness $K(x_1)$ (Eq.(III.28)) depends not only on the displacement at the considered position x_1 but also on the flexural shape of the structure. A primary expression of the coupling coefficient from mechanical energy to electrical one is obtained (Eq.(III.27)) which is the same with Eq.(III.18). On a point on the beam, the coupling coefficient is the same for both conversions under the same displacement. In the electrical-to-mechanical energy conversion (Eq.(III.19)), the product of the coefficient and the displacement is proportional to the slope at $x_1 = L_p$, so the charge induced by the effect is uniform for all over beam; in the mechanical-to-eletrical energy conversion the coupling coefficient plays the role alone in the mechanical-to-electrical energy conversion (Eq.(III.25)), which means for different positions on the beam, the force induced by the effect differs. The force effect is not only related to the deformation at $x_1 = L_p$ (which is the case for induced voltage), but also influenced by the displacement at the point where the force is applied. It does not lead to any paradox as the original force could be applied at any point on the beam.

Once the static mechanical behavior obtained, and by considering that the dynamic deformed shape is similar, it is also possible to derive the dynamic mass M_d as:

$$M_d(x_1) = \frac{1}{u_3^2(x_1)}\int_0^{L_b} m(x_1)u_3^2(x_1)dx_1 \tag{III.29}$$

with $m(x_1)$ the lineic mass of the beam, defined from the material dimensions and the respective densities ρ_b and ρ_p of the substrate and polymer:

$$\begin{cases} m(x_1) = w(h_b\rho_b + h_p\rho_p) & \text{for} \quad x_1 \in [0, L_p] \\ m(x_1) = wh_b\rho_b & \text{for} \quad x_1 \in]L_p, L_b] \end{cases} \tag{III.30}$$

III.5.4 Global lumped model

Hence, as a summary from the previous two energy analysis, for different positions of observation it is possible to get the equivalent lumped model for an electrostrictive polymer operating in bending mode and considering the displacement at the position x_1:

$$\begin{cases} M_d(x_1)\ddot{u}_3(x_1) + Ku_3(x_1) = F - \dfrac{1}{2}\alpha(x_1)V^2 \\ I = \alpha(x_1)V\dot{u}_3(x_1) + \alpha(x_1)u_3(x_1)\dot{V} - C_0\dot{V} \end{cases} \tag{III.31}$$

with F the external applied force and I the current flowing out of the polymer. Furthermore, dynamic losses can also be introduced through a structural damping coefficient C, yielding the global lumped model:

$$\begin{cases} M_d(x_1)\ddot{u}_3(x_1) + C\dot{u}_3(x_1) + Ku_3(x_1) = F - \dfrac{1}{2}\alpha(x_1)V^2 \\ I = \alpha(x_1)V\dot{u}_3(x_1) + \alpha(x_1)u_3(x_1)\dot{V} - C_0\dot{V} \end{cases} \tag{III.32}$$

where the expression of the model parameters are summarized as follows:

$$\begin{cases} M_d(x_1) = \dfrac{1}{u_3^2(x_1)}\displaystyle\int_0^{L_b} m(x_1)u_3^2(x_1)dx_1 \\ K(x_1) = \dfrac{1}{u_3^2(x_1)}\left\{Ac_p^E w\displaystyle\int_0^{L_b}\left[\frac{\partial^2 u_3}{\partial x_1^2}\right]^2 dx_1 + c_b I_b\int_0^{L_b}\left[\frac{\partial^2 u_3}{\partial x_1^2}\right]^2 dx_1\right\} \\ \alpha = \dfrac{1}{u_3^2(x_1)}\left[\left(\dfrac{M_{31}(1-\nu_p^E)h_b c_b c_p^E w}{h_p}\right)\left(\dfrac{h_p + h_b}{h_b c_b + h_p c_p^E}\right)\left(\dfrac{\partial u_3}{\partial x_1}(L_p)\right)\right] \\ C_0 = \dfrac{wL_p\varepsilon_{33}^S}{h_p} \end{cases} \tag{III.33}$$

III.6 Several examples for beams with electrostrictive polymers

The electromechanical coefficient α and the stiffness K depend on the displacement of the beam, in the following sections, several boundary conditions will be proposed and the corresponding coefficients will be discussed.

Table III.1: Parameters for a clamped-free beam

L_b (mm)	L_p (mm)	h_b (μm)	h_p (μm)
54	39	70	53

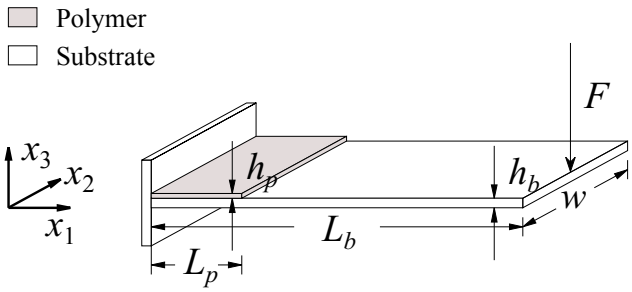

Figure III-5: Clamped-free beam with a force F at one end

III.6.1 Clamped-free beam with a force F at free end

The configuration of the system is given in Fig.(III-5) with parameters in Table (III.1). The resolution of the displacement on the beam is composed of one for the active part (attached with polymer film) and one for the passive part (without the attached film). From Section(III.4) a general solution has been given (Eq.(III.6)). The substrate is considered to be homogeneous thus H^c_{33} becomes the product of the Young's modulus Y_E and the area moment of inertia I (or the second moment of area).

For the active part with an electrostrictive polymer film, the polymer film is supposed to satisfy the assumptions of Euler-Bernoulli beam theory, which brings the expressions of strain and stress in x_1 direction (Eq.(III.8)). The strain is associated with the displacement along x_3 direction by the neutral axis.

$$S_1 = -(x_3 - h_n)\frac{\partial^2 u_3}{\partial x_1^2} \tag{III.34}$$

The moment applied on the polymer (active part) is obtained by an integration on the beam.

$$\begin{aligned} M^a &= w\int_{-h_n}^{h_b+h_p-h_n} T_1 x_3 dx_3 \\ &= w\int_{-h_n}^{h_b-h_n} T_1 x_3 dx_3 + w\int_{h_b-h_n}^{h_b+h_p-h_n} T_1 x_3 dx_3 \\ &= -A\frac{\partial^2 u_3}{\partial x_1^2} + BE_3^2 \end{aligned} \tag{III.35}$$

with the neutral axis in the active part to be:

$$h_n^a = \frac{h_b^2 c_b + 2h_b h_p c_p^E + h_p^2 c_p^E}{2(h_b c_b + h_p c_p^E)}$$

and the parameters A and B being defined as:

$$\begin{cases} A = \dfrac{w}{12}\left[\dfrac{c_b^2 h_b^4 + 4c_b c_p^E h_b^3 h_p + 6c_b c_p^E h_b^2 h_p^2 + 4c_b c_p^E h_b h_p^3 + (c_p^E)^2 h_p^4}{c_b h_b + c_p^E h_p}\right] \\ B = -\dfrac{w}{2}\left(\dfrac{h_b + h_p}{c_b h_b + c_p^E h_p}\right)\left(1 - \upsilon_p^E\right) c_p^E c_b h_p h_b M_{31} \end{cases}$$

For the passive part without polymer, the neutral axis becomes $h_n^p = \frac{1}{2}h_b$ and the moment by integration is:

$$M^p = w\int_{-h_n^p}^{h_b - h_n^p} T_1 x_3 dx_3 = -w\int_{-h_n^p}^{h_b - h_n^p} c_b x_3^2 \frac{\partial^2 u_3}{\partial x_1^2} dx_3 \tag{III.36}$$

For points on the beam in the surface $(x_1,\ 0,\ x_3)$, the external moment induced by the force F is :

$$M^e = (L_b - x_1)F \tag{III.37}$$

Combinations of Eq.(III.36) and Eq.(III.37) and of Eq.(III.35) and Eq.(III.37) lead to solutions of displacements on the passive and active parts:

$$\begin{cases} u_3^p(x_1) = -\dfrac{12}{c_b h_b^3 w} F\left(\dfrac{L_b}{2}x_1^2 - \dfrac{1}{6}x_1^3\right) + a_1 x_1 + a_2 \\ u_3^a(x_1) = \dfrac{1}{A}\left(\dfrac{B}{2}E_3^2 - \dfrac{FL_b}{2}\right)x_1^2 + \dfrac{1}{6A}Fx_1^3 \end{cases} \tag{III.38}$$

where the superscripts a and p denote respectively the active part and the passive part.

The boundary conditions are that the displacement and velocity at $x_1 = 0$ are null and the displacement and slope at the position $x_1 = L_p$ are the same for both equations for the passive part and the active part (Eq.(III.39)), which lead to the expressions of a_1 and a_2

(Eq.(III.40)).

$$\begin{cases} u_3(0) = 0 \\ \dfrac{du_3}{dt}(0) = 0 \\ u_3^p(L_p) = u_3^a(L_p) \\ \left(\dfrac{\partial u_3^p}{\partial t}\right)(L_p) = \left(\dfrac{\partial u_3^a}{\partial t}\right)(L_p) \end{cases} \tag{III.39}$$

$$\begin{cases} a_1 = \dfrac{BL_p}{A}E_3^2 + \left(\dfrac{12L_bL_p}{c_bh_b^3w} - \dfrac{6L_p^2}{c_bh_b^3w} - \dfrac{L_bL_p}{A} + \dfrac{L_p^2}{2A}\right)F \\ a_2 = -\dfrac{BL_p^2}{2A}E_3^2 + \left(-\dfrac{6L_bL_p^2}{c_bh_b^3w} + \dfrac{4A}{c_bh_b^3w} + \dfrac{L_bL_p^2}{2A} - \dfrac{L_p^3}{3A}\right)F \end{cases} \tag{III.40}$$

The displacement of the passive part is then given as:

$$u_3^p = \frac{BL_p}{A}\left(x_1 - \frac{L_p}{2}\right)E_3^2 + \left(b_3x_1^3 + b_2x_1^2 + b_1x_1 + b_0\right)F \tag{III.41}$$

with

$$\begin{cases} b_0 = -\dfrac{6L_bL_p^2}{c_bh_b^3w} + \dfrac{4L_p^3}{c_bh_b^3w} + \dfrac{L_bL_p^2}{2A} - \dfrac{L_p^3}{3A} \\ b_1 = \dfrac{12L_bL_p}{c_bh_b^3w} - \dfrac{6L_p^2}{c_bh_b^3w} - \dfrac{L_bL_p}{A} + \dfrac{L_p^2}{2A} \\ b_2 = -\dfrac{6L_b}{c_bh_b^3w} \\ b_3 = \dfrac{2}{c_bh_b^3w} \end{cases}$$

According to the general expressions of the electromechanical coefficient, for a clamped-free beam the coefficients for the passive part and the active part are respectively:

$$\begin{cases} \alpha_p = \dfrac{N\left(-2L_bL_p + L_p^2\right)}{2A} \dfrac{\dfrac{2BL_p}{-2L_bL_p + L_p^2}E_3^2 + F}{\dfrac{BL_p}{A}\left(x_1 - \dfrac{L_p}{2}\right)E_3^2 + \left(b_3x_1^3 + b_2x_1^2 + b_1x_1 + b_0\right)F} \\ \alpha_a = N\left(-2L_bL_p + L_p^2\right) \dfrac{\dfrac{2BL_p}{-2L_bL_p + L_p^2}E_3^2 + F}{Bx_1^2E_3^2 + \left(\dfrac{1}{3}x_1^3 - L_bx_1^2\right)F} \end{cases} \tag{III.42}$$

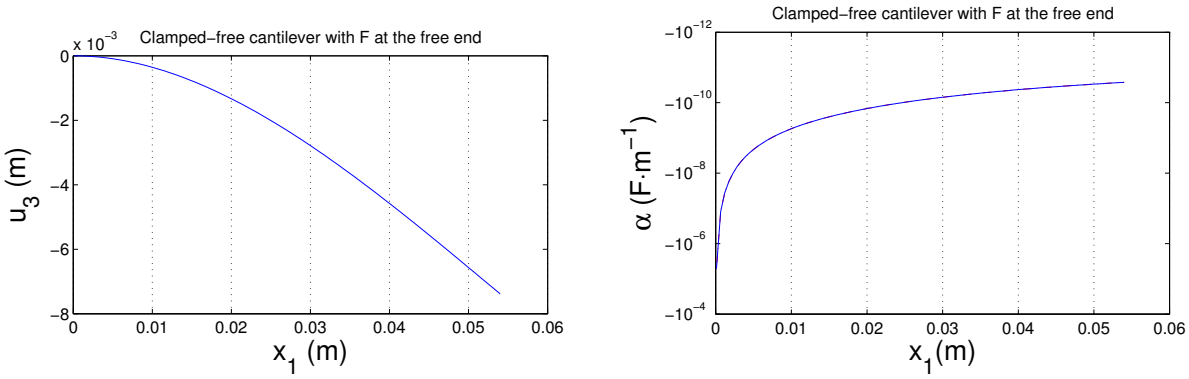

(a) u (b) α

Figure III-6: The displacement and the electromechanical coefficient for a clamped-free beam attached with an electrostrictive polymer film with an applied force of 10^{-2} N

The electric field is set to be 10^7 V m^{-1} and the force is 10^{-2} N. With other given parameters, for the coefficient α_p, the terms $\left(\frac{2BL_p}{-2L_bL_p+L_p^2}E_3^2\right)$ and $\left[\frac{BL_p}{A}\left(x_1-\frac{L_p}{2}\right)E_3^2\right]$ in the coefficient α_p are of magnitude 10^{-6}, while the other term $\left[\left(b_3x_1^3+b_2x_1^2+b_1x_1+b_0\right)F\right]$ is of magnitude 10^{-3}. For the coefficient α_a, the term $(Bx_1^2E_3^2)$ is of magnitude of 10^{-10} and the term $\left[\left(\frac{1}{3}x_1^3-L_bx_1^2\right)F\right]$ is of magnitude of 10^{-7}. Thus the coefficient α_p could be approximated to:

$$\begin{cases} \alpha_p = \dfrac{N\left(-2L_bL_p+L_p^2\right)}{2A\left(b_3x_1^3+b_2x_1^2+b_1x_1+b_0\right)} \\ \alpha_a = \dfrac{N\left(-2L_bL_p+L_p^2\right)}{\dfrac{1}{3}x_1^3-L_bx_1^2} \end{cases} \tag{III.43}$$

The electromechanical coefficients are actually independent of applied force F.

The electromechanical coefficient α is in inverse proportion to the displacement. Observation of Fig.(III-6(a)) and Fig.(III-6(b)) shows that on a point far from the fixed end, the displacement is greater corresponding to a lower electromechanical coefficient. The electromechanical factor αu depends on the displacement on position $x_1 = L_p$ (Eq.(III.18)). To evaluate this relationship, the length of polymer L_p is varied from 0 to L_b and the variation of αu is shown in Fig.(III-7). The product of electromechanical coefficient and the displacement grows rapidly when the ratio of length of polymer to length of the beam (L_p/L_b) is increased from 0 to 0.2, it increases about ten times; then the increase velocity of αu becomes rather gently until the the polymer and the beam are of the same length. The electromechanical effect can be largely weakened when the polymer is rather short, and may be gently enhanced

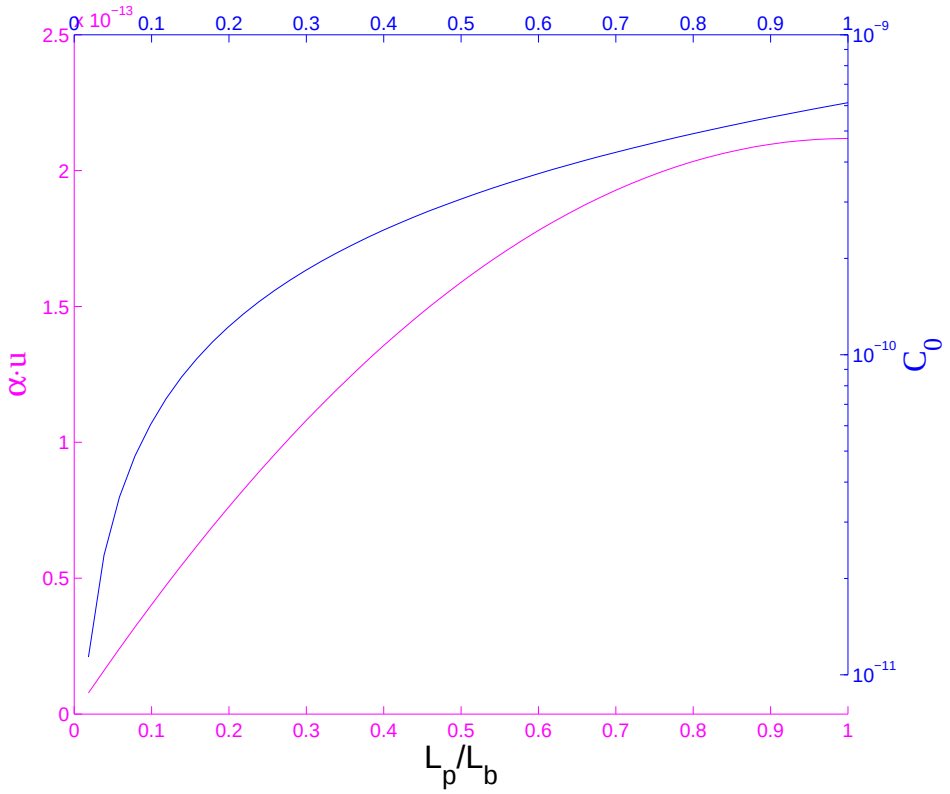

Figure III-7: The electromechanical coupling factor αu varying with the ratio of length of polymer to that of the beam

Table III.2: Parameters for a bimorph beam

L_b (mm)	L_p (mm)	h_b (μm)	h_p (μm)
54	39	70	53

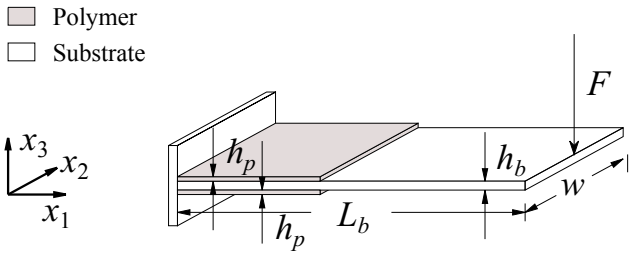

Figure III-8: Clamped-free bimorph beam

when the length is increased. The capacitance of polymer C_0 defined in Eq.(III.17) is of the magnitude about 10^{-9} F, while in Fig.(III-7) the electromechanical effect factor αu is observed to reach a maximum of about 10^{-13} F. Even an increase of length of the polymer has enhanced the electromechanical coupling, it is still rather minor. However, when the beam serves as a sensor (polarized by a constant field and actuated by a mechanical oscillation), the current according to the charge (Eq.(III.19)) is given as:

$$I_{ac} = \alpha V_{dc} \dot{u} \tag{III.44}$$

Although the electromechanical coefficient α is of small value, it describes the dynamic state and cannot be neglected.

III.6.2 Clamped-free bimorph beam with the force at the free end

The beam is fixed at one end and attached respectively to the lower side and to the upper side an electrostrictive polymer film with the same length of the beam (Fig.(III-8)) and the parameters are in Table (III.2). The strain and stress in Eq.(III.34) and Eq.(III.8) are still valid for this case with the neutral axis being adjusted to Eq.(III.45) for both passive and active parts.

$$h_n = \frac{2h_p + h_b}{2} \tag{III.45}$$

The moment on the part with polymer is:

$$\begin{aligned} M^a &= w\int_{-\frac{h_b}{2}-h_p}^{\frac{h_b}{2}+h_p} T_1 x_3 dx_3 \\ &= -A'\frac{\partial^2 u_3}{\partial x_1^2} + B'\left(E_3|_1^2 - E_3|_2^2\right) \end{aligned} \tag{III.46}$$

with $E_3|_1$ the electric field applied to the upper side of polymer film, $E_3|_2$ the electric field applied to the lower side of polymer film on supposing that $(E_3|_1 > E_3|_2)$ and with

$$\begin{cases} A' &= w\left[\frac{c_p}{12}\left((h_b+2h_p)^3 - h_b^3\right) + \frac{c_b}{12}h_b^3\right] \\ B' &= -\frac{w}{2}\left(1-\upsilon_p^E\right)c_p^E M_{31}\left(h_b h_p + h_p^2\right) \end{cases}$$

The moment on the passive part without polymer is the same with previous case as the substrate configuration is invariant:

$$M^p = -w\int_{-h_n^p}^{h_b-h_n^p} c_b x_3^2 \frac{\partial^2 u_3}{\partial x_1^2} dx_3 \tag{III.47}$$

A force F is applied at the free end of beam and forms an external moment as:

$$M = (L_b - x_1)F \tag{III.48}$$

An analysis of Eq.(III.46), Eq.(III.47) and Eq.(III.48) reveals that they are actually similar to the three corresponding equations in the previous case (Eq.(III.35), Eq.(III.36) and Eq.(III.37)) except for the difference of neutral axis, of parameters (A, B and A', B') and of electric fields, indicating similar forms of solutions. Combine respectively Eq.(III.48) and Eq.(III.47), Eq.(III.48) and Eq.(III.46). The displacement on the passive and active parts are respectively:

$$\begin{cases} u_3^p(x_1) = -\frac{12}{c_b h_b^3 w}F\left(\frac{L_b}{2}x_1^2 - \frac{1}{6}x_1^3\right) + a_1' x_1 + a_2' \\ u_3^a(x_1) = \frac{1}{A'}\left[\frac{B'}{2}\left(E_3|_1^2 - E_3|_2^2\right) - \frac{FL_b}{2}\right]x_1^2 + \frac{1}{6A'}Fx_1^3 \end{cases} \tag{III.49}$$

The boundary conditions stay the same with Eq.(III.39) and the parameters for displace-

ment on the passive part are given as:

$$\begin{cases} a_1' = \dfrac{B'L_p}{A'}\left(E_3|_1^2 - E_3|_2^2\right) + \left(\dfrac{12L_bL_p}{c_bh_b^3w} - \dfrac{6L_p^2}{c_bh_b^3w} - \dfrac{L_bL_p}{A'} + \dfrac{L_p^2}{2A'}\right)F \\ a_2' = -\dfrac{B'L_p^2}{2A'}\left(E_3|_1^2 - E_3|_2^2\right) + \left(-\dfrac{6L_bL_p^2}{c_bh_b^3w} + \dfrac{4A'}{c_bh_b^3w} + \dfrac{L_bL_p^2}{2A'} - \dfrac{L_p^3}{3A'}\right)F \end{cases} \tag{III.50}$$

The displacement of the passive part can be also expressed as:

$$u_3^p = \frac{B'L_p}{A'}\left(x_1 - \frac{L_p}{2}\right)\left(E_3|_1^2 - E_3|_2^2\right) + \left(b_3'x_1^3 + b_2'x_1^2 + b_1'x_1 + b_0'\right)F \tag{III.51}$$

with

$$\begin{cases} b_0' = -\dfrac{6L_bL_p^2}{c_bh_b^3w} + \dfrac{4L_p^3}{c_bh_b^3w} + \dfrac{L_bL_p^2}{2A'} - \dfrac{L_p^3}{3A'} \\ b_1' = \dfrac{12L_bL_p}{c_bh_b^3w} - \dfrac{6L_p^2}{c_bh_b^3w} - \dfrac{L_bL_p}{A'} + \dfrac{L_p^2}{2A'} \\ b_2' = -\dfrac{6L_b}{c_bh_b^3w} \\ b_3' = \dfrac{2}{c_bh_b^3w} \end{cases}$$

According to the general expressions of the electromechanical coefficient, for a clamped-free beam the coefficients for the passive part and the active part as a function of the considered position are respectively given by:

$$\begin{cases} \alpha_p = \dfrac{N\left(-2L_bL_p + L_p^2\right)}{2A'} \dfrac{\dfrac{2B'L_p}{-2L_bL_p + L_p^2}\left(E_3|_1^2 - E_3|_2^2\right) + F}{\dfrac{B'L_p}{A'}\left(x_1 - \dfrac{L_p}{2}\right)\left(E_3|_1^2 - E_3|_2^2\right) + \left(b_3'x_1^3 + b_2'x_1^2 + b_1'x_1 + b_0'\right)F} \\ \alpha_a = N\left(-2L_bL_p + L_p^2\right) \dfrac{\dfrac{2B'L_p}{-2L_bL_p + L_p^2}\left(E_3|_1^2 - E_3|_2^2\right) + F}{B'x_1^2\left(E_3|_1^2 - E_3|_2^2\right) + \left(\dfrac{1}{3}x_1^3 - L_bx_1^2\right)F} \end{cases} \tag{III.52}$$

Like introduced in the previous section, the terms containing the electric field are much

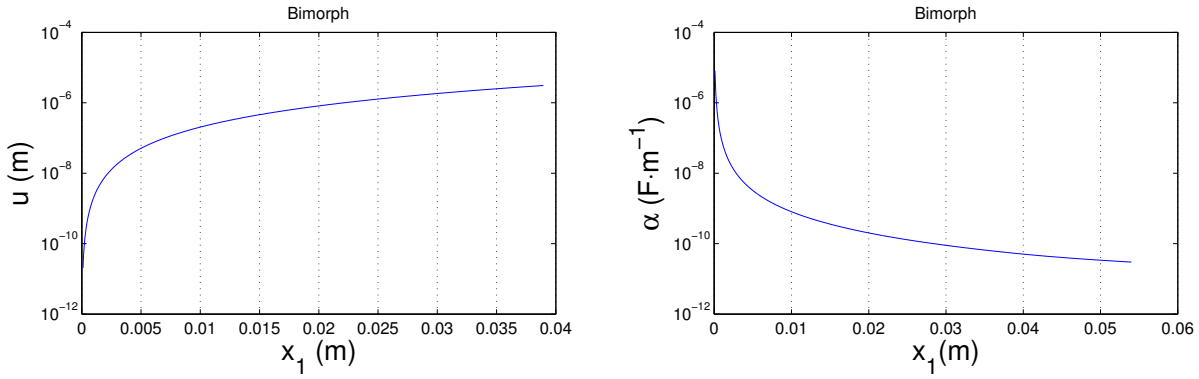

(a) u (b) α

Figure III-9: The displacement and electromechanical coefficient for a clamped-free bimorph beam

inferior to those containing the force, the coefficients can be approximated to:

$$\begin{cases} \alpha_p = \dfrac{N\left(-2L_bL_p + L_p^2\right)}{2A'\left(b'_3x_1^3 + b'_2x_1^2 + b'_1x_1 + b'_0\right)} \\ \alpha_a = \dfrac{N\left(-2L_bL_p + L_p^2\right)}{\dfrac{1}{3}x_1^3 - L_bx_1^2} \end{cases} \tag{III.53}$$

Similar to the case in the previous section, the coefficients are also independent of applied force F.

Not surprisingly, the electromechanical coefficient for a bimorph beam is also a reciprocal function of the displacement (Fig.(III-9)). The product of the electromechanical coefficient and the displacement increases with the ratio of the length of the polymer to that of the beam less gently compared to the previous case (Fig.(III-10)), which indicates a greater influence occurs with the existence of a supplementary polymer film.

III.7 Experimental results for a unimorph cantilever

The model is set up through the energetic analysis and leads to an electromechanical coefficient α_t (the subscript t is added to differentiate from the experimentally measured one). The objective of the experiment is first to validate the theoretical model of electromechanical coefficient; then to evaluate the energy harvesting ability of the system.

The measurement of coefficient α is inspired by the expression of charge (Eq.III.19) which

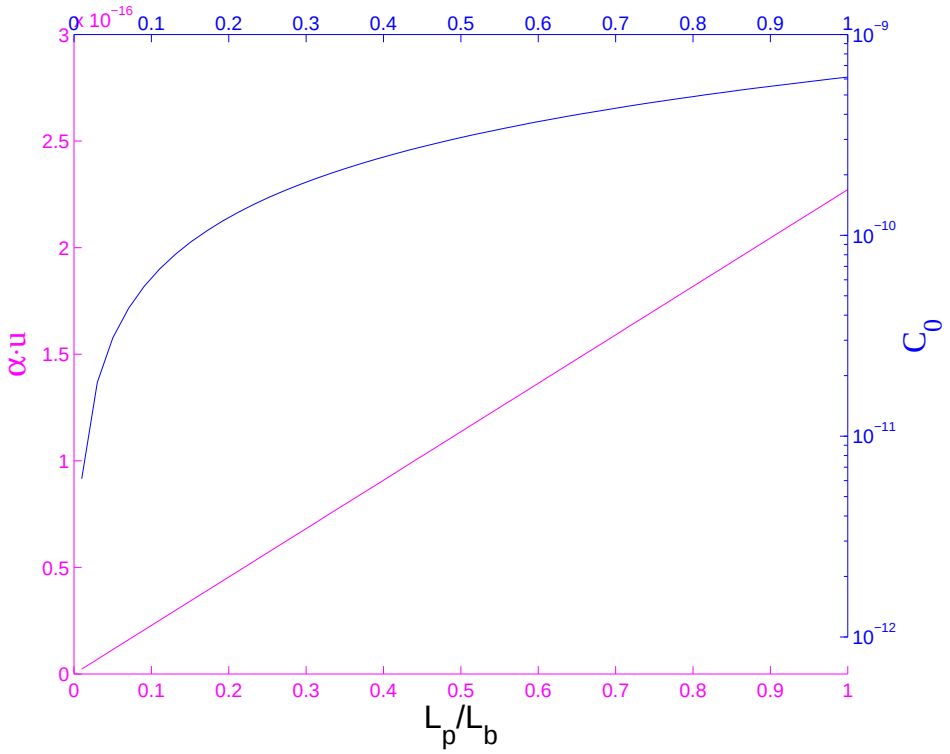

Figure III-10: The electromechanical coupling factor αu varying with the ratio of length of polymer for a clamped-free bimorph beam

leads to an induced outgoing current I:

$$I = -C_0\dot{V} + \alpha\dot{V}u + \alpha V\dot{u} \tag{III.54}$$

where the voltage on polymer is composed of V_{dc} and V_{ac}. The former one is external and constant for polarizing the polymer, the latter one is generated by the polymer under vibration when a load is connected in series. The current may then be described as a function of voltage and resistance R in the circuit:

$$\frac{V_{ac}}{R} = -C_0\dot{V} + \alpha\dot{V}u + \alpha V\dot{u} \tag{III.55}$$

As the voltage generated by the polymer is far less than that of polarization, the voltage V is approximated to V_{dc} .

By the Fourier transformation, V_{ac} is equal to:

$$V_{ac} = \frac{RV_{dc}}{1 + jRC_0\omega - jR\omega u\alpha}\alpha(j\omega u) \tag{III.56}$$

In the previous calculation, the term αu is usually negligible compared to C_0, so the term $(-jR\omega u\alpha)$ is negligible in the following. As the expression $(j\omega u)$ is equivalent to the velocity, the equation above sheds light on the measurement of electromechanical coefficient which may be given by the resistance, the frequency, the polarization voltage, the measured voltage and measured velocity. The equation of measured voltage (Eq.(III.56)) can be further simplified. As the magnitude of C_0 (experimental) is about 10^{-10}, and those of α (theoretical), u (experimental) and ω (experimental) are respectively 10^{-11}, 10^{-2} and 10. In the experiment, the applied resistance is of magnitude between 10^6 and 10^7. All above conditions lead to the term $RC_0\omega$ to be far less than 1. Eq.(III.56) is further approximated to

$$V_{ac} \approx -RV_{dc}\upsilon\alpha \tag{III.57}$$

where υ denotes the velocity. As a conclusion, to measure the coefficient α, a small load R (so that $R_iC_0\omega \ll 1$) needs to be connected in the circuit containing the polymer; the current on the load I ($I = V_{ac}/R$) or the voltage V_{ac} and the velocity on the given position are necessary to be measured.

In terms of energy generation, the measurement of average harvested power is relatively simple as in:

$$P = R\ i_{RMS}^2 \tag{III.58}$$

Table III.3: Parameters of the steel substrate

Steel substrate					
Length	54 mm	Thickness	83μm	Width	17 mm
Young's modulus	210 GPa	Poisson's ratio	0.29	Density	8000 kg m^{-3}

Table III.4: Parameters of the polymer film

Film of polyurethane			
Length	39 mm	Thickness	80 μm
Width	17 mm	Short-circuit Young's modulus	30 GPa
Short circuit Poisson's ratio	0.49	Density	1100 kg m^{-3}
Capacitance	310 pF	Relative permittivity	4

with i_{RMS} the measured RMS current. However, it should be paid attention that the load R to harvest energy is much more important than that in the measurement of current which is explained before. Based on the generated voltage V_{ac} (Eq.(III.56)), the RMS harvested power thus is expressed as:

$$P_{rms} = \frac{R\omega^2\alpha^2 V_{dc}^2}{2\left[1+(RC_0\omega)^2\right]}u^2 \tag{III.59}$$

The optimal value of resistance to maximize the harvested power is then:

$$R_{opt} = \frac{1}{C_0\omega} \tag{III.60}$$

To maximize the scavenged energy, the load R_h to harvest should be around the optimal value $1/(C_0\omega)$ which means $R_hC_0\omega \approx 1$; however, as explained before, to simplify the measurement of coefficient, the corresponding load R_c needs to satisfy $R_cC_0\omega \ll 1$, indicating that $R_c \ll R_h$. That is why it is required to pay attention to the load values for different measurements.

III.7.1 Experimental setup and results

Among several beam configurations, the clamped-free unimorph beam with a polymer film at the clamped end is chosen for validating the model. The parameters of the beam and the polymer film (polyurethane) is given in Table(III.3) and Table(III.4).

In the experimental setup for coefficient measurement (Fig.(III-11)), the polymer is put in series with a resistance $R_c = 1$ MΩ ($R_c \ll R_{opt} = 22.8$ MΩ as explained above) which helps to measure the current in the circuit. For the electromechanical coupling activation, the polymer is polarized by a high external voltage. The substrate is made of steel whose free end is oscillated by a magnetic coil which generates a sinusoidal magnetic force. The

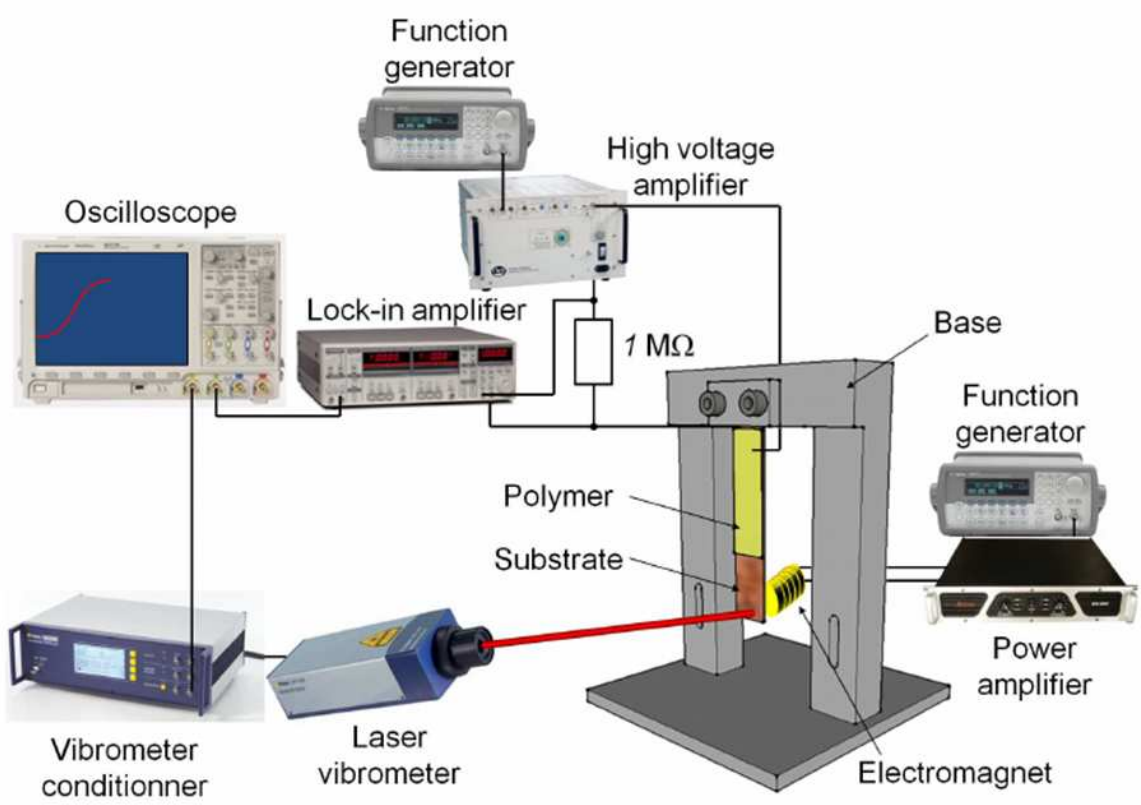

Figure III-11: Schematic of the experimental setup

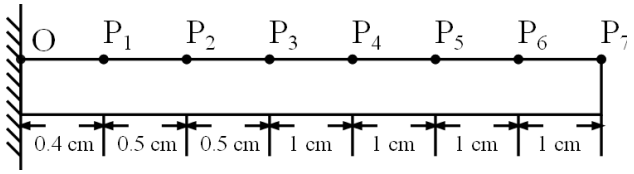

Figure III-12: Seven positions on the substrate where velocities are measured

Table III.5: Measured RMS voltages on R_c (1 MΩ) when the polymer is polarized respectively by 500 V and 1000 V

$R_c = 1$ MΩ						
V_{RMS} (mV) @ 500 V	2.474	2.552	2.559	2.625	2.574	2.645
V_{RMS} (mV) @ 1000V	5.098	4.898	5.054	4.962	5.011	4.955

magnetic coil receives a sinusoidal magnetic signal of a frequency 22.5 Hz which is close to the resonance frequency of the beam, to generate a significant vibration of the beam which still satisfies the Euler-Bernoulli conditions. A laser vibrometer is utilized to measure the velocity of the beam. The velocities at seven positions in the substrate are measured (Fig.(III-12)) with:

The system is polarized respectively by voltages of 500 V and 1000 V. The root mean square voltage V_{RMS} (V_{ac}) on R_c is measured by Agilent 10073C lock-in amplifier and reported in Table(III.5). As there are uncertainties in the measurement, for each polarization case six measurements have been recorded and the final RMS voltage is the average value. The peak values Y_{pk} measured by the laser vibrometer at seven positions are given in Table(III.6) with a sensitivity of 100 mm s^{-1} V^{-1}. The peak value of velocity is equal to the product of Y_{pk} and the velocity sensitivity (Table(III.6)). With measured voltage and velocities and according to Eq.(III.57), the experimental electromechanical coefficients at seven positions are given in Fig.(III-13).

The experimental and theoretical electromechanical coefficients have shown a generally good coincidence when the polymer is polarized respectively by 500 V and 1000 V, which is a relatively good support for the theoretical model. In addition, the product of velocity and electromechanical coefficient is constant for seven positions under two polarization cases (for

Table III.6: Peak values of velocity sensor output and corresponding velocities at the positions from P_1 to P_7

Position	P_1	P_2	P_3	P_4	P_5	P_6	P_7
Y_{pk} (mV)	40	156.250	281.25	687.5	1193.75	1725	2200
ν_{pk} (m s^{-1})	4×10^{-3}	0.0156	0.0281	0.0688	0.1193	0.1725	0.22

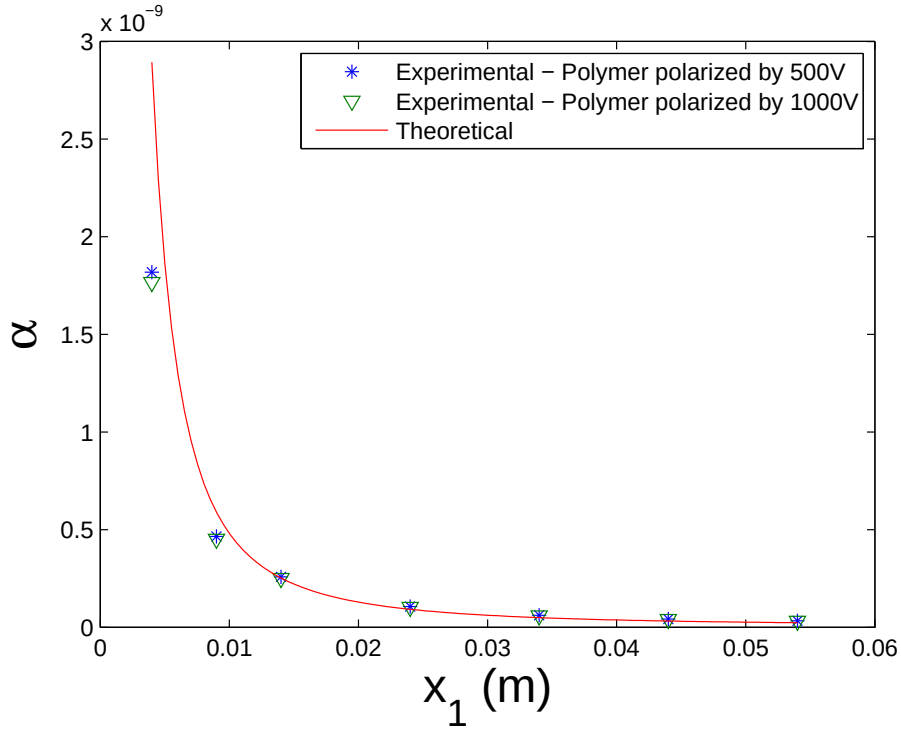

Figure III-13: Experimental and theoretical electromechanical coefficients along the beam

500 V the product is 7.2733×10^{-12} A^2 s^3 kg^{-1} m^{-2}, for 1000 V the product is 7.0659×10^{-12} A^2 s^3 kg^{-1} m^{-2}), corresponding well with the expression of coefficient α (Eq.(III.18)) - more precisely speaking, in Eq.(III.18) the product is the coefficient with displacement; as the displacement in the experiment is sinusoidal, the velocity and displacement has a linear relationship ($\|v\| = \|\omega u\|$); the constancy of αv could lead to that of αu. In Fig.(III-13) for the position nearest to the clamped end, the measurements under 500 V and 1000 V are similar, but show a relatively large difference from the theoretical result, which is possibly caused by an error in velocity measurement at point 1 as the experimental measured velocity is larger than the theoretical velocity. At point 1, the velocity is rather small and may be smaller than or approximate to the smallest precision of device, giving rise to a difference between the measurements and theoretical results. The electromechanical coefficient experiences a sharp drop from point 1 to point 3 and the reciprocal relationship between the velocity and the coefficient shown in Eq.(III.18) helps to explain this phenomenon. From position 1 to position 3 the velocity increases relatively rapidly (but always has small values, actually the oscillation of beam in the experiment is small enough to satisfy the Euler-Bernoulli theory) - small velocity leads to great coefficient value, and the tendency of velocity increase corresponds to a drop of coefficient. While from position 4 to position 7, the displacement is

Table III.7: Currents passing through the polymer when eleven progressively increasing resistances are put respectively in series with R_c

	R_1	R_2	R_3	R_4	R_5	R_6	R_7	R_8	R_9	R_{10}	R_{11}
R (MΩ)	2	5.7	11	14	16	19	26	31	46	61	91
i_{RMS} (nA)@ 500 V	0.15	0.5	0.6	0.9	1.1	1.15	1	0.85	0.7	0.52	0.37
i_{RMS} (nA)@ 1000 V	0.28	0.91	1.26	1.91	1.87	2.02	1.91	1.79	1.41	1.180	0.82
	0.31	1.07	1.35	1.99	1.96	1.98	1.94	1.81	1.42	1.20	0.85
	0.29	1.01	1.16	2.00	1.89	2.03	2.02	1.74	1.41	1.16	0.85
	0.32	1.10	1.34	1.99	1.85	2.00	2.00	1.83	1.41	1.16	0.85

larger, corresponding to greater increasing velocities, however, this great velocity constrains electromechanical coefficient to rather small values and a very small variation of α at those points. For all seven positions on the beam, the measurements under 500 V and 1000 V coincide well, which indicates that the electromechanical coefficient is independent of the polarization voltage and serves as a collateral verification for Eq.(III.18).

The value of optimal load given by Eq.(III.60) is 22.8 MΩ with $C_0 = 310$ pF and the resonance frequency to be about 22.5 Hz. Eleven resistances varying from 2 MΩ to 91 MΩ have been put in series with R_c to harvest energy, so the load R_h is equal to the sum of R_c and the resistance in series. The root mean square currents passing by the polymer for different R_h are measured by a lock-in amplifier and Agilent 10073C and listed in Table(III.7).

The experimental harvested electrical power in Fig.(III-14) is based on Eq.(III.58) with the resistance $R_h = R_c + R_i$ $(i = 1, ..., 11)$. The theoretical power calculation is based on Eq.(III.59). As explained above, the product of coefficient α and the velocity is constant along the beam, those two values are taken that measured on position P_7. The experimental results show a generally similar tendency with theoretical ones as the resistance R_h increases. However, firstly, harvested power for small resistances is clearly weaker than estimated; secondly, the optimal resistances have shifted to right for the two polarization cases. Both phenomena might be caused by measurement uncertainties but also interfacial losses which may be understood as an interfacial damping impedance Z. The impedance along with R_h becomes the R in harvested power expression (Eq.(III.59)), the actual harvested power P' becomes $P' = P\,(R_h/(R_h + Z))$. For small loads, the impedance is able to significantly reduce the harvested power; greater loads are preferable to neglect its influence, as a consequence the optimal load is larger than theoretical one. Generally speaking, despite the interfacial losses, large loads are preferable for the system; the power variation has shown an existence of optimal resistances which can help to harvest about 10 times more power

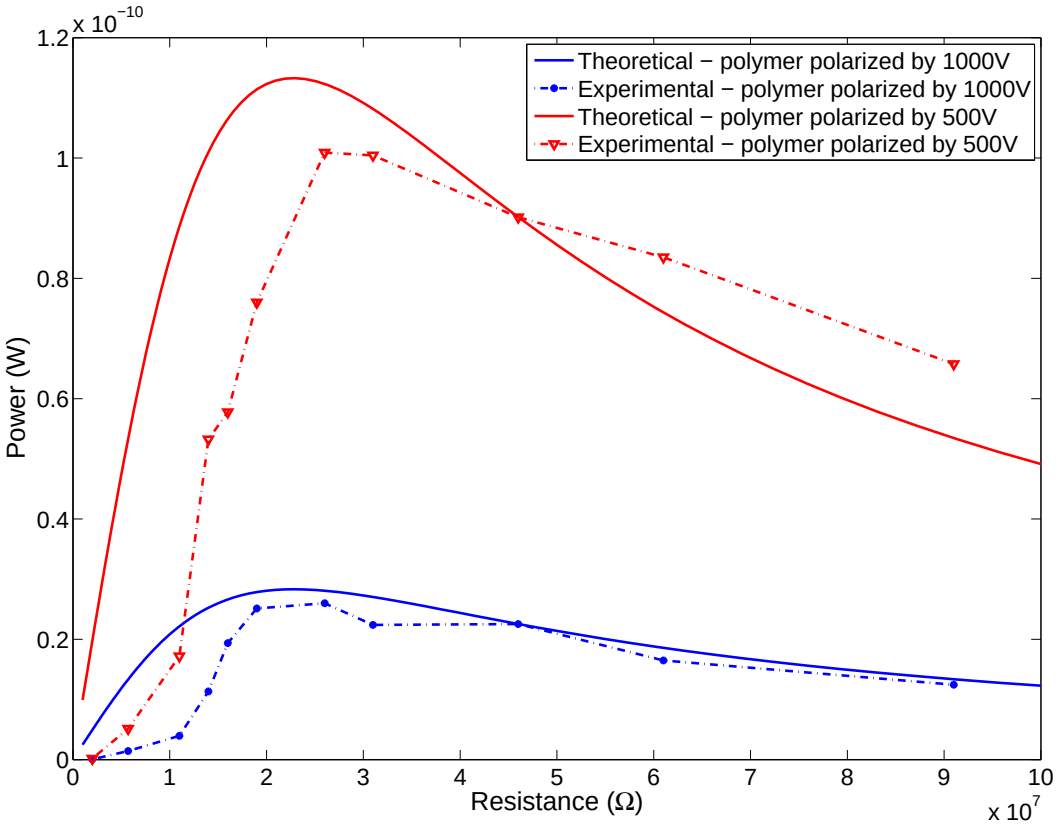

Figure III-14: Experimental and theoretical harvested power for different loads

than small loads; for loads larger than the optimal value, they could also keep a relatively significant power production compared to small loads.

III.8 Conclusion

This chapter has been devoted to the macroscopic modeling of electrostrictive generator based on a beam (a lumped model for different positions of observation). The analysis is based on energy conversion - electrical energy conversion and mechanical energy conversion. The general model was established both from the electrical aspect and the mechanical aspect. From the analysis of the two aspects, an electromechanical coefficient α was introduced to describe the electromechanical coupling of system and this coefficient is dependent on the displacement on the beam and on the variation of displacement with respect to beam length [LWR+14].

Two detailed models have been analyzed: clamped-free beam with a polymer film at-

tached at the clamped end and clamped-free bimorph beam, both with a force F exercised at the free end. In the first configuration, the electrostrictive polymer was polarized by a bias electric field; in the second configuration, the two polymers were polarized by two different bias electric fields. Through approximation of relative parameters, it is found that for both systems the electromechanical coefficient is rather slightly influenced by the applied force and electric fields, but dependent on the position on the beam and on configuration parameters. The coefficient decreases when the position on the beam is far from the clamped end.

Experimental results of the first model has shown a relatively good agreement between theoretical coefficients and experimental coefficients which were measured at seven positions on the beam for two excitation forces. Similar to theoretical results, experimental coefficients are reduced along the beam when the position gets farther from the clamped end. A series of resistances have been applied to harvest mechanical energy. For the two excitation forces, experimental results have demonstrated a shift compare with theoretical ones which is properly caused by measurement uncertainties and interfacial losses. According to the power variation tendency with respect to resistance values, optimal resistances exist which are able to increase the harvested power by $2 - 10$ times.

Chapter IV

Thermal energy harvesting using ferromagnetic materials

Besides mechanical energy, thermal energy is another omnipresent source in nature. In this chapter, a thermal energy harvesting device based on time-varying temperature is proposed. The device benefits from the drastic magnetic permeability change of soft ferromagnetic materials around the Curie temperature (the phase transition).

First characteristics of ferromagnetic materials and the principles of permeability change around the Curie temperature are introduced. Then the system composed of ferromagnetic materials, ferrite and a coil and installed in a magnetic field is introduced, following with an analysis of the energy conversion principles. Detailed conditions - the magnetic field generated by a current or by permanent magnets are introduced. The latter case has been further analyzed along with its parameters' characteristics, and a model on its electrical behavior is set up.

Theoretical trapezoidal and sinusoidal temperature variations with permanent magnets are presented. Experimentally, a temperature variation similar to partial sinusoidal shape is tested. Experimentally generated voltages and harvested power are discussed.

IV.1 Introduction

Thermal energy harvesting is usually based on thermoelectric and pyroelectric effects as introduced in Chapter I. A thermal energy generator based on ferromagnetic material has

been reported by Ujihara *et al.* [UCL07]. They have proposed an energy harvester utilizing a ferromagnetic material combined with a spring and a magnet to harvest electrical energy from thermal energy by an oscillatory movement that is then converted into electricity through piezoelectric effect. In the device, a soft ferromagnetic material is suspended on serpentine springs near a hard magnetic material as depicted in Fig.(IV-1). Initially, the soft ferromagnet is in the cold state below its Curie temperature and the hard magnetic material produces an attractive force. When the soft ferromagnet passes through the Curie point, it becomes paramagnetic and the attractive force is dramatically reduced allowing the serpentine springs to force the soft magnetic material back to contact the cold source. Once in contact with the cold source, the soft ferromagnetic material cools below Curie temperature, restoring the attractive magnetic force toward the hard magnetic material. In summary, the principles of the device is to convert spatial thermal gradient into mechanical vibration that is further converted into electricity by piezoelectric effect. Hence, in terms of energy flow, the thermal energy is first converted into mechanical energy, then into electrical energy. In this chapter, the proposed energy harvesting device also benefits from this characteristic to harvest thermal energy, but from temporal thermal gradient and without mechanical intermediate conversion stage. Before a detailed description of this energy harvesting method, a brief introduction of ferromagnetic materials is given.

IV.2 Ferromagnetic materials

IV.2.1 Characteristics of ferromagnetic materials

According to the magnetic moment under zero applied field, materials can be classified into three groups. In diamagnetic materials, this moment is zero for each atom; in param-

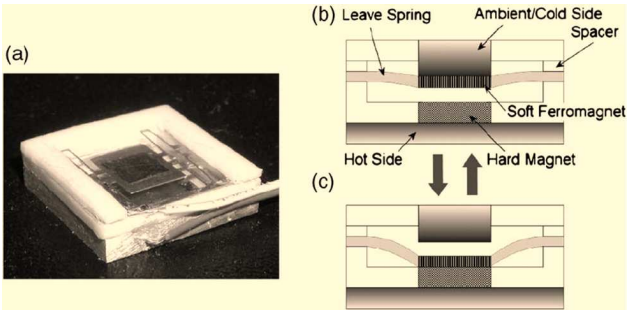

Figure IV-1: (a) Actual device, (b) cross section during cooling, and (c) cross section during heating. [UCL07]

agnetic materials this moment is non-zero for each atom, but averages to zero over many atoms; and in ferromagnets even the average is not zero. The presence of a spontaneous magnetization produced by a parallel alignment of spins is the origin of ferromagnetism. In ferromagnetic materials the magnetic moments of the individual atoms interact strongly with each other. This interaction creates a certain degree of order even in the absence of an applied field, which is the cause of a non-zero average magnetic moment under zero field.

At zero applied field, for a sufficiently high temperature the thermal fluctuations overcome the exchange interaction between the spins, thus eliminating the ferromagnetic order, leading to a vanishing spontaneous magnetization and making the material as disordered as a paramagnet. This transition point is named the Curie point (or Curie temperature) in ferromagnets.

Ferromagnetic materials demonstrate hysteresis and temperature dependence. Pierre-Weiss (1907) was able to explain the principal aspects of ferromagnetism by means of two assumptions: the existence of the molecular field and the existence of domain structure. Heisenberg contributed to the explanation of the molecular field in terms of exchange forces in 1926 [Hei26][Gho89]. Landau and Lifshitz gave the explanation of the origin of domains in terms of magnetic field energy in 1935 [LL35]. Weiss assumed that in a ferromagnetic material there exists an effective field which he called the molecular field which could be produced at the site of one spin by the interaction of neighboring spins. The interaction between them originates from the quantum-mechanical properties of spins. The intensity of the field was assumed to be proportional to the magnetization and the field was considered to align the neighboring spins against thermal fluctuations which tends to a complete disorder of these dipoles. The ensemble of non-interacting spins is subject to thermal agitation and can be magnetized only if an extremely high magnetic field is applied. Such a molecular field is sufficient to explain the temperature-dependence and the paramagnetism above the Curie point[Chi97][Aha96].

However, the model of molecular field gives rise to a constant magnetization M at any temperature below T_{Curie}. Weiss then assumed that the ferromagnets are composed of many domains to explain the unusual field-dependence. The existence of these domains may be inferred from the character of the magnetization curve itself, and it is also a well-established experimental fact observed by several techniques [CT61][CI66][SUK+90][SSW94]. Real ferromagnets at zero applied fields are subdivided into domains which are magnetized in different directions. Domain structure is a natural consequence of the various contributions to the energy - exchange, anisotropy, and magnetic - of a ferromagnetic body. The essential reason

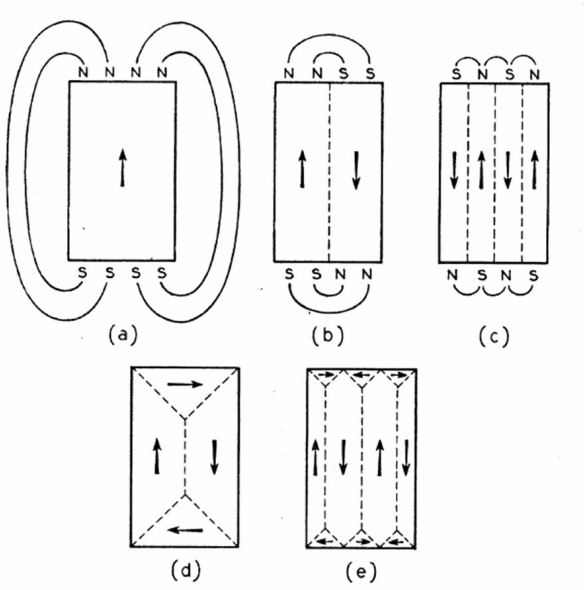

Figure IV-2: The origin of domains [Kit49]

why domains exist is that their formation in general reduces the magnetic field energy which would be associated with a saturated magnetic configuration.

The origin of domains may be understood by considering the structures in Fig.(IV-2), each representing a cross section through a ferromagnetic single crystal. In (a) we have a saturated configuration consisting of a single domain; as a consequence of the magnetic "poles" formed on the surfaces of the crystal this configuration will have a high value of the magnetic energy $1/8\pi \int H^2 dV$ (where H denotes the magnetic field and V denotes the volume of ferromagnetic material). The magnetic energy for square cross section will be of the order of $I_s \approx 10^6$ ergs cm^{-3} (1 erg $= 10^{-7}$ J); I_s denotes the saturation magnetization [Kit49].

In (b) the magnetic energy has been reduced by a factor of roughly one-half as a result of dividing the crystal into two domains magnetized in opposite directions. The subdivision process may be carried further as in (c): with N domains it turns out that the magnetic energy is reduced (because of the reduced spatial extension of the field) to approximately $1/N$ of the magnetic energy of the saturated configuration (a). It is possible to devise domain arrangements such as (d) for which the magnetic energy is zero. The extent to which the subdivision of the closure configuration (e) proceeds will depend on the energy requirements of the domains of closure. The subdivision into domains does not continue indefinitely, but does so until the energy expended in forming an additional boundary layer (domain wall) is greater than the accompanying reduction in magnetostatic energy [Kit49]. Many different

domain structures have been observed, even in the same material, applied fields and cooling from above the Curie temperature generate many new domain structures.

IV.2.2 Curie-Weiss law

The magnetization of a material, M, is defined as the magnetic moment per unit volume or per unit mass of a material. It is dependent on the individual magnetic dipole moments of the atoms in the material and on the interactions of these spins with each other. The susceptibility of a material, χ, indicates how dramatically a material responds to an applied magnetic field, and is defined as the ratio of the magnetization of the material, M, and the applied magnetic field, H (Eq.(IV.1)) [SHBS14]. Above the Curie temperature, the material becomes paramagnetic. The Curie-Weiss law describes the magnetic susceptibility χ of a ferromagnet in the paramagnetic region above the Curie point:

$$\chi = \frac{M}{H} = \frac{C}{T - T_{Curie}} \tag{IV.1}$$

where C denotes a constant. Detailed deductions may be found in the first chapter of [Aha96].

IV.3 Theoretical modeling

The most convenient parameter for describing the ease with which a soft ferromagnetic material can be magnetized by an external field H is the magnetic permeability μ, which is defined as the ratio of the flux density in the material, B, and the external field, H:

$$\mu = \frac{B}{H} \tag{IV.2}$$

It should be appreciated that μ is not a constant, but a function of the applied field H. The typical variation of μ with H is shown in Fig.(IV-3) [McC94]).

In this chapter, the soft ferromagnetic material in the model analyzed in simulation and in experiments is magnetized by a permanent magnet with quasi-constant magnetic field over the considered temperature range. The external interference is from thermal energy. So only the dependence of the magnetic permeability on the temperature, not that of the permeability on applied field, will be considered in this chapter.

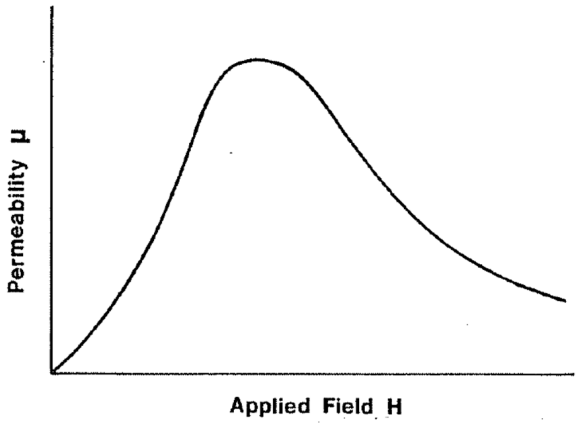

Figure IV-3: Dependence of magnetic permeability on applied field [McC94]

IV.3.1 Energy conversion principles

Before introducing the energy conversion principles, we may first have a brief understanding of magnetocaloric effect. The magnetocaloric effect is a magneto-thermo coupling phenomenon in which a temperature change occurs when a magnetic field is applied under adiabatic conditions. In an adiabatic process, under the application of an external magnetic field the external temperature increases as the domains release thermal energy as they are reorientated; when the external field is reduced, the temperature drops as the domains absorb the thermal energy due to their disorientation (thermal agitation increases) [TS03][KDA+05]. The principle applied in this chapter is in the reverse direction - a change in magnetic field induced by temperature variation.

Soft ferromagnetic materials may experience a drastic change in permeability around the Curie temperature, which relates the thermal energy with magnetic energy. Combined with an electromagnetic coupling, this characteristic could help to harvest thermal energy. Faraday's law of induction is a basic law of electromechanics and describes two phenomena: the motional electromotive force (EMF) generated by a magnetic force on a moving wire (Lorentz force), and the transformer EMF generated by an electric force due to a changing magnetic field (due to the Maxwell-Faraday equation). For the latter phenomenon, more precisely, the changing magnetic field mentioned in this phenomenon could either be referred as a result of the movement of magnet - for the magnet in motion and the conductor at rest, there arises in the neighborhood of the magnet an electric field with a certain definite energy, producing a current at the places where parts of the conductor are situated [Eo05], or be referred as the change in magnetic field itself. The thermal energy generator proposed in this chapter would like to benefit from the permeability change with temperature and from

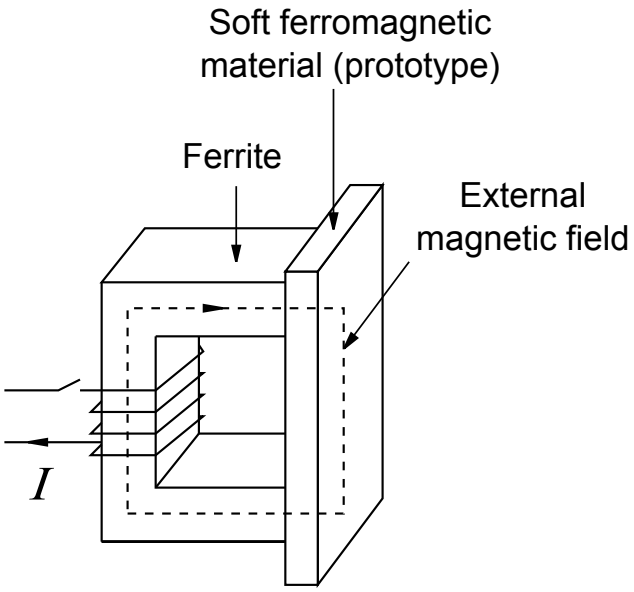

Figure IV-4: Primary design of a thermal generator

an electromagnetic coupling (the change in magnetic field itself), to harvest thermal energy.

The primary design of such a generator is that a soft ferromagnetic plate is placed in an external magnetic field, attached to a U-shape ferrite to form a loop and a coil is wound around the ferrite (as depicted in Fig.(IV-4)). The soft ferromagnetic material will either be warmed from being below the Curie point to be above it, or in the reverse direction. Power could be extracted during each process of which the physical proceeding will be introduced in the following.

Temperature of ferromagnetic material is raised from below the Curie point to above it. First, suppose the original state of the ferromagnetic material is beneath the Curie point. The external magnetic field magnetizes both the ferrite and the ferromagnetic material, and under continuous magnetization they both generate their own magnetic field B_f and B_p. Then the warming device warms the ferromagnetic material and increases its temperature to be superior to the Curie point. As mentioned above, the exchange interaction between the spins is overcome by the thermal fluctuation and the material is as disordered as a paramagnet. The application of the warming device sharply decreases the magnetic permeability, which leads to a weakening of magnetic field B_p. The moment the temperature on ferromagnetic material is raised above the Curie point, the induced magnetic flux in it experiences a considerable drop, followed with the decrease of magnetic flux in the ferrite. This is the origin of current generation in the circuit. The harvested electrical energy may

be considered as the partial conversion of varying thermomagnetic and magnetic energies in the ferromagnetic material, ferrite and this change in magnetic energy is actually from the provided thermal energy. Qualitatively, the harvested energy should not be superior to the thermomagnetic and magnetic energy variation of the system. An increase of the initial magnetic energy (the external magnetic field) will help to improve harvested energy, which will be discussed in Section (IV.4.2).

Temperature on ferromagnetic material is lowered from being above the Curie point to be below it. The original state of the ferromagnetic material is above the Curie temperature. Similar to the previous case, the external magnetic field magnetizes both the ferrite and the material. Then cooling device cools the ferromagnetic material and lowers its temperature to be below the Curie point. In the low temperature status, thermal fluctuation is largely reduced, the exchange interaction between the spins increases the locally acting field, until, at a critical Curie temperature a spontaneous magnetization occurs (P214 in [Hip95]), the material regains its ferromagnetic order and becomes ferromagnetic again, corresponding to a sudden increase of permeability which leads to an increase in the magnetic flux in ferromagnetic material followed with a general flux increase in the system, which satisfies the condition mentioned above - the change in the magnetic field itself. The current is then generated in the circuit.

In this case, no thermal energy is provided to the system, actually it is the material that provided certain amounts of thermal energy to warm the cooling device to reach the final status. The internal thermal energy has also contributed to the reorientation of spins . The harvested electrical power comes from the variation in thermomagnetic coupling energy and in magnetic energy in ferromagnetic material and should be inferior to this energy variation. When the original magnetic field B_p is enhanced (which may be caused by an enhancement of the external magnetic field), the harvested power could be increased accordingly.

A simplified equivalent system Such a system can be simplified as a model depicted in Fig.(IV-5). The ferrite and soft ferromagnetic material along with the circuit are equivalent to the conversion system which is connected with a generator-receptor system which could generate the magnetic field and harvest energy. The conversion part is put in contact either with a hot reservoir or a cold reservoir.

The thermal energy variation may be expressed as below:

$$dQ = TdS_E = C_h dT + \gamma_c T dH \tag{IV.3}$$

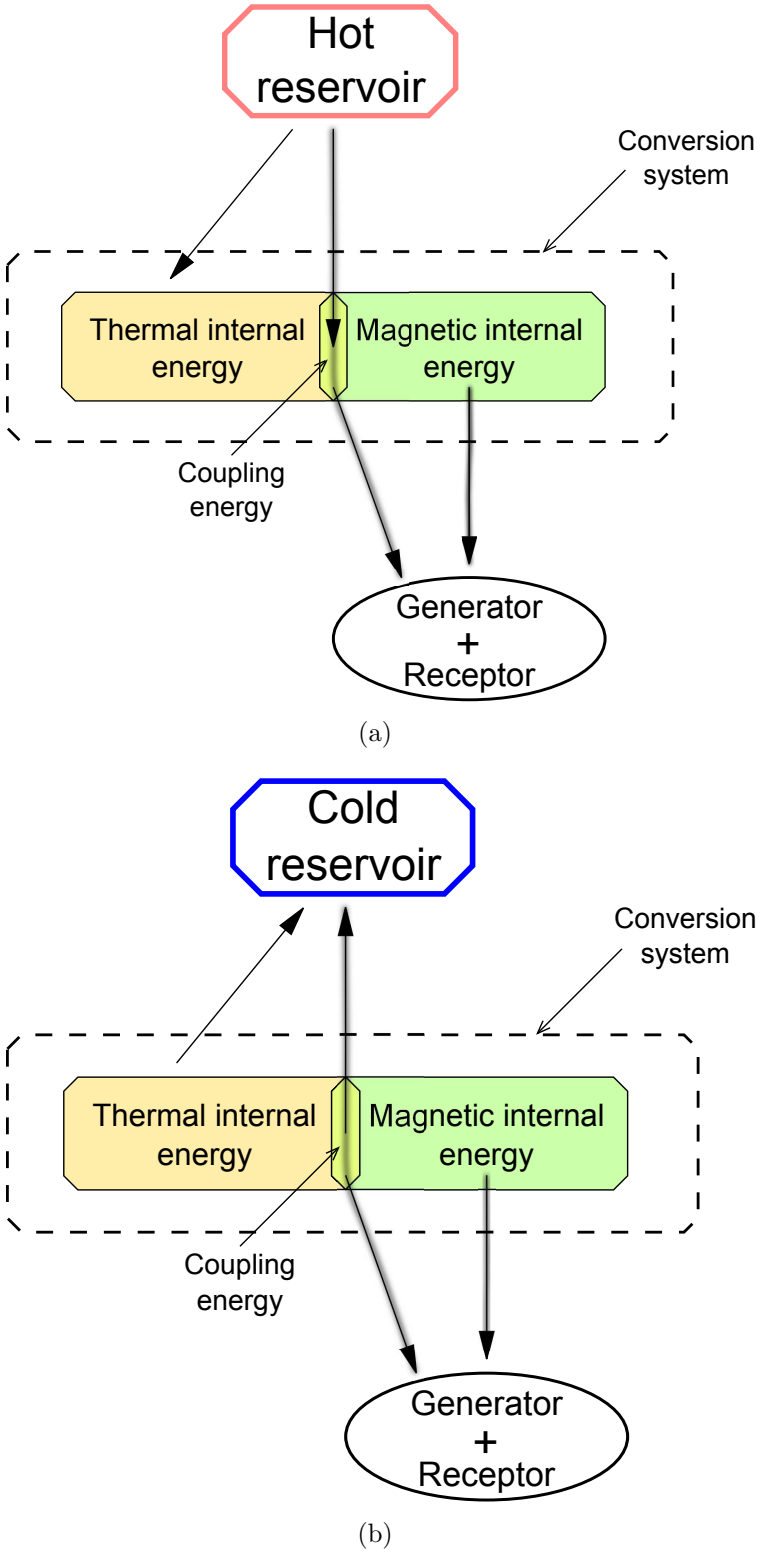

Figure IV-5: Diagram of a simple thermal energy converting system: (a) The system is warmed up (b) The system is cooled down

where Q denotes the thermal energy, S_E the entropy of system, T the temperature. C_h is the general heat capacity and γ_c is the coupling coefficient. The magnetic energy variation in the system is:

$$dW = HdB = \mu HdH + \gamma_c HdT \tag{IV.4}$$

For the two processes introduced above (temperature variation from below T_{Curie} to above T_{Curie}, or in the reverse direction), when the ferromagnetic material is warmed up (Fig.(IV-5(a))), thermal energy is transferred from the hot reservoir to the ferrite and to the ferromagnetic material, causing thermal energy variation in the conversion system ($(C_h dT)$ in Eq.(IV.3)), magnetic energy variation ((μHdH) in Eq.(IV.4)) and the variation in coupling energy ($(\gamma_c TdH)$ in Eq.(IV.3) and $(\gamma_c HdT)$ in Eq.(IV.4)). The variation in magnetic energy and coupling energy may be partially converted into electrical energy and be harvested. When the ferromagnetic material is cooled down (Fig.(IV-5(b))), thermal energy is transferred from the conversion system to the cold reservoir, correspondingly, the thermal internal energy and coupling energy is reduced. The variation in coupling energy and in magnetic energy could then be partially harvested by the generator-receptor system.

IV.3.2 Energy harvesting cycle

The generator (external magnetic field) could help to form an energy harvesting cycle depicted in Fig.(IV-6). Under the control of generator, the $B-H$ variation has followed a triangle cycle as depicted in Fig.(IV-6(a)) and the corresponding $S_E - T$ cycle is depicted in Fig.(IV-6(b)). The system is magnetized by an increasing magnetic field at a constant temperature T_1 from A to B; then the magnetic field H is held constant, at the same time the temperature is raised from T_1 to T_2, following path BC; the magnetic field H is gradually reduced to 0 (the point D coincides with A in the $B-H$ cycle); at last, the system is cooled down to T_1 (path DA).

The corresponding energy conversion system is depicted in Fig.(IV-7). Following path AB, the generator generates a magnetic field to magnetize the system from $H_1 = 0$ to H_2, at the same time the temperature on the system is held constant. As mentioned in the magnetocaloric effect, the application of an external magnetic field will lead to an increase in temperature and this part of thermal energy is transferred to the thermal source which is actually at a low temperature. Then the temperature of the thermal source is increased from a cold temperature T_c to a hot temperature T_h (following path BC), thermal

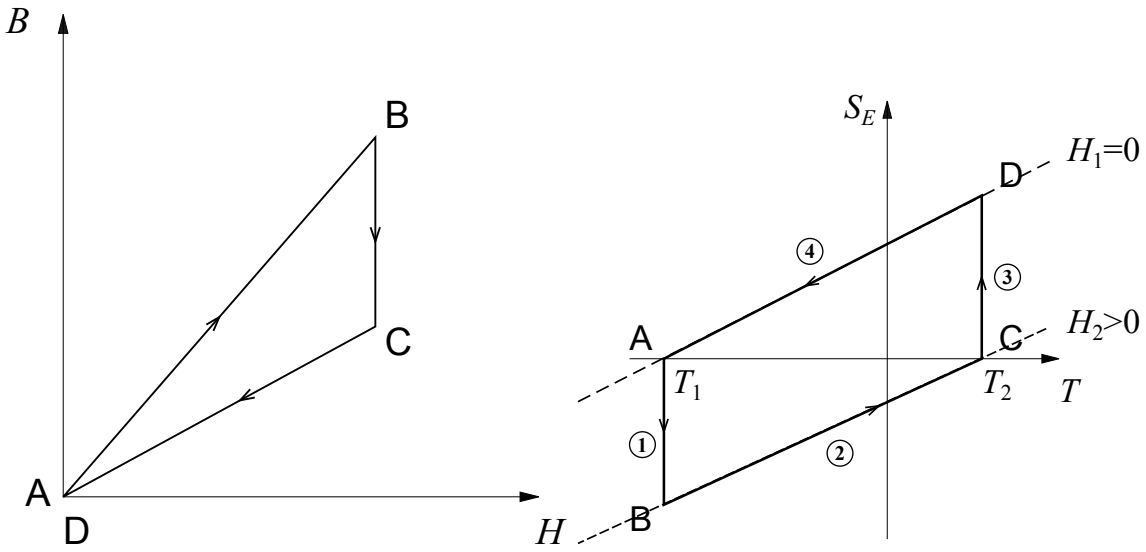

(a) B-H variation cycle (b) S-T variation cycle

Figure IV-6: Magnetic energy harvesting cycles

energy is transferred from the thermal source to the conversion system, inducing variations in the thermomagnetic coupling energy and the magnetic energy which are harvested by the generator-receptor part. When the magnetic field is eliminated and energy is returned to the generator, again because of magnetocaloric effect, the temperature on the conversion system is reduced and the system absorbs thermal energy from the thermal source which is actually in a high temperature status. At last, following path DA, the temperature of thermal source is decreased from T_h to T_c and thermal energy provided to the conversion system is returned to the thermal source.

The time-varying thermal source presented in Fig.(IV-7) may be interpreted as one thermal source containing two reservoirs (hot and cold) and each one is in contact with the conversion system in different periods of time. We may observe that, in step 1 (path AB), energy flows from the generator-receptor system to the temporarily cold source; in step 2 and 3 (path BC and CD), energy flows from the temporarily hot source to the generator-receptor system (while the energy flows in two steps are caused by different reasons); in step 4, there is only energy exchange between the temporarily cold reservoir and the conversion system.

Such an energy harvesting cycle may be formed with the aid of a circuit as depicted in Fig.(IV-9). The generator is electric circuit 1, the receptor is electric circuit 2 in which a load may be connected to harvest energy.

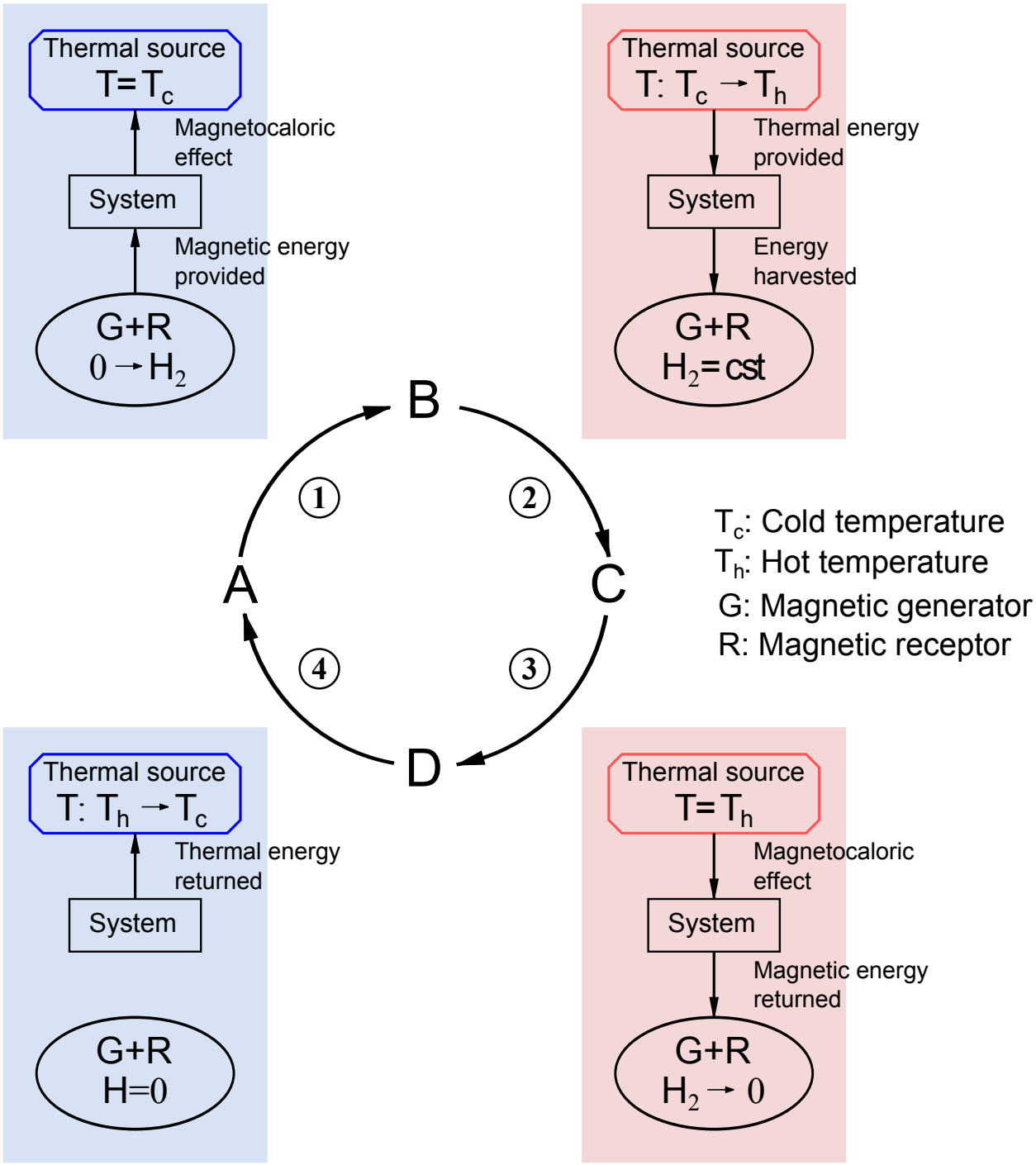

Figure IV-7: Four steps of thermal energy harvesting system in one cycle

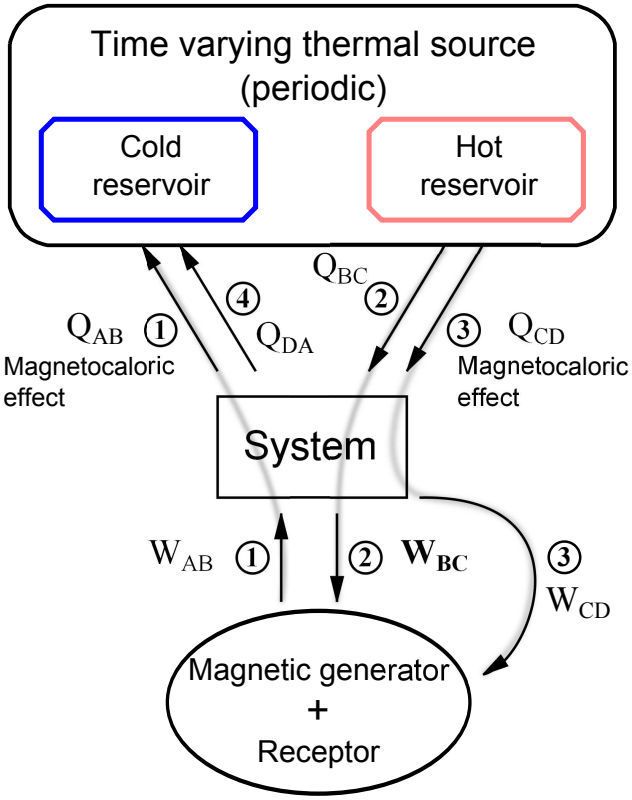

Figure IV-8: Thermal harvesting system for four steps in the cycle (Fig.(IV-6))

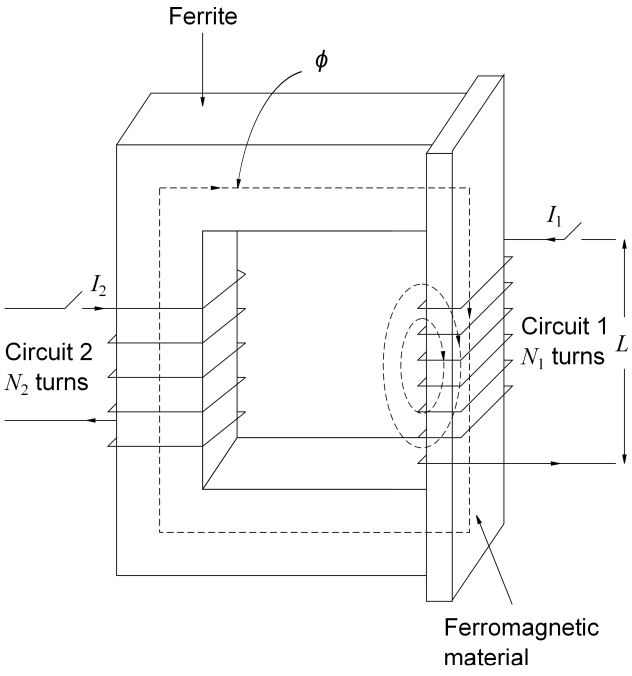

Figure IV-9: The system with two circuits and without magnet

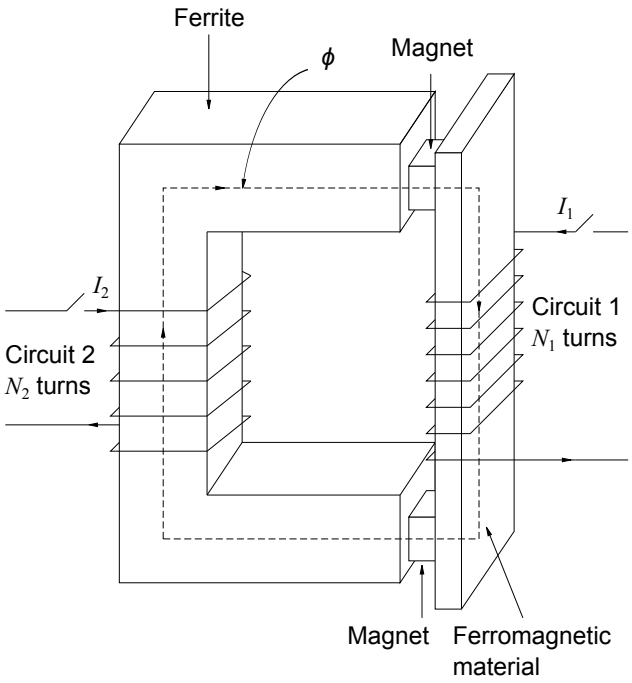

Figure IV-10: Schematic diagram of energy harvesting system

IV.3.3 External magnetic field by a permanent magnet

The generator may also be a passive source - a permanent magnet. In this section, the external magnetic field is provided by a permanent magnet, while the circuit 1 will be kept at first as a possible regulation for the magnetic flux in the ferromagnetic field. The configuration is slightly modified: two magnets are added at two ends of ferrite to be the origin of a bias magnetic field which exists in the magnet, the ferrite and the ferromagnetic material (Fig.(IV-10)). The magnetic field in the magnet is:

$$B_a = B_r + \mu_a H_a \tag{IV.5}$$

where B_a stands for the magnetic flux density in a magnet, μ_a its magnetic permeability, H_a its magnetic field strength and B_r the remnant magnetization of permanent magnet materials (P5 in [McC94]) . The magnetic field in the ferrite is:

$$B_f = \mu_f(T) H_f \tag{IV.6}$$

where B_f stands for the magnetic flux density in the ferrite, μ_f its magnetic permeability

and H_f its magnetic field strength. The magnetic field in the ferromagnetic material is:

$$B_p = \mu_p H_p \tag{IV.7}$$

where B_p stands for the magnetic flux density in the ferromagnetic material, μ_p its magnetic permeability and H_p its magnetic field strength.

Based on the analysis in the previous section, the energy harvesting model could be based on the oscillation of magnetic field in the ferromagnetic material either caused by temperature variation or by Circuit 1, inducing a chain reaction in both magnet and ferrite. To know the influence of permeability change on the system caused by temperature variation, analysis of the magnetic flux in the system has been made. According to Gauss' law for magnetism, the equality among the magnetic flux in the ferrite, the magnet and the ferromagnetic material leads to:

$$B_a S_a = B_f S_f = B_p S_p = \phi \tag{IV.8}$$

Applying Ampère's law to the above equation:

$$N_1 I_1 + N_2 I_2 = H_a l_a + H_f l_f + H_p l_p \tag{IV.9}$$

where N_1, N_2 denote respectively the number of turns of two circuits, l_a, l_f, l_p are respectively the lengths of the magnet, ferrite and ferromagnetic material. Consider at the moment of temperature variation there is no current yet passing the circuit cycling the ferrite or the ferromagnetic material. The magnetic field in the magnet, the ferrite, and in the ferromagnetic material is:

$$H_a l_a + H_f l_f + H_p l_p = NI = 0$$

Based on equations above, we get:

$$B_a = B_r + \mu_a \left(-\frac{l_f}{l_a}\frac{S_a}{S_f}\frac{B_a}{\mu_f} - \frac{l_p}{l_a}\frac{S_a}{S_p}\frac{B_a}{\mu_p} \right) \tag{IV.10}$$

which leads to:

$$B_a = \frac{B_r}{\left(1 + \dfrac{l_f S_a \mu_a}{l_a S_f \mu_f}\right) + \dfrac{\mu_a S_a l_p}{S_p l_a}\dfrac{1}{\mu_p}} \tag{IV.11}$$

For linear, non-dispersive materials (such that $B = \mu H$ where μ is frequency-independent),

the energy density is:

$$E = \frac{\mathbf{B}\cdot\mathbf{H}}{2} = \frac{\mathbf{B}\cdot\mathbf{B}}{2\mu} = \frac{\mu\mathbf{H}\cdot\mathbf{H}}{2} \tag{IV.12}$$

The magnetic energy in the magnet is then described as:

$$\begin{aligned} E_{ma} &= \frac{B_a^2}{2\mu_a} \\ &= \frac{B_r^2}{2\left[\left(1+\frac{l_f S_a \mu_a}{l_a S_f \mu_f}\right)+\frac{\mu_a S_a l_p}{S_p l_a}\frac{1}{\mu_p}\right]^2 \mu_a} \end{aligned} \tag{IV.13}$$

The magnetic field in the soft ferromagnetic material is:

$$B_p = \frac{S_a}{S_p}B_a = \frac{B_r}{\left(\frac{S_p}{S_a}+\frac{l_f S_p \mu_a}{l_a S_f \mu_f}\right)+\frac{\mu_a l_p}{l_a}\frac{1}{\mu_p}} \tag{IV.14}$$

while the magnetic energy in the prototype is:

$$\begin{aligned} E_{mp} &= \frac{B_p^2}{2\mu_p} \\ &= \frac{B_r^2}{2\left[\left(\frac{S_p}{S_a}+\frac{l_f S_p \mu_a}{l_a S_f \mu_f}\right)+\frac{\mu_a l_p}{l_a}\frac{1}{\mu_p}\right]^2 \mu_p} \\ &= \frac{1}{2}\frac{B_r^2}{\left(\frac{S_p}{S_a}+\frac{l_f S_p \mu_a}{l_a S_f \mu_f}\right)^2 \mu_p + \left(\frac{\mu_a l_p}{l_a}\right)^2 \frac{1}{\mu_p} + 2\left(\frac{S_p l_p}{S_a l_a}\mu_a + \frac{S_p l_p l_f}{S_f l_a^2}\frac{\mu_a^2}{\mu_p}\right)} \end{aligned} \tag{IV.15}$$

As the temperature increases, the permeability of ferrite μ_p is reduced, accordingly: the magnetic fields B_a and B_f are enhanced; the magnetic energy in the magnet E_{ma} increases. The magnetic energy in the prototype E_{mp} depicted in Fig.(IV-11), theoretically, will reach its maximum at:

$$\mu_p^{\text{opt}} = \frac{S_a S_f l_p \mu_f}{S_p S_f l_a \mu_f + S_a S_p l_f \mu_a}\mu_a \tag{IV.16}$$

It is possible to understand the change in magnetic field B_p with Eq.(IV.14), but it is difficult to determine the precise magnetic energy variation in the prototype. At the moment of temperature variation, the permeability μ_p determines the change in magnetic energy in the

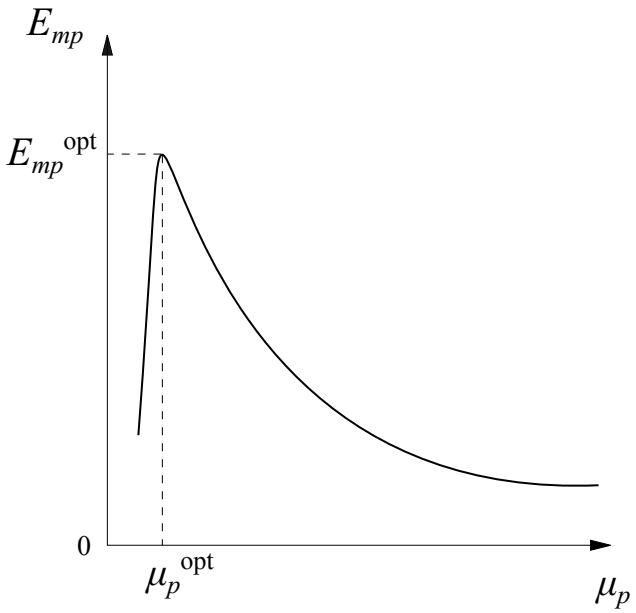

Figure IV-11: The relation between the magnetic energy in the prototype and its magnetic permeability

prototype. However, it is still possible to have a general view of energy flux in the whole system.

The harvested energy in such a system could be predicted by calculating the voltage generated in the conversion system. By combination of Eq.(IV.8) and Eq.(IV.9), a relation between the magnetic flux and currents is established:

$$\left[\frac{l_a}{S_a\mu_a}+\frac{l_f}{S_f\mu_f}+\frac{l_p}{S_p\mu_p(T)}\right]\phi = N_1I_1+N_2I_2+\frac{l_aB_r}{\mu_a} \tag{IV.17}$$

With the reluctance of the system $\mathcal{R}$ equal to

$$\mathcal{R}(T)=\frac{l_a}{S_a\mu_a}+\frac{l_f}{S_f\mu_f}+\frac{l_p}{S_p\mu_p(T)} \tag{IV.18}$$

the magnetic flux ϕ can also be expressed as:

$$\phi=\frac{N_1I_1}{\mathcal{R}(T)}+\frac{N_2I_2}{\mathcal{R}(T)}+\frac{l_aB_r}{\mu_a}\frac{1}{\mathcal{R}(T)} \tag{IV.19}$$

The voltage on the passive load $V=-N_2\dfrac{d\phi}{dt}$ (the electromotive force $\mathcal{E}$) could therefore

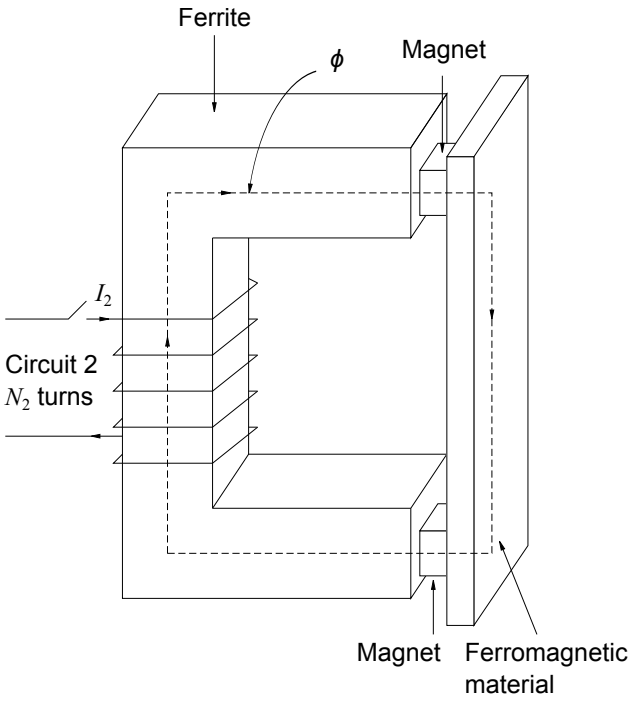

Figure IV-12: Schematic diagram of energy harvesting system

be expressed as following:

$$V = \frac{N_1 N_2 I_1}{\mathcal{R}^2(T)} \frac{d\mathcal{R}(T)}{dt} - \frac{N_1 N_2}{\mathcal{R}(T)} \frac{dI_1}{dt} + \frac{N_2^2 I_2}{\mathcal{R}^2(T)} \frac{d\mathcal{R}(T)}{dt} - \frac{N_2^2}{\mathcal{R}(T)} \frac{dI_2}{dt} + \frac{N_2 l_a B_r}{\mu_a} \frac{1}{\mathcal{R}^2(T)} \frac{d\mathcal{R}(T)}{dt} \quad \text{(IV.20)}$$

As mentioned above, Circuit 1 in the system has a role to regulate the energy harvesting cycle, the magnetic flux pattern, etc., which means this circuit is an external electrical interference. In this chapter, we would like to concentrate on the thermal influence on energy harvesting, so Circuit 1 is removed (Fig.(IV-12)) (no electrical external interference) and the voltage of the second load becomes

$$V = \frac{N_2^2 I_2}{\mathcal{R}^2(T)} \frac{d\mathcal{R}(T)}{dt} - \frac{N_2^2}{\mathcal{R}(T)} \frac{dI_2}{dt} + \frac{N_2 l_a B_r}{\mu_a} \frac{1}{\mathcal{R}^2(T)} \frac{d\mathcal{R}(T)}{dt} \quad \text{(IV.21)}$$

Consider the load in Circuit 2 R_0 ($I_2 = \frac{V}{R_0}$), then the voltage only depends on one variable - the system reluctance $\mathcal{R}$.

$$\frac{dV}{dt} = \left[\frac{1}{\mathcal{R}(T)} \frac{d\mathcal{R}(T)}{dt} - \frac{R_0 \mathcal{R}(T)}{N_2^2} \right] V + \frac{l_a R_0}{N_2 \mu_a} \frac{1}{\mathcal{R}} \frac{d\mathcal{R}(T)}{dt} \quad \text{(IV.22)}$$

Table IV.1: Phytherm55 ($Ni_{30}Fe$) with $T_{Curie} = 55\,°C$ (ArcelorMittal)

	Hard	Annealed
B (100Oe) at -20 °C(Gauss)	4000-5000	4500-5500
B (100Oe) at 0 °C(Gauss)	2750-4000	3500-4500
B (100Oe) at 20 °C(Gauss)	1750-3000	2250-3250
B (100Oe) at 40 °C(Gauss)	750-1750	1000-1750
B (100Oe) at 60 °C(Gauss)	≤ 1000	≤ 750

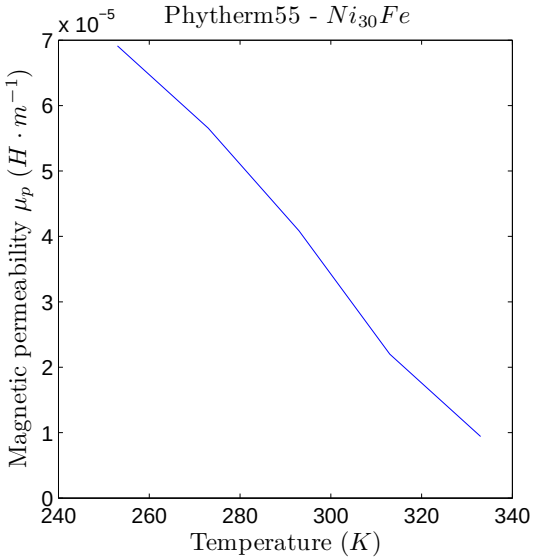

Figure IV-13: The variation of magnetic permeabilty to temperature for $Ni_{30}Fe$

IV.3.4 Approximation for one circuit with magnet

The variable $\mathcal{R}(T)$ adds the difficulty in solving Eq.(IV.22). A possible simplification for the solution of this equation is realized through a simplification of the reluctance. First, an analysis of this variable is necessary. Look back to Eq.(IV.18), the reluctance is determined by the characteristics of the ferromagnetic material (the permeability dependence on the temperature). The ferromagnetic material utilized in this chapter is $Ni_{30}Fe$, also named phytherm55. The data provided by ArcelorMittal in Table(IV.1) shows a quasi-linear relationship between the magnetic permeability and the temperature (Fig.(IV-13)). By approximation, the magnetic permeability of $Ni_{30}Fe$ depends linearly on the temperature:

$$\mu_p = k(T - T_0') \tag{IV.23}$$

k and T_0' denote the slope (negative value) and a constant of temperature. By calculation, the slope k is approximated to -7.5×10^{-7} H·m^{-1}·K^{-1} and T_0' is approximated to 345.6 K.

With the linearity between the permeability and the temperature, the reluctance of system is approximated to

$$\mathcal{R}(T) = \frac{l_a}{S_a\mu_a} + \frac{l_f}{S_f\mu_f} + \frac{l_p}{S_pk(T-T_0')} \tag{IV.24}$$

After a development in the first order of Taylor expansion, the above equation becomes:

$$\begin{aligned}\mathcal{R}(T) &\approx -\frac{l_p}{S_pk}\frac{1}{(T_1-T_0')^2}T + \left[\frac{l_p}{S_pk}\frac{2T_1-T_0'}{(T_1-T_0')^2} + \frac{l_a}{S_a\mu_a} + \frac{l_f}{S_f\mu_f}\right] \\ &= g_1T + g_0\end{aligned} \tag{IV.25}$$

where T_1 is a working temperature, and

$$\begin{cases} g_0 = \dfrac{l_p}{S_pk}\dfrac{2T_1-T_0'}{(T_1-T_0')^2} + \dfrac{l_a}{S_a\mu_a} + \dfrac{l_f}{S_f\mu_f} \\ g_1 = -\dfrac{l_p}{S_pk}\dfrac{1}{(T_1-T_0')^2} \end{cases}$$

Also developed in the first order of Taylor expansion, the reciprocal of the reluctance is approximatedy to

$$\begin{aligned}\frac{1}{\mathcal{R}(T)} \approx\ & \frac{k(T-T_0')}{k\left(\dfrac{l_a}{S_a\mu_a}+\dfrac{l_f}{S_f\mu_f}\right)T_1 + \left[\frac{l_p}{S_p} - k\left(\dfrac{l_a}{S_a\mu_a}+\dfrac{l_f}{S_f\mu_f}\right)T_0'\right]} \\ & + \frac{-k^2\left(\dfrac{l_a}{S_a\mu_a}+\dfrac{l_f}{S_f\mu_f}\right)(T_1-T_0')}{\left[k\left(\dfrac{l_a}{S_a\mu_a}+\dfrac{l_f}{S_f\mu_f}\right)T_1 + \left(\dfrac{l_p}{S_p} - k\left(\dfrac{l_a}{S_a\mu_a}+\dfrac{l_f}{S_f\mu_f}\right)T_0'\right)\right]^2}(T-T_1) \\ & + \frac{k\left[k\left(\dfrac{l_a}{S_a\mu_a}+\dfrac{l_f}{S_f\mu_f}\right)T_1 + \left(\dfrac{l_p}{S_p} - k\left(\dfrac{l_a}{S_a\mu_a}+\dfrac{l_f}{S_f\mu_f}\right)T_0'\right)\right]}{\left[k\left(\dfrac{l_a}{S_a\mu_a}+\dfrac{l_f}{S_f\mu_f}\right)T_1 + \left(\dfrac{l_p}{S_p} - k\left(\dfrac{l_a}{S_a\mu_a}+\dfrac{l_f}{S_f\mu_f}\right)T_0'\right)\right]^2}(T-T_1) \\ =\ & f_1T + f_0\end{aligned} \tag{IV.26}$$

where

$$
\begin{aligned}
f_0 \;=\; & \frac{k(T-T_0')}{k\left(\frac{l_a}{S_a\mu_a}+\frac{l_f}{S_f\mu_f}\right)T_1+\left[\frac{l_p}{S_p}-k\left(\frac{l_a}{S_a\mu_a}+\frac{l_f}{S_f\mu_f}\right)T_0'\right]} \\
& -\frac{-k^2\left(\frac{l_a}{S_a\mu_a}+\frac{l_f}{S_f\mu_f}\right)(T_1-T_0')}{\left[k\left(\frac{l_a}{S_a\mu_a}+\frac{l_f}{S_f\mu_f}\right)T_1+\left(\frac{l_p}{S_p}-k\left(\frac{l_a}{S_a\mu_a}+\frac{l_f}{S_f\mu_f}\right)T_0'\right)\right]^2}T_1 \\
& -\frac{k}{\left[k\left(\frac{l_a}{S_a\mu_a}+\frac{l_f}{S_f\mu_f}\right)T_1+\left(\frac{l_p}{S_p}-k\left(\frac{l_a}{S_a\mu_a}+\frac{l_f}{S_f\mu_f}\right)T_0'\right)\right]}T_1
\end{aligned}
$$

and

$$
\begin{aligned}
f_1 \;=\; & \frac{-k^2\left(\frac{l_a}{S_a\mu_a}+\frac{l_f}{S_f\mu_f}\right)(T_1-T_0')}{\left[k\left(\frac{l_a}{S_a\mu_a}+\frac{l_f}{S_f\mu_f}\right)T_1+\left(\frac{l_p}{S_p}-k\left(\frac{l_a}{S_a\mu_a}+\frac{l_f}{S_f\mu_f}\right)T_0'\right)\right]^2} \\
& +\frac{k}{\left[k\left(\frac{l_a}{S_a\mu_a}+\frac{l_f}{S_f\mu_f}\right)T_1+\left(\frac{l_p}{S_p}-k\left(\frac{l_a}{S_a\mu_a}+\frac{l_f}{S_f\mu_f}\right)T_0'\right)\right]}
\end{aligned}
$$

The above equations help to approximate Eq.(IV.22) to Eq.(IV.27). In the experiment which will be introduced in Section(IV.5), the temperature varies around the Curie temperature and the variation is around $30K$ which is comparably small in comparison with $T_{Curie} = 328K$.

$$
\frac{dV}{dt} = \left[g_1(f_1T+f_0)\frac{dT}{dt} - \frac{R_0}{N_2^2}(g_1T+g_0)\right]V + \frac{l_aB_rR_0}{N_2\mu_a}g_1(f_1T+f_0)\frac{dT}{dt} \tag{IV.27}
$$

$$
\frac{dV}{dt} = \left[-\frac{R_0}{N_2^2}(g_1\tilde{T}+g_0)\right]V + \frac{l_aB_rR_0}{N_2\mu_a}g_1(f_1\tilde{T}+f_0)\frac{dT}{dt} \tag{IV.28}
$$

where $\tilde{T}$ is the average value of temperature during one cycle.

In addition, an estimating of the orders of magnitude of g_0, g_1, f_0 and f_1 (the orders of magnitude are respectively 10^9, 10^6, 10^{-7} and 10^{-10}) shows that the terms related with f_0 and f_1 may be negligible compared with those related with g_0 and g_1. Those analysis lead to a further approximation of Eq.(IV.22).

Thus, after a series of simplification Eq.(IV.22) is approximated to an ordinary differential equation (ODE), which facilitates the computation when the magnetic permeability

of material follows a linear variation with a small temperature oscillation. Detailed comparisons between the original method and the simplified one will be given in the theoretical analysis (Section(IV.4)).

IV.4 Analysis for one circuit with magnet

In this section, the simulation method Runge-Kutta algorithm will be introduced and the theoretical results of harvested voltage and energy under sinusoidally and trapezoidally varying temperature will be presented and discussed.

IV.4.1 Simulation - by Runge-Kutta algorithm

There are several numerical differential equation methods to solve a differential equation including the Euler method, Runge-Kutta methods, linear multistep methods, Taylor series methods, hybrid methods, etc. Among the above methods, for solving $y' = f(x, y)$ single-step methods require only the numerical solution y_n to calculate the next value y_{n+1}, while the multistep methods may request several past values for the computation of the next one. The Runge-Kutta methods are the best known one-step methods, which originate from a generalization of the Euler method by Runge (1895). Further developments are made by Heun (1900) and Kutta (1901). Nyström (1925) has contributed to the development of first order equation methods and proposed special methods for second order differential equations. Kutta has completely characterized the set of Runge-Kutta methods of order 4 and proposed the first methods of order 5. The sixth order methods were first introduced in the work of Hu$\check{\text{t}}$a (1956, 1957).

Compared with the multistep methods, the Runge-Kutta methods utilize many more evaluations of the derivative to attain the same accuracy, which may be considered as a major disadvantage of the methods. While early studies have focused on explicit Runge-Kutta methods, interest has recently be moved to include implicit methods which are recognized as an appropriate solution for stiff differential equations[But08].

The resolution of Eq.(IV.22) will be solved numerically with the classical fourth order Runge-Kutta method (explicit). In this chapter only the methods are given, detailed deductions may be found in [AP98] (p75 - p79). The Runge-Kutta methods are applied in this chapter to solve Eq.(IV.22) and Eq.(IV.28) for voltage. As the latter equation is actually an ordinary differential equation (ODE) and may be solved by the Fourier transform, the Runge-Kutta methods are mainly for the resolution of Eq.(IV.22):

$$\frac{dV}{dt} = \left[\frac{1}{\mathcal{R}(T(t))}\frac{d\mathcal{R}(T(t))}{dt} - \frac{R_0\mathcal{R}(T(t))}{N_2^2}\right]V + \frac{l_a R_0}{N_2\mu_a}\frac{1}{\mathcal{R}}\frac{d\mathcal{R}(T(t))}{dt}$$

This equation may be expressed in a simpler form as:

$$\begin{cases} \dot{V} &= f(V,t) \\ V(t_0) &= V_0 \end{cases} \tag{IV.29}$$

where the derivative of the voltage is a function of the voltage and time, the boundary condition of voltage at time t_0 is given. Consider the numerical solution V_n at instant $t = t_n$ is already known, the formula for deduction of V_{n+1} at instant t_{n+1} is given as:

$$\begin{aligned} Y_1 &= V_n \\ Y_2 &= V_n + \frac{h}{2}f\left(t_n, Y_1\right) \\ Y_3 &= V_n + \frac{h}{2}f\left(t_{n+\frac{1}{2}}, Y_2\right) \\ Y_4 &= V_n + hf\left(t_{n+\frac{1}{2}}, Y_3\right) \\ V_{n+1} &= V_n + \frac{h}{6}\left(f\left(t_n, Y_1\right) + 2f\left(t_{n+\frac{1}{2}}, Y_2\right) + 2f\left(t_{n+\frac{1}{2}}, Y_3\right) + f\left(t_{n+1}, Y_4\right)\right) \end{aligned} \tag{IV.30}$$

It needs to pay attention that the formula above is based on an assumption that the voltage V is a function of time t, however, the problem is that the connection between them is not direct but influenced by the dependence of magnetic permeability on temperature $\mu(T)$ (Eq.(IV.18)) and $T(t)$ the variation of temperature with respect to t. For the former element, as in Table(IV.1) the relationship between the permeability and the temperature could usually be found in publications and then be applied for computation after a curve fitting, which does not cause difficulties in the iteration in Eq.(IV.30). For the latter one, in the simulation it has rather minor influence on the iteration if the temperature is pre-given as a function of time, while for calculation of experimental results with an irregularly varying temperature, it is difficult to identify a function for the application in the iteration (Eq.(IV.30)). To solve this problem, the formula Eq.(IV.29) is altered as:

$$\begin{cases} \dot{V} &= f(V,T(t)) \\ V(T(t_0)) &= V_0 \end{cases} \tag{IV.31}$$

This indicates that an iteration based on time is altered to an iteration based on temperature. Detailed operation is that all temperature variation, either pre-given curve or a curve fitting

Table IV.2: The parameters of the system containing ferromagnetic materials

Ferrite			Magnet			Prototype	
l_f (m)	S_f (m^2)	μ_f ($H{\cdot}m^{-1}$)	l_a (m)	S_a (m^2)	μ_a ($H{\cdot}m^{-1}$)	l_p (m)	S_p (m^2)
0.125	3.75×10^{-4}	10^{-3}	0.004	7.854×10^{-5}	$\sim 4\pi \times 10^{-7}$	0.035	5.5×10^{-5}

result, will be stored as a group of discrete data corresponding to a group of discrete time data. For each t_i there is a corresponding $T(t_i)$ which may be applied in Eq.(IV.30). A comparison between the altered iteration and the original one has been made respectively under a sinusoidal temperature and a trapezoidal temperature, and hardly no difference has been observed. Attention should be paid to the iteration length of time as the simulation stability is relatively sensible. For a period of 1 s, the iteration length needs to be inferior to 10^{-4} s. Other parameters might also influence the maximum iteration length like the resistance R_0, the magnetic field B_r, the permeability of magnet μ_a and the permeability of ferrite μ_f, which will be discussed in next section.

IV.4.2 Parametric analysis

The analysis of energy conversion in Section (IV.3.1) sheds light on possible parameters which may influence the harvested energy - B_r, μ_a (the magnetic permeability of magnet) and μ_f. In addition, usually the load in the circuit to harvest energy will influence final results. Consider the four parameters in another visual angle. The differential equation for the voltage (Eq.(IV.22)) can be considered as a function of the reluctance which is composed of four parameters R_0, B_r, μ_a and μ_p. The understanding of their influences on the induced voltage and harvested power will help to optimize the system performance: according to the influences of μ_f (ferrite), B_r (magnet) and μ_a (magnet), appropriate materials could be chosen as the ferrite and magnet. An optimal resistance R_{0opt} may also be applied to the system to maximize the harvested energy.

The initial parameters of the system in Fig.(IV-12) are given in Table (IV.2) (the data given here are for a primary understanding of the system, some parameters may be changed in the experiment). As mentioned above, the slope k and T_0' for describing the relationship between permeability and temperature are respectively approximated to -7.5×10^{-7} $H{\cdot}m^{-1}{\cdot}K^{-1}$ and 345.6 K. Besides, other possible constants or parameters which will be utilized are: the vacuum permeability μ_0 1.2566×10^{-6} $H \cdot m^{-1}$, the original magnetic flux density B_r set to be 0.1 T and the resistance R_0 to harvest coupling energy 1 Ω.

The analysis of parameters is made under a sinusoidal temperature variation. Its period is

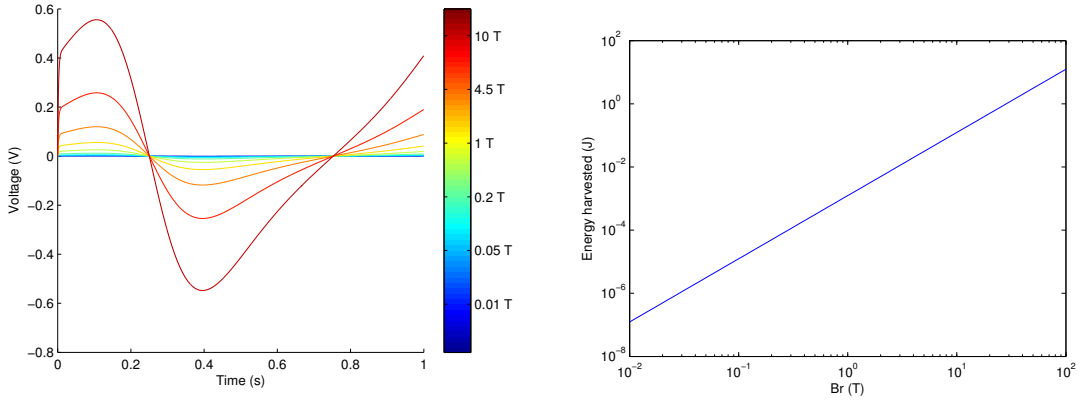

(a) Voltage under different magnetic fields

(b) Relation between the harvested energy and the magnetic field

Figure IV-14: Influence of the magnetic field B_r

1 s, the average temperature is 295 K and the amplitude is 15 K. One of the four parameters will be varied when the other three stay invariable to observe their respective influences on the average power in a period.

❖ Influence of B_r on the induced voltage

In Section (IV.3.1), it has been analyzed that the harvested power mainly comes from the magnetic energy variation $\|\Delta\mu_p H_{p0}^2\|$. An enhancement of the initial magnetic field H_{p0} clearly will help to increase the available energy. The initial field is the common effect of ferrite, ferromagnetic material and the magnet. However, the effect of magnet is much important than those of the ferrite and ferromagnetic material. To clarify this point, first consider a system with magnet and without circuit (Fig.(IV-15)). The corresponding magnetic flux is simplified from Eq.(IV.19):

$$\phi = \frac{l_a B_r}{\frac{l_a}{S_a} + \frac{l_f}{S_f}\frac{\mu_a}{\mu_f} + \frac{l_p}{S_p}\frac{\mu_a}{\mu_p(T)}} \tag{IV.32}$$

As the permeability of magnet μ_a is far less than those of soft ferromagnetic materials, the magnetic flux in Eq.(IV.32) is approximated to:

$$\phi \approx B_r S_a \tag{IV.33}$$

From the above equation, we may see that the initial magnetic flux is linear with the remnant magnetic flux density of magnet B_r. As conclusion, a hard ferromagnetic material with strong magnetic fields will generate a high initial field in the soft ferromagnetic material and

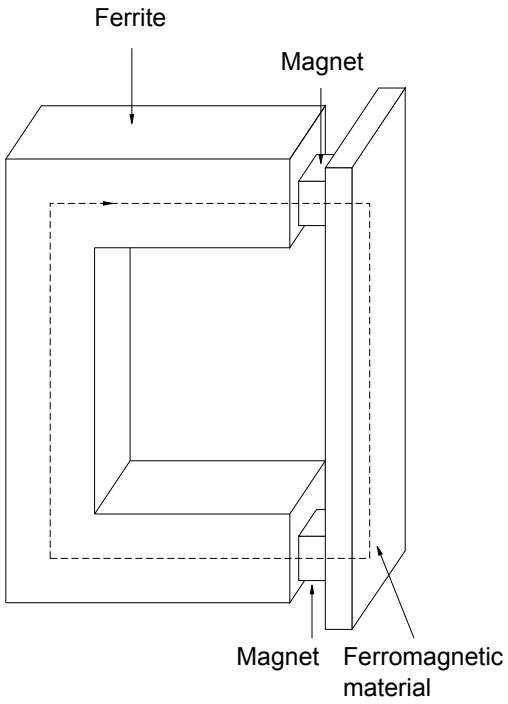

Figure IV-15: The system with magnet and without circuit

Table IV.3: Rare-earth magnets

Magnet	B_r (T)	T_{Curie} (°C)	$(BH)_{max}$ (kJ·m^{-3})
$Nd_2Fe_{14}B$ (sintered)	$1.0 - 1.4$	$310 - 400$	$200 - 440$
$Nd_2Fe_{14}B$ (bonded)	$0.6 - 0.7$	$310 - 400$	$60 - 100$
$SmCo_5$ (sintered)	$0.8 - 1.1$	720	$120 - 200$
$Sm(Co,Fe,Cu,Zr)_7$ (sintered)	$0.9 - 1.15$	800	$150 - 240$
Alnico (sintered)	$0.6 - 1.4$	$700 - 860$	$10 - 88$
Sr-ferrite (sintered)	$0.2 - 0.4$	450	$10 - 40$

provide more available energy. In reality, rare-earth magnets are capable of providing strong magnetic fields (table(IV.3)). According to calculation (Fig.(IV-14)), when the magnetic field B_r increases from 0.01 T to 100 T (it is increased 10^4 times, the magnetic field 100 T is not quite realistic and it is given to show the variation tendency of generated voltage and energy with respect to B_r), the generated voltage shows a relatively even variation tendency and the energy harvested in one cycle is in a quasi quadratic relation with the field (the harvested power is increased about 10^8 times).

❖ Influence of μ_f on the induced voltage

The analysis of the magnetic permeability of ferrite μ_f is a little more complicated to apply the same method as for B_r. The value of permeability μ_f is of magnitude 10^{-3}, while the magnitudes of μ_p and μ_a are respectively 10^{-5} and 10^{-7}. At first sight, the parameter μ_f

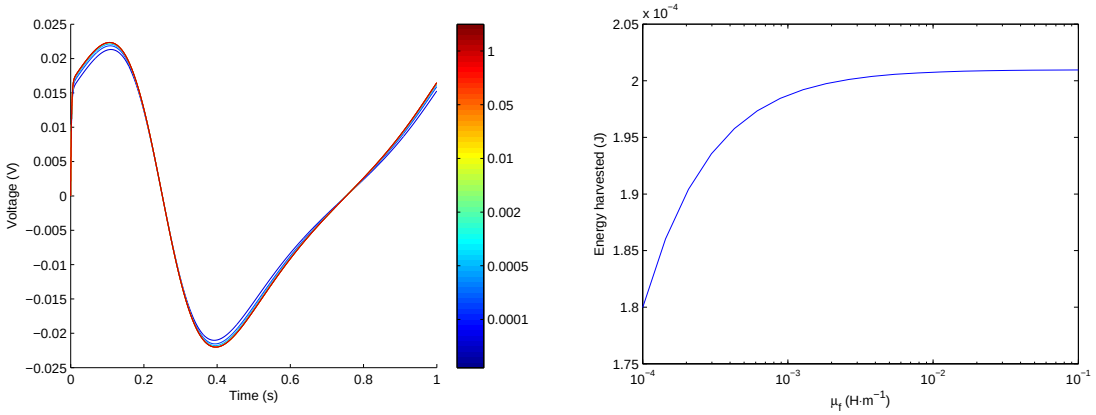

(a) Voltage under different magnetic fields (b) Relation between the harvested energy and μ_f

Figure IV-16: Influence of the ferrite μ_f

Table IV.4: Ferrite with a permeability superior to 10^{-3} H·m^{-1}

Medium	Metglas	Iron (99.95% pure (Fe annealed in H)	Nanoperm	Mu-metal
Permeability μ (H·m^{-1})	1.26	0.25	0.1	2.5×10^{-2}
Medium	Permalloy	Iron (99.8% pure)	Electrical steel	Ferritic stainless steel (annealed)
Permeability μ (H·m^{-1})	1.0×10^{-2}	6.3×10^{-3}	5.0×10^{-3}	1.26×10^{-3} - 2.26×10^{-3}
Medium	Cobalt-Iron Fe annealed in H)			
Permeability μ (H·m^{-1})	2.3×10^{-2}			

would have rather important influence on the harvested energy. According to the calculation results (Fig.(IV-16)), the generated voltage experiences rather small changes when its value is increased from 10^{-4} to 10^{-1} and the energy is increased a mere 1.11 times for a 10^3 times increase of μ_f. The harvested energy does show to be raised by the increase of μ_f, but this influence is negligible compared to that of B_r. So the choice of ferrite in the system has comparably small influence on the system. Still possible choices of ferrite are given in Table(IV.4) for materials with permeability superior to 10^{-3} H·m^{-1}.

❖ Influence of μ_a on the induced voltage

The analysis of magnetic permeability of magnet μ_a becomes a little more interesting. On one hand, through an observation of Eq.(IV.19) we may find that μ_a and μ_f have similar

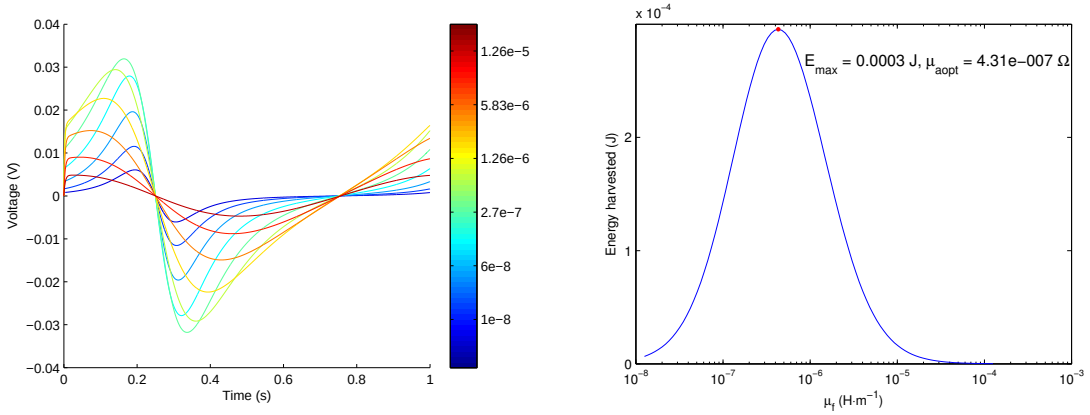

(a) Voltage under different μ_a

(b) Relation between the harvested energy and μ_a

Figure IV-17: Influence of the magnet μ_a

influence tendencies on the final results (for their similar positions in the equation). So the first deduction is made: the same as μ_f, an increase of μ_a will lead to a harvested energy increase. On the other hand, the magnetic energy variation in the prototype is largely determined by H_p which is induced by H_a with $H_a = B_r/\mu_a$. An increase of μ_a will also give rise to the weakening the magnetic field H_a and decrease the available energy. Combine the two deductions, the energy increasing ability of μ_a encounters a dramatic drop when it exceeds a certain value (the same tendency for the generated voltage). In Fig.(IV-17(b)) the optimal value of μ_a can increase the harvested energy by about 30 times compared to a small or large value. As both μ_a and B_r are parameters of magnet, a hard ferromagnetic material with strong field and moderate permeability would be a reasonable choice.

❖ Influence of R_0 on the induced voltage

In Fig.(IV-18(a)), each line represents the induced voltage under different resistances and the color from blue to red indicates an increase of resistance. When the resistance is under 1Ω, the generated voltage gradually evolves - the first extremum keeps increasing at first, then drops slowly to a constant value when the resistance exceeds a certain value (the absolute value of the first extremum is always superior to that of the second one), its second extremum decreases continuously even when the resistance reaches the certain value which causes a change of variation tendency of the first extremum (in this process, the absolute value of the second extremum approaches gradually to that of the first one); when its value exceeds 1 Ω, the voltage begins to stabilize. The voltage evolution in Fig.(IV-18(a)) helps to get a presumption that an optimal resistance may exist to maximize the harvested energy.

In Fig.(IV-18(b)), the optimal resistance is 0.0066 Ω which is rather small, corresponding

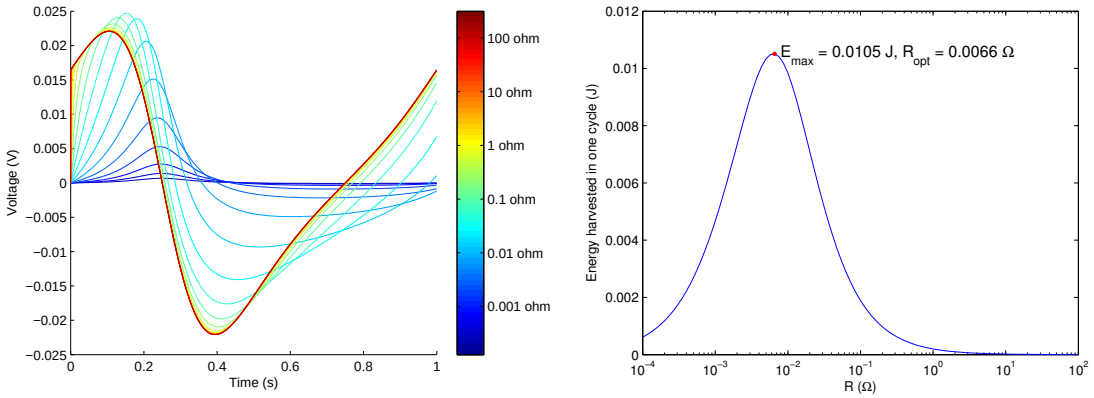

(a) The evolution of voltage with the variation of R_0

(b) Relation between harvested energycycle and R_0

Figure IV-18: Influence of the resistance R

to an optimal energy 0.0105 J. The order of magnitude of harvested energy decreases from about 100 times (from 10^{-4} J to about 10^{-6} J) when the resistance is raised from 1 Ω to 100 Ω. In reality, the optimal value of resistance varies while the other parameters change (B_r, μ_a, etc.), however, its value is usually small which is relatively difficult to fulfill in consideration of the internal resistance. In spite of this drawback, the influence of resistance still serves as a guidance for maximizing the harvested energy.

IV.4.3 Trapezoidal simulation

In this section, the temperature is in linear variation with respect to time. First, the temperature stabilizes at a low temperature, then increases linearly from a low temperature to a high temperature, stabilizes for a few seconds and decreases linearly to the same low temperature again, keeping constant at this temperature for several seconds, forming a whole cycle. The average temperature in one cycle is the Curie temperature 328 K. The amplitude varies from 330.5 K to 343 K (Fig.(IV-19)), with different slopes of ramp. The ferromagnetic prototype chosen in this chapter has a quasi linear permeability variation with respect to temperature. The characteristics of voltage are mainly given by temperature variation, which facilitates the analysis. At first, we may guess that a linear temperature variation will lead to a uniform generated voltage as the magnetic flux is linearly changed. However, the results show that the linear temperature increases corresponds with a nonlinear voltage increase. In the first place, a conjecture for this phenomenon is due to an accumulation of temperature increase, however, when the temperature begins to decrease from the high temperature (there

is no accumulation effect of temperature variation at all), the generated voltage is also high. Generally, the voltage (the electromotive force $\mathcal{E}$) induced by variation in the magnetic field is:

$$\mathcal{E} = -N\frac{d\phi}{dt} \tag{IV.34}$$

where N is the coil number and ϕ is the magnetic flux equal to BS with S the surface past by B. Then it may be assumed that this nonlinearity is actually related to the temperature value which means in a more thermally agitated status, the system tends to generate higher voltage.

We further notice that even the temperature increase starts from a smaller value (red line - 30 K in (Fig.(IV-19))), the corresponding generated voltage is greater than that with an increase from a greater value (yellow line - 25 K in (Fig.(IV-19))). The difference between them is the temperature slope, and evidently in some circumstances the temperature increasing (or decreasing) velocity has more important influences on generated voltage than the temperature value. Fig.(IV-20) has confirmed this assumption. For the same temperature amplitude, when the period is decreased from 10 s to 1 s (which means an increase of slope), the highest generated voltage shows a linear increase with the slope. It is easy to understand with Eq.(IV.34) as the same temperature variation leads to the same flux change, and this flux change generates higher voltage when it is accomplished in shorter time.

The analysis above is based on the solution of the original method (Eq.(IV.22)), the approximation method proposed in Section (IV.3.4) will be applied in the following. In Fig.(IV-21) the original results (cyan line) and approximation results (red dashed line) are given for temperature variations from 5 K to 20 K with an average temperature 328 K. The approximation solution is also dependent on the temperature slope (as the slope increases, the order of magnitude of generated voltage is raised therewith), but less dependent on the temperature value compared with the previous solution (the generated voltage shows milder increase or decrease of the velocity along with the temperature variation). This minor difference from the original solution does not cause considerable errors until the temperature becomes larger enough and may not be negligible compared to the operating point. In Fig.(IV-22), the quasi-independence of temperature value causes evident errors. The approximation method may serve as a replacement for original method under limited calculation resources or other limited conditions only when the temperature variation is relatively small compared with the average temperature.

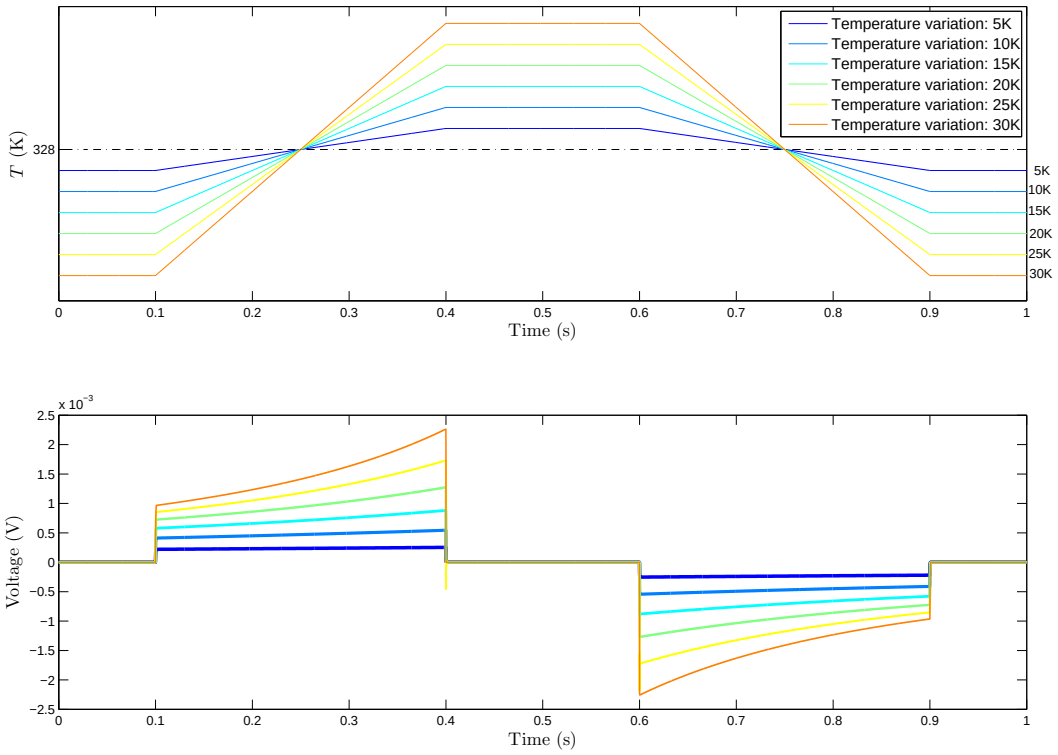

Figure IV-19: Induced voltage when the temperature varies sinusoidally with the amplitude from 5 K to 30K

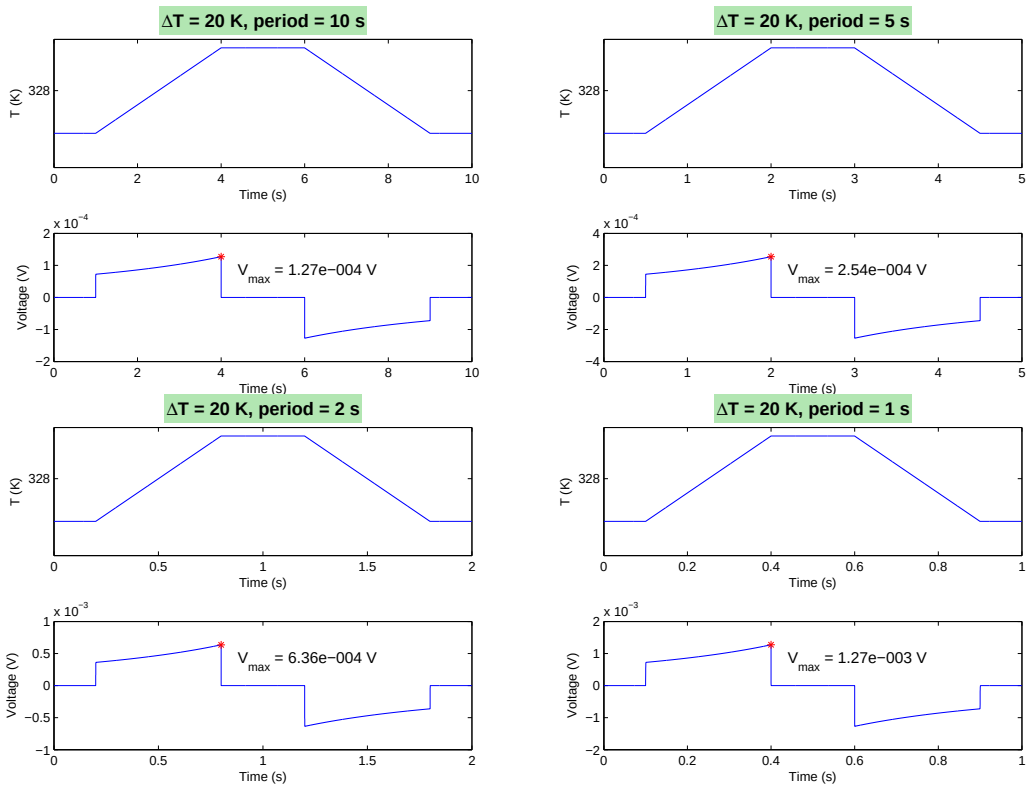

Figure IV-20: Induced voltage under several temperature variation periods

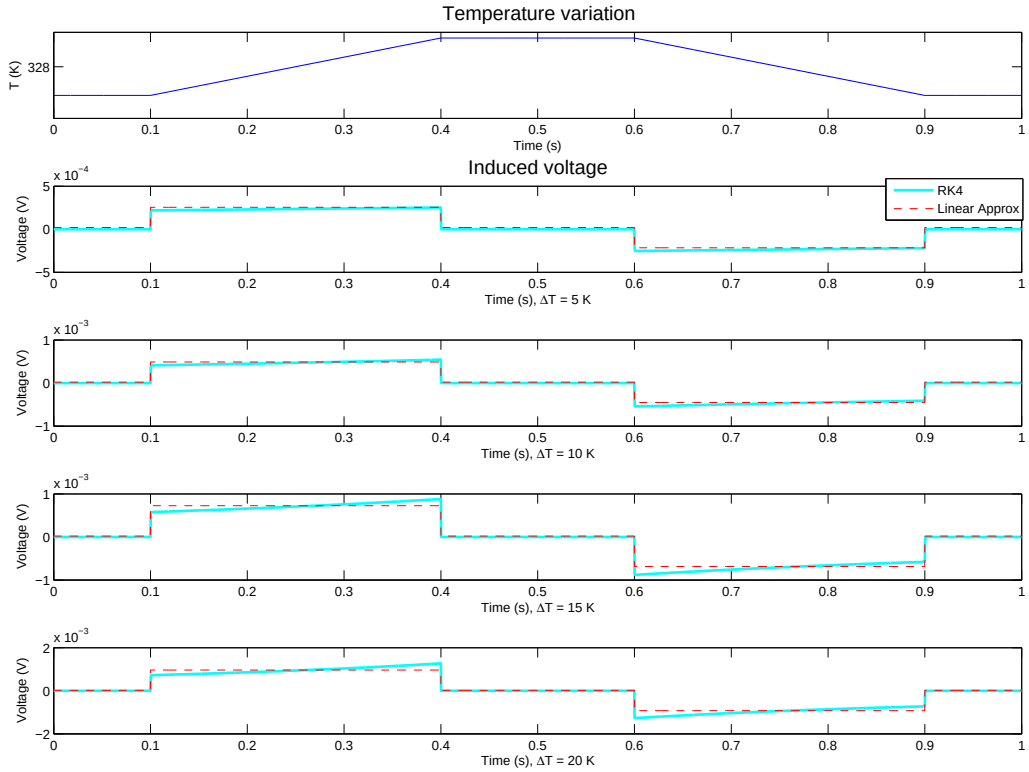

Figure IV-21: Voltage on R_0: Solutions of Eq.(IV.22) and Eq.(IV.28) with temperature variation (amplitude to amplitude) from $5K$ to $20K$

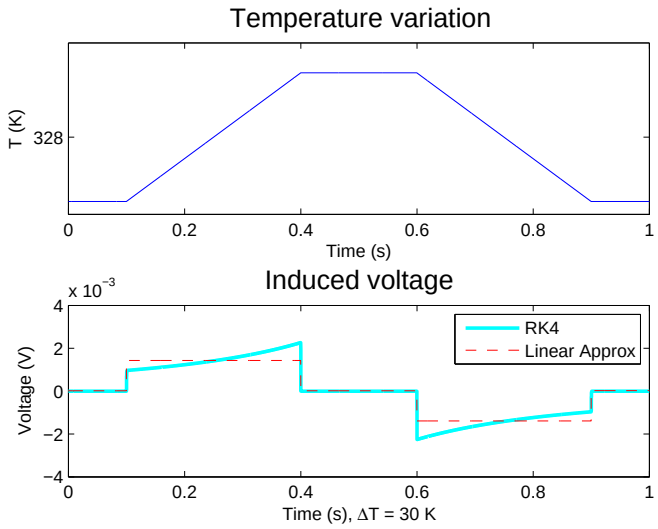

Figure IV-22: Voltage on R_0: Solutions of Eq.(IV.22) and Eq.(IV.28) with temperature variation (amplitude to amplitude) to be $30K$

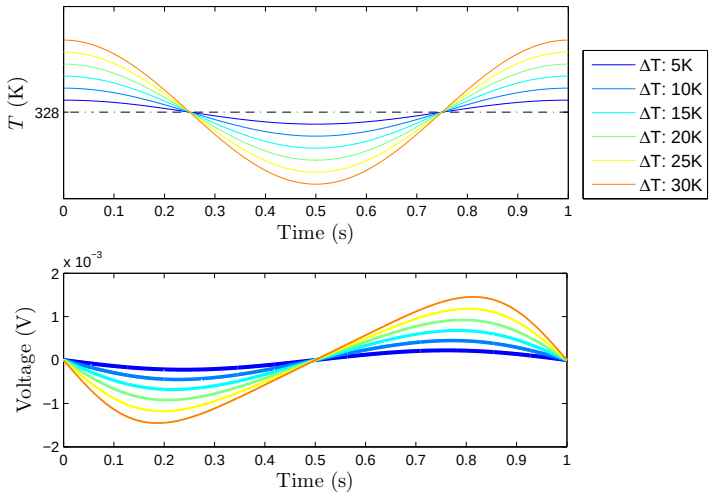

Figure IV-23: Induced voltage when the temperature varies sinusoidally with the amplitude from 5 K to 30K

IV.4.4 Sinusoidal simulation

In this section, the temperature variation is of sinusoidal form. The temperature is varied nonlinearly. The average temperature during one cycle is the Curie temperature T_{Curie} - 328 K.

In Fig.(IV-23), the temperature function is of period 1 s with amplitude from 2.5 K to 15 K. The temperature variation begins from the highest value, corresponding to a zero temperature change, so the generated voltages all begin from the same value 0 V. Highest beginning temperature and rapidest temperature change velocity lead to highest generated voltage (red line). However, unlike the trapezoidal simulation where highest temperature, velocity and generated voltage happen at the same time, the sinusoidal simulation shows a slight phase difference for the occurrence of maximum. The conjecture in the previous section may help to explain this phenomenon - the voltage is dependent on the temperature value. Consider the first quarter period where the absolute value of slope increases with a decrease of temperature. As higher slope leads to higher voltage, the absolute value of voltage keeps increasing at first; at the same time, the decrease of temperature weakens the voltage rise. The combination effect of these two factors make happen an appearance in advance of the maximum voltage. Similarly, in the last quarter period, normally the maximum voltage occurs at the highest slope (0.75 s), while the temperature increase also contributes to voltage rise and delays the maximum voltage.

The influence of temperature change velocity has been shown in Fig.(IV-24) where the

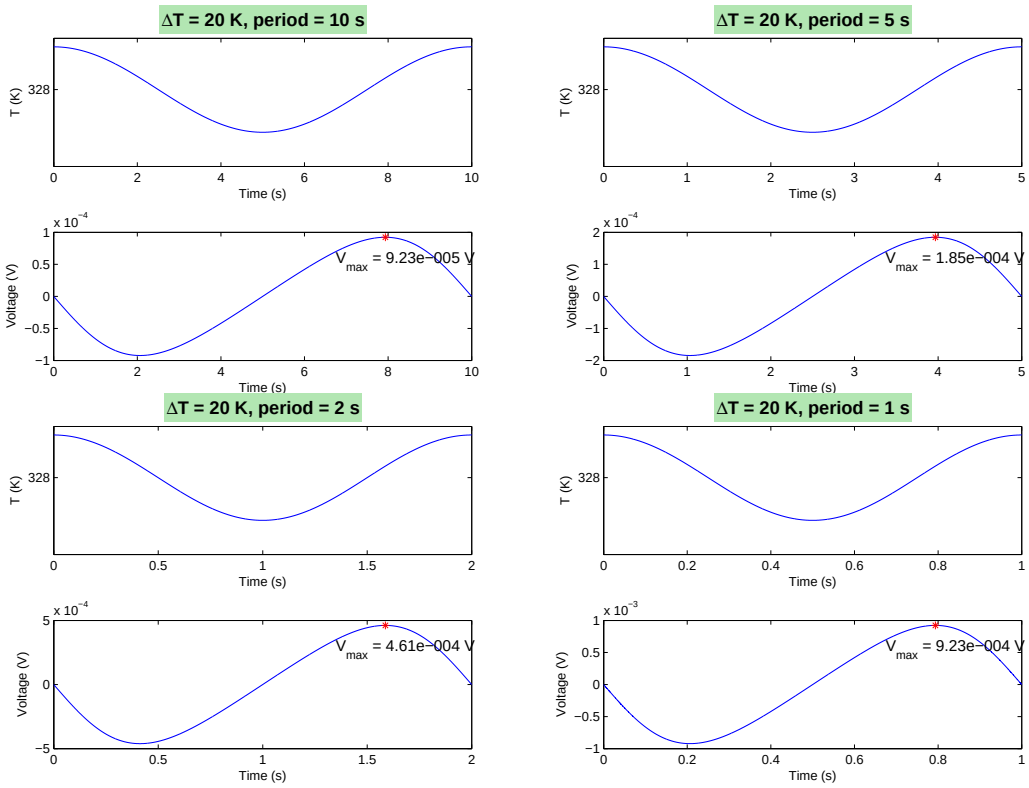

Figure IV-24: Induced voltage under several temperature variation periods

period is reduced from 10 s to 1 s (an increase of slope). Like in the trapzoidal simulation, the maximum voltage also shows a linear increase with the slope as faster magnetic flux change will induce higher voltage.

The application of approximation method in Fig.(IV-25) demonstrates the dependence of generated voltage on temperature change velocity remains while that of voltage on temperature value is waned. With the basic assumption of approximation method - temperature variation is negligible compared to the average temperature, results of the two methods coincide relatively well in Fig.(IV-25). The difference of the two results magnifies with temperature amplitude: when the temperature variation increases to 30 K, as shown in Fig.(IV-22) the phase difference characteristic in approximated results almost vanishes, causing an inevitable error.

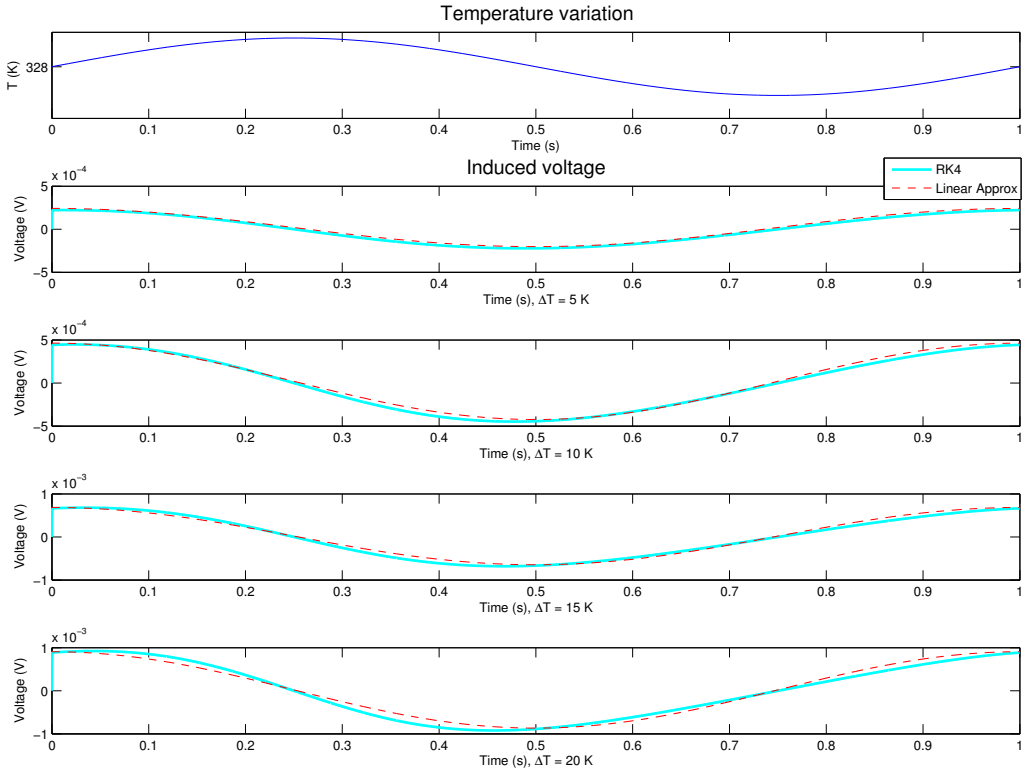

Figure IV-25: Voltage on R_0: Solutions of Eq.(IV.22) and Eq.(IV.28) with temperature variation (amplitude to amplitude) from $5K$ to $20K$

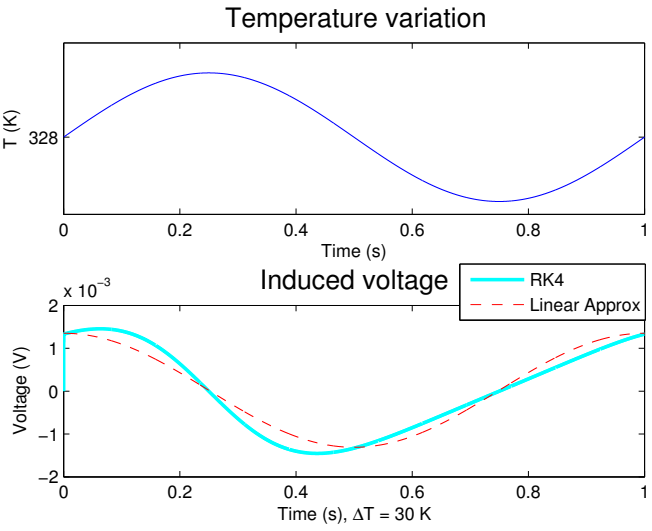

Figure IV-26: Voltage on R_0: Solutions of Eq.(IV.22) and Eq.(IV.28) with temperature variation (amplitude to amplitude) to be $30K$

IV.4.5 Influence of temperature variation velocity on the voltage

As explained in Section (IV.3.1), the magnetic energy of the system goes through a series of changes during the cycle and those changes give rise to a variation of magnetic flux Φ which according to Faraday's law (Eq.(IV.34)) induces the voltage. According to the equation, a faster magnetic flux variation, i.e. a faster temperature change will induce higher voltage. In previous two sections, in both trapezoidal and sinusoidal simulations generated voltage has shown a dependence on the temperature change velocity. A more detailed analysis of this dependence is presented in this section.

In Fig.(IV-27), the temperature is stable at first, then experiences a decrease which follows a certain sinusoidal function (one half period), and stabilizes at a low temperature in the end. During the temperature decrease, the derivative of temperature with respect to time firstly decreases to a minimum value, then raises back to zero at the same speed; correspondingly, the voltage decreases to a peak value and rises again to zero and this variation is not all symmetrical to the peak value (the phase difference mentioned in previous section). The objective of such a temperature change definition is for the same temperature variation and different slope which could guarantee that the change in magnetic flux ϕ is of the same quantity but the changing time differs; as shown in Fig.(IV-28), the minimum generated voltage is quasi linear with the temperature change velocity. This gives a direct view of influence of slopes: the same magnetic energy change happens in different time range, certainly gives rise to different voltages. Such a design is also a preparation for experimental analysis as in the experiment, the temperature will experience a similar trajectory.

IV.5 Experimental results and discussion

As mentioned in Section (IV.3.4), the ferromagnetic prototype is the Ni-Fe alloy - $Ni_{30}Fe$, also named Phytherm55 with the Curie point to be 55 °C and a quasi linear varying permeability with respect to temperature.

As shown in Fig.(IV-29), two round magnets are attached at two ends of the ferrite, the ferromagnetic prototype $Ni_{30}Fe$ made in square plate shape is attached to the two magnets. A resistance R is connected in the coil with 500 turns to harvest energy and the voltage on the load is demonstrated in an oscilloscope. A thermocouple is attached to the ferromagnetic material to detect the temperature. The parameters of the system are already given in previous section (Table (IV.2)). The prototype could be warmed up by an air heater or cooled down by the compressed air within a temperature range from about 60 °C to about

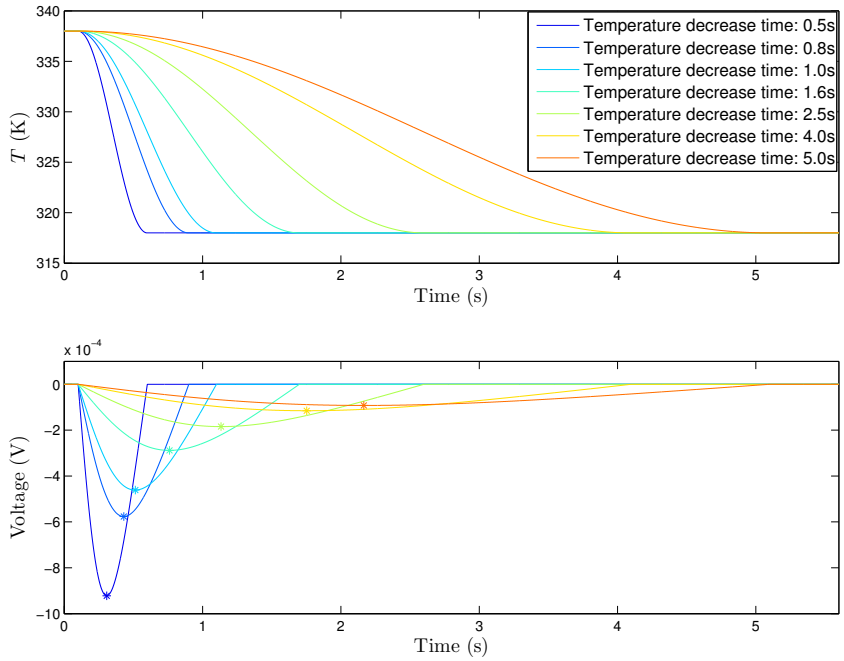

Figure IV-27: Temperatures with different slopes and corresponding voltages

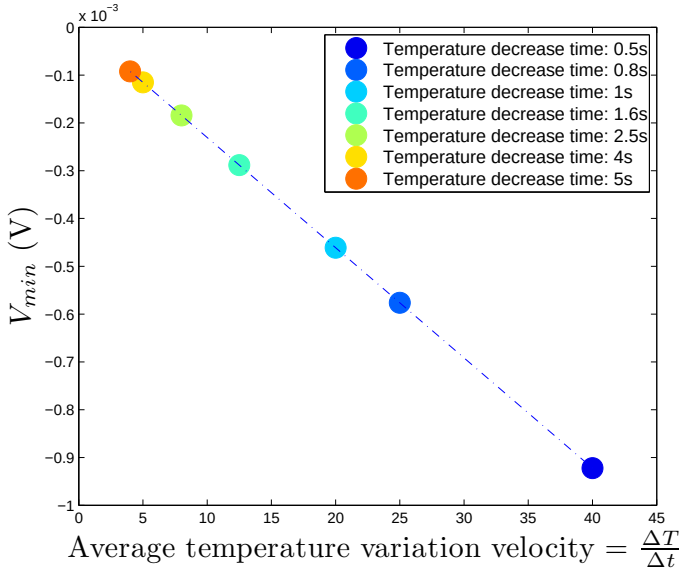

Figure IV-28: Relation between the average slope of temperature variation and the peak value of generated voltage

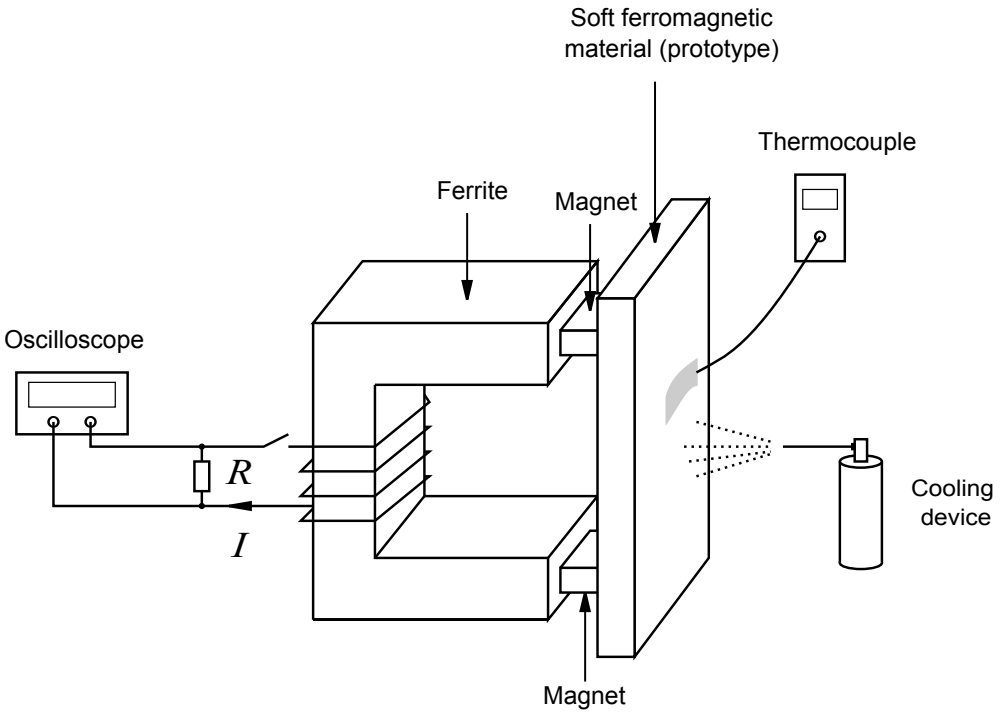

Figure IV-29: Experimental setup for a cooling process

−40 °C. The warming-up process takes more than 5 s while the cooling-down takes less than 1 s; with the existence of noises, it is difficult to observe an evident change of voltage in the former process while in the latter one a peak value appears, the different performances in voltage generation may be explained by the contribution of temperature slope, which has been mentioned in Section(IV.4.5). Consider the difficulty of voltage observation in the warming-up process, it is difficult to form a complete thermal cycle. In the trapezoidal simulation, the temperature decrease and increase shows a symmetric phenomenon; in the sinusoidal simulation, the phenomena are quasi-symmetric for the temperature decrease and increase. The experiment will focus on the cooling process (which may be considered as a study on a half cycle) and try to reveal the relationship between temperature and generated energy.

According to the calculation based on experimental parameters, the optimal resistance is less than 1 Ω while the internal resistance of the coil is 2.2 Ω. As the load optimized power cannot be reached, it is possible to encounter a relatively low harvested power. In order to approach the optimal resistance as closely as possible, a set of resistances begins from small loads are applied: they are composed of 1 Ω, 2 Ω, 5 Ω, 10 Ω, 20 Ω, 40 Ω, 50 Ω, 100 Ω resistances. Temperature variation and generated voltages under different resistances are demonstrated in Fig.(IV-30): the cyan lines are experimental results, the blue dashed

lines are theoretical results calculated with Runge-Kutta method, and the red dotted lines are theoretical results calculated with Runge-Kutta method with a linear approximation.

The room temperature is between 21 °C and 22 °C. The temperature variation of prototype starts at the ambient temperature, then the prototype is cooled down by the compressed air to about −40 °C. Similar to the simulation in Section (IV.4.5), the violent temperature decrease gives rise to a rapidly changing voltage; after the cooling down process, the material is slowly warmed up by the surroundings, which could be considered as a quasi-steady status and we could barely observe any change of the voltage. In all cases in the figure, the experimental peak values are slightly superior to the theoretical ones. It is mainly caused by the experimental setup. As the compressed air cools the ferromagnetic plate from its center, it takes a very short period of time for the square shape material to be completely cooled down, however this short period of time does have a considerable influence on the observed results. If the thermocouple is placed right in the center of the square, it records a temperature curve which would make theoretical results superior to the reality, as the actual average temperature of the whole ferromagnetic material is not exactly the same with the record; if the probe is placed on the edge, the thermocouple would record a temperature curve with a delay and with a peak value inferior to the reality. So the placement of the probe is rather critical in the experiment, its distance to the center should be small enough to record the peak value of temperature variation, and at the same time be able to take into consideration the heat transfer. Besides, the compressed air is pumped manually to the prototype through a straw, the air in the straw arrives on the surface of ferromagnetic plate before the compressed cold one and this air serves as a disturbance (sometimes as a warming up) to the prototype. As a consequence, a small hump is observed right before the cooling down process when the resistance equals to 2 Ω, 5 Ω (Fig.(IV-30)), etc. This influence could be lightened by pre-cooling the straw.

The maximum instantaneous powers in Fig.(IV-31) vary from about 10^{-8} W to about 10^{-6} W in an irregular way and show inevitable errors when the resistance in series is less than 5 Ω. For one reason, the detection position of temperature may lead to errors of amplitude and of phase; besides, the manual operation cannot guarantee the exactly same position to cool down; moreover, when the resistance is small (less than the internal resistance 2.2 Ω), the measurement is disturbed by the internal resistance despite of data post-processing. As the system resistance is always superior to the optimal value, the maximum power was expected to shown a decrease with the increase of resistance (here, the system resistance is the sum of internal resistance and external resistance for harvesting energy, but the power

is still based on the value of external resistance). However, in Fig.(IV-31) the power varies dramatically, which is because the manual cooling cannot guarantee the exactly same temperature variation. The differences between the peak values of voltage in Fig.(IV-30) and power in Fig.(IV-31) are not only caused by the different resistances, but also by the different temperature variations. As the temperature decrease velocity cannot be controlled, in order to observe the influence of resistance on the voltage the temperature variation factor should be eliminated - the average power during the decrease process will be normalized by being divided by the average temperature decrease slope (Fig.(IV-32)). This helps to show a more reasonable power variation (and for energy in Fig.(IV-33)) with respect to load. Clearly smaller loads are preferable choices as the corresponded powers are increased about 30 times compared with that of higher loads. However, it should be noticed that even the highest instantaneous power in Fig.(IV-31) is less than 7×10^{-7} W and the harvested energy in the considered time period is less than 10^{-5} J.

Suppose the optimal resistance could be reached, the highest power for optimal load under same circumstances won't exceed 10^{-5} W. In Section (IV.3.1), the energy conversion process has explained that the harvested energy comes from temperature-variation-caused magnetic energy change which depends on the prototype volume and its ferromagnetic characteristics and which may be of limited quantity.

IV.6 Conclusion

This chapter concentrated on thermal energy harvesting based on ferromagnetic materials by temperature variation around the Curie temperature. The design concept is composed of a soft ferromagnetic material, a U-shape ferrite and a coil wound around the ferrite. The whole system is put in a magnetic field which could be either caused by a constant current or a permanent magnet. When the temperature on the soft ferromagnetic material (prototype) is varied around its Curie point, its magnetic permeability is drastically changed and this variation induces a change in magnetic field passing through the coil and generates a voltage which could be harvested. Generally speaking, whether the prototype is heated or cooled, the energy conversion part could be considered to be in contact with a hot and cold reservoirs; the thermal energy is transfered from the hot reservoir to the cold reservoir; at the same time the energy conversion part is able to convert a part of this transfered thermal energy into electrical energy [LWS+14].

Detailed analysis has been made for the model where the magnetic field is provided by a

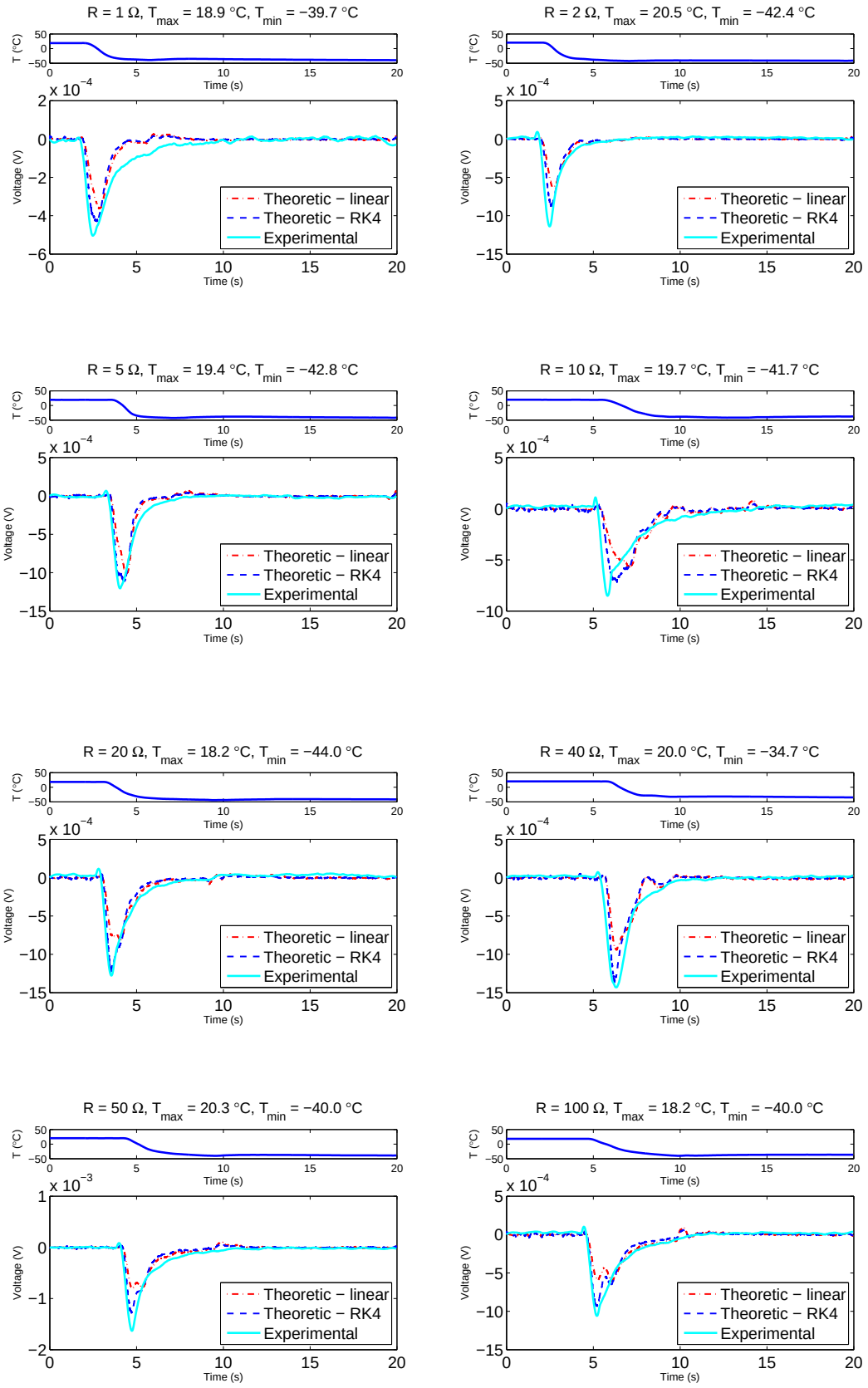

Figure IV-30: Generated voltages for 8 resistances in series

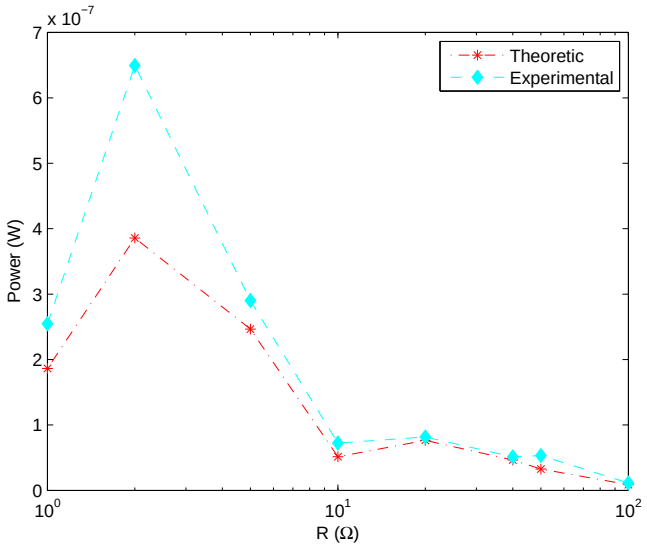

Figure IV-31: Peak value of instantaneous power under different resistances

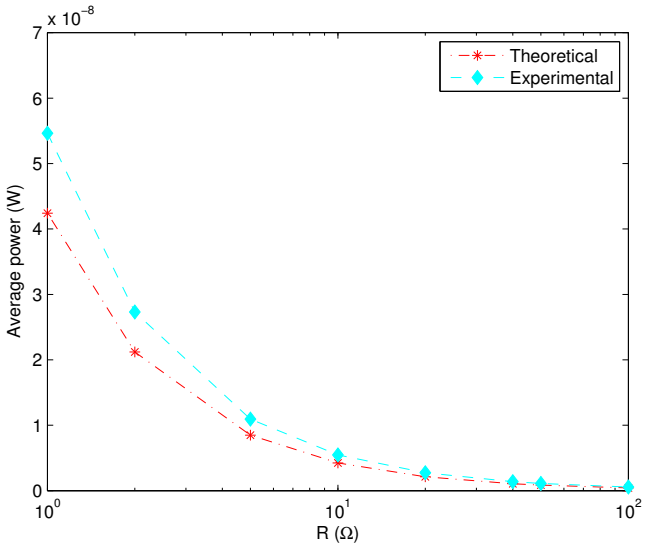

Figure IV-32: Average power under different resistances

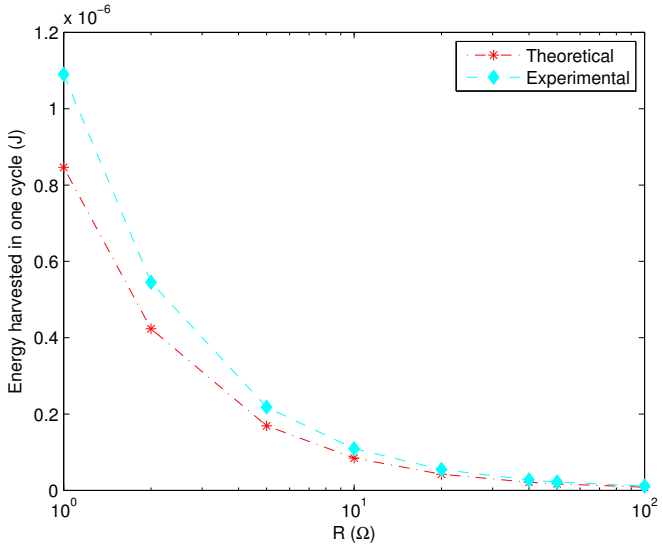

Figure IV-33: Havested energy under different resistances

permanent magnet. Simulations results have shown that an enhancement of the remnant field of magnet B_r can largely increase the harvested power, however a compromise between the remnant field and its permeability has to be made to optimize the performance of the system; a ferrite with large magnetic permeability is also preferable for increasing the harvested power; when a load is connected in the energy harvesting circuit, optimal resistances exist which may raise the harvested power by about 10 times. Simulation results have shown that for both trapezoidal and sinusoidal temperature variations, the temperature change and the corresponding changing velocity are approximately linear with the harvested power.

Experiments have been carried out on this model. The voltage induced on the energy harvesting load generally agrees with the theoretically predicted one for different resistances put in series. However, the generated power is relatively low (the maximal power is 7×10^{-7} W); even ideally the system optimal resistance could be reached, the maximum power would not exceed 10^{-5} W. However, this method sheds light on more possibilities of harvesting thermal energy, besides thermoelectric and pyroelectric method, thermomagnetic coupling combined with electromagnetic coupling could also harvest energy from thermal energy variation, which is thrilling news and forecasts a more flourishing energy harvesting field.

Chapter V

Conclusion and perspectives

This work has been dedicated to some mechanical and thermal energy harvesting techniques. More precisely, attention has been paid to electrostatic energy harvesting based on variable capacitors, electrostrictive generators based on bending beam configuration and thermal energy harvesting taking advantage of soft ferromagnetic materials.

Electrostatic energy harvesting based on fractal configuration The capacitor configuration proposed in this thesis is based on a comb shape capacitor with in-plane overlap varying configuration. The improvement concept is inspired by the self-similarity patterns of fractal geometry in order to increase the capacitance variation during the vibration which is critical to harvested energy. The proposed mountain shape capacitor structure may be constructed either in a progressive or a degressive way. For example, in the degressive way, the construction is to gradually add fingers of smaller widths between larger fingers to benefit from structure in a better way. In the progressive way, the capacitor is of similar configuration except the construction order is different. Thus the capacitor is composed of a range of fingers of different lengths and by different arrangements the capacitors can be classified in different orders, e.g. a capacitor consisting of fingers of length from l_1 to $3^{n-1}l_1$ is considered to be of order n.

Simulation results have shown that for different vibration amplitudes, the capacitors of different orders show different performances. For progressive series of capacitors, when the amplitude is relatively small, capacitors of low order have high capacitance variation as it benefits from numerous fingers which add to vertical overlapping surfaces; when the amplitude increases and fingers of small heights no longer overlap, capacitors of high orders begin to show better performance, benefiting from high fingers. In applications, when choosing from the progressive series of capacitors, it is preferable to choose the capacitor order accord-

ing to vibration amplitudes to optimize the system performance. For the degressive series of capacitors, capacitors of high orders are usually reasonable choices.

Besides, for both series a capacitor of high order has relatively significant mass. In applications, on one hand the order of capacitor is preferable to be less than 6 thus not to influence its integration in microscale systems; on the other hand, the mass of capacitor may help to decrease the resonance frequency of system.

Future work may be cast to discover more possibilities of fractal geometry to improve the space utilization in the capacitor.

Lumped model of bending electrostrictive transducers The model of such a system is established by energy conversion analysis. From the electrical aspect, the provided electrical energy is composed of electrical energy stored in the system and of coupling electromechanical energy. A coefficient is found critical to the same coupling energy and defined as the electromechanical coefficient α; from the mechanical aspect, the provided electrical energy is composed of mechanical energy stored in the beam and the coupling electrical energy and similarly a coefficient is found to be critical to the coupling energy, denoting the equivalence between direct and converse effect. This electromechanical coefficient is dependent on the flexural displacement of the beam and on the slope of displacement with respect to the axis x_1 along the beam.

Theoretical analysis have been carried out for a clamped-free unimorph beam and a clamped-free bimorph beam. For both cases and under realistic conditions, the electromechanical coefficient can be considered to be independent of the bias electric field and of the force applied at the free end of the beam. It decreases along the beam axis and is largely reduced at the free end of the beam. A beam with an electrostrictive polymer film attached to the clamped end has been experimented. The measured coefficients show relatively good agreement with theoretical results. When the system is connected with a series of loads to harvest energy, optimal resistances exist which may improve the harvested power by $2 - 10$ times.

Thermal energy harvesting based on soft ferromagnetic materials Ferromagnetic materials experience a sharp permeability change around their Curie temperature. The aim is to profit from this permeability change to harvest thermal energy. A soft ferromagnetic material (prototype) is attached to a U-shape ferrite wound round by a coil and this system is put in a magnetic field. When a temperature change around the Curie point (T_C) occurs on the ferromagnetic material (the change may be an increase from being below T_C to being

above it, or reverse), the associated magnetic permeability variation gives rise to a change in magnetic field of the system which induces a voltage in the coil.

Such a system can be simplified as a conversion system in contact with a hot reservoir and a cold reservoir, which is magnetized by a generator of magnetic field. The thermal energy is transferred from the hot reservoir to the cold one, during this process a part of transferred thermal energy is converted by the conversion system into electrical energy. At the same time, if a load is connected in the coil, the energy could be harvested.

The magnetic generator could either be a constant current or a permanent magnet. The latter case has been further analyzed. The induced voltage can be calculated with system parameters and by theoretical analysis, it is found that an enhancement of remnant magnetic field of magnet B_r and of ferrite permeability μ_f can help to increase harvested power, while the magnet permeability μ_a (a compromise between the permeability and the remnant field has to be made) and the connected harvesting load have optimal values to maximize harvested power.

In the experiment, a system with soft ferromagnetic materials, ferrite and magnets has been tested. The prototype is cooled from the ambient temperature (21 °C) to about −40 °C. When connected with different resistances, the system generates voltages from $10^{-4} - 10^{-3}$ V and the experimental and theoretical results show good agreements for different resistances. However, the harvested power is relatively low (for the optimal load, the harvested power is about 10^{-7} W). Future work may be concentrated on the improvement of system in order to increase the harvested power.

Perspectives The results presented here, especially for the first and last subjects, have actually a vast space to explore or to be improved. For example, the fractal-based capacitor may be further explored for applications and capacitance variation; the thermal energy harvesting device may be improved by parametric optimization and ferromagnetic material choice. Besides, the first subject has been inspired by fractal geometry which is a relatively accurate description of nature; bio-inspired devices would also be rather explorable choices.

Appendix A

The degressive series of capacitors of order from 1 to 3

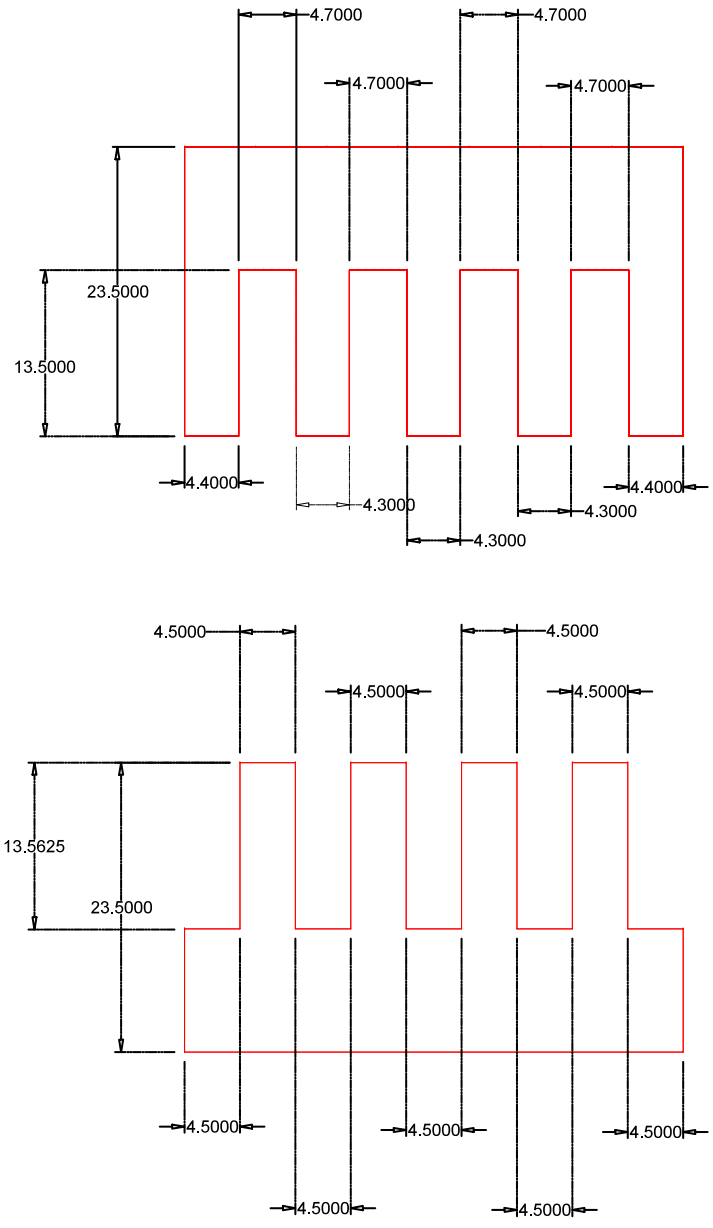

Figure A-1: The degressive series of fractal-based capacitors of order 1 (unit: mm)

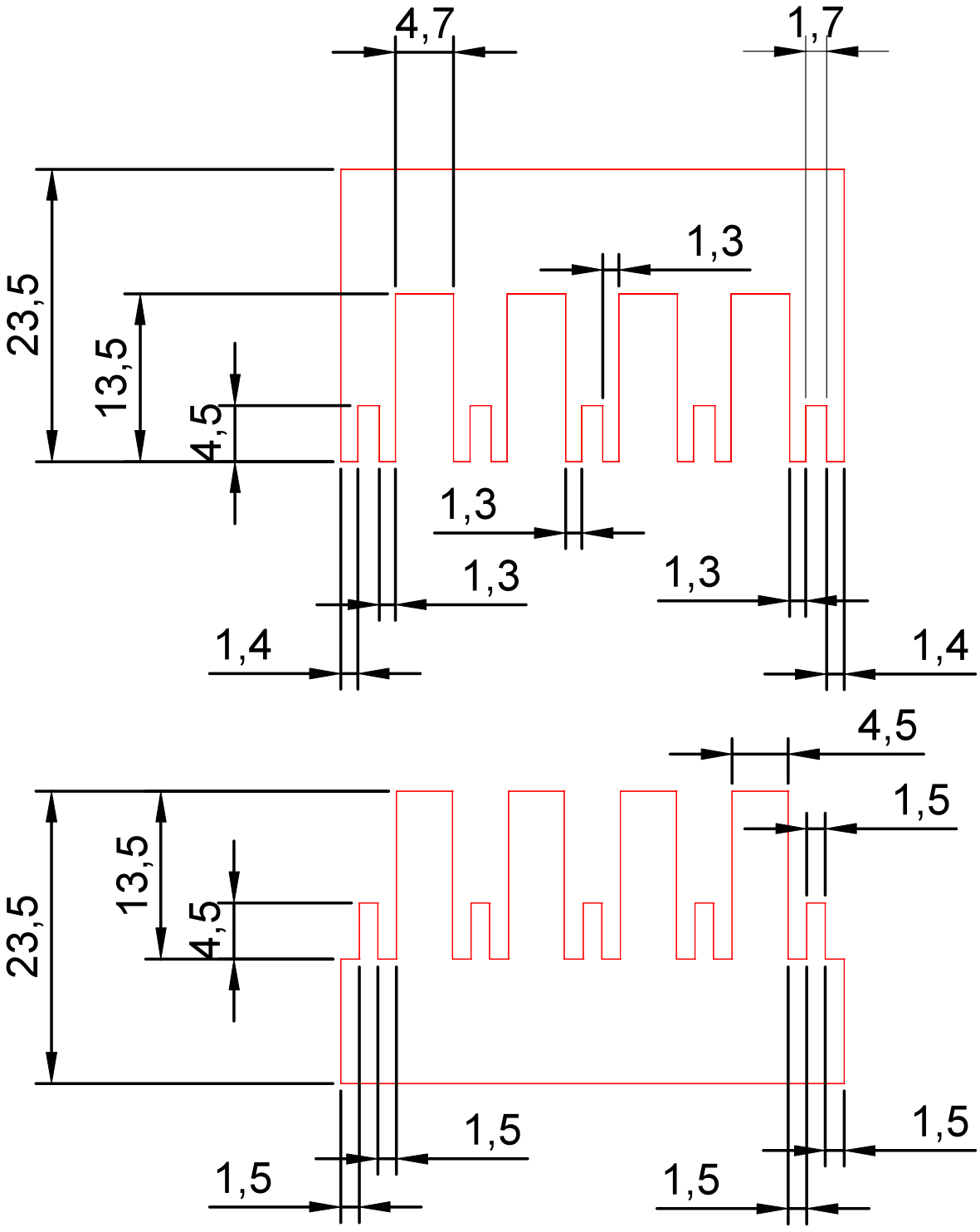

Figure A-2: The degressive series of fractal-based capacitors of order 2 (unit: mm)

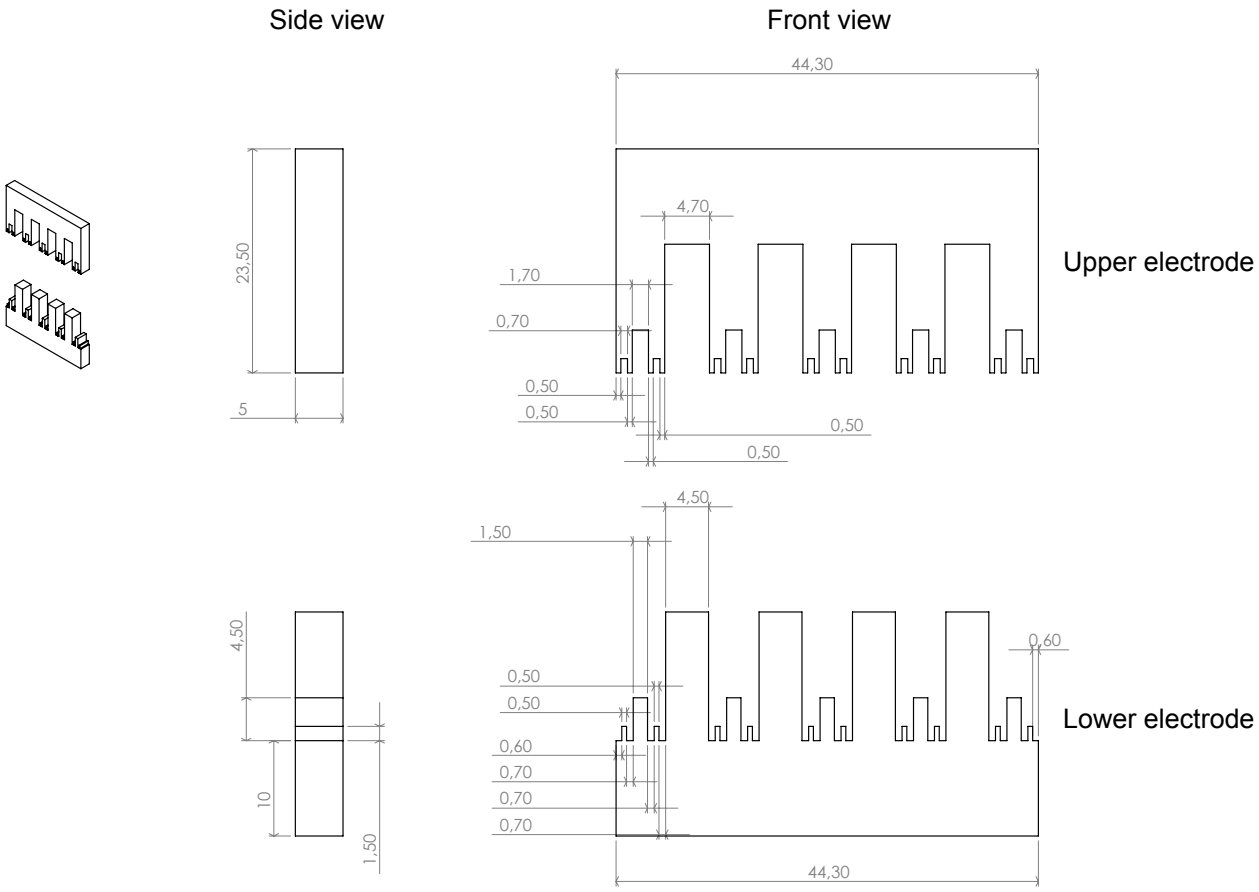

Figure A-3: The degressive series of fractal-based capacitors of order 3 (unit: mm)

References

[Aha96] Amikam Aharoni. *Introduction to the Theory of Ferromagnetism*, volume 2. Clarendon Press Oxford, 1996. 99, 101

[AP98] Uri M. Ascher and Linda R. Petzold. *Computer Methods for Ordinary Differential Equations and Differential-Algebraic Equations*. SIAM, August 1998. 118

[AP10] Harry A. Atwater and Albert Polman. Plasmonics for improved photovoltaic devices. *Nature Materials*, 9(3):205–213, March 2010. 31

[AS07] Steven R Anton and Henry A Sodano. A review of power harvesting using piezoelectric materials (2003-2006). *Smart Materials and Structures*, 16(3):R1–R21, June 2007. 2, 3

[ASK04] YSNKY Arakawa, Y. Suzuki, and N. Kasagi. Micro seismic power generator using electret polymer film. *Proc. PowerMEMS*, 187:190, 2004. 17

[Bal07] Rüdiger G. Ballas. *Piezoelectric Multilayer Beam Bending Actuators: Static and Dynamic Behavior and Aspects of Sensor Integration*. Springer, March 2007. 70

[BC04] Yoseph Bar-Cohen, editor. *Electroactive Polymer (EAP) Actuators as Artificial Muscles: Reality, Potential, and Challenges, Second Edition*. SPIE, 1000 20th Street, Bellingham, WA 98227-0010 USA, March 2004. 19, 64

[BC09] O. A. Bauchau and James I. Craig. *Structural Analysis: With Applications to Aerospace Structures*. Springer, August 2009. 68

[BDLV10] D. Bouchouicha, F. Dupont, M. Latrach, and L. Ventura. Ambient RF energy harvesting. In *International Conference on Renewable Energies and Power Quality*, pages 1–4, 2010. xix, 29, 30

[BJ00] James W. Baish and Rakesh K. Jain. Fractals and cancer. *Cancer research*, 60(14):3683–3688, 2000. 38

[BJCL11] Katherine E. Bulgrin, Y. Sungtaek Ju, Greg P. Carman, and Adrienne S. Lavine. An investigation of a tunable magnetomechanical thermal switch. *Journal of Heat Transfer*, 133(10):101401–101401, August 2011. 29

[BKGS06] Shawna R. Brown, Susan M. Kauzlarich, Franck Gascoin, and G. Jeffrey Snyder. Yb14mnsb11: New high efficiency thermoelectric material for power generation. *Chemistry of materials*, 18(7):1873–1877, 2006. xix, 22

[BKWD13] C. R. Bowen, H. A. Kim, P. M. Weaver, and S. Dunn. Piezoelectric and ferroelectric materials and structures for energy harvesting applications. *Energy & Environmental Science*, 7(1):25–44, December 2013. 7, 25

[BL94] Michael Batty and Paul A. Longley. *Fractal cities: a geometry of form and function*. Academic Press, 1994. 38

[BN80] A. S. Bhalla and R. E. Newnham. Primary and secondary pyroelectricity. *physica status solidi (a)*, 58(1):K19–K24, March 1980. 26

[BOST04] Nagendra B. Bharatula, Stijn Ossevoort, Mathias Stäger, and Gerhard Tröster. Towards wearable autonomous microsystems. In Alois Ferscha and Friedemann Mattern, editors, *Pervasive Computing*, number 3001 in Lecture Notes in Computer Science, pages 225–237. Springer Berlin Heidelberg, January 2004. 11

[Bov96] Carl Bovill. *Fractal Geometry in Architecture and Design*. Springer Science & Business Media, March 1996. 38

[Bro84] William C. Brown. The history of power transmission by radio waves. *Microwave Theory and Techniques, IEEE Transactions on*, 32(9):1230–1242, 1984. 30

[Bro91] William C. Brown. An experimental low power density rectenna. In *IEEE MTT-S International Microwave Symposium Digest*, volume 1, pages 197–200, 1991. 30

[Bro96] William C. Brown. The history of wireless power transmission. *Solar energy*, 56(1):3–21, 1996. 30

[Bro07] Harlan J. Brothers. Structural scaling in bach's cello suite no. 3. *Fractals*, 15(01):89–95, 2007. 38

[BTW06] S P Beeby, M J Tudor, and N M White. Energy harvesting vibration sources for microsystems applications. *Measurement Science and Technology*, 17(12):R175–R195, December 2006. xviii, 3, 4, 5, 6

[Bul80] Bulova. Bulova thermatron, 1980. http://doensen.home.xs4all.nl/p.html. 23

[Bul82] Bulova. Bulova 2467 thermatron 1982, 1982. http://www.crazywatches.pl/bulova-2467-thermatron-1982. xix, 23

[But08] John C. Butcher. *Numerical Methods for Ordinary Differential Equations*. John Wiley & Sons, April 2008. 118

[CAZS02] Kuo-Shen Chen, Arturo A. Ayón, Xin Zhang, and S. Mark Spearing. Effect of process parameters on the surface morphology and mechanical performance of silicon structures after deep reactive ion etching (DRIE). *Microelectromechanical Systems, Journal of*, 11(3):264–275, 2002. 41

[CGF10] A. Cuadras, M. Gasulla, and V. Ferrari. Thermal energy harvesting through pyroelectricity. *Sensors and Actuators A: Physical*, 158(1):132–139, March 2010. 26

[CGG+10] Pierre-Jean Cottinet, Daniel Guyomar, Benoit Guiffard, Laurent Lebrun, and Chatchai Putson. Electrostrictive polymers as high-performance electroactive polymers for energy harvesting. In *Piezoelectric Ceramics*. Ernesto Suaste-Gomez (Ed.), 2010. 66

[CGL+11] Pierre-Jean Cottinet, D. Guyomar, M. Lallart, B. Guiffard, and L. Lebrun. Investigation of electrostrictive polymer efficiency for mechanical energy harvesting. *IEEE Transactions on Ultrasonics, Ferroelectrics and Frequency Control*, 58(9):1842–1851, September 2011. 19

[CH10] Harrison Hoon Seok Chang and Zhaorong Huang. Laminate composites with enhanced pyroelectric effects for energy harvesting. *Smart Materials and Structures*, 19(6):065018, 2010. 26

[Chi97] Soshin Chikazumi. *Physics of Ferromagnetism*. Oxford University Press, February 1997. 99

[CI66] Roy Carey and Evan David Isaac. Magnetic domains and techniques for their observation. 1966. 99

[CJ09] Gilhwan Cha and Y. Sungtaek Ju. Reversible thermal interfaces based on microscale dielectric liquid layers. *Applied physics letters*, 94(21):211904, 2009. 29

[CJ13] Gilhwan Cha and Y. Sungtaek Ju. Pyroelectric energy harvesting using liquid-based switchable thermal interfaces. *Sensors and Actuators A: Physical*, 189:100–107, 2013. xix, 28, 29

[CKT+13] Zhuo Cao, E Koukharenko, M J Tudor, R N Torah, and S P Beeby. Screen printed flexible bi $_2$ te $_3$ -sb $_2$ te $_3$ based thermoelectric generator. *Journal of Physics: Conference Series*, 476:012031, December 2013. 25

[CLG+12] Jean-Fabien Capsal, Mickaël Lallart, Jeremy Galineau, Pierre-Jean Cottinet, Gaël Sebald, and Daniel Guyomar. Evaluation of macroscopic polarization and actuation abilities of electrostrictive dipolar polymers using the microscopic debye/langevin formalism. *Journal of Physics D: Applied Physics*, 45(20):205401, May 2012. 64, 65

[CT61] D. J. Craik and R. S. Tebble. Magnetic domains. *Reports on progress in physics*, 24(1):116, 1961. 99

[CXB+99] Z.-Y. Cheng, T.-B. Xu, Vivek Bharti, Shexi Wang, and Q. M. Zhang. Transverse strain responses in the electrostrictive poly(vinylidene fluoride–trifluorethylene) copolymer. *Applied Physics Letters*, 74(13):1901, 1999. 66

[DC02] Edward F. DeLong and Paul Chandler. Power from the deep. *nature biotechnology*, 20(8):788–789, 2002. 32

[DCZ12] Huan Deng, Zheng Chen, and Feng Zhao. Energy from plants and microorganisms: Progress in plant-microbial fuel cells. *ChemSusChem*, 5(6):1006–1011, June 2012. 32

[Dev54] A.F. Devonshire. Theory of ferroelectrics. *Advances in Physics*, 3(10):85–130, 1954. 65

[DGG+11] M. E. Dokukin, N. V. Guz, R. M. Gaikwad, C. D. Woodworth, and I. Sokolov. Cell surface as a fractal: normal and cancerous cervical cells demonstrate

different fractal behavior of surface adhesion maps at the nanoscale. *Physical review letters*, 107(2):028101, 2011. 38

[DJJJ+05] Ghislain Despesse, Thomas Jager, Chaillout Jean-Jacques, Jean-Michel Léger, Andrea Vassilev, Skandar Basrour, Benoit Charlot, and others. Fabrication and characterization of high damping electrostatic micro devices for vibration energy scavenging. In *Proc. Design, Test, Integration and Packaging of MEMS and MOEMS*, pages 386–390, 2005. 13

[DYH+11] Xiangnan Dang, Hyunjung Yi, Moon-Ho Ham, Jifa Qi, Dong Soo Yun, Rebecca Ladewski, Michael S. Strano, Paula T. Hammond, and Angela M. Belcher. Virus-templated self-assembled single-walled carbon nanotubes for highly efficient electron collection in photovoltaic devices. *Nature Nanotechnology*, 6(6):377–384, June 2011. 31

[Edg93] Gerald A. Edgar. *Classics on Fractals*. Basic Books, 1993. 38

[Eo05] Albert Einstein and others. On the electrodynamics of moving bodies. *Annalen der Physik*, 17(891):50, 1905. 102

[Eve95] Carl JG Evertsz. Fractal geometry of financial time series. *Fractals*, 3(03):609–616, 1995. 38

[EYS+99] Sylvie Eury, Rattikorn Yimnirun, V. Sundar, Paul J. Moses, Sei-Joo Jang, and Robert E. Newnham. Converse electrostriction in polymers and composites. *Materials chemistry and physics*, 61(1):18–23, 1999. 64

[Fal13] Kenneth Falconer. *Fractal geometry: mathematical foundations and applications*. John Wiley & Sons, 2013. xx, 39, 40

[FDPF+11] L. Francioso, C. De Pascali, I. Farella, C. Martucci, P. Cretì, P. Siciliano, and A. Perrone. Flexible thermoelectric generator for ambient assisted living wearable biometric sensors. *Journal of Power Sources*, 196(6):3239–3243, March 2011. 24

[Fis95] Yuval Fisher. *Fractal image compression with quadtrees*. Springer, 1995. 38

[GBLR05] Daniel Guyomar, Adrien Badel, Elie Lefeuvre, and Claude Richard. Toward energy harvesting using active materials and conversion improvement by non-

linear processing. *Ultrasonics, Ferroelectrics and Frequency Control, IEEE Transactions on*, 52(4):584–595, 2005. xix, 7, 8, 67

[Gho89] Barry Gholson. *Psychology of Science: Contributions to Metascience*. Cambridge University Press, July 1989. 99

[GJTBW04] P. Glynne-Jones, M.J. Tudor, S.P. Beeby, and N.M. White. An electromagnetic, vibration-powered generator for intelligent sensor systems. *Sensors and Actuators A: Physical*, 110(1-3):344–349, February 2004. xix, 9, 10

[Gre01] Martin A. Green. Third generation photovoltaics: Ultra-high conversion efficiency at low cost. *Progress in Photovoltaics: Research and Applications*, 9(2):123–135, 2001. 31

[GSLK08] Daniel Guyomar, Gael Sebald, Elie Lefeuvre, and Akram Khodayari. Toward heat energy harvesting using pyroelectric material. *Journal of intelligent material systems and structures*, 2008. 26

[HA08] Nicholas S. Hudak and Glenn G. Amatucci. Small-scale energy harvesting through thermoelectric, vibration, and radiofrequency power conversion. *Journal of Applied Physics*, 103(10):101301, 2008. 29

[Har11] Adnan Harb. Energy harvesting: State-of-the-art. *Renewable Energy*, 36(10):2641–2654, October 2011. 11

[HBW99] Seon M. Han, Haym Benaroya, and Timothy Wei. Dynamics of transversely vibrating beams using four engineering theories. *Journal of Sound and Vibration*, 225(5):935–988, September 1999. 68

[Hei26] Werner Heisenberg. Über die spektra von atomsystemen mit zwei elektronen. *Zeitschrift für Physik*, 39(7-8):499–518, 1926. 99

[HFM11] Daniel Hoffmann, Bernd Folkmer, and Yiannos Manoli. Analysis and characterization of triangular electrode structures for electrostatic energy harvesting. *Journal of Micromechanics and Microengineering*, 21(10):104002, October 2011. xix, 13, 15

[HHB+12] Lenka Halámková, Jan Halámek, Vera Bocharova, Alon Szczupak, Lital Alfonta, and Evgeny Katz. Implanted biofuel cell operating in a living snail.

Journal of the American Chemical Society, 134(11):5040–5043, March 2012. 33

[HHM+04] J.A. Hagerty, F.B. Helmbrecht, W.H. McCalpin, R. Zane, and Z.B. Popovic. Recycling ambient microwave energy with broad-band rectenna arrays. *IEEE Transactions on Microwave Theory and Techniques*, 52(3):1014–1024, March 2004. 30

[Hip95] Arthur Robert Von Hippel. *Dielectrics and Waves*. Artech House, Incorporated, 1995. 104

[HZZS08] Wei Hong, Xuanhe Zhao, Jinxiong Zhou, and Zhigang Suo. A theory of coupled diffusion and large deformation in polymeric gels. *Journal of the Mechanics and Physics of Solids*, 56(5):1779–1793, 2008. 64

[IGM03] Ioannis Ieropoulos, John Greenman, and Chris Melhuish. Imitating metabolism: Energy autonomy in biologically inspired robots. In *Proceedings of the AISB*, volume 3, pages 191–4, 2003. 32

[Iku02] Michio Ikura. Conversion of low-grade heat to electricity using pyroelectric copolymer. *Ferroelectrics*, 267(1):403–408, January 2002. 27

[ILSS13] Molla R. Islam, Xue Li, Keady Smyth, and Michael J. Serpe. Polymer-based muscle expansion and contraction. *Angewandte Chemie International Edition*, 52(39):10330–10333, September 2013. 8

[Inm13] Daniel J. Inman. *Engineering Vibrations*. Pearson Education, February 2013. 68

[Jac93] Arnaud E. Jacquin. Fractal image coding: A review. *Proceedings of the IEEE*, 81(10):1451–1465, 1993. 38

[JCJ12] Yanbing Jia, Gilhwan Cha, and Yongho Sungtaek Ju. Switchable thermal interfaces based on discrete liquid droplets. *Micromachines*, 3(1):10–20, 2012. 29

[KDA+05] Thorsten Krenke, Eyüp Duman, Mehmet Acet, Eberhard F. Wassermann, Xavier Moya, Lluis Mañosa, and Antoni Planes. Inverse magnetocaloric effect in ferromagnetic ni–mn–sn alloys. *Nature Materials*, 4(6):450–454, June 2005. 102

[KF03] Udo Karthaus and Martin Fischer. Fully integrated passive UHF RFID transponder IC with 16.7-μw minimum RF input power. *Solid-State Circuits, IEEE Journal of*, 38(10):1602–1608, 2003. 30

[KHY08] Michail E. Kiziroglou, Cairan He, and Eric M. Yeatman. Non-resonant electrostatic energy harvesting from a rolling mass. In *Medical Devices and Biosensors, 2008. ISSS-MDBS 2008. 5th International Summer School and Symposium on*, pages 318–321. IEEE, 2008. xix, 15, 16

[KHY09] M.E. Kiziroglou, C. He, and E.M. Yeatman. Rolling rod electrostatic microgenerator. *IEEE Transactions on Industrial Electronics*, 56(4):1101–1108, April 2009. 15

[KHY10] M. E. Kiziroglou, C. He, and E. M. Yeatman. Flexible substrate electrostatic energy harvester. *Electronics letters*, 46(2):166–167, 2010. xix, 16, 17

[Kit49] Charles Kittel. Physical theory of ferromagnetic domains. *Reviews of Modern Physics*, 21(4):541, 1949. xxi, 100

[KK13] H. Kim and S. Kwon. Water-responsive polymer composites on the move. *Science*, 339(6116):150–151, January 2013. 8

[KKL+06] J. Y. Kim, S. H. Kim, H.-H. Lee, K. Lee, W. Ma, X. Gong, and A. J. Heeger. New architecture for high-efficiency polymer photovoltaic cells using solution-based titanium oxide as an optical spacer. *Advanced Materials*, 18(5):572–576, March 2006. 31

[KKPG98] John Kymissis, Clyde Kendall, Joseph Paradiso, and Neil Gershenfeld. Parasitic power harvesting in shoes. In *Wearable Computers, 1998. Digest of Papers. Second International Symposium on*, pages 132–139. IEEE, 1998. xviii, 4, 5

[KNH+99] M. Kishi, H. Nemoto, T. Hamao, M. Yamamoto, S. Sudou, M. Mandai, and S. Yamamoto. Micro thermoelectric modules and their application to wristwatches as an energy source. In *Thermoelectrics, 1999. Eighteenth International Conference on*, pages 301–307. IEEE, 1999. 23

[KSFOS12] Sevan Karabetoglu, Altug Sisman, Z. Fatih Ozturk, and Turker Sahin. Characterization of a thermoelectric generator at low temperatures. *Energy Conversion and Management*, 62:47–50, October 2012. 24

[KWC14] Sun Jin Kim, Ju Hyung We, and Byung Jin Cho. A wearable thermoelectric generator fabricated on a glass fabric. *Energy & Environmental Science*, 7(6):1959–1965, May 2014. 25

[Lac93] Étienne Du Tremolet de Lacheisserie. *Magnetostriction: theory and applications of magnetoelasticity*. CRC Press, June 1993. 20

[Lan05] Sidney B. Lang. Pyroelectricity: from ancient curiosity to modern imaging tool. *Physics Today*, 58(8):31–36, 2005. 25

[Lau12] L. Laursen. Snails in a race for biological energy harvesting. *IEEE Spectrum*, 49(5):19–19, May 2012. 33

[LCC+09] Lun-De Liao, P.C.-P. Chao, Jian-Ting Chen, Wei-Dar Chen, Wei-Hsuan Hsu, Chi-Wei Chiu, and Chin-Teng Lin. A miniaturized electromagnetic generator with planar coils and its energy harvest circuit. *IEEE Transactions on Magnetics*, 45(10):4621–4627, October 2009. 11

[LCG+14] Qiang Leng, Lin Chen, Hengyu Guo, Jianlin Liu, Guanlin Liu, Chenguo Hu, and Yi Xi. Harvesting heat energy from hot/cold water with a pyroelectric generator. *Journal of Materials Chemistry A*, 2(30):11940–11947, July 2014. 27

[LCGL12] Mickaël Lallart, Pierre-Jean Cottinet, Daniel Guyomar, and Laurent Lebrun. Electrostrictive polymers for mechanical energy harvesting. *Journal of Polymer Science Part B: Polymer Physics*, 50(8):523–535, April 2012. 64

[LCL+10] Mickaël Lallart, Pierre-Jean Cottinet, Laurent Lebrun, Benoît Guiffard, and Daniel Guyomar. Evaluation of energy harvesting performance of electrostrictive polymer and carbon-filled terpolymer composites. *Journal of Applied Physics*, 108(3):034901, 2010. 19, 66

[LCS+14] Mickaël Lallart, Jean-Fabien Capsal, Gaël Sebald, Pierre-Jean Cottinet, and Daniel Guyomar. Converse electrostrictive effect in dielectric polymers. *Sensors and Actuators B: Chemical*, 190:259–264, January 2014. 64, 74

[LG01] Malcolm E. Lines and Alastair M. Glass. *Principles and applications of ferroelectrics and related materials*. Clarendon press Oxford, 2001. 25

[LGM+12] Felix Y. Lee, Sam Goljahi, Ian M. McKinley, Christopher S. Lynch, and Laurent Pilon. Pyroelectric waste heat energy harvesting using relaxor ferroelectric 8/65/35 PLZT and the olsen cycle. *Smart Materials and Structures*, 21(2):025021, 2012. xix, 27

[LGRE06] Nigel Lesmoir-Gordon, Will Rood, and Ralph Edney. *Introducing Fractal Geometry*. Icon Books, Limited, 2006. 38, 39

[LL35] LALE Landau and Es Lifshitz. On the theory of the dispersion of magnetic permeability in ferromagnetic bodies. *Phys. Z. Sowjetunion*, 8(153):101–114, 1935. 99

[LLC+12] Xinyu Li, Sheng-Guo Lu, Xiang-Zhong Chen, Haiming Gu, Xiao-shi Qian, and Q. M. Zhang. Pyroelectric and electrocaloric materials. *Journal of Materials Chemistry C*, 1(1):23–37, November 2012. 26

[LLL04] F. Lu, H. P. Lee, and S. P. Lim. Modeling and analysis of micro piezoelectric power generators for micro-electromechanical-systems applications. *Smart Materials and Structures*, 13(1):57, 2004. 6

[LMNW01] Gabriele A. Losa, Danilo Merlini, Theo F. Nonnenmacher, and Ewald R. Weibel. *Fractals in Biology and Medicine: III*, volume 3. Springer, 2001. 38

[Lov06] Derek R. Lovley. Bug juice: harvesting electricity with microorganisms. *Nature Reviews Microbiology*, 4(7):497–508, July 2006. 32

[LRHZ05] Yiming Liu, Kai Liang Ren, Heath F. Hofmann, and Qiming Zhang. Investigation of electrostrictive polymers for energy harvesting. *Ultrasonics, Ferroelectrics and Frequency Control, IEEE Transactions on*, 52(12):2411–2417, 2005. 19, 66, 67

[LRS+12] Mickaël Lallart, Claude Richard, Pisan Sukwisut, Lionel Petit, Daniel Guyomar, and Nantakan Muensit. Electrostrictive bending actuators: Modeling and experimental investigation. *Sensors and Actuators A: Physical*, 179:169–177, June 2012. 66, 67

[LSH+05] Gang Li, Vishal Shrotriya, Jinsong Huang, Yan Yao, Tom Moriarty, Keith Emery, and Yang Yang. High-efficiency solution processable polymer pho-

tovoltaic cells by self-organization of polymer blends. *Nature Materials*, 4(11):864–868, November 2005. 31

[LST+01] W. Lehmann, H. Skupin, C. Tolksdorf, E. Gebhard, R. Zentel, P. Krüger, M. Lösche, and F. Kremer. Giant lateral electrostriction in ferroelectric liquid-crystalline elastomers. *Nature*, 410(6827):447–450, 2001. 66

[LWR+14] Mickaël Lallart, Liuqing Wang, Claude Richard, Lionel Petit, and Daniel Guyomar. Lumped model of bending electrostrictive transducers for energy harvesting. *Journal of Applied Physics*, 112(12), September 2014. 94

[LWS+14] Mickaël Lallart, Liuqing Wang, Gaël Sebald, Lionel Petit, and Daniel Guyomar. Analysis of thermal energy harvesting using ferromagnetic materials. *Physics Letters A*, 378(43):3151–3154, September 2014. 137

[LZZ+12] Byung Yang Lee, Jinxing Zhang, Chris Zueger, Woo-Jae Chung, So Young Yoo, Eddie Wang, Joel Meyer, Ramamoorthy Ramesh, and Seung-Wuk Lee. Virus-based piezoelectric energy generation. *Nature Nanotechnology*, 7(6):351–356, May 2012. 7

[Man67] Benoit B. Mandelbrot. How long is the coast of britain. *Science*, 156(3775):636–638, 1967. 39

[Man83] Benoit B. Mandelbrot. *The Fractal Geometry of Nature*. Henry Holt and Company, 1983. 39

[MC03] Makoto Mizuno and Derek G. Chetwynd. Investigation of a resonance microgenerator. *Journal of Micromechanics and Microengineering*, 13(2):209, 2003. 17

[McC94] R. A. McCurrie. *Ferromagnetic materials: structure and properties*. Academic, 1994. xxi, 101, 102, 110

[MDSK03] E Müller, Č Drašar, J Schilz, and W.A Kaysser. Functionally graded materials for sensor and energy applications. *Materials Science and Engineering: A*, 362(1-2):17–39, December 2003. 22

[Met14] Metglas, 2014. http://www.metglas.com/. 20

[MGAL13] M. Ma, L. Guo, D. G. Anderson, and R. Langer. Bio-inspired polymer composite actuator and generator driven by water gradients. *Science*, 339(6116):186–189, January 2013. xix, 8

[MH14] Benoit Mandelbrot and Richard L. Hudson. *The Misbehavior of Markets: A fractal view of financial turbulence*. Basic books, 2014. 38

[MLB+12] Patrick P. Mercier, Andrew C. Lysaght, Saurav Bandyopadhyay, Anantha P. Chandrakasan, and Konstantina M. Stankovic. Energy extraction from the biologic battery in the inner ear. *Nature Biotechnology*, 30(12):1240–1243, December 2012. 32

[MMCS05] Minhong Mi, Martin H. Mickle, Chris Capelli, and Harold Swift. RF energy harvesting with multiple antennas in the same space. *Antennas and Propagation Magazine, IEEE*, 47(5):100–106, 2005. 30

[MMH+06] P. Miao, P. D. Mitcheson, A. S. Holmes, E. M. Yeatman, T. C. Green, and B. H. Stark. Mems inertial power generators for biomedical applications. *Microsystem Technologies*, 12(10-11):1079–1083, September 2006. 15

[MMMA+01] Scott Meninger, Jose Oscar Mur-Miranda, Rajeevan Amirtharajah, Anantha P. Chandrakasan, and Jeffrey H. Lang. Vibration-to-electric energy conversion. *Very Large Scale Integration (VLSI) Systems, IEEE Transactions on*, 9(1):64–76, 2001. xix, 12, 13, 36

[MMS+04] Paul D. Mitcheson, Peng Miao, Bernard H. Stark, E. M. Yeatman, A. S. Holmes, and T. C. Green. MEMS electrostatic micropower generator for low frequency operation. *Sensors and Actuators A: Physical*, 115(2):523–529, 2004. xix, 14, 16

[MNBC08] Keith J. Morton, Gregory Nieberg, Shufeng Bai, and Stephen Y. Chou. Wafer-scale patterning of sub-40 nm diameter and high aspect ratio (> 50: 1) silicon pillar arrays by nanoimprint and etching. *Nanotechnology*, 19(34):345301, 2008. 41

[MRC05] Kaïs Mrabet, Rachid Rahouadj, and Christian Cunat. An irreversible thermodynamic model for semicrystalline polymers submitted to multisequence loading at large strain. *Polymer Engineering & Science*, 45(1):42–51, January 2005. 64

[MRS+05] F. Marty, L. Rousseau, B. Saadany, B. Mercier, O. Français, Y. Mita, and T. Bourouina. Advanced etching of silicon based on deep reactive ion etching for silicon high aspect ratio microstructures and three-dimensional micro- and nanostructures. *Microelectronics Journal*, 36(7):673–677, July 2005. 41

[MVA+04] John DW Madden, Nathan A. Vandesteeg, Patrick A. Anquetil, Peter GA Madden, Arash Takshi, Rachel Z. Pytel, Serge R. Lafontaine, Paul A. Wieringa, and Ian W. Hunter. Artificial muscle technology: physical principles and naval prospects. *Oceanic Engineering, IEEE Journal of*, 29(3):706–728, 2004. 67

[MXLM11] P Mane, Jingsi Xie, K K Leang, and K Mossi. Cyclic energy harvesting from pyroelectric materials. *IEEE Transactions on Ultrasonics, Ferroelectrics and Frequency Control*, 58(1):10–17, January 2011. 26

[MYR+08] P.D. Mitcheson, E.M. Yeatman, G.K. Rao, A.S. Holmes, and T.C. Green. Energy harvesting from human and machine motion for wireless electronic devices. *Proceedings of the IEEE*, 96(9):1457–1486, September 2008. 5, 17

[NVBP10] Ashcon Navid, Damien Vanderpool, Abubakarr Bah, and Laurent Pilon. Towards optimization of a pyroelectric energy converter for harvesting waste heat. *International Journal of Heat and Mass Transfer*, 53(19):4060–4070, 2010. 27

[OB82] R. B. Olsen and D. D. Brown. High efficieincy direct conversion of heat to electrical energy-related pyroelectric measurements. *Ferroelectrics*, 40(1):17–27, 1982. 27

[OB92] W. Olthuis and P. Bergveld. On the charge storage and decay mechanism in silicon dioxide electrets. *Electrical Insulation, IEEE Transactions on*, 27(4):691–697, 1992. 17

[OBB85] Randall B. Olsen, David A. Bruno, and J. Merv Briscoe. Pyroelectric conversion cycles. *Journal of Applied Physics*, 58(12):4709–4716, 1985. 27

[OE83] Randall B. Olsen and Diane Evans. Pyroelectric energy conversion: hysteresis loss and temperature sensitivity of a ferroelectric material. *Journal of applied physics*, 54(10):5941–5944, 1983. 27

[OHBL02] Geffrey K. Ottman, Heath F. Hofmann, Archin C. Bhatt, and George A. Lesieutre. Adaptive piezoelectric energy harvesting circuit for wireless remote power supply. *Power Electronics, IEEE Transactions on*, 17(5):669–676, 2002. 7

[Ols82] Randall B. Olsen. Ferroelectric conversion of heat to electrical EnergyA demonstration. *Journal of Energy*, 6(2):91–95, 1982. 28

[Pau14] Douglas Paul. Thermoelectric energy harvesting. In Giorgos Fagas, editor, *ICT - Energy - Concepts Towards Zero - Power Information and Communication Technology*. InTech, February 2014. 20, 21

[Pet89] Edgar E. Peters. Fractal structure in the capital markets. *Financial Analysts Journal*, pages 32–37, 1989. 38

[Pet94] Edgar E. Peters. *Fractal market analysis: applying chaos theory to investment and economics*, volume 24. John Wiley & Sons, 1994. 38

[PI08] Shashank Priya and Daniel J. Inman. *Energy Harvesting Technologies*. Springer, November 2008. 64, 66

[Pic09] Clifford A. Pickover. *The Math Book: From Pythagoras to the 57th Dimension, 250 Milestones in the History of Mathematics*. Sterling Publishing Company, Inc., 2009. 38

[Pri07] Shashank Priya. Advances in energy harvesting using low profile piezoelectric transducers. *Journal of Electroceramics*, 19(1):167–184, October 2007. xxiii, 2

[PS05] Joseph A. Paradiso and Thad Starner. Energy scavenging for mobile and wireless electronics. *Pervasive Computing, IEEE*, 4(1):18–27, 2005. 23

[RABR04] Cecilia D. Richards, Michael J. Anderson, David F. Bahr, and Robert F. Richards. Efficiency of energy conversion for devices containing a piezoelectric component. *Journal of Micromechanics and Microengineering*, 14(5):717, 2004. 6

[Rao86] S. S. Rao. *Mechanical vibrations*. Addison-Wesley Longman, Incorporated, 1986. 68

[RFvSvH12] Michael Renaud, Paolo Fiorini, Rob van Schaijk, and Chris van Hoof. Corrigendum: Harvesting energy from the motion of human limbs: the design and analysis of an impact-based piezoelectric generator. *Smart Materials and Structures*, 21(4):049501, April 2012. 5

[RKW12] Shankar Karanilam Thundiparambu Ravindran, Michael Kroener, and Peter Woias. A bimetallic micro heat engine for pyroelectric energy conversion. *Procedia Engineering*, 47:33–36, 2012. 28

[RO10] A. W. Richards and G. M. Odegard. Constitutive modeling of electrostrictive polymers using a hyperelasticity-based approach. *Journal of Applied Mechanics*, 77(1):014502, 2010. 65

[Rou03] Shadrach Joseph Roundy. *Energy scavenging for wireless sensor nodes with a focus on vibration to electricity conversion.* PhD thesis, University of California, Berkeley, 2003. 37

[RSF+05] Michael Renaud, Tom Sterken, Paolo Fiorini, Robert Puers, Kris Baert, and Chris Van Hoof. Scavenging energy from human body: design of a piezoelectric transducer. In *Solid-State Sensors, Actuators and Microsystems, 2005. Digest of Technical Papers. TRANSDUCERS'05. The 13th International Conference on*, volume 1, pages 784–787. IEEE, 2005. 4

[RSS06] Miriam Rosenbaum, Uwe Schröder, and Fritz Scholz. Investigation of the electrocatalytic oxidation of formate and ethanol at platinum black under microbial fuel cell conditions. *Journal of Solid State Electrochemistry*, 10(10):872–878, October 2006. 32

[RW04] S Roundy and P K Wright. A piezoelectric vibration based generator for wireless electronics. *Smart Materials and Structures*, 13(5):1131–1142, October 2004. xix, 5, 6

[RWN09] E Romero, R O Warrington, and M R Neuman. Energy scavenging sources for biomedical sensors. *Physiological Measurement*, 30(9):R35–R62, September 2009. 4, 15

[RWP02] Shad Roundy, Paul K. Wright, and Kristofer SJ Pister. Micro-electrostatic vibration-to-electricity converters. In *ASME 2002 International Mechanical*

Engineering Congress and Exposition, pages 487–496. American Society of Mechanical Engineers, 2002. 37

[RWR03] Shad Roundy, Paul K. Wright, and Jan Rabaey. A study of low level vibrations as a power source for wireless sensor nodes. *Computer communications*, 26(11):1131–1144, 2003. 2, 5, 56

[SAFW02] Marc Strasser, Robert Aigner, Martin Franosch, and Gerhard Wachutka. Miniaturized thermoelectric generators based on poly-si and poly-SiGe surface micromachining. *Sensors and Actuators A: Physical*, 97:535–542, 2002. xix, 23, 24

[SBK08] Ibrahim Sari, Tuna Balkan, and Haluk Kulah. An electromagnetic micro power generator for wideband environmental vibrations. *Sensors and Actuators A: Physical*, 145-146:405–413, July 2008. 11

[SBK10] Ibrahim Sari, Tuna Balkan, and Haluk Külah. An electromagnetic micro power generator for low-frequency environmental vibrations based on the frequency upconversion technique. *Journal of Microelectromechanical Systems*, 19(1):14–27, February 2010. xix, 11, 12

[Ses99] G. H. Sessler. *Electrets*. Laplacian Press, 1999. 17

[SFB+03] Tom Sterken, Paolo Fiorini, Kris Baert, RAPR Puers, and GABG Borghs. An electret-based electrostatic/spl mu/-generator. In *TRANSDUCERS, Solid-State Sensors, Actuators and Microsystems, 12th International Conference on, 2003*, volume 2, pages 1291–1294. IEEE, 2003. xix, 17, 18

[SFB+04] Tom Sterken, Paolo Fiorini, Kris Baert, Gustaaf Borghs, and Robert Puers. Novel design and fabrication of a MEMS electrostatic vibration scavenger. *Proc. PowerMEMS*, pages 18–21, 2004. 17

[SHBS14] K. Sandeman, C. Hopwood, D. Brook, and L. Sallows. *Ferromagnetic Materials*. University of Cambridge. http://www.doitpoms.ac.uk/tlplib/ferromagnetic/printall.php, 2014. 101

[SLG08] Gael Sebald, Elie Lefeuvre, and Daniel Guyomar. Pyroelectric energy conversion: optimization principles. *Ultrasonics, Ferroelectrics and Frequency Control, IEEE Transactions on*, 55(3):538–551, 2008. 27

[SLW07] Y C Shu, I C Lien, and W J Wu. An improved analysis of the SSHI interface in piezoelectric energy harvesting. *Smart Materials and Structures*, 16(6):2253–2264, December 2007. 67

[SN92] V. Sundar and R. E. Newnham. Electrostriction and polarization. *Ferroelectrics*, 135(1):431–446, 1992. 65

[Sny04] G. Jeffrey Snyder. Application of the compatibility factor to the design of segmented and cascaded thermoelectric generators. *Applied physics letters*, 84(13):2436–2438, 2004. 22

[Sny08] G. Jeffrey Snyder. Small thermoelectric generators. *The Electrochemical Society Interface*, 17(3):54, 2008. 23

[SOWM08] C.R. Saha, T. O'Donnell, N. Wang, and P. McCloskey. Electromagnetic generator for harvesting energy from human motion. *Sensors and Actuators A: Physical*, 147(1):248–253, September 2008. xix, 10

[SP01] Nathan S. Shenck and Joseph A. Paradiso. Energy scavenging with shoe-mounted piezoelectrics. *Ieee Micro*, 21(3):30–42, 2001. xviii, 4, 5

[Spa51] D. C. Spanner. The peltier effect and its use in the measurement of suction pressure. *Journal of Experimental Botany*, 1951. 20

[SPG08] Gael Sebald, Sebastien Pruvost, and Daniel Guyomar. Energy harvesting based on ericsson pyroelectric cycles in a relaxor ferroelectric ceramic. *Smart Materials and Structures*, 17(1):015012, February 2008. 27, 28

[SS99] Ingo Stark and Matthias Stordeur. New micro thermoelectric devices based on bismuth telluride-type thin solid films. In *Thermoelectrics, 1999. Eighteenth International Conference on*, pages 465–472. IEEE, 1999. 24

[SSW94] T. J. Silva, S. Schultz, and Dieter Weller. Scanning near-field optical microscope for the imaging of magnetic domains in optically opaque materials. *Applied physics letters*, 65(6):658–660, 1994. 99

[ST08] G. Jeffrey Snyder and Eric S. Toberer. Complex thermoelectric materials. *Nature Materials*, 7(2):105–114, February 2008. 21

[Sta06] Ingo Stark. Invited talk: Thermal energy harvesting with thermo life. In *Wearable and Implantable Body Sensor Networks, 2006. BSN 2006. International Workshop on*, pages 19–22. IEEE, 2006. 24

[Str07] Julius Adams Stratton. *Electromagnetic theory*, volume 33. John Wiley & Sons, 2007. 65

[Stu13] Andrew Morrison Stumpff, 2013. Law is a Fractal: The Attempt to Anticipate Everything. 38

[SUK+90] M. R. Scheinfein, J. Unguris, M. H. Kelley, D. T. Pierce, and R. J. Celotta. Scanning electron microscopy with polarization analysis (SEMPA). *Review of scientific instruments*, 61(10):2501–2527, 1990. 99

[SY97] C. Shearwood and R.B. Yates. Development of an electromagnetic microgenerator. *Electronics Letters*, 33(22):1883, 1997. 9

[Tak91] T. Takamatsu. Life time of thermal electrets of carnauba wax, esters, fatty acids and alcohols. In *Electrets, 1991.(ISE 7) Proceedings., 7th International Symposium on (Cat. No. 91CH3029-6)*, pages 106–110. IEEE, 1991. 17

[Tay06] Richard P. Taylor. Reduction of physiological stress using fractal art and architecture. *Leonardo*, 39(3):245–251, 2006. 38

[TCET09] Can Ozan Tan, Michael A. Cohen, Dwain L. Eckberg, and J. Andrew Taylor. Fractal properties of human heart period variability: physiological and methodological implications. *The Journal of physiology*, 587(15):3929–3941, 2009. 38

[TKK+02] Ryoichi Tashiro, Nobuyuki Kabei, Kunimasa Katayama, E. Tsuboi, and Kiichi Tsuchiya. Development of an electrostatic generator for a cardiac pacemaker that harnesses the ventricular wall motion. *Journal of Artificial Organs*, 5(4):0239–0245, 2002. xix, 13, 14

[TRS+02] Leonard M. Tender, Clare E. Reimers, Hilmar A. Stecher, Dawn E. Holmes, Daniel R. Bond, Daniel A. Lowy, Kanoelani Pilobello, Stephanie J. Fertig, and Derek R. Lovley. Harnessing microbially generated power on the seafloor. *Nature Biotechnology*, 20(8):821–825, August 2002. 32

[TS03] A. M. Tishin and Y. I. Spichkin. *The Magnetocaloric Effect and its Applications*. CRC Press, September 2003. 102

[TSKS06] Takumi Tsutsumino, Yuji Suzuki, Nobuhide Kasagi, and Yoshihiko Sakane. Seismic power generator using high-performance polymer electret. In *Micro Electro Mechanical Systems, 2006. MEMS 2006 Istanbul. 19th IEEE International Conference on*, pages 98–101. IEEE, 2006. 17

[TTO+00] Hideki Takayasu, Misako Takayasu, Mitsuhiro P. Okazaki, Kouhei Marumo, and Tokiko Shimizu. Fractal properties in economics. *arXiv preprint cond-mat/0008057*, 2000. 38

[UCL07] M. Ujihara, G. P. Carman, and D. G. Lee. Thermal energy harvesting device using ferromagnetic materials. *Applied Physics Letters*, 91(9):093508, 2007. xxi, 98

[WDJ99] Brendt Wohlberg and Gerhard De Jager. A review of the fractal image coding literature. *Image Processing, IEEE Transactions on*, 8(12):1716–1729, 1999. 38

[Wil00] Stuart Wilkinson. "gastrobots"–benefits and challenges of microbial fuel cells in foodpowered robot applications. *Autonomous Robots*, 9(2):99–111, 2000. 32

[WKP10] Banqiu Wu, Ajay Kumar, and Sharma Pamarthy. High aspect ratio silicon etch: a review. *Journal of Applied Physics*, 108(5):051101, 2010. 41

[WLP+14] L.Q. Wang, M. Lallart, L. Petit, L. Lebrun, P.J. Cottinet, and D. Guyomar. Low-cost charge of electrostrictive polymers for efficient energy harvesting. *Journal of Intelligent Material Systems and Structures*, Accepted:167–184, 2014. 67

[WLS+07] Sheng Wang, Kwok Ho Lam, Cheng Liang Sun, Kin Wing Kwok, Helen Lai Wa Chan, Ming Sen Guo, and Xing-Zhong Zhao. Energy harvesting with piezoelectric drum transducer. *Applied Physics Letters*, 90(11):113506, 2007. 20

[WSH+01] C. B. Williams, C. Shearwood, M. A. Harradine, P. H. Mellor, T. S. Birch, and R. B. Yates. Development of an electromagnetic micro-generator. In *Circuits, Devices and Systems, IEE Proceedings-*, volume 148, pages 337–342. IET, 2001. xix, 9

[Wu13] Yi Chieh Wu. *Analyse et considérations pratiques de techniques de conversion et récupération d'énergie piézoélectrique linéaires et non-linéaires*. PhD thesis, INSA de Lyon, September 2013. xix, 6, 7

[WY08] Lei Wang and F G Yuan. Vibration energy harvesting by magnetostrictive material. *Smart Materials and Structures*, 17(4):045009, August 2008. 20

[YHD12] Zhaochu Yang, Einar Halvorsen, and Tao Dong. Power generation from conductive droplet sliding on electret film. *Applied Physics Letters*, 100(21):213905, 2012. xix, 18, 19

[YWSS05] Junghoon Yeom, Yan Wu, John C. Selby, and Mark A. Shannon. Maximum achievable aspect ratio in deep reactive ion etching of silicon due to aspect ratio dependent transport and the microloading effect. *Journal of Vacuum Science & Technology B: Microelectronics and Nanometer Structures*, 23(6):2319, 2005. 41

[ZBZ98a] Q. M. Zhang, Vivek Bharti, and X. Zhao. Giant electrostriction and relaxor ferroelectric behavior in electron-irradiated poly (vinylidene fluoride-trifluoroethylene) copolymer. *Science*, 280(5372):2101–2104, 1998. 66

[ZBZ+98b] Xing-Zhong Zhao, Vivek Bharti, Q. M. Zhang, T. Romotowski, F. Tito, and R. Ting. Electromechanical properties of electrostrictive poly(vinylidene fluoride–trifluoroethylene) copolymer. *Applied Physics Letters*, 73(14):2054–2056, October 1998. 66

[ZCA+13] A. Zebda, S. Cosnier, J.-P. Alcaraz, M. Holzinger, A. Le Goff, C. Gondran, F. Boucher, F. Giroud, K. Gorgy, H. Lamraoui, and P. Cinquin. Single glucose biofuel cells implanted in rats power electronic devices. *Scientific Reports*, 3, March 2013. 33

[ZS08] Xuanhe Zhao and Zhigang Suo. Electrostriction in elastic dielectrics undergoing large deformation. *Journal of Applied Physics*, 104(12):123530, 2008. 64

FOLIO ADMINISTRATIF

THÈSE SOUTENUE DEVANT L'INSTITUT NATIONAL DES SCIENCES APPLIQUÉES DE LYON

NOM : **WANG** DATE de SOUTENANCE : **05 Novembre 2014**

Prénoms : **Liuqing**

TITRE : **Etude et développement de nouveaux matériaux et systèmes électroactifs pour la récupération d'énergie - Development of energy harvesting systems based on new electroactive materials and structures**

NATURE : **Doctorat** Numéro d'ordre : **2014-ISAL-0083**

École Doctorale : **Électronique, Électrotechnique et Automatique de Lyon**
Spécialité : **Énergie et Systèmes**

Cote B.I.U. - Lyon : T 50/210/19 / et bis CLASSE :

RÉSUMÉ :
La croissance formidable des dispositifs sans fils et autonomes (réseaux de capteurs, objets connectés) voit actuellement son développement limité par les batteries qui présente une durée de vie limitée et ainsi soulève des problèmes de maintenance. Afin de palier à cette limitation, l'utilisation de l'énergie directement disponible dans l'environnement immédiat du dispositif, conduisant au concept de "récupération d'énergie", est une voie fortement explorée depuis une dizaine d'années.
Ainsi, l'objectif de cette thèse a été de développer de nouvelles techniques et/ou d'utiliser de nouveaux principes de conversion afin de proposer des alternatives aux techniques de récupération d'énergie classiques.
Dans un premier temps, l'optimisation de récupérateurs électrostatiques a été étudiée. Les performances de ces systèmes étant fortement liées à la variation de capacité, une structure fractale, permettant un accroissement important des surfaces en regard entre deux électrodes (et donc de la capacité) lorsque ces dernières sont proches, a été proposée et modélisée. Il est ainsi montrer un accroissement significatif des possibilités de récupération d'énergie ; ces dernières étant étroitement liées à l'amplitude de vibration du système.
Le second axe de recherche de cette thèse s'est attelé à développer un modèle haut niveau simple mais précis pour les structure utilisant des polymères électrostrictifs fonctionnant en flexion. Une analyse énergétique a permis de mettre en place un modèle électromécanique masse-ressort-amortisseur couplé avec une source de courant contrôlée par les excitations mécaniques et électriques du système, permettant ainsi une conception plus aisée du microgénérateur.
Enfin, la dernière partie de cette thèse s'est intéressée à la conversion d'énergie thermique utilisant la variation de perméabilité des matériaux ferromagnétiques, ouvrant de nouvelles possibilités de conversion de l'énergie. En particulier, une technique simple et autonome consiste à créer un champ magnétique de polarisation à l'aide d'un aimant, permettant une variation du flux magnétique lors d'un changement de température, qui peut être converti sous forme électrique à l'aide d'un bobinage.

MOTS-CLÉS : **Conversion d'énergie, Récupération d'énergie, Systèmes électroactifs, Electrostatique, Electrostriction, Ferromagnétisme**

Laboratoire(s) de recherche : **Laboratoire de Génie Électrique et Ferroélectricité (LGEF) - INSA Lyon**

Directeur de thèse : **Pr. Lionel PETIT**
Co-directeur de thèse : **Dr. Mickaël LALLART**

Président du Jury : **Pr. Benoît GUIFFARD**
Composition du Jury :
Pr. Yves BERNARD, Dr.-HDR Frédéric GIRAUD, Pr. Benoît GUIFFARD, Dr. Adrien BADEL, Dr.-HDR Gaël SEBALD, Pr. Lionel PETIT, Dr. Mickaël LALLART